Theses and Dissertations

May 2017

# Investigation of Membrane Receptors' Oligomers Using Fluorescence Resonance Energy Transfer and Multiphoton Microscopy in Living Cells

Ashish K. Mishra
*University of Wisconsin-Milwaukee*

www.manaraa.com

INVESTIGATION OF MEMBRANE RECEPTORS' OLIGOMERS USING FLUORESCENCE

RESONANCE ENERGY TRANSFER AND MULTIPHOTON MICROSCOPY

IN LIVING CELLS

by

Ashish K. Mishra

A Dissertation Submitted in

Partial Fulfillment of the

Requirements for the Degree of

Doctor of Philosophy

in Physics

at

The University of Wisconsin-Milwaukee

May 2017

# ABSTRACT

INVESTIGATION OF MEMBRANE RECEPTORS' OLIGOMERS USING FLUORESCENCE
RESONANCE ENERGY TRANSFER AND MULTIPHOTON MICROSCOPY
IN LIVING CELLS

by

Ashish K. Mishra

The University of Wisconsin-Milwaukee, 2017
Under the Supervision of Professor Valerica Raicu

Investigating quaternary structure (oligomerization) of macromolecules (such as proteins and nucleic acids) in living systems (*in vivo*) has been a great challenge in biophysics, due to molecular diffusion, fluctuations in several biochemical parameters such as pH, quenching of fluorescence by oxygen (when fluorescence methods are used), etc.

We studied oligomerization of membrane receptors in living cells by means of Fluorescence (Förster) Resonance Energy Transfer (FRET) using fluorescent markers and two photon excitation fluorescence micro-spectroscopy. Using suitable FRET models, we determined the stoichiometry and quaternary structure of various macromolecular complexes. The proteins of interest for this work are : (1) sigma-1 receptor and (2) rhodopsin, are described as below.

(1) Sigma-1 receptors are molecular chaperone proteins, which also regulate ion channels. S1R seems to be involved in substance abuse, as well as several diseases such as Alzheimer's. We studied S1R in the presence and absence of its ligands haloperidol (an antagonist) and pentazocine +/- (an agonist), and found that at low concentration they reside as a mixture

of monomers and dimers, and that they may form higher order oligomers at higher concentrations.

(2) Rhodopsin is a prototypical G protein coupled receptor (GPCR) and is directly involved in vision. GPCRs form a large family of receptors that participate in cell signaling by responding to external stimuli such as drugs, thus being a major drug target (more than 40% drugs target GPCRs). Their oligomerization has been largely controversial. Understanding this may help understanding the functional role of GPCRs oligomerization, and may lead to the discovery of more drugs targeting GPCR oligomers. It may also contribute toward finding a cure for Retinitis Pigmentosa, which is caused by a mutation (G188R) in rhodopsin, a disease which causes blindness and has no cure so far. Comparing healthy rhodopsin's oligomeric structure with that of the mutant, may give cues to find the cure.

iv

*Dedicated with love,*

*To my wife, daughter and my parents*

# TABLE OF CONTENTS

viii

x

xii

# LIST OF FIGURES

xvi

xvii

# ACKNOWLEDGEMENTS

First and foremost, I wish to thank my major advisor, Professor Valerică Raicu -- notably for his encouragement, patience and involvement in my work, all of which have played a direct role in helping me become the experimentalist I am today. I joined his research group in the fall of 2010, primarily because of the particular research he was involved in, and because of what I had heard about him personally; in either regard, I have not been disappointed. The first project he assigned me was on developing microfluidic channels, which helped me learning how to use two photon microscope and about fluorescence signal detection. As I learned these techniques, he encouraged me to work on membrane receptors. Having little background in experimental biophysics, I started doing experiments to address important problems of protein-protein interaction under his supervision. Prof. Raicu always showed confidence in me and taught me to tackle complex problems by starting with the simple ones that I understand, then building up, step by step, to form a firm foundation.

Professor Julie A. Oliver (Department of Biological Sciences at the University of Wisconsin-Milwaukee), taught me the experimental techniques required for cell culture and gene expression in mammalian cells, which I needed to study protein-protein interaction. I would like to thank her for her time and patience to teach me these techniques. Additionally, I thank Dr. Oliver and her previous lab assistant, Amber Grupe, for advising/helping me on cell culture and gene expression and for letting me use her tissue culture facility.

# Chapter 1: Introduction

The main objective of this chapter is to present the general framework of the research described in this thesis. It is divided into three sections, as follow: section 1 includes levels of protein structures and types of bonds associated with different levels of protein structures; section 2 reviews characteristics and properties of G Protein-Coupled Receptors (GPCRs); and section 3 describes the structure and functions of a sigma-1 receptor (S1R).

## 1.1 Protein structure

Proteins are structurally the most complex molecules on Earth. They evolved through billions of years to get their current level of sophistication. Proteins consist of one of more arrays of amino acid residues and come in a variety of shapes and sizes. They perform a vast variety of functions in living organisms. Most proteins are between 50 and 2000 amino acids long [1]. The average protein size for humans is 375 amino acids, and the average amino acid molecular weight is 100 Da ($1 \, \text{Da} = 1.67 \times 10^{-27}$ kg), which brings the average human protein molecular weight to 37.5 kDa [2].

Most proteins fold into unique three-dimensional structures. Some of them do it on their own, based on the chemical and physical interactions of constituent amino acids, while others need assistance from specialized molecules called molecular chaperones [3] – a type of protein that assists in protein folding. Protein structure is generally divided into four levels: primary, secondary, tertiary and quaternary. The sequence of amino acids (or the amino acid chain) is called primary structure. The portion of a protein molecule which folds to form a locally organized structure, such as alpha helix or beta sheet (see below), is called secondary structure. The full three-dimensional structure of a molecule is called tertiary structure. The association of two or

1

more protein molecules for functional purposes is called quaternary structure. Each of these structures will be described in detail, below.

### 1.1.1 Physical interactions in protein structures

Covalent forces mediate formation of the basic (primary) structure of proteins. Van der Waals radii and other constraints limit bond angles in a protein molecule. There are three types of forces shaping the protein structure: hydrogen bonds, electrostatic attractions and Van der Waals forces. These forces are about 3 to 300 times weaker than covalent forces, which cause the primary structure of proteins. However, when many weak monovalent bonds act together (in parallel), they provide a definitive shape and stability to a part of the polypeptide chain. Another effect that plays a role in protein folding is *hydrophobicity*. Hydrophobicity is the physical property of a molecule which makes it repel from a mass of water. Therefore, such molecules tend to minimize their exposure to water, such as embedding themselves in plasma membranes, or attaching to other hydrophobic surfaces [4, 5]. There are two types of amino acids:  polar and nonpolar. Nonpolar residues are forced to group together in an aqueous medium in order to minimize their disruptive effect on the hydrogen-bonded network of water molecules. So that nonpolar amino acids of the proteins tend to be on the interior of a protein molecule to minimize interaction with water molecules, while the polar amino acids tend to form hydrogen bonds with water and other polar amino acids, and polar parts of backbone (polypeptide chain).

### 1.1.2 Primary structure

There are several thousands of proteins known and each has its unique sequence of amino acids (i.e., primary structure). Primary structure is a linear structure of amino acids. This gives each protein a unique identity. The amino acids in the primary structure are linked to each other by the peptide bonds. They form a polypeptide backbone, which is a repeated structure of the atoms along

2

with the core of polypeptide chain. The peptide bonds are covalent in nature. Primary structure is constructed during a phase of protein (bio)synthesis, which is called *translation*.

This repeated chain of three atoms (amide N, alpha carbon $C_{alpha}$ and carbonyl C) is also called the protein backbone. By convention, the protein sequence is reported, starting from N (amine) group and ending at C (carboxyl) group. The unbranched chains of amino acids are called polypeptides. However, the amino acid can also cross-link, often by disulfide bonds.

Proteins (or polypeptides) are polymer chains. The monomeric units of these biopolymers are amino acids (referred to an amino acid residue in biochemistry). Short chains of amino acids are linked covalently by peptide (amine) bonds, which form between the carboxyl (COOH) group of one amino acid and the amine ($NH_2$) group of another amino acid (see figure 1.1).

A shown in figure 1.1, there are twenty-two amino acids, that comprise all of the proteins. The position of each amino acid in a protein determines the structure and shape of each protein molecule, and describes its function in a cell.

3

# HYDROPHOBIC (NONPOLAR) AMINO ACIDS

### Alanine (Ala, A)

$$^{+}H_3N - \overset{\overset{\displaystyle H}{|}}{\underset{\underset{\displaystyle CH_3}{|}}{C}} - COO^{-}$$

### Isoleucine (Ile, I)

$$^{+}H_3N - \overset{\overset{\displaystyle H}{|}}{C} - COO^{-}$$
$$H - \overset{}{C} - CH_3$$
$$CH_2$$
$$CH_3$$

### Leucine (Leu, L)

$$^{+}H_3N - \overset{\overset{\displaystyle H}{|}}{C} - COO^{-}$$
$$CH_2$$
$$CH$$
$$H_3C \qquad CH_3$$

### Methionine (Met, M)

$$^{+}H_3N - \overset{\overset{\displaystyle H}{|}}{C} - COO^{-}$$
$$CH_2$$
$$CH_2$$
$$S$$
$$CH_3$$

### Phenylalanine (Phe, F)

$$^{+}H_3N - \overset{\overset{\displaystyle H}{|}}{C} - COO^{-}$$
$$CH_2$$

### Proline (Pro, P)

$$^{+}H_2N - \overset{\overset{\displaystyle H}{|}}{C} - COO^{-}$$
$$H_2C \qquad CH_2$$
$$CH_2$$

### Tryptophan (Trp, W)

$$^{+}H_3N - \overset{\overset{\displaystyle H}{|}}{C} - COO^{-}$$
$$CH_2$$
$$C = CH$$
$$NH$$

### Valine (Val, V)

$$^{+}H_3N - \overset{\overset{\displaystyle H}{|}}{C} - COO^{-}$$
$$CH$$
$$H_3C \qquad CH_3$$
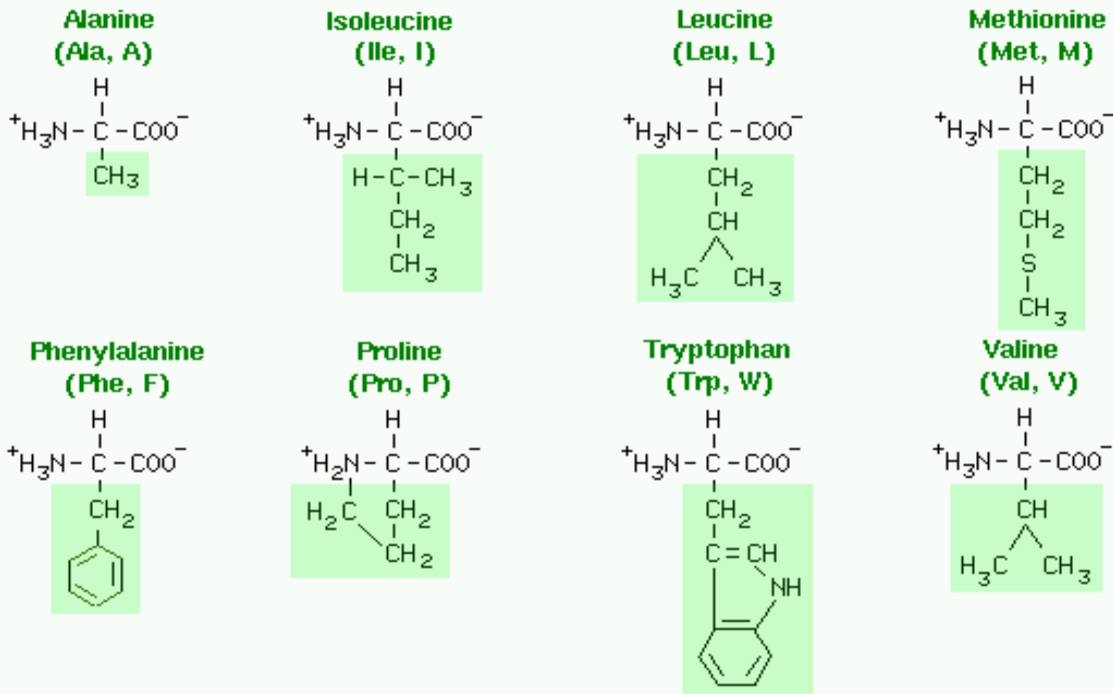
# HYDROPHILIC (POLAR) UNCHARGED AMINO ACIDS

### Asparagine (Asn, N)

$$^{+}H_3N - \overset{\overset{\displaystyle H}{|}}{C} - COO^{-}$$
$$CH_2$$
$$C$$
$$H_2N \qquad O$$

### Cysteine (Cys, C)

$$^{+}H_3N - \overset{\overset{\displaystyle H}{|}}{C} - COO^{-}$$
$$CH_2$$
$$SH$$

### Glutamine (Gln, Q)

$$^{+}H_3N - \overset{\overset{\displaystyle H}{|}}{C} - COO^{-}$$
$$CH_2$$
$$CH_2$$
$$C$$
$$H_2N \qquad O$$

### Glycine (Gly, G)

$$^{+}H_3N - \overset{\overset{\displaystyle H}{|}}{C} - COO^{-}$$
$$H$$

### Serine (Ser, S)

$$^{+}H_3N - \overset{\overset{\displaystyle H}{|}}{C} - COO^{-}$$
$$CH_2OH$$

### Threonine (Thr, T)

$$^{+}H_3N - \overset{\overset{\displaystyle H}{|}}{C} - COO^{-}$$
$$H - C - OH$$
$$CH_3$$

### Tyrosine (Tyr, Y)

$$^{+}H_3N - \overset{\overset{\displaystyle H}{|}}{C} - COO^{-}$$
$$CH_2$$
$$OH$$

4

**POSITIVELY-CHARGED AMINO ACIDS**

Arginine (Arg, R)    Histidine (His, H)    Lysine (Lys, K)

**NEGATIVELY-CHARGED AMINO ACIDS**

Aspartic Acid (Asp, D)    Glutamic Acid (Glu, E)

**Figure 1.1. The twenty amino acids found in proteins.** There are an equal number of polar and non-polar side chains. However, some side chains listed here are long enough to have some non-polar properties. This figure is adapted, with permission, from [1].

In the alpha amino acid (also called amino acid residue), each residue contains a backbone and a side chain. The side chain is unique to each amino acid. Amino acid sequence partly decides the shape of a protein.

### 1.1.3 Secondary structure

Amino acids in the primary structure interact with their near neighbors via hydrogen bonds. This interaction gives the linear chain of amino acids (primary structure) [2, 6, 7], a local structure called secondary structure. There are two types of secondary structure found; (1) α helixes and (2) β sheets or β barrels, as shown in figure 1.2.

Secondary structures are also called *protein domains*. Twisting a single polypeptide chain around itself (which forms a rigid cylindrical shape), creates an alpha helix. For each fourth peptide of the chain, a hydrogen bond is formed between the carboxyl group and the neighboring amine group of the chain. Each turn of the helix contains 3.6 amino acids. Alpha helixes are found in the abundance of membrane proteins such as transporter proteins and receptors. The transmembrane

5

domains (which fall within the lipid bilayer) of these proteins usually consist of alpha helixes, which largely contain amino acids with nonpolar side chains. Another type of secondary structure is called *structural motif,* which is a three-dimensional structure common to several different proteins. An example of structural motif is motif is coiled-coil which is created by coiling of several alpha helixes together.  The hydrophilic backbone is shielded from the hydrophobic environment of the membrane by hydrogen bonding to itself, forming an alpha helix and by protruding nonpolar side chains.

In some other proteins, consisting of coiled-coils, most of the nonpolar side chains are on the same side, which causes many alpha helixes to twist around each other to shield nonpolar side chains inward, giving these proteins a particular rigid structure, e.g., alpha-keratin, which form intracellular fibers.

The core of the most proteins are arranged in beta sheets. These beta sheets are formed either from the regions of polypeptide backbone, running in a same direction or in an opposite direction, termed as parallel or antiparallel beta sheets respectively. In both cases, these participating backbone segments are held tightly by hydrogen bonds between peptides of neighboring sheets, which provide the sheets with a very rigid structure. A single protein can contain multiple alpha helixes and beta sheets.
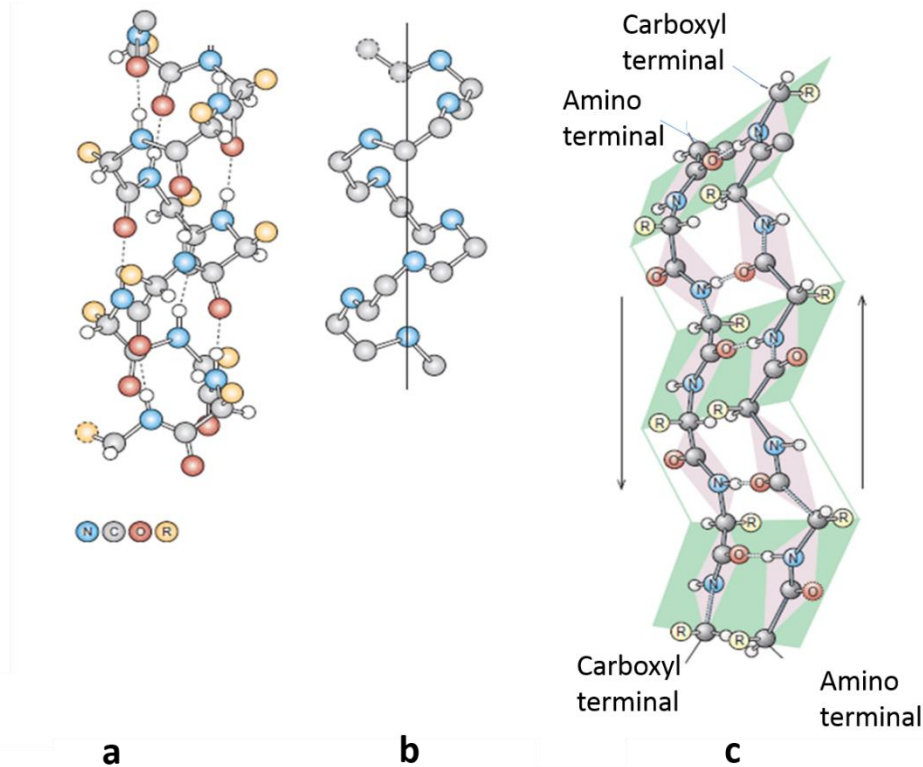
**Figure 1.2. An example of protein secondary structure. (a)**: The positions of the amino acids in the α-helix are shown with the helical backbone in gray and blue. The dashed lines represent hydrogen bonds between hydrogen and oxygen atoms on nearby amino acids. The small white circle represents hydrogen atoms. **(b):** A simplified rendition of the α-helix, showing only the atoms in helical backbone. **(c)**: An antiparallel β-sheet. Two polypeptide chains are arranged side by side, with hydrogen bonds (dashed line) between them. The green and white planes show that the β-sheet is pleated. The chains are antiparallel in the sense that the amino terminus of one and the carboxyl terminus of the other amino acids are at the top. The arrows run from the amino to carboxyl terminus of the two β-strands. The arrows indicate that the two β-strands, running from amino to carboxyl terminals, are in the opposite directions. Parallel β -sheets, in which the b-strands run in the same direction, also exists. This figure is adapted, with permission, from [8].

Alpha helix and beta-pleated sheets are the most common forms of the secondary structure. Another type of secondary structure is a *turn*. These turns connect alpha helix and beta-pleated sheets in a protein.

## 1.1.4 Tertiary structure

How proteins fold into an overall three-dimensional structure, is called tertiary structure. Tertiary structures consist of a single polypeptide chain (backbone) and several secondary structures or

7

protein domains. Proteins fold into a lowest energy conformation, which are the conformation with minimum free energy. Many proteins fold into a roughly spherical looking shape, could be defined as the globular shaped proteins. There are several classes of globular proteins because there are many ways of folding into a roughly spherical shape.

Scientists, often need to denature proteins using certain chemical (e.g., detergents) or physical agents to purify them out of their native cell environment. The denaturing process breaks non-covalent bonds, thereby linearizing the polypeptides. But after the purification, when detergents are removed, these proteins refold (renature) to form shapes of single conformation, which minimize the energy. This proves that the amino acids and their positions in the polypeptides have the complete information needed to form a three-dimensional stable structure and do not need necessarily any external help to fold. However, there are proteins called molecular chaperones (for example, the sigma-1 receptor, which is investigated in this thesis) which assist other proteins in folding. The key reason for the need of molecular chaperones is the crowded cytoplasmic/endoplasmic environment when the proteins are formed, in which their hydrophobic regions can associate with those of other proteins around, rather than folding locally into secondary structures. This process forms larger non-functional aggregates and not the desired single proteins. Molecular chaperones prevent the proteins from forming such large aggregates at the secondary structural level, and enhances the reliability of protein folding. Although proteins are complex in structure, there are multiple ways of representing their structure, for instance, polypeptide backbone model, ribbon model, and wire models representing amino acid side chains, and solid spheres representing amino acid residues.

8

## 1.1.5 Quaternary structure

A large fraction of cellular proteins associate in groups of two or more proteins forming a protein-complex. The structure of the proteins association complexes at this level is called quaternary structure. A quaternary structure is stabilized with noncovalent interactions and disulfide bonds. Each subunit of the quaternary structure is called a monomer. When two monomers associate, their quaternary structure is called a dimer. Association of more than two monomers is called an oligomer. The oligomer of three and four subunits are named trimer and tetramer respectively. Similarly, for the oligomers of order higher than four; penta, hexa, octa, deca, etc. -mer nomenclature is used. The association of like proteins is called *homo-oligomer* (or *homo dimer* in case of two proteins). And in the case of the complexes formed of subunits from different species, their structure is called *hetero-oligomer*. This dissertation research work focuses on investigating the quaternary structure of two membrane proteins, which are sigma-1 receptor and rhodopsin.

## 1.1.6 Protein domains

Besides the above-mentioned levels of protein structure, there is another unit of protein structure called protein domain, which is of vital importance as divulged by studies of evolution, conformation and function of proteins. Domains are secondary structures of proteins, which are also called motifs. A protein domain, a contiguous part of protein can fold independently of the rest of the protein molecule and form a compact stable structure.

There are several such domains, which are common in many proteins. These folded domains are mostly independent of folding of other domains of the same protein. Therefore, each domain is like an independent subunit when it comes to folding.

A protein domain generally contains 40 to 350 amino acids. A domain is the modular unit from which many proteins are constructed. Different domain often has different functional roles,

9

like functions in signaling pathways, regulatory roles, participating in catalytic activities, etc. A short protein can be made of a single domain, or a large protein can have several dozens of domains linked by short, relatively unstructured part of polypeptide chain, which act as flexible pivots between the domains.

Proteins [2, 9] are divided into three categories based on their tertiary structure, that are as follows:

- Globular proteins [10]

- Fibrous proteins  [11]

- Membrane proteins [4, 11]

Membrane proteins, which are more relevant to this dissertation work, are described below.

## 1.1.7 Membrane proteins

Membrane portions, as the name suggest, are located in the cell plasma membranes. Plasma membranes of cells are very thin layers (~ 5-10 nm) which consist of a bi-layered matrix of phosphor-lipids and contains proteins superficially or fully integrated into the bi-layer.
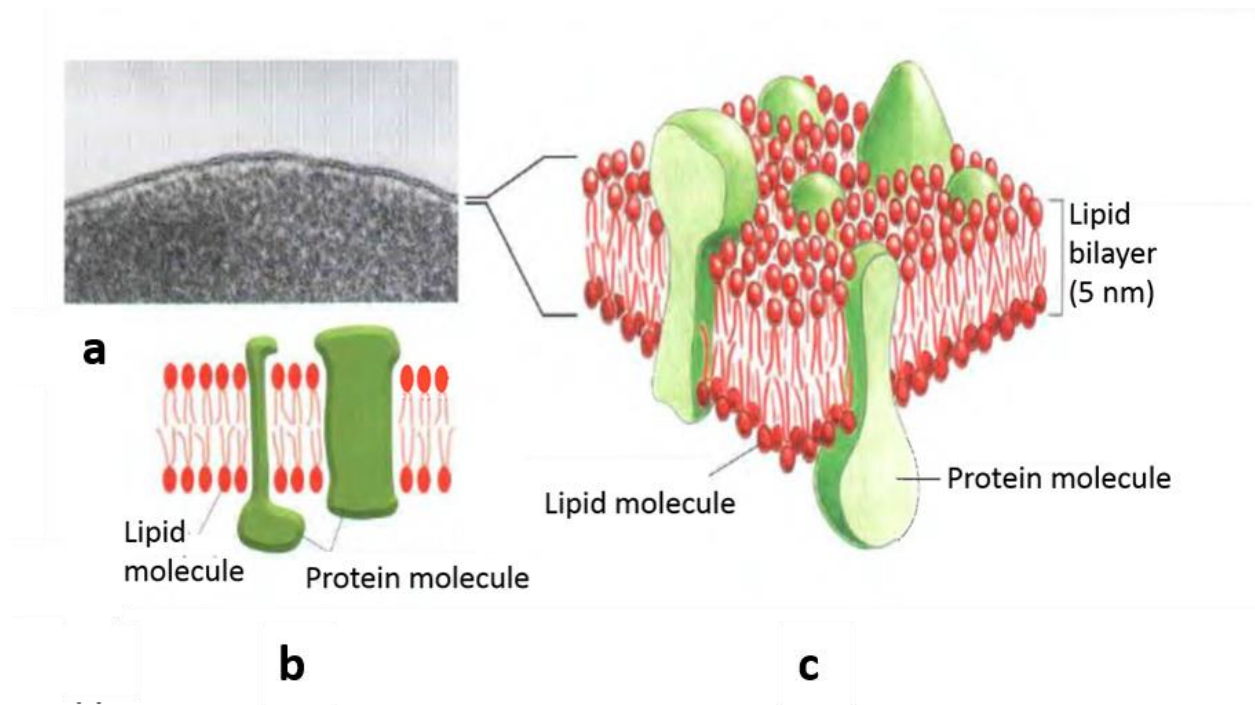
**Figure 1.3. Three views of a cell membrane. (a):** An electron micrograph of a plasma membrane (of a human red blood cell) seen in cross section. **(b)** and **(c)** show two-dimensional and three-dimensional views of a cell membrane and the general disposition of its lipid and protein constituents. This figure is reproduced with permission from [2].

There are three types of membrane proteins:

- peripheral membrane proteins

-  integral membrane proteins

- glycosyl-phosphatidylinositol-anchored (GPI) membrane proteins

Peripheral proteins are temporarily attached to membranes, which can detach with an interaction of polar regent. The integral proteins just sit in the membrane while GPI proteins are attached to membranes through covalent bonds.

## 1.2 G Protein-coupled receptors (GPCRs)

The GPCRs are the largest family of receptors in the human body [12] and constitute a preferred target for therapeutic drugs. More than 40% drugs target GPCRs [13]. Their structural diversity

11

allows them to control many physiological activities. GPCRs bind with a variety of extracellular molecules, called ligands, such as proteins or peptides, enzymes, nucleotides and amines. The understanding\ of GPCRs' secondary structure is important because this helps in locating receptor-ligand binding pocket. When a ligand binds to a receptor, the receptor undergoes a conformational change, which activates the signaling pathway or cascade [14] .

The GPCR superfamily is classified in subfamilies denoted by A to F, α, β γ, and δ, or by numbers 1 to 5. Since the GPCRs are so diverse in their primary structure, a phylogenetic classification is used [15]. Phylogenetic classification is based on evolutionary ancestry, generating tree like classification, called cladograms., which are group of organisms that include ancestor species and its descendants.
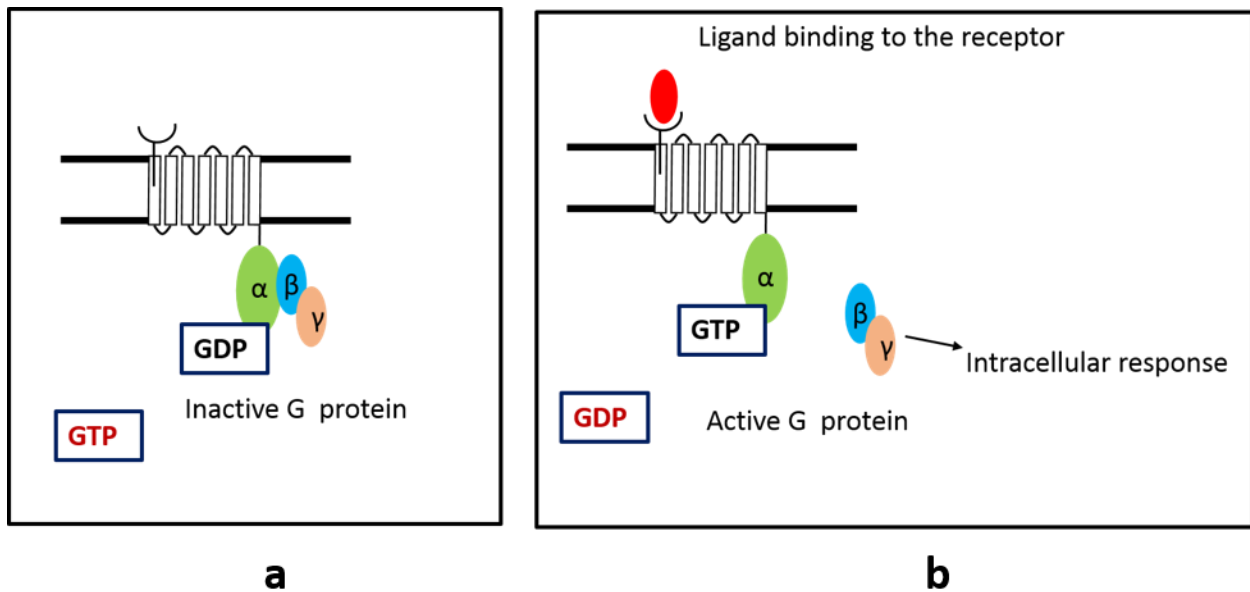


**Figure 1.4. Schematic illustrations of a G protein-coupled receptor (GPCR).** The GPCR consists of a cytosolic region, a ligand-binding extracellular region and seven transmembrane domains. The receptor is associated with a trimeric GTP-binding protein (G protein) consisting of three subunits called α, β and γ.**(a)** When no signal molecule is present; the G protein binds to GDP and is inactive. **(b)** Upon binding of a signal protein to the ligand-binding site, a conformational change of the receptor occurs. This enables the receptor to interact with the α subunit of the associated G protein, which then exchanges its bound GDP to GTP. This activates the G protein and causes the βγ subunit to dissociate, thus enabling it to relay the signal by regulating the activity of additional intracellular signaling proteins.

المنارة للاستشارات

www.manaraa.com

## 1.2.1 GPCR structure

First high-resolution crystal structure of a GPCR was presented by Palczewski and colleagues in year 2000 when they succeeded to crystalize bovine rhodopsin [16]. GPCRs have seven hydrophobic transmembrane regions, commonly represented as helix I, helix II and so on up to helix VII, which is the common for all members of the GPCR superfamily.
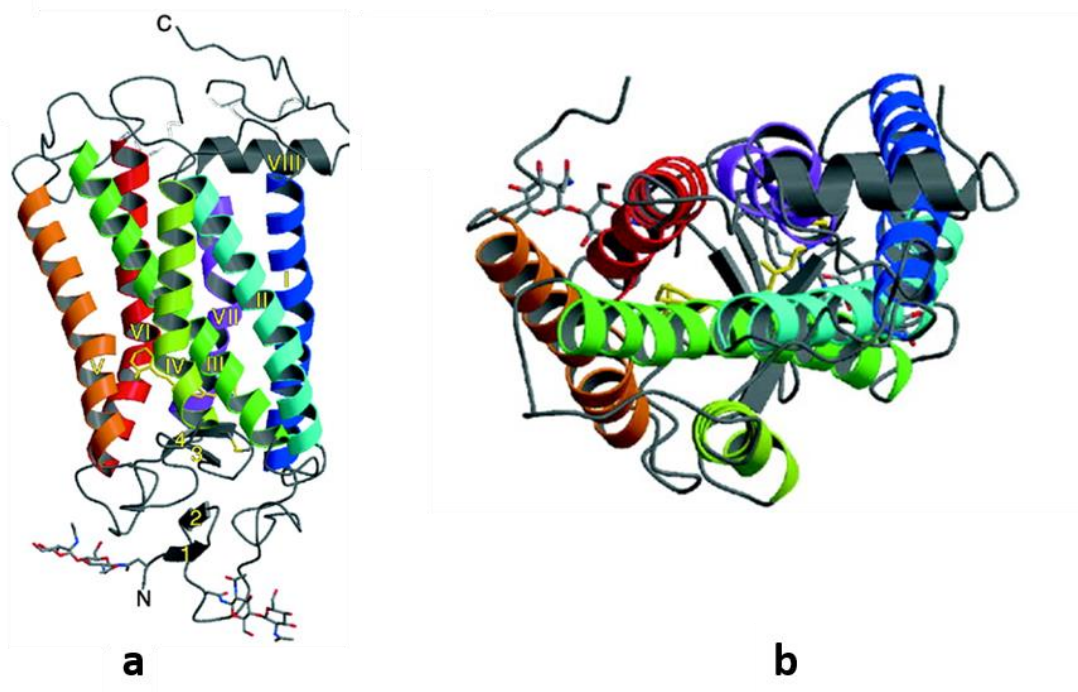


**Figure 1.5: Ribbon drawings of rhodopsin. (a):** Parallel to the plane of the membrane (stereo view), **(b):** A view into the membrane plane is seen from the cytoplasmic. This figure is reproduced with permission from [5].

The GPCRs are among the oldest proteins, which are found in five of the six kingdoms of life (except in Archaea). However, the GPCRs in plantae and bacteria do not interact with G proteins. Hence, although the names suggest, interaction with G proteins is not the common basis to all the GPCRs. However, those found in Animalia, Fungi and Protozoa are coupled with G proteins, but

there is almost no sequence similarity between the GPCRs found in Protozoa or Fungi and in Animalia.

One of the reasons for evolutionary success of GPCRs to metazoans (their natural selection) was metazoans' ability to expand, specialize and efficiently communicate, which leads to the structural diversity of the GPCRs [17, 18].

The GPCR structure knowledge can be applied to structure-based drug discovery [19]. GPCR Researches have shown, in the absence of a ligand, that the GPCRs can exist in a dynamic equilibrium of inactive (R) and active ($R^*$) states (in the presence of G protein, the active state can also convert to signaling states), and the distribution of these states can vary drastically. Binding of an agonist can shift the equilibrium towards active state (characterized by large scale structural change towards receptor's intracellular side) and binding of an antagonist can shift the equilibrium towards inactive state [20-22].

## 1.2.2 G protein binding and signaling

In the activation process, one of the major changes happens in the receptor's intercellular side, that is helix V swings away in coordination with helix VI. These two helixes are hypothesized to be in direct or indirect contact with G proteins. This phenomenon was proposed as a global toggle switch [23]. The movement of helix III and VII may also occur but their role in G proteins signaling is not clear.

Ligand-dependent activation of the GPCRs is very intriguing because binding of ligands to the vastly diverse extracellular pockets produces large-scale conformational changes on the intracellular side. Understanding ligand-dependent activity is important to selectively and efficiently design drugs [24-26].

14

### 1.2.3 Allosteric modulation of GPCRs

The GPCR signaling, which is triggered by binding of an agonist or antagonist ligand to a GPCR, can be affected by a number of endogenous or exogenous modulators such as regulatory proteins, lipids, sterols and ions [24, 27, 28]. This phenomenon is called allosteric modulation.

### 1.2.4 GPCR dimerization and oligomerization

The growing numbers of publications indicate that the GPCRs exist as dimer or oligomer and these dimers or oligomers may be important for G protein activation for at least some GPCR families [29-36]. GPCR dimerization and oligomerization has been extensively studied by using numerous techniques such as the Förster Resonance Energy Transfer (FRET), Bioluminescence Resonance Energy Transfer (BRET), cross-linking, time resolved spectroscopy and molecular simulations [37, 38]. The results of dimerization/oligomerization studies are systematically collected in a database, which is GPCR-OKB [39]. Crystallographic studies have revealed parallel dimers with substantial protein-protein interface for several receptors, including the array of dimers for rhodopsin [40], as shown in figure 1.6, κ-opioid [41] and μ-opioid [42] receptors.
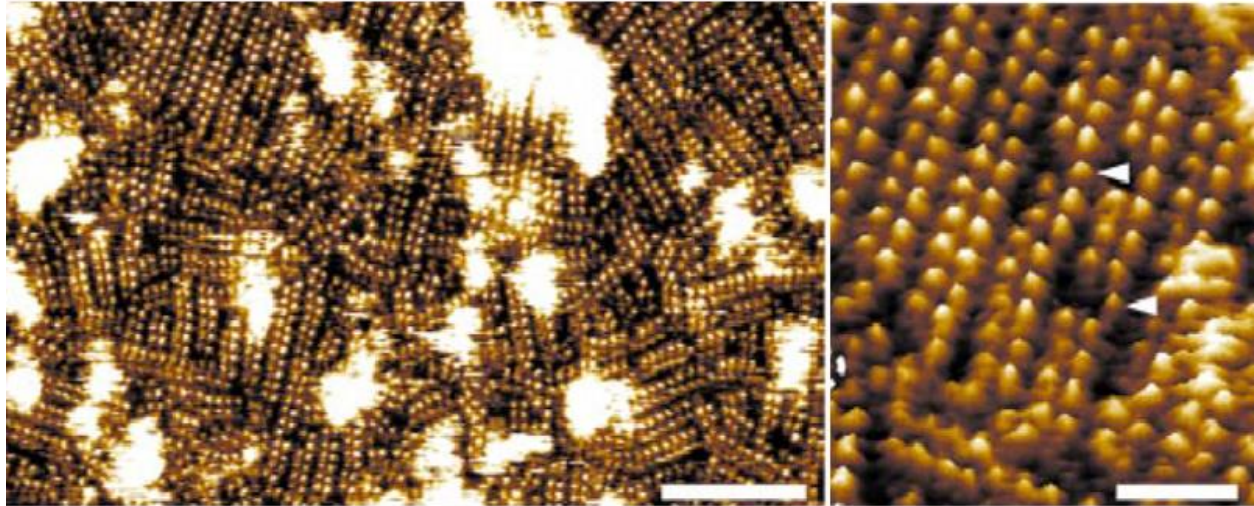
**Figure 1.6. Images showing organizations and topography of the cytoplasmic surface of rhodopsin.**
**(a)** Topography obtained using atomic-force microscopy (AFM), showing the paracrystalline arrangement of rhodopsin dimers in the native disc membrane **(b)** Magnification of a region of the topography in **a**, showing rows of rhodopsin dimers. This figure is reproduced with permission from [40].

Overall, there are two clusters of symmetric interfaces in the GPCRs based on the crystal structures, which agree with the biochemical data for rhodopsin [43], serotonin [44] and dopamine D2 [45], among other GPCRs. One of them (interface A) engages helixes I, II and VIII, and the other type (interface B) involves helixes V and VI (see figure 1.7).
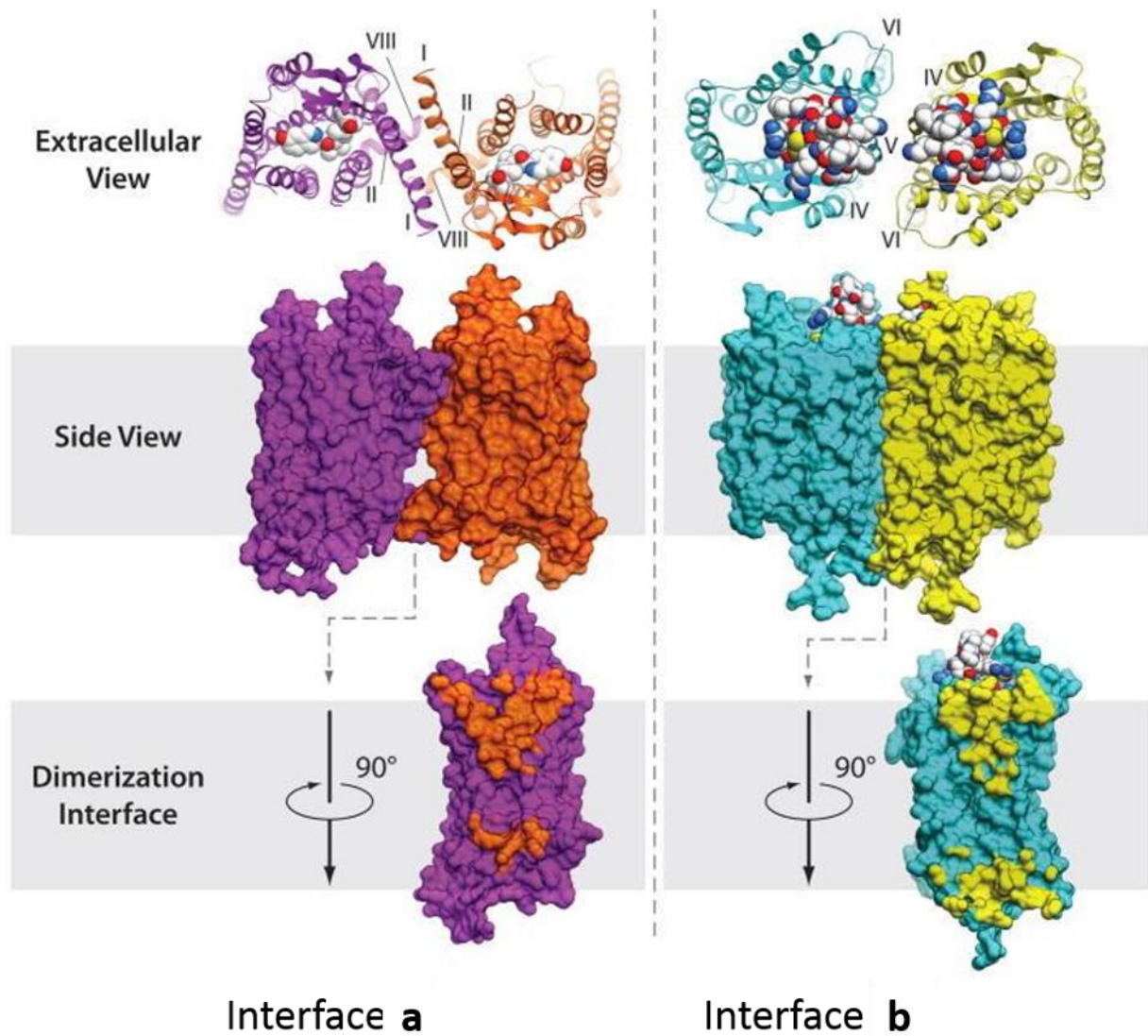
**Figure 1.7. Two major types of symmetric dimer interfaces observed in GPCR structures.** (**a**) A representative structure of dimer interfaces with contacts via helices I, II, VIII is shown here for κ-opioid, PDB code 3DJH. This Interface has also been observed within μ-opioid, rhodopsin and opsin structures. (**b**) Another cluster of dimer interface involves contacts via helices IV, V, VI (cyan and yellow) for CXCR4 complex PDB code 3OE0. Similar orientation of subunits has also been observed in μ-opioid structure, PDB code 3DKL, with an extensive interface formed via helices V and VI. This figure is, adopted with permission, from [34].

Complementary insights into GPCR structure and function are obtained through using molecular simulations and modeling [46, 47]. Advanced molecular dynamics simulations of longer temporal durations (~ 10 ms), have allowed for large conformational changes to be investigated, thus

17

capturing the receptor dynamics, which is not possible using the crystal structures. Further structure, biophysical and computational studies, including time resolved single molecule studies will help in characterizing the GPCRs, and finding more allosteric sites for selective modulations.

The GPCR superfamily contains at least 799 human GPCRs [48], however there are fewer which could be considered as drug-targets for diseases because of their physiological functions. There is a large cluster of GPCRs, which does not seem to represent potential drug target, is sensory receptors, for instance, olfactory receptors (there are 388 receptors in this class only), rhodopsin (or opsin) receptors (but that doesn't mean all other members of the rhodopsin family couldn't be drug targets), etc. At least 46 GPCRs have already been successfully targeted by drugs. The GPCRs can be divided into to three main families: i) Rhodopsin (more than 39 GPCRs), ii) Secretin (4 GPCRs) and iii) Glutamate (3 GPCRs) [49]. However, there are still more than 300 receptors, which have not been used as drug targets, and about half of them are orphan receptors whose ligands are unknown. This means that they do not have any other GPCRs, which are close to them in primary structure. Since the clusters of receptors based on phylogenetic classifications bind with similar ligands, these orphan receptors could be useful for those types of drugs which are very different in molecular structure than those already being used.

So far, only a small fraction of human GPCRs have been used as drug targets, such as, 17% of peptide or protein binding, 29% of biogenic amine binding, 20% of lipid like binding [50], etc. Biogenic amine binding receptors have been used the most as drug targets because they are used to treat cardiovascular diseases. Peptide receptors are the least utilized in term of their druggability. But due to their specificity and physiological roles, such as regulation of body weight, immune system related and pain sensation; they could be future drug targets. This is why it is likely that GPCR family will continue to get attention from the drug-developers. To better understand and

utilize the structural diversity and functionality of GPCRs, detailed knowledge of their secondary, tertiary and quaternary structure is needed.

## 1.3 Sigma-1 receptor (S1R)

Psychostimulant abuse has been a serious social problem in industrialized and developing countries [51, 52]. However, identifying an effective pharmacological cure has been elusive so far. Sigma-1 Receptor (S1R) is one of the major physiological substances implicated in the substance abuse issues. S1R has been known to interact with several drugs, for instance, cocaine and methamphetamine, interacting with them in brain and heart. Therefore, the receptor appears to be a logical target for the substance abuse therapy development efforts.

S1R is a membrane-bound, ligand-mediated molecular chaperone which interacts with various ion gated channels and GPCRs [53, 54]. Prior to the sigma receptor family identification, researchers considered the sigma receptors as one of the opioid receptors because some of the most common opioid ligands, e.g., naloxone, which is an antagonist to opioid receptors, also interacted with sigma receptors [40]. In 1976, Martin reported that the effect of *N*-allylnormetazocine ((-)-ANMC) or alazocine and benzomorphan could only be seen for some of the opioid family receptors, which led to categorize them in a new family [55, 56], which was named as sigma receptor family. Sigma-1 receptor is a member of sigma receptor family with the only other member being sigma-2 receptor. Sigma-2 receptor was discovered to be different than S1R, based on ligand selectivity in the receptor binding assay [57].

Since the discovery of sigma-1 receptor, many preclinical studies have implicated sigma-1 receptor in several diseases including amyotrophic lateral sclerosis (ALS) [58], neurogenic pain [59], addiction to methamphetamine [60], cocaine [61], and alcohol [62], amnesia [63], depression

19

[64], Alzheimer's disease [65], schizophrenia [66], stroke [67], retinal neural degeneration [68], HIV and immunity [69], and cancer [70].

Involvement of S1R was demonstrated in the cases of HIV infection and schizophrenia by molecular biological silencing of the receptor. S1R suppresses the production of reactive oxidation stress (ROS) in retina, lung, liver, and cultured mammalian cells [71-73].

Nanoparticles coupled with Sigma-1 Receptor ligand have shown potential for targeted delivery of antitumor drugs in animals [74], however, any clinical study reporting their testing with cancer patients is not reported.

The mammalian S1R receptor was first cloned in 1996 from guinea pig [75]. The cloning was performed by radioactive labeling followed by protein purification processes. Sigma-2 receptor has not been cloned yet. Sigma-1 receptor is a small (28 kDa, 223 amino acids) transmembrane protein which is mainly localized in the endoplasmic reticulum (ER) regions. It is especially enriched in the mitochondria associated membranes (MAM). Localization studies have also reported their presence in neuron nuclear, mitochondrial and plasma membrane of the central nervous system (CNS) and in CNS-associated immune and endocrine tissues. The varied sites at which S1Rs are present, suggest their activity via multiple physiological and pathological pathways.

A model for the S1R structure is shown in Figure 1.9. As per this model, S1R consists of three domains, out of which two are transmembrane regions. The folding of the receptor into the three domains was assumed to make a ligand-binding pocket.

20
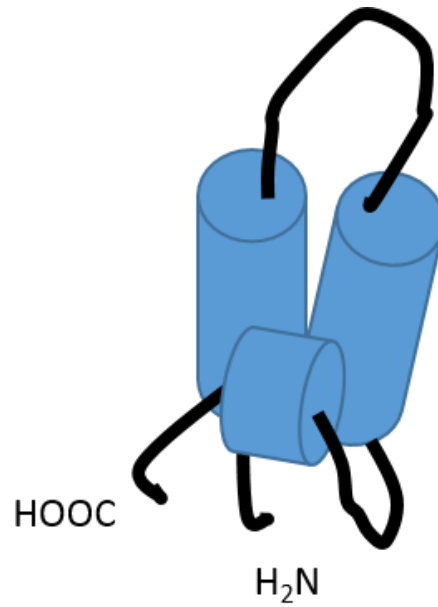
**Figure 1.8. Models of the sigma-1 receptor ligand binding region.** A model of the sigma-1 receptor-binding region was proposed by Chu *et al.* [76]. Three domains of the receptor are shown. Two of them (the longer domains in the figure) are transmembrane. The locations of C and N terminuses were reported as D188 and H154 respectively.

The mechanism of S1R action has been difficult to understand due to the absence of similarity of its sequence to any other known mammalian proteins. Cloning of S1R has helped advance this understanding and provided insight into potential avenues for future investigation that will hopefully lead to a better understanding of relationships between the S1R and the aforementioned diseases. However, the current level of research has not reached to give a good understanding of a link between diseases and the mechanism of action of S1R.

S1Rs reside in ER membranes, although their interaction with the ion channels in plasma membranes has been reported [77]. The most researched mechanism of the S1R activity is related to its interaction with ion channels, especially calcium and potassium ion channels. A possible explanation to this is given that the overexpression of S1R agonists might cause translocation of the receptor from ER to the plasma membrane, where it was reported to interact with the ion channels. Ligand mediated S1R modulation of $Ca^2+$ channels began the investigation of molecular

21

action of S1R historically, and since then it has become the main areas of investigating the receptor's molecular action. In the presence of micromolar concentration of S1R ligand haloperidol, the calcium ion concentration increased in colon cancer cells and mammary adenocarcinoma cells [78]. By contrast, in the presence of another sigma receptor ligand pentazocine, the $Ca^{2}+$ channel current decreased [79]. An important study reported that the S1R agonists potentiate N-Methyl-D-aspartic acid (NMDA)-induced neuronal firing, while haloperidol blocks the potentiation [63, 80]. S1R colocalization with potassium channels is shown in Figure 1.10.



a                                        b                                        c
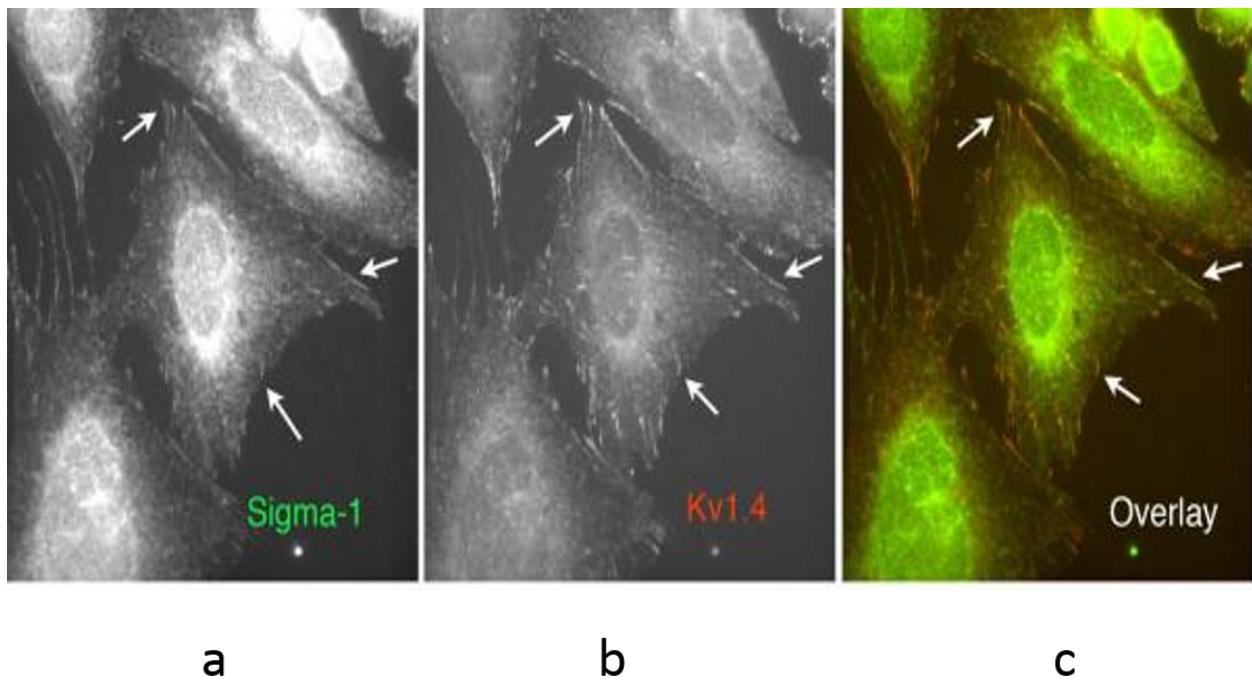
**Figure 1.9. Sigma-1 receptor colocalization.** Endogenous sigma-1 receptors colocalize with Kv1.4 potassium channel. **(a)** Sigma-1 receptors alone. **(b)** Potassium channels alone. **(c)** The overlap of sigma-1 receptors and potassium Kv1.4 channels. This figure is reproduced, with permission, from [84].

Using cultured frog pituitary cells, it was shown that S1R ligand (+) pentazoncine decreased outbound current of potassium, while the presence of the receptor's antagonist NE100,

22

blocked the decrease [81]. Similar studies suggested that ligand mediated S1R regulate sodium [82] and chloride [83] channels.

S1R is also indicated in regulatory pathways for cell survival or cell death. In general, S1R agonists promote cell survival and the receptor's antagonists lead to cell death. The S1R antagonist, rimcazole inhibited tumor survival [70, 85].

S1R were also found to exist in lipid rafts at the ER membranes [86]. Lipid rafts are proposed to be cholesterol-enriched microdomains which serve as a platform for ion channels, receptors and kinases [87]. Exact relation between S1R and lipid drafts is not known but it has been shown that the overexpression of S1R caused reconstitution of lipid rafts [88].

# References

[1] R. Bowen, Amino Acids, in, vol. 2016, 2012.

[2] J.A. Bruce Albert , Lewis Julian,  Raff Martin , Roberts Keith , Walter Peter Molecular Biology of the Cell, 5th edition (2007).

[3] G.M. Cooper, R.E. Hausman, The cell, Sinauer Associates Sunderland, 2000.

[4] K.L. Pierce, L.M. Luttrell, R.J. Lefkowitz, New mechanisms in heptahelical receptor signaling to mitogen activated protein kinase cascades, Oncogene, 20 (2001).

[5] V. Raicu, A. Popescu, Integrated molecular and cellular biophysics, Springer, 2008.

[6] P.R. Selvin, The renaissance of fluorescence resonance energy transfer, Nature structural biology, 7 (2000) 730-734.

[7] B.W. Van Der Meer, G. Coker, S.-Y.S. Chen, Resonance energy transfer: theory and data, Wiley-VCH, 1994.

[8] R.F. Weaver, Molecular Biology 5th Edition (2012).

[9] A. VLAMIS-GARDIKAS, A. Holmgren, Concluding Remarks and Perspectives Thioredoxin target proteins seem to be divided into several categories. Thiore-doxin interacts with (1) members of the thioredoxin system;(2) thioredoxin in-teracting proteins such as Ref-1;(3) thioredoxin binding proteins;(4) substrates of thioredoxin. Thioredoxin seems to exert its function by these multiple ways of, Structure, 2 (1994) 853.

[10] J. Garnier, D.J. Osguthorpe, B. Robson, Analysis of the accuracy and implications of simple methods for predicting the secondary structure of globular proteins, Journal of molecular biology, 120 (1978) 97-120.

[11] A.R. Clapp, I.L. Medintz, H. Mattoussi, Förster resonance energy transfer investigations using quantum-dot fluorophores, ChemPhysChem, 7 (2006) 47-57.

[12] H. Chen, S. Kim, L. Li, S. Wang, K. Park, J.-X. Cheng, Release of hydrophobic molecules from polymer micelles into cell membranes revealed by Förster resonance energy transfer imaging, Proceedings of the National Academy of Sciences, 105 (2008) 6596-6601.

[13] B. Wetzl, M. Gruber, B. Oswald, A. Dürkop, B. Weidgans, M. Probst, O.S. Wolfbeis, Set of fluorochromophores in the wavelength range from 450 to 700 nm and suitable for labeling proteins and amino-modified DNA, Journal of Chromatography B, 793 (2003) 83-92.

[14] C.I. Richards, S. Choi, J.-C. Hsiang, Y. Antoku, T. Vosch, A. Bongiorno, Y.-L. Tzeng, R.M. Dickson, Oligonucleotide-stabilized Ag nanocluster fluorophores, Journal of the American Chemical Society, 130 (2008) 5038-5039.

[15] T. Attwood, J. Findlay, Design of a discriminating fingerprint for G-protein-coupled receptors, Protein Engineering, 6 (1993) 167-176.

[16] K. Palczewski, T. Kumasaka, T. Hori, C.A. Behnke, H. Motoshima, B.A. Fox, I. Le Trong, D.C. Teller, T. Okada, R.E. Stenkamp, M. Yamamoto, M. Miyano, Crystal structure of rhodopsin: A G protein-coupled receptor, Science (New York, N.Y.), 289 (2000) 739-745.

[17] D.M. Perez, The evolutionarily triumphant G-protein-coupled receptor, Molecular pharmacology, 63 (2003) 1202-1205.

[18] D.M. Perez, From plants to man: the GPCR "tree of life", Molecular pharmacology, 67 (2005) 1383-1384.

[19] T. Ha, T. Enderle, D. Ogletree, D. Chemla, P. Selvin, S. Weiss, Probing the interaction between two single molecules: fluorescence resonance energy transfer between a single donor and a single acceptor, Proceedings of the National Academy of Sciences, 93 (1996) 6264-6268.

[20] B.K. Kobilka, X. Deupi, Conformational complexity of G-protein-coupled receptors, Trends in pharmacological sciences, 28 (2007) 397-406.

[21] R. Seifert, K. Wenzel-Seifert, Constitutive activity of G-protein-coupled receptors: cause of disease and common property of wild-type receptors, Naunyn-Schmiedeberg's archives of pharmacology, 366 (2002) 381-416.

[22] R. Nygaard, T.M. Frimurer, B. Holst, M.M. Rosenkilde, T.W. Schwartz, Ligand binding and micro-switches in 7TM receptor structures, Trends in pharmacological sciences, 30 (2009) 249-259.

[23] T.W. Schwartz, T.M. Frimurer, B. Holst, M.M. Rosenkilde, C.E. Elling, Molecular mechanism of 7TM receptor activation--a global toggle switch model, Annu Rev Pharmacol Toxicol, 46 (2006) 481-519.

[24] Z.G. Gao, K.A. Jacobson, Keynote review: allosterism in membrane receptors, Drug discovery today, 11 (2006) 191-202.

[25] E.J. Whalen, S. Rajagopal, R.J. Lefkowitz, Therapeutic potential of beta-arrestin- and G protein-biased agonists, Trends in molecular medicine, 17 (2011) 126-139.

[26] P. Keov, P.M. Sexton, A. Christopoulos, Allosteric modulation of G protein-coupled receptors: a pharmacological perspective, Neuropharmacology, 60 (2011) 24-35.

[27] L. Shi, J.A. Javitch, The binding site of aminergic G protein-coupled receptors: the transmembrane segments and second extracellular loop, Annu Rev Pharmacol Toxicol, 42 (2002) 437-467.

[28] C. Valant, J. Robert Lane, P.M. Sexton, A. Christopoulos, The best of both worlds? Bitopic orthosteric/allosteric ligands of g protein-coupled receptors, Annu Rev Pharmacol Toxicol, 52 (2012) 153-178.

[29] Stephane Angers, Ali Salahpour, M. Bouvier, DIMERIZATION: An Emerging Concept for G Protein–Coupled Receptor Ontogeny and Function, Annual Review of Pharmacology and Toxicology, 42 (2002) 409-435.

[30] L.A. Devi, Heterodimerization of G-protein-coupled receptors: pharmacology, signaling and trafficking, Trends in pharmacological sciences, 22 (2001) 532-537.

[31] S. Bulenger, S. Marullo, M. Bouvier, Emerging role of homo- and heterodimerization in G-protein-coupled receptor biosynthesis and maturation, Trends in pharmacological sciences, 26 (2005) 131-137.

[32] J.A. Javitch, The ants go marching two by two: oligomeric structure of G-protein-coupled receptors, Molecular pharmacology, 66 (2004) 1077-1082.

[33] V. Raicu, M.R. Stoneman, R. Fung, M. Melnichuk, D.B. Jansma, L.F. Pisterzi, S. Rath, M. Fox, J.W. Wells, D.K. Saldin, Determination of supramolecular structure and spatial distribution of protein complexes in living cells, Nat Photon, 3 (2009) 107-113.

[34] S. Patowary, E. Alvarez-Curto, T.R. Xu, J.D. Holz, J.A. Oliver, G. Milligan, V. Raicu, The muscarinic M3 acetylcholine receptor exists as two differently sized complexes at the plasma membrane, Biochem J, 452 (2013) 303-312.

[35] G. Milligan, G protein-coupled receptor hetero-dimerization: contribution to pharmacology and function, British journal of pharmacology, 158 (2009) 5-14.

[36] P. Maurice, M. Kamal, R. Jockers, Asymmetry of GPCR oligomers supports their functional relevance, Trends in pharmacological sciences, 32 (2011) 514-520.

[37] A.A. Kaczor, J. Selent, Oligomerization of G protein-coupled receptors: biochemical and biophysical methods, Current medicinal chemistry, 18 (2011) 4606-4634.

[38] J. Selent, A.A. Kaczor, Oligomerization of G protein-coupled receptors: computational methods, Current medicinal chemistry, 18 (2011) 4588-4605.

[39] G. Khelashvili, K. Dorff, J. Shan, M. Camacho-Artacho, L. Skrabanek, B. Vroling, M. Bouvier, L.A. Devi, S.R. George, J.A. Javitch, M.J. Lohse, G. Milligan, R.R. Neubig, K. Palczewski, M. Parmentier, J.P. Pin, G. Vriend, F. Campagne, M. Filizola, GPCR-OKB: the G Protein Coupled Receptor Oligomer Knowledge Base, Bioinformatics (Oxford, England), 26 (2010) 1804-1805.

[40] D. Fotiadis, B. Jastrzebska, A. Philippsen, D.J. Muller, K. Palczewski, A. Engel, Structure of the rhodopsin dimer: a working model for G-protein-coupled receptors, Current opinion in structural biology, 16 (2006) 252-259.

[41] H. Wu, D. Wacker, M. Mileni, V. Katritch, G.W. Han, E. Vardy, W. Liu, A.A. Thompson, X.P. Huang, F.I. Carroll, S.W. Mascarella, R.B. Westkaemper, P.D. Mosier, B.L. Roth, V. Cherezov, R.C. Stevens, Structure of the human kappa-opioid receptor in complex with JDTic, Nature, 485 (2012) 327-332.

[42] A. Manglik, A.C. Kruse, T.S. Kobilka, F.S. Thian, J.M. Mathiesen, R.K. Sunahara, L. Pardo, W.I. Weis, B.K. Kobilka, S. Granier, Crystal structure of the micro-opioid receptor bound to a morphinan antagonist, Nature, 485 (2012) 321-326.

[43] M.S. Taylor, H.K. Fung, R. Rajgaria, M. Filizola, H. Weinstein, C.A. Floudas, Mutations affecting the oligomerization interface of G-protein-coupled receptors revealed by a novel de novo protein design framework, Biophys J, 94 (2008) 2470-2481.

[44] F. Mancia, Z. Assur, A.G. Herman, R. Siegel, W.A. Hendrickson, Ligand sensitivity in dimeric associations of the serotonin 5HT2c receptor, EMBO reports, 9 (2008) 363-369.

[45] W. Guo, E. Urizar, M. Kralikova, J.C. Mobarec, L. Shi, M. Filizola, J.A. Javitch, Dopamine D2 receptors form higher order oligomers at physiological expression levels, The EMBO journal, 27 (2008) 2293-2304.

[46] D. Fotiadis, Y. Liang, S. Filipek, D.A. Saperstein, A. Engel, K. Palczewski, The G protein-coupled receptor rhodopsin in the native membrane, FEBS letters, 564 (2004) 281-288.

[47] D. Sengupta, A. Chattopadhyay, Molecular dynamics simulations of GPCR-cholesterol interaction: An emerging paradigm, Biochimica et biophysica acta, 1848 (2015) 1775-1782.

[48] D.E. Gloriam, R. Fredriksson, H.B. Schioth, The G protein-coupled receptor subset of the rat genome, BMC genomics, 8 (2007) 338.

[49] M.C. Lagerstrom, H.B. Schioth, Structural diversity of G protein-coupled receptors and significance for drug discovery, Nat Rev Drug Discov, 7 (2008) 339-357.

[50] T.K. Bjarnadottir, D.E. Gloriam, S.H. Hellstrand, H. Kristiansson, R. Fredriksson, H.B. Schioth, Comprehensive repertoire and phylogenetic analysis of the G protein-coupled receptors in human and mouse, Genomics, 88 (2006) 263-273.

[51] A. Odejide, Status of drug use/abuse in Africa: A review, International journal of mental health and addiction, 4 (2006) 87-102.

[52] M.G. Monteiro, A World Health Organization perspective on alcohol and illicit drug use and health, European Addiction Research, 7 (2001) 98-103.

[53] T.-P. Su, T. Hayashi, T. Maurice, S. Buch, A.E. Ruoho, The sigma-1 receptor chaperone as an inter-organelle signaling modulator, Trends in pharmacological sciences, 31 (2010) 557-566.

[54] D. Fontanilla, M. Johannessen, A.R. Hajipour, N.V. Cozzi, M.B. Jackson, A.E. Ruoho, The hallucinogen N, N-dimethyltryptamine (DMT) is an endogenous sigma-1 receptor regulator, Science (New York, N.Y.), 323 (2009) 934-937.

[55] T.P. Su, E.D. London, J.H. Jaffe, Steroid binding at sigma receptors suggests a link between endocrine, nervous, and immune systems, Science (New York, N.Y.), 240 (1988) 219-221.

[56] T.P. Su, Evidence for sigma opioid receptor: binding of [3H]SKF-10047 to etorphine-inaccessible sites in guinea-pig brain, The Journal of pharmacology and experimental therapeutics, 223 (1982) 284-290.

[57] S.B. Hellewell, A. Bruce, G. Feinstein, J. Orringer, W. Williams, W.D. Bowen, Rat liver and kidney contain high densities of sigma 1 and sigma 2 receptors: characterization by ligand binding and photoaffinity labeling, European journal of pharmacology, 268 (1994) 9-18.

[58] A. Al-Saif, F. Al-Mohanna, S. Bohlega, A mutation in sigma-1 receptor causes juvenile amyotrophic lateral sclerosis, Annals of neurology, 70 (2011) 913-919.

[59] M. Kinoshita, Y. Matsuoka, T. Suzuki, J. Mirrielees, J. Yang, Sigma-1 receptor alters the kinetics of Kv1.3 voltage gated potassium channels but not the sensitivity to receptor ligands, Brain research, 1452 (2012) 1-9.

[60] E.C. Nguyen, K.A. McCracken, Y. Liu, B. Pouw, R.R. Matsumoto, Involvement of sigma (sigma) receptors in the acute actions of methamphetamine: receptor binding and behavioral studies, Neuropharmacology, 49 (2005) 638-645.

[61] J. Sharkey, K.A. Glen, S. Wolfe, M.J. Kuhar, Cocaine binding at sigma receptors, European journal of pharmacology, 149 (1988) 171-174.

[62] T. Maurice, M. Casalino, M. Lacroix, P. Romieu, Involvement of the sigma 1 receptor in the motivational effects of ethanol in mice, Pharmacology, biochemistry, and behavior, 74 (2003) 869-876.

[63] F.P. Monnet, G. Debonnel, J.L. Junien, C. De Montigny, N-methyl-D-aspartate-induced neuronal activation is selectively modulated by sigma receptors, European journal of pharmacology, 179 (1990) 441-445.

[64] R. Bergeron, G. Debonnel, C. De Montigny, Modification of the N-methyl-D-aspartate response by antidepressant sigma receptor ligands, European journal of pharmacology, 240 (1993) 319-323.

[65] K. Yamada, T. Nabeshima, Animal models of Alzheimer's disease and evaluation of anti-dementia drugs, Pharmacol Ther, 88 (2000) 93-113.

[66] H. Ishiguro, T. Ohtsuki, M. Toru, M. Itokawa, J. Aoki, H. Shibuya, A. Kurumaji, Y. Okubo, A. Iwawaki, K. Ota, H. Shimizu, H. Hamaguchi, T. Arinami, Association between polymorphisms in the type 1 sigma receptor gene and schizophrenia, Neuroscience letters, 257 (1998) 45-48.

[67] C.T. Ajmo, Jr., D.O. Vernon, L. Collier, K.R. Pennypacker, J. Cuevas, Sigma receptor activation reduces infarct size at 24 hours after permanent middle cerebral artery occlusion in rats, Current neurovascular research, 3 (2006) 89-98.

[68] P.M. Martin, M.S. Ola, N. Agarwal, V. Ganapathy, S.B. Smith, The sigma receptor ligand (+)-pentazocine prevents apoptotic retinal ganglion cell death induced in vitro by homocysteine and glutamate, Brain research. Molecular brain research, 123 (2004) 66-75.

[69] M.D. Roth, K.M. Whittaker, R. Choi, D.P. Tashkin, G.C. Baldwin, Cocaine and sigma-1 receptors modulate HIV infection, chemokine receptors, and the HPA axis in the huPBL-SCID model, Journal of leukocyte biology, 78 (2005) 1198-1203.

[70] B.A. Spruce, L.A. Campbell, N. McTavish, M.A. Cooper, M.V. Appleyard, M. O'Neill, J. Howie, J. Samson, S. Watt, K. Murray, D. McLean, N.R. Leslie, S.T. Safrany, M.J. Ferguson, J.A. Peters, A.R. Prescott, G. Box, A. Hayes, B. Nutley, F. Raynaud, C.P. Downes, J.J. Lambert, A.M. Thompson, S. Eccles, Small molecule antagonists of the sigma-1 receptor cause selective release of the death program in tumor and self-reliant cells and inhibit tumor growth in vitro and in vivo, Cancer research, 64 (2004) 4875-4886.

[71] C. Bucolo, F. Drago, L.R. Lin, V.N. Reddy, Sigma receptor ligands protect human retinal cells against oxidative stress, Neuroreport, 17 (2006) 287-291.

[72] A. Pal, D. Fontanilla, A. Gopalakrishnan, Y.K. Chae, J.L. Markley, A.E. Ruoho, The sigma-1 receptor protects against cellular oxidative stress and activates antioxidant response elements, European journal of pharmacology, 682 (2012) 12-20.

[73] A.K. Mishra, T. Mavlyutov, D.R. Singh, G. Biener, J. Yang, J.A. Oliver, A. Ruoho, V. Raicu, The sigma-1 receptors are present in monomeric and oligomeric forms in living cells in the presence and absence of ligands, Biochem J, 466 (2015) 263-271.

[74] A. van Waarde, A.A. Rybczynska, N.K. Ramakrishnan, K. Ishiwata, P.H. Elsinga, R.A. Dierckx, Potential applications for sigma receptor ligands in cancer diagnosis and therapy, Biochimica et biophysica acta, 1848 (2015) 2703-2714.

[75] M. Hanner, F.F. Moebius, A. Flandorfer, H.G. Knaus, J. Striessnig, E. Kempner, H. Glossmann, Purification, molecular cloning, and expression of the mammalian sigma1-binding site, Proceedings of the National Academy of Sciences of the United States of America, 93 (1996) 8072-8077.

[76] U.B. Chu, S. Ramachandran, A.R. Hajipour, A.E. Ruoho, Photoaffinity labeling of the Sigma-1 Receptor with N-(3-(4-nitrophenyl)propyl)-N-dodecylamine (4-NPPC12) – Evidence for Receptor Dimers, Biochemistry, 52 (2013) 859-868.

[77] T.P. Su, T. Hayashi, D.B. Vaupel, When the endogenous hallucinogenic trace amine N,N-dimethyltryptamine meets the sigma-1 receptor, Science signaling, 2 (2009) pe12.

[78] P.J. Brent, G. Pang, G. Little, P.J. Dosen, D.F. Van Helden, The sigma receptor ligand, reduced haloperidol, induces apoptosis and increases intracellular-free calcium levels [Ca2+]i in colon and mammary adenocarcinoma cells, Biochemical and biophysical research communications, 219 (1996) 219-226.

[79] H. Zhang, J. Cuevas, Sigma receptors inhibit high-voltage-activated calcium channels in rat sympathetic and parasympathetic neurons, Journal of neurophysiology, 87 (2002) 2867-2879.

[80] F.P. Monnet, M.P. Morin-Surun, J. Leger, L. Combettes, Protein kinase C-dependent potentiation of intracellular calcium influx by sigma1 receptor agonists in rat hippocampal neurons, The Journal of pharmacology and experimental therapeutics, 307 (2003) 705-712.

[81] O. Soriani, F.L. Foll, F. Roman, F.P. Monnet, H. Vaudry, L. Cazin, A-Current down-modulated by sigma receptor in frog pituitary melanotrope cells through a G protein-dependent pathway, The Journal of pharmacology and experimental therapeutics, 289 (1999) 321-328.

[82] Z.X. Cheng, D.M. Lan, P.Y. Wu, Y.H. Zhu, Y. Dong, L. Ma, P. Zheng, Neurosteroid dehydroepiandrosterone sulphate inhibits persistent sodium currents in rat medial prefrontal cortex via activation of sigma-1 receptors, Experimental neurology, 210 (2008) 128-136.

[83] A. Renaudo, S. L'Hoste, H. Guizouarn, F. Borgese, O. Soriani, Cancer cell cycle modulated by a functional coupling between sigma-1 receptors and Cl- channels, The Journal of biological chemistry, 282 (2007) 2259-2267.

[84] T.A. Mavlyutov, A.E. Ruoho, Ligand-dependent localization and intracellular stability of sigma-1 receptors in CHO-K1 cells, Journal of molecular signaling, 2 (2007) 8.

[85] M. Achison, M.T. Boylan, T.R. Hupp, B.A. Spruce, HIF-1alpha contributes to tumour-selective killing by the sigma receptor antagonist rimcazole, Oncogene, 26 (2007) 1137-1146.

[86] T. Hayashi, T.P. Su, Sigma-1 receptors (sigma(1) binding sites) form raft-like microdomains and target lipid droplets on the endoplasmic reticulum: roles in endoplasmic reticulum lipid compartmentalization and export, The Journal of pharmacology and experimental therapeutics, 306 (2003) 718-725.

[87] K. Simons, E. Ikonen, How cells handle cholesterol, Science (New York, N.Y.), 290 (2000) 1721-1726.

30

[88] M. Takebayashi, T. Hayashi, T.P. Su, Sigma-1 receptors potentiate epidermal growth factor signaling towards neuritogenesis in PC12 cells: potential relation to lipid raft reconstitution, Synapse (New York, N.Y.), 53 (2004) 90-103.

# Chapter 2: Förster resonance energy transfer (FRET) theory and the kinetic model of FRET

The key objective of writing this chapter is to provide an overview of the FRET theory and the kinetic model of FRET for oligomeric complexes, as this is the key concept upon which the whole dissertation is based. This chapter has been organized in three sections. The first section describes FRET, the second section gives an overview of Förster's theory, and the third section explains the kinetic theory of FRET.

## 2.1 Fluorescence

FRET is a process of non-radiate energy transfer from an optically excited donor to an unexcited acceptor of energy, via a process of dipole-dipole interaction. Although, in principle can be applied to a broad range of electromagnetic radiation, FRET is popularly used in the visible range of the electromagnetic spectrum to investigate interactions of biological macromolecules. IN most studies, both molecules involved in FRET, i.e., the donor and the acceptor, are fluorescent. Therefore, the FRET acronym also stands for Fluorescence Resonance Energy Transfer [1, 2].

The term fluorescence came into existence when George G. Stokes observed in 1852 that when mineral fluorspar (calcium fluoride) was exposed to electromagnetic radiation in ultraviolet region, it would emit visible light. Stokes' study of fluorescence led to the formulation of Stokes' law, which states that the wavelength of fluorescent light is always greater than the wavelength of excitation. Thus, for any fluorescent molecule, the wavelength of emission is larger than the wavelength of absorption. Molecules that display fluorescence are called fluorophores or fluorochromophores [3-5].

## 2.1.1 Jablonski diagram

The Jablonski diagram, shown in figure 2.1, is a schematic depiction of the energy levels in a fluorescent molecule, giving different energy states and their vibrational sub-divisions in the order of increasing energy in the vertical direction. States of different spin-multiplicity are arranged in horizontal columns. This diagram helps in understanding of resonance energy transfer, and difference between fluorescence and phosphorescence. The difference between the two types of luminescence will be discussed later in this chapter.
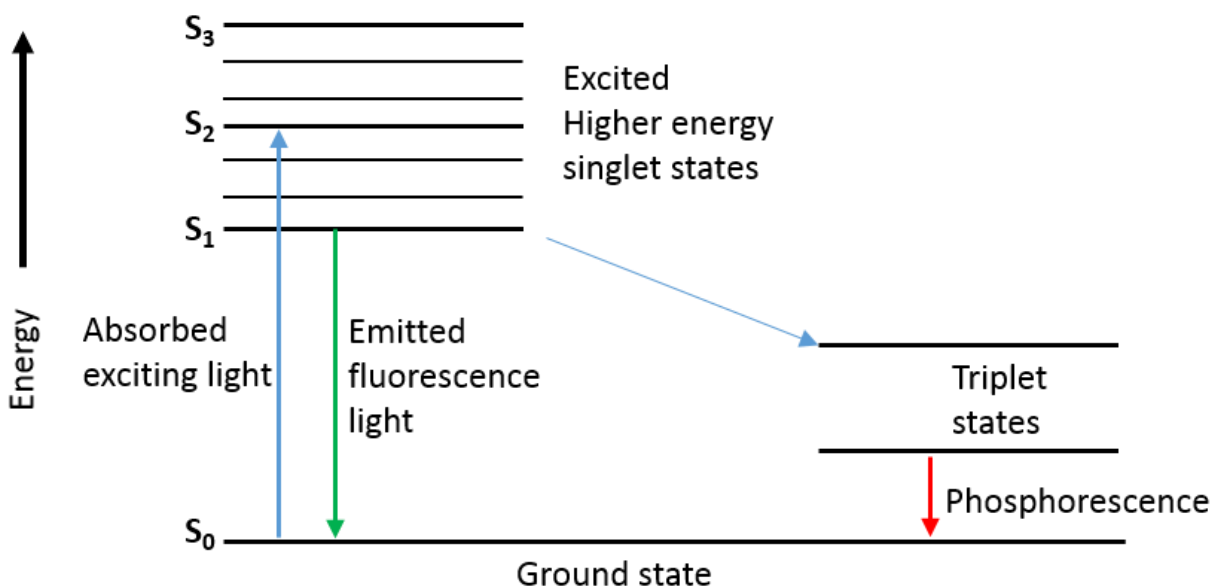


**Figure 2.1 Jablonski diagram, showing energy-states and interstate crossing diagram.** This diagram shows absorbance of light and its emission as fluorescence or phosphorescence. Interstate crossing occurs when the molecule de-excites via travelling to the triplet state, giving off phosphorescence.

FRET is a technique which reports proximity of two neighboring molecules (for their distance <10 nm). It is a very sensitive proximity reporter since FRET depends on the 6$^{th}$ power

of the reciprocal of intermolecular distance. Investigation of GFP [6]-based FRET pairs such as GFP2 and YFP, and advancement in FRET fluorescence imaging technologies, have established FRET as a very powerful technique in many areas, especially biological sciences.

### 2.1.2 Fluorescence vs phosphoresce

Phosphorescence [7] occurs when an excited state electron enters to a triplet state [8, 9] via intersystem crossing [10], and from there it's de-excitation to the ground state is forbidden classically because it requires its spin to flip in order to re-emit energy, but quantum mechanically there is some probability for this transition to happen [9]. However, due to much weaker probability than that for the fluorescence events, it could take seconds to hours for phosphorescence to re-emit [11].

### 2.1.3 Rate of de-excitation (Γ)

When laser of suitable wavelength is shone on a fluorescent molecule, an electron of the outer shell of its atom is kicked to a singlet excited state, and from there, it first goes through vibrational relaxation (which are non-radiative), to trickle down to the lowest vibration state of that singlet state and then it can de-excite via multiple radiative ($\Gamma^{r,D}$) and non-radiative ($\Gamma^{nr,D}$) pathways.

## 2.2 FRET

FRET is frequently used to measure both intra-molecular and inter-molecular distances in living cells [12-14]. When an excited dipolar molecule is near to an unexcited dipolar molecule, then a non-radiative energy transfer can take place, from the excited molecule (donor) to the unexcited molecule (acceptor) without involving photons, and this process is called a resonance energy transfer or RET. When this energy transfer happens between the molecules, which have their emission wavelength peaks in the visible spectrum, their emission is called fluorescence and the

phenomenon is called Fluorescent Resonance Energy Transfer or Förster Resonance Energy Transfer (FRET) [15-22].

The electric field E of an excited dipole (donor) with a charge $q^D$ interacts with the electric field of another unexcited dipole (acceptor) of charge $q^A$, as $q^A$.E, and vise-versa. This causes the transition dipole moments (t.d.m.) of the two molecules to interact with each other, called dipole-dipole coupling [23, 24]. This dipole-dipole coupling can cause the two dipoles to reorient and, in the process, energy is transferred from the excited donor to the acceptor molecule. The energy transfer via dipole-dipole coupling is a non-radiative pathway of energy transfer.[25, 26].

There are three spatial regions of the electric field due to a dipole, near field (where E is proportional to $r^{-2}$, far field (which varies as $r^{-1}$), and the region between near and far field. When the acceptor molecule is in the range of the near field, its interaction with the E field of the donor is the strongest, and for the resonance energy transfer, only the near field interaction is strong enough to cause relative change in the dipole orientation. There are both classical and quantum theories to explain this non-radiative energy transfer. J. Perrin [27] first proposed a classical theory of FRET.
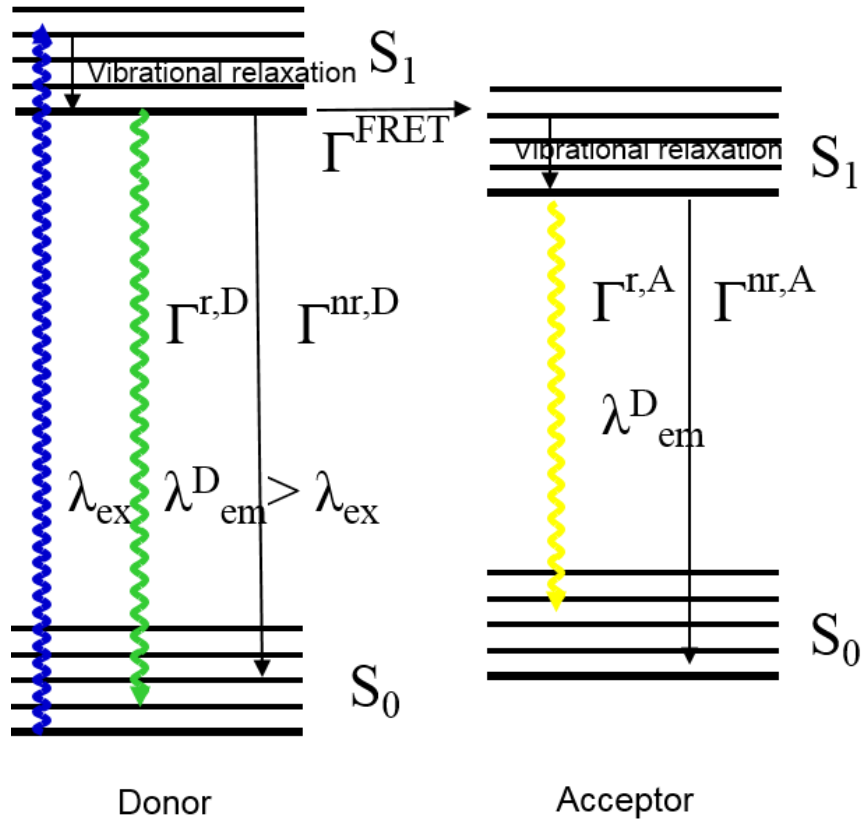
**Figure 2.2 Energy transfer between donor and acceptor molecule.** Donor excitation $\lambda^D_{ex}$ (blue arrow) takes donor from its ground state $S_0$ to its (first) excited state $S_1$, where the excited molecule settles through vibration relaxation, and then is de-excited giving off donor fluorescence $\Gamma^{r,D}$ (green arrow) at $\lambda^D_{em}$. In the presence of an acceptor, the donor can also be de-excited by transferring its energy via FRET to the acceptor. Excited acceptor after going through vibration relaxation, de-excites via acceptor emission $\Gamma^{r,A}$ (yellow arrow) at $\lambda^A_{ex}$. Both donor and acceptor can also be de-excited via non-radiate pathways $\Gamma^{nr,D}$ and $\Gamma^{nr,A}$ respectively.

Förster suggested that, since energy conservation cannot be violated, energy transfer from a donor transition dipole to an acceptor dipole can only be possible when there is an equal difference of the energies between the excited and the ground states of the two species. However,

36

he had also observed that, even though there needs to be same frequency absorbed as emitted, which is a condition of resonance, there is no single frequency of transfer; instead, there is a range of frequencies or band of frequency at which an acceptor can absorb photons.

A combination of a FRET donor and acceptor are called a *FRET pair*. A good choice of a FRET pair is based on the following factors:

1. Large spectral overlap

2. Large Stokes shift

3. High quantum yield

## 2.2.1 Spectral overlap

The overlap between the donor emission and the acceptor excitation (or absorption) is called *spectral overlap*. A good overlap of the bandwidths (spectra) of donor emission and acceptor absorption results in a higher energy transfer efficiency and hence stronger FRET signal. For that purpose, the choice of the FRET pair or donor and acceptor molecules is critical.
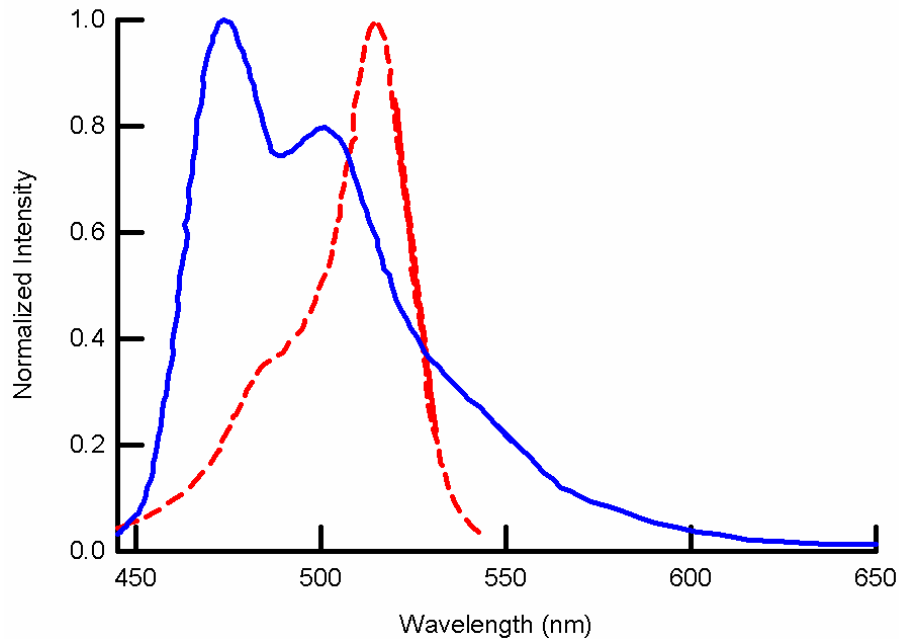


**Figure 2.3 Spectral overlap of donor emission and acceptor absorption.** Blue line shows emission spectrum of the donor (Turquoise) fused to rhodopsin and expressed in Chinese hamster Ovary (CHO)

37

cells, measured in our lab, and the red dotted curve shows the absorption (excitation) spectrum of sYFP2, which is an acceptor of energy when in the vicinity of an excited Turquoise molecule. The sYFP2 spectrum is replotted with the data extracted from literature [17].

There are many good FRET pairs have been used in the proximity or interaction studies [18, 19, 21, 28-30]. The choice also depends on the imaging system used, which includes the compatibility with the laser and the detection camera.

## 2.2.2 Stokes shift

The Stokes shift or Stokes distance is the distance between the maxima of the bands of fluorescent excitation and emission of the same electron [20, 25, 31]. It applies to both donor and acceptor molecules, and each fluorophore has a distinct Stokes shift. A large Stokes shift is needed to resolve the fluorescence of emissions of the donor and the acceptor.


## 2.2.3 Quantum yield (QY)

The quantum yield [32, 33] ] of fluorescence is given by the following equation

$$Quantum\ Yield\ = \#\ of\ photon\ emitted/\#\ of\ photon\ absorbed. \tag{2.1}$$

Values of the quantum yield ranges between 0 and 1. Measuring quantum yield is rather difficult. There are several criteria to be considered for accurate determination of the quantum yield, including effects of concentration, which can cause self-quenching, and the effect of solvent on the quantum yields. Some good methods for measuring the quantum yields of fluorescence were described by Brouwer A.M. [33] .

## 2.2.4 Origin and properties of fluorescent proteins

The Green fluorescent protein (GFP) was first isolated form the jellyfish Aquorea Victoria[34, 35] Later it was mutated to give several spectral variants, for example, CFP, YFP, red fluorescent proteins, etc [6, 36-41]  Scientists Roger Chen, Y.Tsien, Osamu Shimomura, and Martin Chalfie were awarded Nobel prize in chemistry in 2008 for the discovery and development of GFP.

Both natural and synthetic (when fluorophores are attached chemically, also called dyes) variations of fluorescent proteins are used. Fluorescence photons have several properties such as:

- Spectrum

- Lifetime

- Polarization

The above properties are exploited for fluorescence imaging analysis. There are several applications of FRET such as:

- Single molecule tracking, for which a very sensitive detection and fast image acquisition is used.

- Fluorescent correlation spectroscopy (FCS), which tracks fluorescence fluctuations over time.

## 2.3 Förster theory

The FRET efficiency, E, derived by Förster is given by the following expression:

$$E = \frac{1}{1 + (r/R_0)^6},$$

$$(2.2)$$

where r is the distance between the two molecules, and $R_o$ is the Förster radius, which is the distance for which 50% of the donor energy is transferred via FRET, and $R_o$ [5, 42, 43] and is defined as

$$R_0{}^6 = \frac{9(ln10)}{128\,\pi^5 N_A} \frac{k^2 Q_D}{n^4} \, J,$$

$$(2.3)$$

where J is the spectral overlap integral (defined below), and $k$ is the orientation factor and, which is given by

$$k = \hat{\mu}_A \cdot \hat{\mu}_D - 3(\hat{\mu}_D \cdot R)(\hat{\mu}_A \cdot R_{DA}),$$

$$(2.4)$$

39

where $\hat{\mu}_A$ and $\hat{\mu}_D$ are the dipole moments of the donor and acceptor dipoles respectively. R is the displacement vector between the two dipoles. The orientation factor ($k$) can also be expressed in terms of the angles by the following

$$k^2 = (\cos \theta_\tau - 3 \cos \theta_D \cos \theta_A)^2 = (\sin \theta_D \sin \theta_A \cos \Phi - 2 \cos \theta_D \sin \theta_A)^2, \qquad (2.5)$$

where $\theta_\tau$ is the angle between the donor and acceptor dipoles. The remaining variables of the above equations are defined in the figure legend of Figure 2.4. The isotropic average value of $k^2$ is 2/3 [44, 45].

The spectral overlap integral in equation (2.3), depends on the spectral overlap of the donor emission spectrum and acceptor excitation spectrum and is given by:

$$J = \frac{\int f_D(\lambda) \, \epsilon_A(\lambda) \lambda^4 d\lambda}{\int f_D(\lambda) \, d\lambda} = \int \overline{f_D(\lambda)} \, \epsilon_A(\lambda) \lambda^4 d\lambda, \qquad (2.6)$$

where $\lambda$ is the wavelength, $f_D$ is the donor intensity at wavelength $\lambda$ and $\overline{f_D}$ is the average donor intensity over the wavelength range, and $\epsilon_A$ is the permittivity of the medium [25].
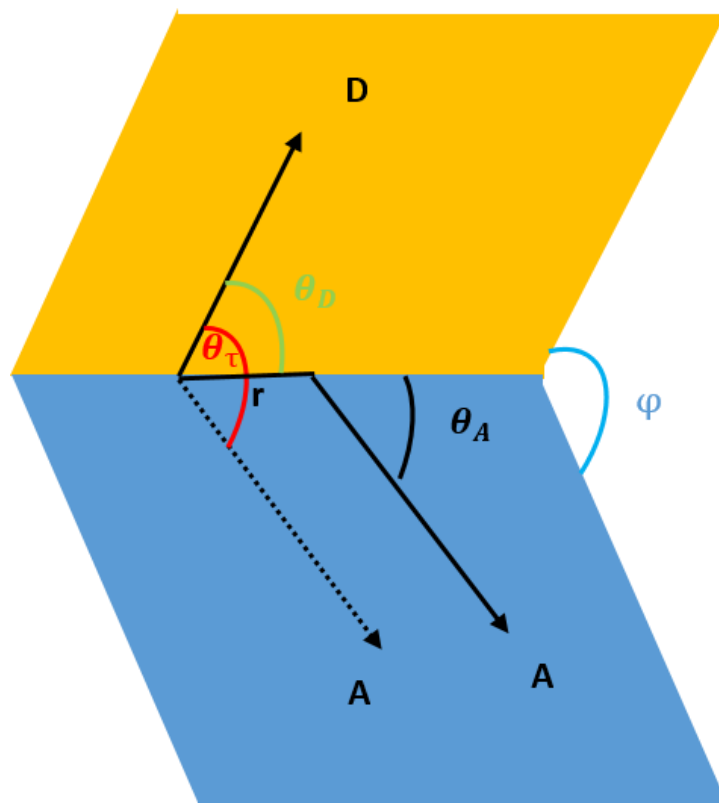
**Figure 2.4 The schematic diagram of the transition dipole directions.** $\theta^D$ and $\theta^A$ are the angles for the donor (D) and acceptor (A) dipole orientations, with reference to the line joining D and A (along $r$) respectively in their respective planes. The two planes intersect each other at an angle $\Phi$, whereas $\theta^\tau$ is the angle between the instantaneous directions of the two dipoles.

Förster reckoned that, since the energy conservation cannot be violated, energy transfer from a donor dipole to acceptor dipole can only be possible when there is the same difference between the excited and the ground state energy levels of the two species. Since the same frequency is accepted, as emitted, which is a condition of resonance. Nevertheless, Förster observed that there is no single frequency of transfer; instead, there is a range of frequencies (or wavelengths), which gives spectrum of emission and excitation, for the donor and acceptor of the energy respectively. Especially in the solutions, the excitation and the emission spectrums of

41

energy further broaden, because of the physical interaction of the fluorescent molecules with their environment, specifically, their collision with the other solution molecules.

From the equation given in the FRET section above, it can be noted that the rate of energy transfer is dependent on factors that are as follows:

- Distance between donor and acceptor

- Spectral overlap

- Relative dipole orientation

By means of depolarization and de-quenching of fluorescence, J Perrin and F Perrin [46, 47] observed intermolecular energy migration, which was found in solutions of moderate concentration where majority of the molecules were not associated to each other.

When a polarized light excites a fluorescent molecule, the excited molecules will be arranged anisotropically that is having directionality. However, in times between subsequent excitations, the molecules will rearrange themselves isotropically by Brownian rotational motion (diffusion), which is on the scale of $10^{-8}$ sec, giving an unpolarized fluorescent emission.

On the other hand, in the viscous solutions, there is not always enough time for the excited molecules to change their orientation completely to be isotropically distributed before they emit. Hence, this is to say that the fluorescence is partially polarized. The maximum value of the degree of depolarization is up to 50% and it has been found that even increasing concentration of the solution lead to very small changes in depolarization [48].

Oscillating electric charge causes coupling with a radiation field, thus the emission of energy occurs in the surrounding region. Mutual electrostatic force of two charged molecules causes coupling of the oscillators of adjacent molecules. At the same frequencies, this lead to transfer of

42

energy, in the same fashion, as energy is transferred in coupled pendulums, where the pendulum in motion transfers its energy mechanically to the other pendulum, which was initially in rest.

In the case of resonance energy transfer (this coupling is called mutual coupling), where the coupling is considerably weaker than the coupling between charge and radiation field, the emission of energy occurs only from the primarily excited oscillator. In the first case coupling of charge with the radiation field, the excitation and the emission is reciprocated by both the molecule participating in the coupling, i.e., when the second molecule emits after being excited by the E field of the first one, the emission of the second one can re-excite the first molecule leading to multiple excitations and de-excitations. Furthermore, in FRET excitations, the re-excitations are distance dependent. The two excitations merge at a distance, which was computed by Perrin by the following equation

$$d_0 \sim \frac{c}{\omega} = \lambda/2\pi \tag{2.7}$$

Using quantum mechanical approach, the mean duration of emission is given by

$$\tau = h \, c^3 / 2\pi M^2 \, \omega^3, \tag{2.8}$$

where h is Plank's constant.

Also, the interaction energy of the two oscillators is equal to the electrostatic energy of both dipoles, given by the following equation

$$U \sim M^2/d^3, \tag{2.9}$$

where d is the distance between the two oscillators.

From here, transfer of the entire energy occur in a time of

$$t_0 = \, \sim h/2\pi U \, \sim h \, d^3/2\pi \, M^2 \tag{2.10}$$

For critical distance $d_0$, the transfer time is equal to the lifetime [43], i.e.

43

$$t_0 = \tau \qquad\qquad\qquad (2.11)$$

On computing, the distance $d_0$ comes equal to 1000 Å, for molecules which absorb at $\lambda = \sim 6000$ Å, which is much larger than the distance obtained from concentration quenching ($\lambda = 50$ Å). This is an inconsistency in Perrin's method, which was noticed by Förster because the condition of exact resonance was not met for the energy transfer. For a spectrum of a dye, it is not a short line but a broad band. The reason behind the broad band is coupling of the electronic motion with the atomic motion within the molecule and with the surrounding solvent. Another reason for the broadness is that emission (fluorescence) spectrum is shifted from the absorption of the same molecule by Stokes' Law and the two show very little overlap [42, 43, 49].

Protein-protein interaction is important to several biological processes, including signal transduction. There have been several theories and model presented to study the kinetics of protein-protein interaction. One of them is probing the kinetics via FRET, or kinetic model of FRET. For a dimeric complex, it has been relatively easier to see consistency between theory and observation, however, for a complex of more than two monomers, it gets complicated. There are two main tasks of this model that are as follows:

- Determination of intermolecular distances
- Investigating the stoichiometry of the protein complexes.

The first can be determined with the measurement of FRET efficiency E and Förster Radius Ro, which is the distance at which the FRET efficiency drops to half of its maximum value. These have been determined using both life time FRET (FLIM) and intensity dependent FRET. Results of FLIM are concentration dependent while intensity dependent FRET is concentration dependent. For the stoichiometry determination, intensity based FRET is more suitable because it can give the

44

ration of donor and acceptor tagged molecules for any quantifiable region of interest such as pixel. Also, it can give the ratio of interacting to total number of molecules.

Due to the complexity of oligomeric determination, the advancement in this research field has been slow over last several decades. A model was given for homo oligomeric species [50] which was inspired from the crosslinking model used by Milligan and the others [51]. Raicu *et al* [52] extended this model to include free monomers and then used it calculate fraction yeast oligomers and average number of the monomers in a oligomer, which was found to be a dimer. This theory makes assumptions that the rate of energy transfer to all the acceptors by a nearby donor is same, and there is negligible energy transfer to the distant monomers of the complex [53]. In oligomeric complexes of the order greater than two (bigger than dimer) there are more than one pathways of the energy transfer from each donor. And, if there are more than one donors, then they can excite acceptor molecule in parallel, *quasi parallel process*, in which each donor has non-zero probability of exciting the same acceptor. However truly parallel (in time) transfer of energy from multiple donors to the same acceptor will violate basic quantum mechanics postulates.

Different methods are used to estimate FRET efficiency, such as acceptor photobleaching [54, 55] , and acceptor stimulated emission [24, 56]. For the oligomer of size bigger than dimers, the multiple pathways for energy transfer from donor to acceptor are available. The FRET efficiency between a donor and an acceptor (DA) pair is called *pairwise FRET efficiency* ($E_p$). When there are only FRET oligomers present in a mixture, then the average FRET efficiency is called true FRET efficiency. However, when there is the presence of donor only or acceptor only complexes (which don't participate in FRET), then the average FRET efficiency is called apparent FRET efficiency (Eapp), assuming the fret complexes are there for functional purposes and remain changed in their geometry throughout the measurement of FRET. At this stage of modeling, the

45

nonspecific interaction between the donors and the acceptors of different complexes is not considered due to crowding or motion [57, 58], which could be more significant at higher concentrations.

FRET efficiency of a dimeric complex is defined based on two types of physical quantities that are as follows:

- Spectroscopic quantities like quantum yields of donor and acceptor, in the presence and absence of the other acceptor or donor, respectively,

- The lifetime or fluorescent intensity, which are experimentally measurable.

FRET is considered only as non-radiative energy transfer and homo FRET (one between two donor or acceptor molecules) and this is not considered in this part of the kinetic theory.

## 2.3.2 Relationship between quantum yield (Q) and FRET efficiency ($E_{app}$)

Quantum yield of donor is defined as rate of deexcitation by the means of photon emission divided total rate of deexcitation. The Quantum yields of donor and acceptor in the absence of acceptor or donor is given by [22] the following two equations

$$Q^D = \Gamma^{r,D}/(\Gamma^{r,D} + \Gamma^{nr,D}), \tag{2.12}$$

and
$$Q^A = \Gamma^{r,A}/(\Gamma^{r,A} + \Gamma^{nr,A}) \tag{2.13}$$

When there is an acceptor in the vicinity of a donor (less than 10 nm) and their spectral profiles match (donor emission and acceptor excitation have overlaps), and the orientation of the transition dipoles is such that there is a dipole coupling between the donor and acceptor molecule, then these conditions present another nonradiative pathway for donor energy transfer to the acceptor via FRET. The quantum yield of the donor in the presence of the acceptor is given by

$$Q^{DA} = \Gamma^{r,D}/(\Gamma^{r,D} + \Gamma^{nr,D} + \Gamma^{FRET}), \tag{2.14}$$

46

and, the apparent FRET efficiency is defined by the following

$$E_{app} = \Gamma^{FRET}/(\Gamma^{r,D} + \Gamma^{nr,D} + \Gamma^{FRET}), \qquad (2.15)$$

where $\Gamma^{r,D}$ and $\Gamma^{r,A}$ are the rates of donor and acceptor deexcitation respectively. $\Gamma^{nr,D}$ is the non-radiative rate of donor excitation and $\Gamma^{FRET}$ is the rate of the energy transferred via FRET.

### 2.3.2 Fluorescence lifetime

Time taken by a fluorophore to return to ground state from a excited state is the deexcitation lifetime, and denoted by $\tau$. The excited molecule emits a photon in the process, when this happens in visible spectrum, it is called fluorescence lifetime. The lifetime can range from picosecond to nanoseconds [5].

The lifetime for donor and acceptor species, is given by the following two equations

$$\tau_D = 1/(\Gamma^{r,D} + \Gamma^{nr,D}), \qquad (2.16)$$

and,

$$\tau_A = 1/(\Gamma^{r,A} + \Gamma^{nr,A}) \qquad (2.17)$$

However, the lifetime for the donor and acceptor changes when FRET occurs. The donor lifetime in the presence of acceptor is given by the following equation [28]:

$$\tau_{DA} = 1/(\Gamma^{r,D} + \Gamma^{nr,D} + \Gamma^{FRET}) \qquad (2.18)$$

From the above equations, it can be seen that the donor life time shortens in the presence of the acceptor.

### 2.4 The kinetic model of FRET

In a multimeric complex, when a donor molecule has several pathways of transferring the energy via FRET, i.e., it transfers energy to more than one acceptor within a few nanometer distance, the quantum yield of the $i$th donor is given by the Kinetic Theory of FRET [52].

47
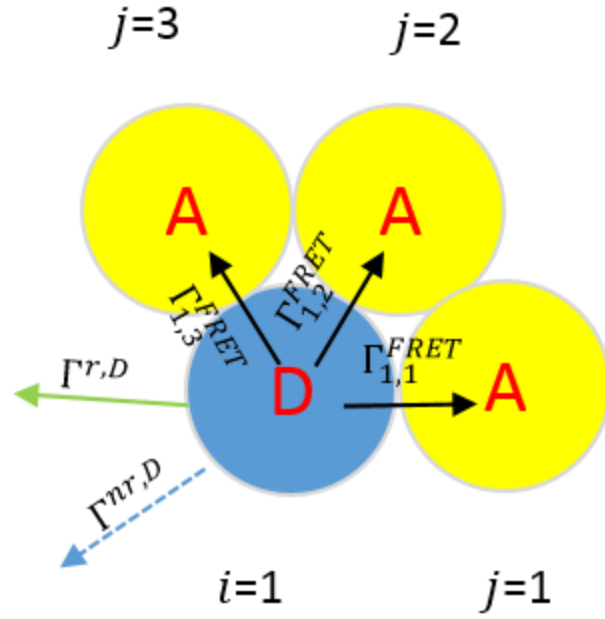
**Figure 2.5 Illustration for donor de-excitation pathways ($\Gamma$).** Donor (D) losing energy via radiative $\Gamma^{r,D}$, non-radiative $\Gamma^{nr,D}$ (e.g., thermal energy lost through vibrational relaxations), and nonradiative energy transfer via FRET $\Gamma_{i,j}^{FRET}$ to neighboring acceptors (A). $i$ and $j$ are the indexes for donor and acceptor positions [20, 52].

$$Q_{i,k,n,q}^{DA} = \Gamma^{r,D} \Big/ \left( \Gamma^{r,D} + \Gamma^{nr,D} + \sum_{j=1}^{n-k} \Gamma_{i,j,q}^{FRET} \right), \tag{2.19}$$

where $n$ is the number of monomers in the complex, $k$ is the number of donors, hence the number

of acceptors is $(n-k)$, and $j$ is a summation index for acceptors, and $\Gamma_{i,j,q}^{FRET} =$

$(\Gamma^{r,D} + \Gamma^{nr,D}) \big/ \left( R_{i,j,q}^{0} \big/ \mathrm{r}_{i,j,q} \right)^{6}$ is the rate constant for a donor-acceptor pair.

Using the above equation, and the relationship between quantum yield and FRET

efficiency, $E_{i,k,n,j}$ can be generalized for the $i$th donor of complex of $n$ molecules and k donors

$$E_{i,k,n,j} = \frac{\sum_{j=1}^{n-k} \Gamma_{i,j,q}^{FRET} / (\Gamma^{r,D} + \Gamma^{nr,D})}{1 + \sum_{j=1}^{n-k} \Gamma_{i,j,q}^{FRET} / (\Gamma^{r,D} + \Gamma^{nr,D})}, \tag{2.20}$$

and the apparent FRET efficiency per donor ($E_{app}$) for the complex is simply the average FRET

efficiency of all donors, as in the equation below

48

$$E_{app} = \sum_{i=1}^{k} E_{i,k,n} \tag{2.20}$$

Using equation 2.20, $E_{app}$ equations can be written for the quaternary structures of various stoichiometry and shape, such as trimers, tetramers, hexamers etc. A few of them are shown in the figure below.



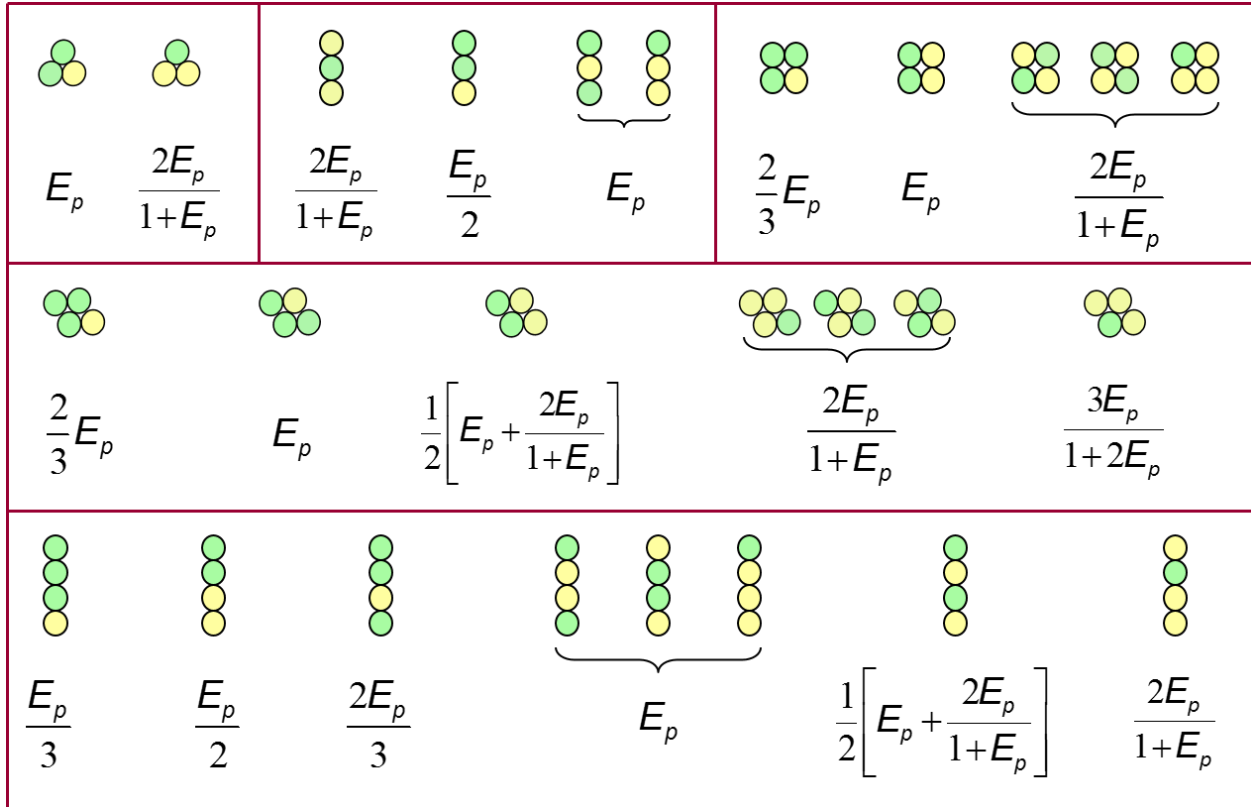**Figure 2.6 Efficiencies predicted for different oligomer shapes and sizes [28].** For any given structure, all the $E_{app}$ expression are related by a single parameter, which is pairwise FRET efficiency or $E_p$.

Using the equations 2.17 and 2.18, the $E_{app}$ expression for a parallelogram tetramer, with a special case being rhombic tetramer (as shown in the second row of Figure 2.6), is derived below.

49

## 2.4.1 Theoretical FRET efficiency for a parallelogram tetramer model

Let us consider a tetramer (i.e., $n = 4$) consisting of $n_D$ donors and $n_A$ acceptors placed in the corners of a parallelogram of sides $r_1$ and $r_2$. Figure 2.7 demonstrates such a tetramer (DDAD) with $n_D = 3$ and $n_A = 1$. If $r_1$ and $r_2$ are the two sides of the parellogram and $\alpha$ is the angle between the two sides of the parellogram then the digonal $r_{d1}$ and $r_{d2}$ are given by:

$$r_{d1} = (r_1{}^2 + r_2{}^2 + 2r_1 r_2 \cos \alpha)^{1/2}, \tag{2.21}$$

and,

$$r_{d1} = (r_1{}^2 + r_1{}^2 - 2r_1 r_2 \cos \alpha)^{1/2}, \tag{2.22}$$

Also, the pairwise FRET efficiency [28, 59] between donor $i = 1$ and acceptor $j = 1$ is given by

$$E_1 = \frac{\left(\frac{R_0}{r_1}\right)^6}{1 + \left(\frac{R_0}{r_1}\right)^6}, \tag{2.23}$$

where, $R_0$ is Forster radius. From Eq. (1.2)

$$\left(\frac{R_0}{r_1}\right)^6 = \frac{E_1}{1 - E_1}. \tag{2.24}$$

Therefore

$$\left(\frac{R_0}{r_k}\right)^6 = \frac{E_1}{1 - E_1} \left(\frac{r_1}{r_k}\right)^6, \tag{2.25}$$

where, $k$ can take values $2$, $d1$ and $d2$.

Now, the apparent FRET efficiency for the configuration shown in Figure 2.7 is given by

$$E_{app} = \frac{1}{3} \sum_{i=1}^{3} E_{ij} = \frac{1}{3} (E_{11} + E_{21} + E_{31}), \tag{2.26}$$

Recognizing $E_{11}$ as $E_1$ and using Eq. (1.3)

$$E_{21} = \frac{\left(\frac{R_0}{r_{d1}}\right)^6}{1 + \left(\frac{R_0}{r_{d1}}\right)^6} = \frac{\frac{E_1}{1 - E_1}\left(\frac{r_1}{r_{d1}}\right)^6}{1 + \frac{E_1}{1 - E_1}\left(\frac{r_1}{r_{d1}}\right)^6}, \tag{2.27}$$
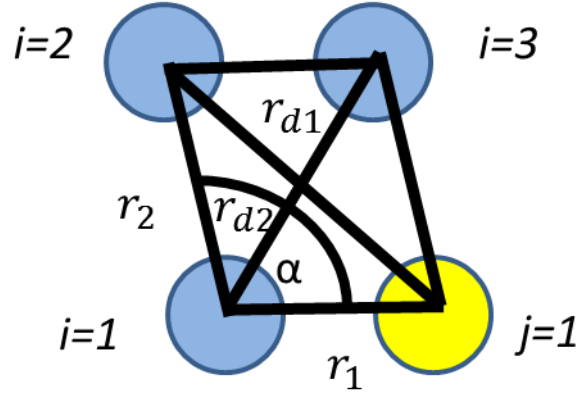
50

**Figure 2.7 Configuration of a parallelogram shaped tetramer model representing three donors and one acceptor.** $r_1$ and $r_2$ represent the two sides of the parellogram, $\alpha$ is the angle between two side of the parellogram, $r_{d1}$ and $r_{d2}$ are the two diagonals of the parellogram. $i$ represents the donors while $j$ the acceptors. $r_{d1}$ is short diagonal distance while $r_{d2}$ is the long diagonal distance.

Similary,

$$E_{31} = \frac{\left(\frac{R_0}{r_2}\right)^6}{1+\left(\frac{R_0}{r_2}\right)^6} = \frac{\frac{E_1}{1-E_1}\left(\frac{r_1}{r_2}\right)^6}{1+\frac{E_1}{1-E_1}\left(\frac{r_1}{r_2}\right)^6}, \tag{2.28}$$

Pluging Eq. (2.6) and Eq. (2.7) into Eq. (2.5), we get

$$E_{app} = \frac{1}{3}\left[E_1 + \frac{\frac{E_1}{1-E_1}\left(\frac{r_1}{r_{d1}}\right)^6}{1+\frac{E_1}{1-E_1}\left(\frac{r_1}{r_{d1}}\right)^6} + \frac{\frac{E_1}{1-E_1}\left(\frac{r_1}{r_2}\right)^6}{1+\frac{E_1}{1-E_1}\left(\frac{r_1}{r_2}\right)^6}\right], \tag{2.29}$$

and,

$$E_{app} = \frac{1}{3}\left[E_1 + \frac{E_1\left(\frac{r_1}{r_2}\right)^6}{1-E_1+E_1\left(\frac{r_1}{r_2}\right)^6} + \frac{E_1\left(\frac{r_1}{r_{d2}}\right)^6}{1-E_1+E_1\left(\frac{r_1}{r_{d2}}\right)^6}\right], \tag{2.30}$$

Equations (2.27) and (2.28) give is the expression for apparent FRET efficency in terms of the sides of the parellogram, the diagonals and pairwise FRET efficiency. Similarly, the FRET efficencicy expressions for the other six possible configurations can be derived and there expressions are tabulated in Table 2.1.

51

**Table 2.1. Parallelogram tetramer configurations, and their FRET efficiencies.**

| Configuration # | Geometric Configurations | FRET Efficiency Per Donor |
|---|---|---|
| 1. |  | **0** |
| 2. |  | $E_1, \dfrac{E_1\left(\frac{r_1}{r_2}\right)^6}{1 - E_1 + E_1\left(\frac{r_1}{r_2}\right)^6}, \dfrac{E_1\left(\frac{r_1}{r_{d2}}\right)^6}{1 - E_1 + E_1\left(\frac{r_1}{r_{d2}}\right)^6}$ |
| 3. |  | |
| 4. |  | $E_1, \dfrac{E_1\left(\frac{r_1}{r_2}\right)^6}{1 - E_1 + E_1\left(\frac{r_1}{r_2}\right)^6}, \dfrac{E_1\left(\frac{r_1}{r_{d1}}\right)^6}{1 - E_1 + E_1\left(\frac{r_1}{r_{d1}}\right)^6}$ |
| 5. |  | |
| 6. | | |
| 7. |  | $\dfrac{E_1\left[\left(\frac{r_1}{r_2}\right)^6 + \left(\frac{r_1}{r_{d1}}\right)^6\right]}{1 - E_1 + E_1\left[\left(\frac{r_1}{r_2}\right)^6 + \left(\frac{r_1}{r_{d1}}\right)^6\right]}, \dfrac{E_1\left[\left(\frac{r_1}{r_2}\right)^6 + \left(\frac{r_1}{r_{d2}}\right)^6\right]}{1 - E_1 + E_1\left[\left(\frac{r_1}{r_2}\right)^6 + \left(\frac{r_1}{r_{d2}}\right)^6\right]}$ |
| 8. |  | |
| 9. |  | $\dfrac{E_1\left[1 + \left(\frac{r_1}{r_{d1}}\right)^6\right]}{1 - E_1 + E_1\left[1 + \left(\frac{r_1}{r_{d1}}\right)^6\right]}, \dfrac{E_1\left[1 + \left(\frac{r_1}{r_{d2}}\right)^6\right]}{1 - E_1 + E_1\left[1 + \left(\frac{r_1}{r_{d2}}\right)^6\right]}$ |
| 10. |  | |
| 11. |  | |

| 12. |  | $$\dfrac{E_1\left[1+\left(\frac{r_1}{r_2}\right)^6\right]}{1-E_1+E_1\left[1+\left(\frac{r_1}{r_2}\right)^6\right]}\,,\,\dfrac{E_1\left[1+\left(\frac{r_1}{r_2}\right)^6\right]}{1-E_1+E_1\left[1+\left(\frac{r_1}{r_2}\right)^6\right]}$$ |
|-----|------|------|
| 13. |  | |
| 14. |  | $$\dfrac{E_1\left[1+\left(\frac{r_1}{r_2}\right)^6+\left(\frac{r_1}{r_{d2}}\right)^6\right]}{1-E_1+E_1\left[1+\left(\frac{r_1}{r_2}\right)^6+\left(\frac{r_1}{r_{d2}}\right)^6\right]}$$ |
| 15. |  | |
| 16. |  | $$\dfrac{E_1\left[1+\left(\frac{r_1}{r_2}\right)^6+\left(\frac{r_1}{r_{d1}}\right)^6\right]}{1-E_1+E_1\left[1+\left(\frac{r_1}{r_2}\right)^6+\left(\frac{r_1}{r_{d1}}\right)^6\right]}$$ |
| 17. |  | **N/A** |

Similarly, $E_{app}$ expressions can be computed for any other geometry. Eapp expressions for parallelogram hexamer and circular octamers are presented in Appendix A.

# References

[1] C. Bordier, Phase separation of integral membrane proteins in Triton X-114 solution, Journal of Biological Chemistry, 256 (1981) 1604-1607.

[2] V. Cherezov, D.M. Rosenbaum, M.A. Hanson, S.G. Rasmussen, F.S. Thian, T.S. Kobilka, H.-J. Choi, P. Kuhn, W.I. Weis, B.K. Kobilka, High-resolution crystal structure of an engineered human β2-adrenergic G protein–coupled receptor, Science (New York, N.Y.), 318 (2007) 1258-1265.

[3] B. Wetzl, M. Gruber, B. Oswald, A. Dürkop, B. Weidgans, M. Probst, O.S. Wolfbeis, Set of fluorochromophores in the wavelength range from 450 to 700 nm and suitable for labeling proteins and amino-modified DNA, Journal of Chromatography B, 793 (2003) 83-92.

[4] C.I. Richards, S. Choi, J.-C. Hsiang, Y. Antoku, T. Vosch, A. Bongiorno, Y.-L. Tzeng, R.M. Dickson, Oligonucleotide-stabilized Ag nanocluster fluorophores, Journal of the American Chemical Society, 130 (2008) 5038-5039.

[5] J. Lakowicz, Principles of fluorescence microscopy, in, Kluwer Academic, New York, 1999.

[6] R.Y. Tsien, The green fluorescent protein, Annual review of biochemistry, 67 (1998) 509-544.

[7] K.A. Franz, W.G. Kehr, A. Siggel, J. Wieczoreck, W. Adam, Luminescent materials, Ullmann's Encyclopedia of Industrial Chemistry, (2000).

[8] S.P. McGlynn, T. Azumi, M. Kinoshita, Molecular spectroscopy of the triplet state, (1969).

[9] D.J. Griffiths, E.G. Harris, Introduction to quantum mechanics, American Journal of Physics, 63 (1995) 767-768.

[10] A.A. Lamola, G.S. Hammond, Mechanisms of photochemical reactions in solution. XXXIII. Intersystem crossing efficiencies, The Journal of Chemical Physics, 43 (1965) 2129-2135.

[11] R.H. Austin, S.S. Chan, T.M. Jovin, Rotational diffusion of cell surface components by time-resolved phosphorescence anisotropy, Proceedings of the National Academy of Sciences, 76 (1979) 5650-5654.

[12] R.B. Sekar, A. Periasamy, Fluorescence resonance energy transfer (FRET) microscopy imaging of live cell protein localizations, J Cell Biol, 160 (2003) 629-633.

[13] K. Truong, M. Ikura, The use of FRET imaging microscopy to detect protein-protein interactions and protein conformational changes in vivo, Current opinion in structural biology, 11 (2001) 573-578.

[14] M.A. Hink, T. Bisselin, A.J. Visser, Imaging protein-protein interactions in living cells, Plant molecular biology, 50 (2002) 871-883.

[15] A. Evers, T. Klabunde, Structure-based drug discovery using GPCR homology modeling: successful virtual screening for antagonists of the alpha1A adrenergic receptor, Journal of medicinal chemistry, 48 (2005) 1088-1097.

[16] F.U. Hartl, Molecular chaperones in cellular protein folding, (1996).

[17] G.J. Kremers, J. Goedhart, E.B. van Munster, T.W. Gadella, Jr., Cyan and yellow super fluorescent proteins with improved brightness, protein folding, and FRET Forster radius, Biochemistry, 45 (2006) 6570-6580.

[18] A.K. Mishra, T. Mavlyutov, D.R. Singh, G. Biener, J. Yang, J.A. Oliver, A. Ruoho, V. Raicu, The sigma-1 receptors are present in monomeric and oligomeric forms in living cells in the presence and absence of ligands, Biochem J, 466 (2015) 263-271.

[19] S. Patowary, E. Alvarez-Curto, T.R. Xu, J.D. Holz, J.A. Oliver, G. Milligan, V. Raicu, The muscarinic M3 acetylcholine receptor exists as two differently sized complexes at the plasma membrane, Biochem J, 452 (2013) 303-312.

[20] V. Raicu, D.R. Singh, FRET spectrometry: a new tool for the determination of protein quaternary structure in living cells, Biophys J, 105 (2013) 1937-1945.

[21] V. Raicu, M.R. Stoneman, R. Fung, M. Melnichuk, D.B. Jansma, L.F. Pisterzi, S. Rath, M. Fox, J.W. Wells, D.K. Saldin, Determination of supramolecular structure and spatial distribution of protein complexes in living cells, Nat Photon, 3 (2009) 107-113.

[22] D.R. Singh, M.M. Mohammad, S. Patowary, M.R. Stoneman, J.A. Oliver, L. Movileanu, V. Raicu, Determination of the Quaternary Structure of a Bacterial ATP-Binding Cassette (ABC) Transporter in Living Cells, Integrative biology : quantitative biosciences from nano to macro, 5 (2013) 312-323.

[23] D.L. Andrews, D.S. Bradshaw, Virtual photons, dipole fields and energy transfer: a quantum electrodynamical approach, European journal of physics, 25 (2004) 845.

[24] E.A. Jares-Erijman, T.M. Jovin, FRET imaging, Nature biotechnology, 21 (2003) 1387-1395.

55

[25] J.R. Lakowicz, Principles of fluorescence spectroscopy, Springer Science & Business Media, 2013.

[26] K.L. Pierce, L.M. Luttrell, R.J. Lefkowitz, New mechanisms in heptahelical receptor signaling to mitogen activated protein kinase cascades, Oncogene, 20 (2001).

[27] J. Perrin, Observations sur la fluorescence, 1925.

[28] V. Raicu, A. Popescu, Integrated molecular and cellular biophysics, Springer, 2008.

[29] A.K. Mishra, M. Gragg, M. Stoneman, G. Biener, J.A. Oliver, P. Miszta, S. Filipek, V. Raicu, P. Park, Quaternary structures of opsin in live cells revealed by FRET spectrometry, Biochemical Journal, (2016) BCJ20160422.

[30] S. Patowary, Luca F. Pisterzi, G. Biener, Jessica D. Holz, Julie A. Oliver, James W. Wells, V. Raicu, Experimental Verification of the Kinetic Theory of FRET Using Optical Microspectroscopy and Obligate Oligomers, Biophysical Journal, 108 (2015) 1613-1622.

[31] J.R. Gispert, Coordination chemistry, Wiley-VCH Weinheim, 2008.

[32] G. Weber, F. Teale, Determination of the absolute quantum yield of fluorescent solutions, Transactions of the Faraday Society, 53 (1957) 646-655.

[33] A.M. Brouwer, Standards for photoluminescence quantum yield measurements in solution (IUPAC Technical Report), Pure and Applied Chemistry, 83 (2011) 2213-2228.

[34] O. Shimomura, The discovery of aequorin and green fluorescent protein, Journal of microscopy, 217 (2005) 3-15.

[35] O. Shimomura, Structure of the chromophore of Aequorea green fluorescent protein, FEBS letters, 104 (1979) 220-222.

[36] M. Chalfie, Green fluorescent protein as a marker for gene expression, Trends in Genetics, 10 (1994) 151.

[37] A. Minta, J. Kao, R.Y. Tsien, Fluorescent indicators for cytosolic calcium based on rhodamine and fluorescein chromophores, Journal of Biological Chemistry, 264 (1989) 8171-8178.

[38] A. Miyawaki, R.Y. Tsien, Monitoring protein conformations and interactions by fluorescence resonance energy transfer between mutants of green fluorescent protein, Methods in enzymology, 327 (2000) 472-500.

[39] R.M. Dickson, A.B. Cubitt, R.Y. Tsien, W. Moerner, On/off blinking and switching behaviour of single molecules of green fluorescent protein, Nature, 388 (1997) 355-358.

[40] K. Brejc, T.K. Sixma, P.A. Kitts, S.R. Kain, R.Y. Tsien, M. Ormö, S.J. Remington, Structural basis for dual excitation and photoisomerization of the Aequorea victoria green fluorescent protein, Proceedings of the National Academy of Sciences, 94 (1997) 2306-2311.

[41] R. Heim, D.C. Prasher, R.Y. Tsien, Wavelength mutations and posttranslational autoxidation of green fluorescent protein, Proceedings of the National Academy of Sciences, 91 (1994) 12501-12504.

[42] T. Forster, Energiewanderung und fluoreszenz, Naturwissenschaften, 33 (1946) 166-175.

[43] T. Förster, Experimentelle und theoretische Untersuchung des zwischenmolekularen Übergangs von Elektronenanregungsenergie, Zeitschrift für naturforschung A, 4 (1949) 321-327.

[44] R.E. Dale, J. Eisinger, W. Blumberg, The orientational freedom of molecular probes. The orientation factor in intramolecular energy transfer, Biophysical journal, 26 (1979) 161.

[45] A.P. Demchenko, Introduction to fluorescence sensing, Springer Science & Business Media, 2008.

[46] F. Perrin, Polarisation de la lumière de fluorescence. Vie moyenne des molécules dans l'etat excité, J. phys. radium, 7 (1926) 390-401.

[47] J. Perrin, Fluorescence et induction moleculaire par resonance, CR Hebd. Seances Acad. Sci, 184 (1927) 1097-1100.

[48] A. Bute-Nandt, H. Friedrich-Freska, St. Hartwig, and G. Scheibe, Z. Physiol. Chem, 274 (1942) 276.

[49] W. Lewschin, Das Gesetz der Spiegelkorrespondenz der Absorptions-und Fluoreszenzspektren. I, Zeitschrift für Physik, 72 (1931) 368-381.

[50] B.D. Adair, D.M. Engelman, Glycophorin A helical transmembrane domains dimerize in phospholipid bilayers: a resonance energy transfer study, Biochemistry, 33 (1994) 5539-5544.

[51] P. Goldsmith, P.S. Backlund Jr, K. Rossiter, A. Carter, G. Milligan, C.G. Unson, A. Spiegel, Purification of heterotrimeric GTP-binding proteins from brain: identification of a novel form of Go, Biochemistry, 27 (1988) 7085-7090.

[52] V. Raicu, Efficiency of resonance energy transfer in homo-oligomeric complexes of proteins, J Biol Phys, 33 (2007) 109-127.

[53] P.D. Moens, D.J. Yee, C.G. dos Remedios, Determination of the radial coordinate of Cys-374 in F-actin using fluorescence resonance energy transfer spectroscopy: effect of phalloidin on polymer assembly, Biochemistry, 33 (1994) 13102-13108.

[54] G. Valentin, C. Verheggen, T. Piolot, H. Neel, M. Coppey-Moisan, E. Bertrand, Photoconversion of YFP into a CFP-like species during acceptor photobleaching FRET experiments, Nature methods, 2 (2005) 801-801.

[55] Y. Gu, W. Di, D. Kelsell, D. Zicha, Quantitative fluorescence resonance energy transfer (FRET) measurement with acceptor photobleaching and spectral unmixing, Journal of microscopy, 215 (2004) 162-173.

[56] C. Li, Y. Zhang, J. Hu, J. Cheng, S. Liu, Reversible Three-State Switching of Multicolor Fluorescence Emission by Multiple Stimuli Modulated FRET Processes within Thermoresponsive Polymeric Micelles, Angewandte Chemie, 122 (2010) 5246-5250.

[57] P. Wolber, B. Hudson, An analytic solution to the Förster energy transfer problem in two dimensions, Biophysical journal, 28 (1979) 197.

[58] T. Dewey, G. Hammes, Calculation on fluorescence resonance energy transfer on surfaces, Biophysical journal, 32 (1980) 1023.

[59] P.R. Selvin, The renaissance of fluorescence resonance energy transfer, Nature structural biology, 7 (2000) 730-734.

# Chapter 3: Technology for FRET imaging

This chapter covers the description of the technology used in FRET imaging. The chapter is divided into three sections. The first section focuses on the major classical methods used for FRET imaging, the second section focuses on optical micro-spectroscopy (OptiMiS), a powerful imaging technology developed by Raicu lab and used as a part of imaging technology in the next two chapters of this thesis, while the last part of the chapter details a method of calculating the pixel level FRET efficiencies of the images generated with the help of spectral FRET-based microscopy.

## 3.1 Review of classical methods

Optical imaging, like fluorescence imaging, are the powerful investigation tools, in biological and biomedical samples, because they are minimally incursive, and can be performed on the living cells or tissues, without causing any damage to them. There are four main parameters which characterize fluorescence: wavelength, lifetime, and polarization. Fluorescence imaging is often performed for investigating the biological samples, and the four parameters mentioned above, or their combinations are used to generate contrasts in image pixels. Fluorescence detection sensitivity extends to single molecules with the help of sophisticated technology in bioengineering and microscopy.

Traditional biochemical or biophysical methods did not provide access to assembly of protein complexes in their natural environment. Thus, the researches using those methods were not conducted under physiological conditions, and therefore always raised doubts as to whether those interactions also exist in live cells. Fluorescence-based techniques, deploying wide field, confocal or multiphoton microscopy, have provided with tools to look into living cells. The other technological developments, which were crucial to *in vivo* observations, occurred due to the success in molecular biology engineering, which enabled with genetically encoded fluorescent

59

labels [1-9]. Development in optical and computational techniques helped in image acquisition. These technological developments led several sophisticated studies ranging from gene expression to intercellular signaling [5, 10-12].

Biochemistry of living systems includes the study of the structural hierarchy of organelle, cells, tissues and living beings. Biological phenomena are based on fundamental physicochemical processes of molecular binding, association, dissociation and conformal changes, diffusion, etc. Fluorescence microscopy is specifically suitable because it presents contrast due to its sensitivity, specificity, and modulation between the ground and the excited states of molecules.

FRET microscopy relies on the signal received in donor and acceptor channels. If FRET occurs, the donor signal will be quenched as well as the acceptor channel signal will be sensitized or increased [13-19]. This can not only give colocalization of donors and acceptors but also provide stoichiometry and shape of molecular association [15, 16, 19].

Diffraction is the limit to conventional optical microscopy. FRET provides a spatial resolution, which far exceeds the diffraction limited resolution. Moreover, FRET is also compatible with super resolution techniques, for instance, Total Internal Reflection Fluorescence (TIRF) microscopy.

There are several types of microscopy, including wide field [20-24], confocal [25-31], multi-photon [32-39] and Total Internal Reflection Fluorescence (TIRF) microscopy [40-44], which can be used to measure FRET. Although the wide field microscopy is a popular microscopy, it is not very unsuitable for FRET studies, because, in the wide field microscopy, the light reaching the detector comes from a thick specimen region causing blur and low spatial resolution. Basic principles and functions of some popular FRET technologies, which include fluorescence lifetime imaging, fluorescence photobleaching, changes in optical polarization, are given below.

## 3.2 Fluorescence lifetime imaging microscopy (FLIM)

FLIM is based on the difference in the exponential decay rates of the fluorophores in the absence and presence of diverse types of fluorophores within FRET range (<10 nm). This method depends on the lifetime rather than the intensity of the fluorophores because it does not need high excitation intensity. Due to lower intensity, this method produces lesser scattering in thick samples than intensity-based methods. The concept of fluorescence lifetime is defined below.

Quantum yield ($Q$), as defined previously, is the ratio of photon emitted to photons decayed, can also be written in terms of decay rates (or rate of deexcitation)

$$Q = \Gamma^r/(\Gamma^r + \Gamma^{nr}) \qquad (4.1)$$

Lifetime ($\tau$) is measure of average time spent in excited state, given as

$$\tau = 1/(\Gamma^r + \Gamma^{nr}) \qquad (4.2)$$

Intensity at a time t is given in term of lifetime as

$$I(t) = I(0).e^{-t/\tau} \qquad (4.3)$$

Quantum yield is proportional to fluorescence lifetime as

$$Q = \tau/\tau^r, \qquad (4.4)$$

where $\tau^r = 1/\Gamma^r$

Measurement of fluorescence lifetime depends on the intensity of excitation, rather than the concentration of fluorophores, on which emission intensity will depend. Thus, regarding this, the lifetime method is more robust than the intensity-based method. In theory, determining fluorescence lifetime provides one of the most direct measurements of FRET. However, measuring lifetime accurately is rather challenging.

61

Fluorescence lifetime images are basically the fluorescence emission intensity maps, where the intensities are determined from the lifetime $\tau$ (as shown in figure 3.1). And, this allows one to compare the two images with different fluorophores. FLIM techniques can be classified into time domain and frequency domain techniques; point scanning and wide field scanning techniques, photon counting, and analog counting techniques.
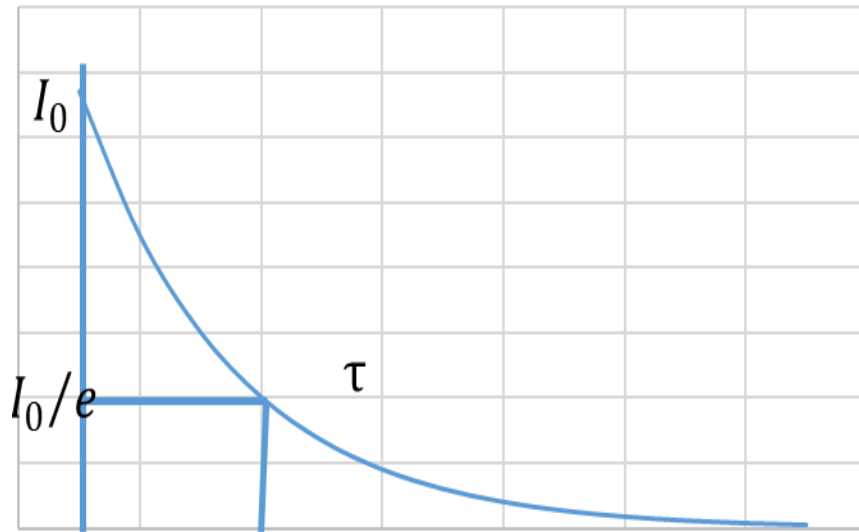


**Figure 3. 1 The diagram shows the exponential nature of fluorescence decay.** Fluorescence lifetime ($\tau$) is the time taken into the decay of fluorescence intensity to 1/e times the initial intensity.

Among all the fluorescence parameters, it is the decay (rate) constant which provides with the most direct insight into the molecular interaction of a fluorophore. However, the rate constants and hence the fluorescence lifetimes depend on the type of fluorophore, its conformation and how it interacts with its environment. It also depends on whether the fluorescence is collected through a few gates (filters) or many channels and whether this happens simultaneously or sequentially. Virtually, all these methods are in use, which results in many instrumental principles. Different principles differ in their photon efficiency, a minimum number of photons required for accuracy, multi-wavelength capability, and optical sectioning capability, etc.

### 3.1.1.1 Time-correlated single-photon counting (TCSPC)

TCSPC [45-48] is a well-established technique, based on fluorescence lifetime which can be used for FRET as well as other measurements, such as those involving the time of flight. Measurement of TCSPC depends on counting single photo, and it requires a reference light source. It's a statistical method which requires a high repetitive light source to obtain enough photons for a precision in the statistical data.
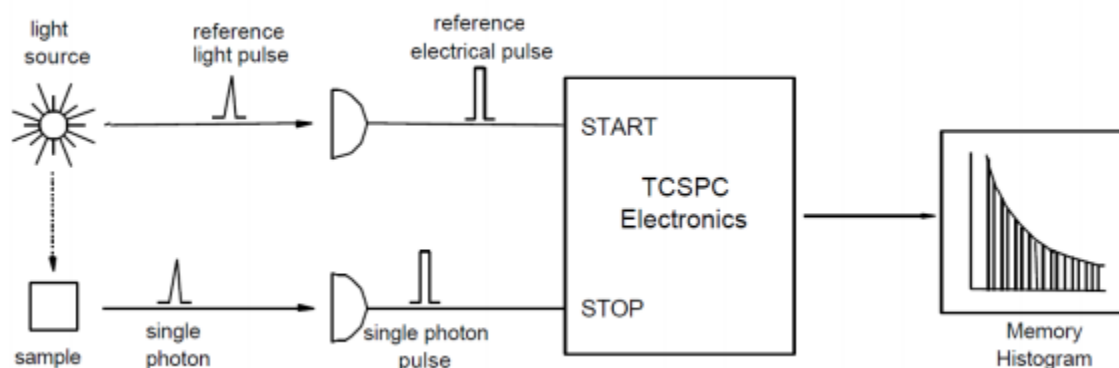


**Figure 3. 2 A schematic of time-correlated single photon counting (TCSPC) FLIM.** This figure is adapted with permission from [49].

TCSPC electronics can be compared to a stopwatch with two inputs. A schematic of this method is shown in figure 3.2. The clock starts with the signal input and ends with the signal output. Time spend in this start-stop event will be recorded in the memory histogram and increases its memory value. In this histogram, the x-axis represents time and the y-axis represents the number of events (photon detections) counted over a time interval. The histogram counts versus channels represent the fluorescence intensity versus time.

### 3.1.2 Photobleaching methods

Live cell imaging with dye-labeled proteins or organelle dyes provided new insights into the dynamics of cellular compartments. Because it takes longer, often several pulses of laser to

photobleach a fluorescent species, usually photobleaching methods required fixed specimens. However live cell imaging study, with the help of photobleaching method, of proteins or other cell organelle has been indirectly reported, which have potential to give dynamics of cellular compartments [3, 50, 51]. However, successful photobleaching experiment of fluorescent proteins in living cells including acceptor and donor photobleaching methods remains a challenge.

### 3.1.2.1 Donor-photobleaching FRET

Photobleaching method of FRET is often applied to fixed specimen because it takes longer to photobleach than just excite molecules. Only the molecules, which are in the excited state, have a chance of photobleaching. Statistically, only a small portion of molecules is in the excited state. Typically, the molecules with longer lifetime have greater chance to photobleach.

Experimentally, it has been found that photobleaching time is inversely proportional to fluorescence lifetime. Donors of resonance energy transfer will exhibit longer lifetime in the absence of resonance energy transfer that means in the absence of acceptors, as compared to when they transfer a portion of their excitation energy via FRET. Thus, donors will be photobleached faster in the resonance energy transfer. In fact, FRET protects them from photobleaching in a way. By measuring rate of photobleaching in the donor only sample, as well as in the donors and acceptors sample, the FRET can be estimated [5, 7, 9, 52].

Since it takes relatively long time to photobleach molecules compared to the other methods of FRET determination, the photobleaching methods are more suitable when temporal data is not important. And, the photobleaching does not affect anything else in the context of the FRET study. In some respects, photobleaching method sounds like intensity-based methods, however fitting the time constants involving multiple components into the photobleaching curve poses additional challenges.

### 3.1.2.2 Acceptor-photobleaching FRET

This method [3, 5, 11, 12, 45] uses donor dequenching in the presence of acceptor, which can use the donor fluorescence intensities before and after destroying the acceptors. Choice of the donor-acceptor pair is important for this method. A desirable choice would be an acceptor, which can be easily photobleached and a donor, which is relatively stable. After the acceptor is photobleached, it can no longer share donor energy. Acceptor photobleaching requires a single sample, and it directly relates FRET to both donor and acceptor molecules.

For quantitative FRET measurements, corrections are needed for the bleed through, that is, there is an overlap in the emission wavelength ranges of the donor and acceptor. One of the methods is to use acceptor emission filter when donor signal is measured and use a donor emission signal filter for measuring the acceptor emission.

For quantitative FRET determination, the concentration of the fluorophores is also required. For that purpose, three different samples and three different filters are used. The three samples are; donor only, acceptor only and donor-acceptor sample. The three filters include the above mentioned two filters and the third filter for the acceptor direct-excitation. Emission of all three samples are passed through these filters, one at a time, and then the data is manipulated using arithmetic for the crossovers and other factors, for instance, the uncontrolled variations in the concentrations.

### 3.1.3 Fluorescence-polarization FRET

The application of fluorescence polarization has unique advantages over other fluorescence-based methods [53, 54]. Polarization is a fundamental property of light. Fluorescent polarization was first described by Perrin [55]. When the plane of an electric field or magnetic field oscillation vector does not change during the propagation of light, it is considered as a plane polarized light.

In fluorescent polarization study, plane polarized light is used for exciting the sample. Fluorescent molecules are transient dipole moments. When the electric field of excitation light and the direction of molecular dipole moment are parallel to each other, the maximum absorption of energy happens. When they are perpendicular to each other, then no light is absorbed. Emission dipole moment can be different than the dipole moment of an excited molecule. And the direction of electric field oscillation of emission is parallel to the direction of the instantaneous dipole moment at the emission state. When an unpolarized light is used for excitation due to the random nature of the molecular dipole moments in a sample, the polarization effect is lost due to averaging out.
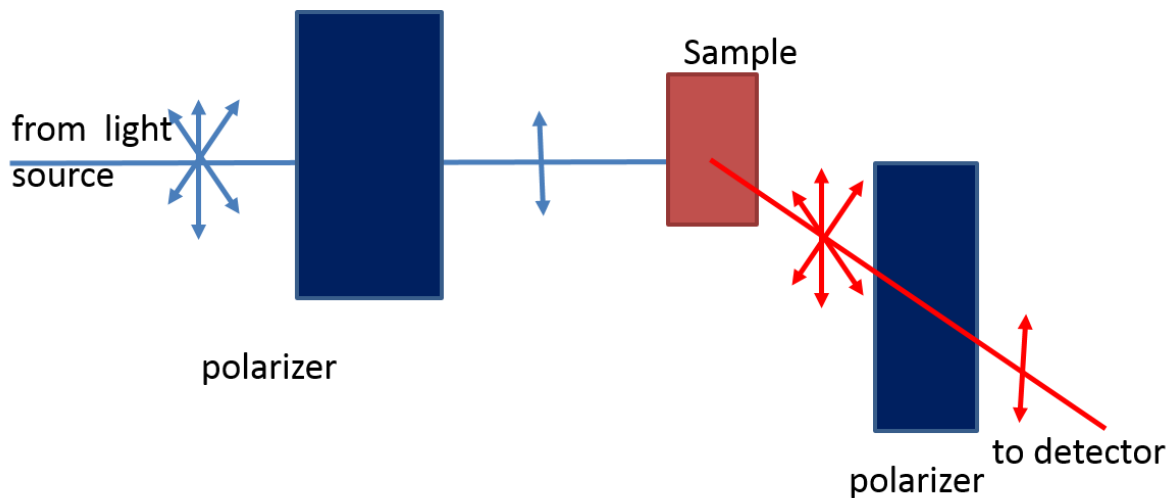


**Figure 3.3 The basic principle of fluorescence polarization.** Two polarizers are used, one each for the excitation of, and the emission from the sample. The first polarizer allows only the plane polarized light to the sample, and the second polarizer, which has its axis parallel to the first, detects the fraction of the emission light which remains parallel to the excitation light.

A monochromatic beam illuminates the fluorophores within the sample. A linear polarizer located in the illumination beam attenuates the randomly oriented polarization states except for those in one plane, thereby generating linearly polarized light. This plane of polarized light also becomes the reference plane. Depending upon the orientation of their absorption dipoles, individual fluorophore molecules are preferentially excited.

66

The emission from the fluorescent sample can be considered as another light source, which is composed of the combination of signals from the emission dipoles of individual fluorophores molecules. If the absorption and emission dipole moments of all the fluorophores were to be aligned with the electric field vector of the illumination beam, then the emission signal would also be plane polarized. However, this is typically not the case. Therefore, the emission signal is partially depolarized due to the random orientation of the fluorophores, even if the fluorophores are completely static.

As the molecules move during the time window of detection, the emission becomes even more depolarized. A polarizer placed in front of the detector is used to detect the intensity of emission light in a given plane of polarization. The intensity measurement made with the emission polarizer oriented orthogonal to the electric field of illumination beam (the *reference* plane) is denoted as $\perp I$ and when the emission polarizer is rotated by 90 degrees with respect to the $\perp I$ measurement direction, $\| I$ measurement is made. figure 3.3 shows the polarization of an unpolarized light.

Using $I_\parallel$, and $I_\perp$, two interchangeable ratio parameters are used to express the degree of depolarization of emission light, as given by the following equations

$$p = \frac{I_\parallel - I_\perp}{I_\parallel + I_\perp} \tag{4.5}$$

$$r = \frac{I_\parallel - I_\perp}{I_\parallel + 2I_\perp} \tag{4.6}$$

where p is polarization ratio and r is emission anisotropy. $I_\parallel$ and $I_\perp$ are intensities measured parallel to and perpendicular to the direction of polarization of the excited light. The depolarization is caused by rotation diffusion. Rotational diffusion can be caused by the interaction of the molecules with the environment and the FRET.

67

One of the advantages of fluorescent polarization method is that the measurements are of ratiometric quality. Hence, they do not depend on the intensity of the excitation light or the concentration of the fluorophores. The measurement of fluorescent polarization or anisotropy study adds another dimension to fluorescent measurements. It, in some ways, compliments time-resolved microscopy i.e. FLIM. There are several methods to study hetero-FRET but to measure homo-FRET there are no other suitable method than using fluorescence polarization [48, 51, 54, 56-61].

## 3.2 Optical micro-spectroscopy (OptiMiS)

OptiMiS is an imaging technology originally developed by Raicu lab [18] and currently commercialized by Aurora Spectral Technology, Wisconsin. OptiMiS uses an Electron-Multiplying Charged Couple Detector (EMCCD) camera for high sensitivity detection of the faintest fluorescence signals and femtosecond lasers for two-photon excitation, which provides image-sectioning capability and a dramatic reduction of the number of molecules at each image pixel. This technology has been used by our group and others [15, 16, 18, 19, 62-66] for FRET imaging and in determination of the quaternary structure of proteins.

OptiMiS offers a spectral resolution of ~1 nm, with 200 available wavelength channels, which are generated using a grating, placed in front of the emission light. A single scan is sufficient to generate the above-mentioned spectral resolution. Image acquisition of a single pixel with the help of OptiMiS is faster than diffusion scale of biological samples, however, the entire image acquisition takes longer than the broadband microscopes. This is due to the fact that to generate spectral resolution, it requires as many photons for each wavelength as the total number of photons needed in the broad bandwidth imaging methods.

The entire image acquisition became much faster in the newer version of OptiMiS which is capable of imaging the sample per line [67] as compared to its previous version which was equipped with raster (or point) scanning [18] only. An image of 440 by 300 pixels at the highest available resolution of 1 nm can be scanned in about 10 seconds. And, relatively lower spectral resolution images like 2, 5, or 10 nm, can be acquired at even faster rates.

Also, the line-scan has reduced photobleaching effect when compared to point scan version of OptiMiS, because the line-scan requires lower excitation power and allows for longer integration time per pixel to generate the similar (point-scan) image contrast [67].

### 3.2.1 OptiMiS set-up

A schematic of OptiMiS and associated technology is shown in figure 3.4. Light from a mode-locked femtosecond Ti: Sapphire laser is passed through a cylindrical mirror which expands the spot width of the light into a line. The line profile of the beam then falls on scanning mirrors (using mirror galvanometers), and thereafter the laser line reflects from a pair of mirrors (M1 and M2), and in between passes through a scanning lens. After reflecting from the M2 mirror, the light passes through the objective lens of the microscope, which in result focuses it onto the sample and excites an entire array of points falling on the line of excitation.
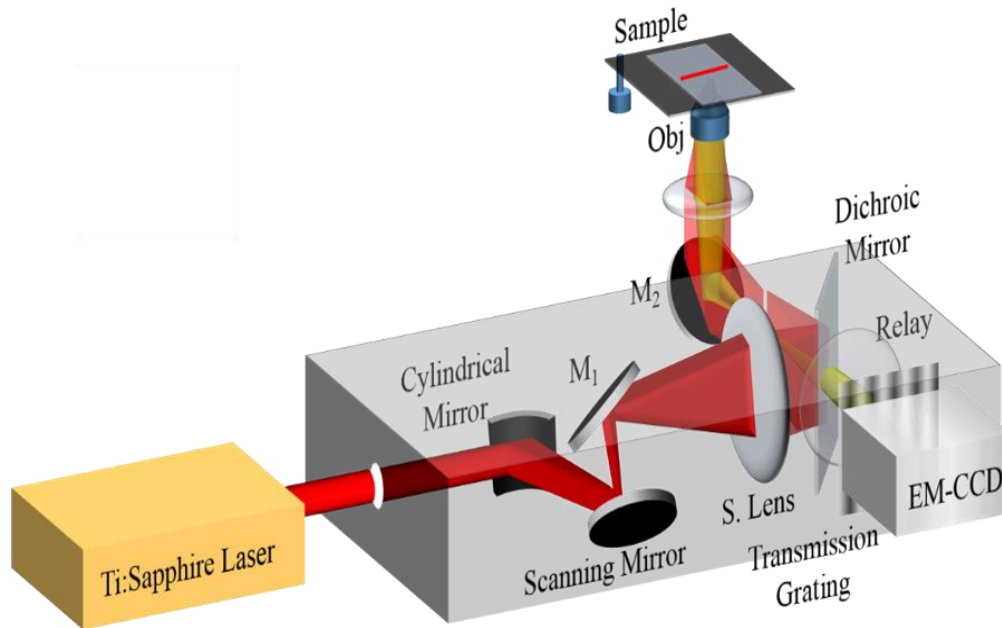
**Figure 3.4: The schematic of OptiMis as a part of the two-photon microscopy system**. The excitation source is a mode-locked femtosecond duration Ti: Sapphire laser. The pulsed laser beam is focused to a diffraction-limited spot via an NA 1.43 oil immersion objective, and the location of this beam focus is scanned within a sample of interest by a pair of computer-controlled galvos. The back-emitted fluorescence is collected by the objective and is incident upon an EM-CCD device. Highlighted here is probably what is the crux of the instrument, a transmission grating placed in the path of the emission which separates the emitted light into different wavelengths before it is incident upon the cooled EM-CCD detection scheme. This figure is adapted with permission from [67].

The fluorescent light emission coming out of the emission passes through the microscope objective again and, after reflecting from the mirror M2, it passes through a grating and a relay lens. The grating disperses the emission light into its wavelength components and relay lens inverts the image and extends the optical tube. A dichroic mirror is also used before the relay lens to block the excitation light out of the final output (emission light). The fluorescent emission falls on the pixel of the EMCCD camera.

70

### 3.2.2 Multi-wavelength imaging using optiMiS

The image can also be captured using a built-in feature of OptiMiS, which allows for imaging at two or more wavelengths. With the help of two wavelength measurements, concentrations can be estimated.[14].

Concentration information is especially helpful when investigating quaternary structure by FRET measurements. Knowing donor and acceptor attached molecules concentration is critically important for intensity based methods. Several analysis methods can exploit the concentration-dependent FRET information, for example, the variation in FRET due to the concentration-dependent equilibrium constants, or FRET dependence on acceptor molar fraction which is the ratio of the number of the acceptors to the total number of donors and acceptor. Application of these methods will be further discussed in Chapter 6. There are two main functions of OptiMiS, that are as follows:

- Scanning (hardware)

- Image reconstruction (software)

The scanning part of OptiMiS includes cylindrical mirror and scanning mirror along with other optical components used between the objective and the EMCCD camera as mentioned above. The image reconstruction is the sophisticated software part, which has evolved over time. The grating converts each point on the sample into a line i.e. breaks the emission signal into the wavelength components. Therefore, after scanning each line on the sample, we get a two-dimensional image.

After scanning the area of interest, which can be set into the pre-scan settings of the OptiMiS module, images of all the line exposures are reconstructed to produce an image for each wavelength. The total number of images is equal to the ratio of the total number of available channels (200) to the chosen spectral resolution. For example, the highest spectral resolution (one)

provides with 200 spectral images with a wavelength separation of ~ 1 nm. This gives a spectrum

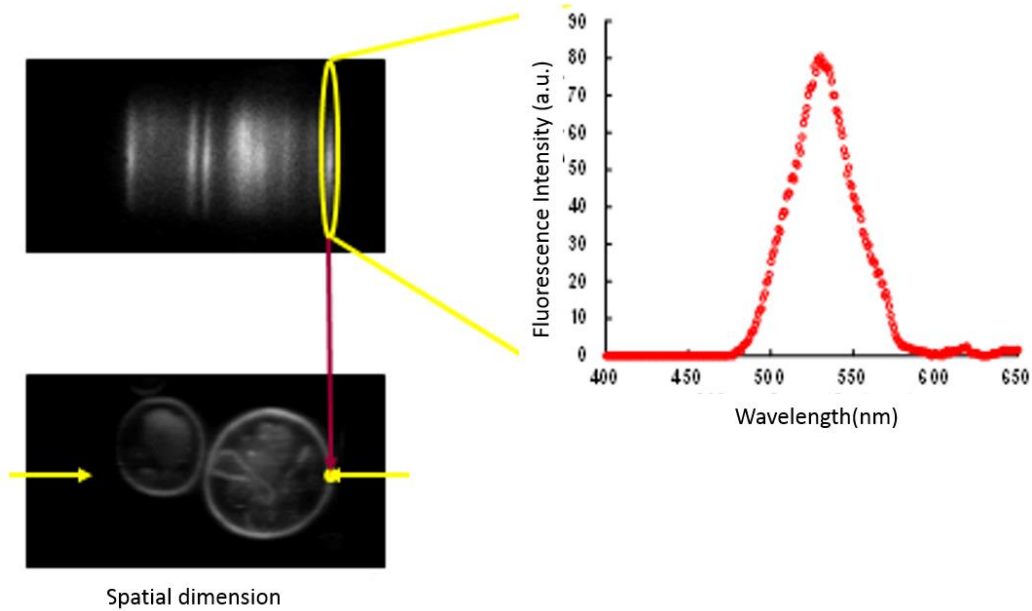for each pixel of the image (or EMCCD camera), also shown in figure 3.5.



Spatial dimension

**Figure 3.5: Spectral imaging of membrane region of a yeast cell expressing GFP2.** Top left image shows the spectral signal corresponding to a line of the yeast cell as shown by the horizontal arrows. The pixel level emission spectrum (right) corresponds to just one pixel as shown by the red arrow. The figure is adapted with permission from [68].

A single pixel emission signal is split into wavelength channels. Thus, a point (voxel) on an object

on sample plane converts into a line of wavelength components. The wavelengths information

corresponding to a single pixel provides a spectrum for that pixel. If more than one fluorescence

markers are in the sample voxel, then the emission spectrum of the pixel has a composite spectrum,

which is a sum of the individual spectrums of all the fluorescence species in that point volume

(voxel) of the sample.

With a prior knowledge of emission spectrums of each participating fluorescent species in

that voxel, the composite emission spectrum can be resolved into its components, giving a fraction

72

of the individual presence of each fluorescent marker at pixel (or voxel, at sample level) level. The separating of the total spectrum into its individual components is called spectral unmixing which will be discussed in more detail in chapters 5 and 6.

OptiMiS TruLine is capable of both point and line scans. However, the line- scan is about 300 times more sensitive than the point-scan.

## 3.3 Using FRET to determine quaternary structure

Various methods are used to determine the shape and size of macromolecular complexes or quaternary structure. These complexes are called oligomers. The complex of two monomers is called dimer. The most sought quaternary structures are of protein complexes. X-ray crystallography, nuclear magnetic resonance, immunoprecipitation are a few examples of the various methods used to investigate the quaternary structure. However, these methods are mainly suitable for *in-vitro* analysis.

Investigation of oligomeric stoichiometry and structure in living systems such as in live cell cultures (*in vivo*) is complex because of the diffusion and rapid spatial and temporal fluctuations of other parameters such as pH of the system.

There are several FRET-based methods which researchers have used to detect the association of the macromolecules. These methods include acceptor photobleaching, sensitized emission, spectral FRET imaging, Fluorescence Lifetime Imaging (FLIM), and polarization anisotropy imaging. These methods have been described in chapter 4. However, most of these methods struggle predicting the quaternary structure of more than two monomers. Many FRET-based methods claimed their finding of "at least" dimers, because of mere detection of FRET guarantees association of monomers, of the same or different type of macromolecules, unless it's

due to the crowding of the molecules. However, experimentally differentiating among the presence of dimers or oligomers, or the mixture of different oligomeric species is non-trivial.

Nevertheless, spectral FRET methods have been able to predict both stoichiometry and structure of various macromolecules oligomers. The only successful methods for investigating oligomeric structure in living cells is pixel-level spectral FRET measurement method, given by Raicu and coworkers [15, 16, 18, 19, 62, 69]. In this method, the distribution of FRET efficiencies is simulated giving FRET models for the various stoichiometries. These models are fitted to the observed experimental FRET efficiency distribution, to determine the best-fit model.

The mathematical framework including equations describing this method is given below. Photon emission intensity of donors in the presence of the acceptors ($F^{DA}$) and the acceptor emission intensity in the presence of the donors ($F^{AD}$) are given by the following two equations

$$F^{DA} = F^D(\lambda_{ex}) - F^D(FRET), \tag{4.4}$$

where $F^D(\lambda_{ex})$ is the donor emission intensity which would have been in the absence of the acceptors, at the excitation wavelength $\lambda_{ex}$, and $F^D(FRET)$ is the donor energy lost due to FRET, and,

$$F^{AD} = F^A(\lambda_{ex}) + F^A(\lambda_{FRET}), \tag{4.5}$$

where $F^A(\lambda_{ex})$ is the acceptor emission due to the acceptor direct excitation at the wavelength $\lambda_{ex}$, and $F^A(FRET)$ is the acceptor emission intensity gained due to FRET.

Apparent FRET efficiency can be defined for the case of donor dequenching (Dq), in the terms of donor energy transferred via FRET and the total donor emission intensity in the absence of the FRET, as the following

$$E_{app}^{Dq} = \frac{F^D(FRET)}{F^D(\lambda_{ex})} \tag{4.6}$$

74

The FRET efficiency can also be defined for acceptor sensitized emission (Ase) by the excited donor, as the following;

$$E_{ap}^{A\,se} = \frac{F^A(FRET)}{F^A(\lambda_{ex})} \tag{4.7}$$

To apply the FRET efficiency equations (4.6) or (4.7), from a single excitation scan we need to have the ability to decompose, the total emission spectrum of donors and acceptors which have the FRET information embedded to it, into the donor and acceptor emission counts ($k^{DA}$ and $k^{AD}$). This can be done if there is a complete spectral information available for the donor and acceptor at the pixel level, i.e., donor only and acceptor only spectrum needs to be acquired separately under the same experimental conditions which are used for collecting the composite emission spectrum of the donor and acceptor. The composite spectrum is unmixed using the normalized spectral integral $w^D$ and $w^A$ for the donor and acceptor. The unmixing method also involves their respective quantum yields $Q^D$ and $Q^A$.

The donor emission intensity in the presence of acceptor and vice versa can be given by equations (4.5) and (4.6) as below

$$F^{DA} = \int_{\lambda_{em}}^{\cdot} i^D(\lambda_{em}) \, d\lambda_{em} = k^{DA} w^D, \tag{4.8}$$

where $i^D(\lambda_{em})$ is the emission intensity of the donors and $k^{DA}$ is the donor emission count in the presence of the acceptor, and $w^D$ is the integral of the donor emission spectrum, normalized to the maximum emission intensity, and\

$$F^{AD} = \int_{\lambda_{em}}^{\cdot} i^A(\lambda_{em}) \, d\lambda_{em} = k^{AD} w^A, \tag{4.9}$$

where $i^A(\lambda_{em})$ is the emission intensity of the acceptor and $k^{AD}$ is the acceptor emission count in the presence of the donor, and $w^A$ is the integral of the donor emission spectrum, normalized to the maximum emission intensity.

$F^D(FRET)$ and $F^A(FRET)$ can be related to each other by the following equations. The total number of excitations ($N^{FRET}$) transferred to the acceptor via FRET by the donor is given by equation (3.7). Which is based on the simple fact, a fraction of the excitations received by the acceptor would have been lost by the donor if there was no FRET (in the absence of the acceptor). This fraction is equal to the quantum yield of the donor ($Q^D$).

$$N^{FRET} Q^D = F^D(FRET) \qquad (4.10)$$

Acceptor will also emit only a fraction of energy transferred to it via FRET, and the fraction being equal to the quantum yield of the acceptor ($Q^A$), as given by equation (3.8).

$$N^{FRET} Q^A = F^A(FRET) \qquad (4.11)$$

Eliminating $N^{FRET}$ using equations (4.10) and (4.11) gives the relationship between the energy lost by the donor and gained by the acceptor due to FRET between them, as the following;

$$F^D(FRET) = \frac{Q^D}{Q^A} F^A(FRET) \qquad (4.82)$$

The acceptor direct excitation at the excitation wavelength used for the FRET measurements could be minimized by using a suitable donor-acceptor pair and by exciting at a suitable wavelength, which excites donor significantly while acceptor direct excitation is minimal. Hence the acceptor emission due to its direct excitation can be ignored. With this approximation, equation (4.12) changes as the following;

$$F^D(FRET) = \frac{Q^D}{Q^A} F^{AD} \qquad (4.13)$$

76

Finally combining the above-mentioned equations, the FRET efficiency expression can be deduced as;

$$E_{app}^{Dq} = \frac{F^D(FRET)}{F^D(\lambda_{ex})} = \frac{1}{1 + \frac{Q^D}{Q^A}\frac{k^{DA}}{k^{AD}}\frac{w^D}{w^A}}$$

(4.14)

The above FRET efficiency expression can be applied at the pixel level, with the information of elementary spectrums of the donor and spectrum and their respective quantum yields. With this information, only a single scan is required to calculate the FRET efficiencies at each pixel of the image. The single scan also helps in avoiding photobleaching.

This method has evolved to get more information and a better estimate for the FRET efficiencies. With two-wavelength excitation scans, more information can be collected. For example, the concentrations of donor and acceptor can be determined with the help of standard solutions of the fluorescent proteins [14, 66, 70] Also, the approximation made by ignoring the acceptor direct excitation, while using the single scan method, is not needed anymore for the two wavelength scanning, making this method more accurate for FRET determination. The two-wavelength method is discussed in more details in chapter 6.

77

# References

[1] R.B. Sekar, A. Periasamy, Fluorescence resonance energy transfer (FRET) microscopy imaging of live cell protein localizations, J Cell Biol, 160 (2003) 629-633.

[2] J. Lippincott-Schwartz, E. Snapp, A. Kenworthy, Studying protein dynamics in living cells, Nature reviews. Molecular cell biology, 2 (2001) 444-456.

[3] G. Valentin, C. Verheggen, T. Piolot, H. Neel, M. Coppey-Moisan, E. Bertrand, Photoconversion of YFP into a CFP-like species during acceptor photobleaching FRET experiments, Nature methods, 2 (2005) 801-801.

[4] R.Y. Tsien, The green fluorescent protein, Annual review of biochemistry, 67 (1998) 509-544.

[5] J. Roszik, J. Szöllősi, G. Vereb, AccPbFRET: an ImageJ plugin for semi-automatic, fully corrected analysis of acceptor photobleaching FRET images, BMC bioinformatics, 9 (2008) 1.

[6] A.H. Clayton, N. Klonis, S.H. Cody, E.C. Nice, Dual-channel photobleaching FRET microscopy for improved resolution of protein association states in living cells, European Biophysics Journal, 34 (2005) 82-90.

[7] M. Tramier, M. Zahid, J.C. Mevel, M.J. Masse, M. Coppey-Moisan, Sensitivity of CFP/YFP and GFP/mCherry pairs to donor photobleaching on FRET determination by fluorescence lifetime imaging microscopy in living cells, Microscopy research and technique, 69 (2006) 933-939.

[8] T. Nagai, K. Ibata, E.S. Park, M. Kubota, K. Mikoshiba, A. Miyawaki, A variant of yellow fluorescent protein with fast and efficient maturation for cell-biological applications, Nature biotechnology, 20 (2002) 87-90.

[9] L. Jürgens, D. Arndt-Jovin, I. Pecht, T.M. Jovin, Proximity relationships between the type I receptor for Fcεe (FcεeRI) and the mast cell function-associated antigen (MAFA) studied by donor photobleaching fluorescence resonance energy transfer microscopy, European journal of immunology, 26 (1996) 84-91.

[10] P. Van Roessel, A.H. Brand, Imaging into the future: visualizing gene expression and protein interactions with fluorescent proteins, Nature cell biology, 4 (2002) E15-E20.

[11] Y. Gu, W. Di, D. Kelsell, D. Zicha, Quantitative fluorescence resonance energy transfer (FRET) measurement with acceptor photobleaching and spectral unmixing, Journal of microscopy, 215 (2004) 162-173.

[12] E. Van Munster, G. Kremers, M. ADJOBO-HERMANS, T.W. Gadella, Fluorescence resonance energy transfer (FRET) measurement by gradual acceptor photobleaching, Journal of microscopy, 218 (2005) 253-262.

[13] N.P. Mahajan, K. Linder, G. Berry, G.W. Gordon, R. Heim, B. Herman, Bcl-2 and Bax interactions in mitochondria probed with green fluorescent protein and fluorescence resonance energy transfer, Nature biotechnology, 16 (1998) 547-552.

[14] A.K. Mishra, M. Gragg, M. Stoneman, G. Biener, J.A. Oliver, P. Miszta, S. Filipek, V. Raicu, P. Park, Quaternary structures of opsin in live cells revealed by FRET spectrometry, Biochemical Journal, (2016) BCJ20160422.

[15] A.K. Mishra, T. Mavlyutov, D.R. Singh, G. Biener, J. Yang, J.A. Oliver, A. Ruoho, V. Raicu, The sigma-1 receptors are present in monomeric and oligomeric forms in living cells in the presence and absence of ligands, Biochem J, 466 (2015) 263-271.

[16] S. Patowary, E. Alvarez-Curto, T.R. Xu, J.D. Holz, J.A. Oliver, G. Milligan, V. Raicu, The muscarinic M3 acetylcholine receptor exists as two differently sized complexes at the plasma membrane, Biochem J, 452 (2013) 303-312.

[17] V. Raicu, D.R. Singh, FRET spectrometry: a new tool for the determination of protein quaternary structure in living cells, Biophys J, 105 (2013) 1937-1945.

[18] V. Raicu, M.R. Stoneman, R. Fung, M. Melnichuk, D.B. Jansma, L.F. Pisterzi, S. Rath, M. Fox, J.W. Wells, D.K. Saldin, Determination of supramolecular structure and spatial distribution of protein complexes in living cells, Nat Photon, 3 (2009) 107-113.

[19] D.R. Singh, M.M. Mohammad, S. Patowary, M.R. Stoneman, J.A. Oliver, L. Movileanu, V. Raicu, Determination of the Quaternary Structure of a Bacterial ATP-Binding Cassette (ABC) Transporter in Living Cells, Integrative biology : quantitative biosciences from nano to macro, 5 (2013) 312-323.

[20] B.K. Kobilka, G protein coupled receptor structure and activation, Biochimica et biophysica acta, 1768 (2007) 794-807.

[21] A.G. Gilman, G proteins: transducers of receptor-generated signals, Annual review of biochemistry, 56 (1987) 615-649.

[22] M. Rodbell, Proteins in membrane transduction, Nature, 284 (1980) 17.

[23] A. Wise, K. Gearing, S. Rees, Target validation of G-protein coupled receptors, Drug discovery today, 7 (2002) 235-246.

[24] K. Palczewski, T. Kumasaka, T. Hori, C.A. Behnke, H. Motoshima, B.A. Fox, I. Le Trong, D.C. Teller, T. Okada, R.E. Stenkamp, Crystal structure of rhodopsin: AG protein-coupled receptor, Science (New York, N.Y.), 289 (2000) 739-745.

[25] J.J. Ruprecht, T. Mielke, R. Vogel, C. Villa, G.F. Schertler, Electron crystallography reveals the structure of metarhodopsin I, The EMBO journal, 23 (2004) 3609-3620.

79

[26] K.D. Ridge, N.G. Abdulaev, M. Sousa, K. Palczewski, Phototransduction: crystal clear, Trends in biochemical sciences, 28 (2003) 479-487.

[27] P. Liebman, G. Entine, Lateral diffusion of visual pigment in photoreceptor disk membranes, Science (New York, N.Y.), 185 (1974) 457-459.

[28] R.A. Cone, Rotational diffusion of rhodopsin in the visual receptor membrane, Nature, 236 (1972) 39-43.

[29] C. Wey, R. Cone, M.A. Edidin, Lateral diffusion of rhodopsin in photoreceptor cells measured by fluorescence photobleaching and recovery, Biophysical journal, 33 (1981) 225.

[30] V.I. Govardovskii, D.A. Korenyak, S.A. Shukolyukov, L.V. Zueva, Lateral diffusion of rhodopsin in photoreceptor membrane: a reappraisal, (2009).

[31] B. Wu, E.Y. Chien, C.D. Mol, G. Fenalti, W. Liu, V. Katritch, R. Abagyan, A. Brooun, P. Wells, F.C. Bi, Structures of the CXCR4 chemokine GPCR with small-molecule and cyclic peptide antagonists, Science (New York, N.Y.), 330 (2010) 1066-1071.

[32] W.R. Zipfel, R.M. Williams, W.W. Webb, Nonlinear magic: multiphoton microscopy in the biosciences, Nature biotechnology, 21 (2003) 1369-1377.

[33] B.M. Binder, T.M. O'Connor, M.D. Bownds, V.Y. Arshavsky, Phosphorylation of non-bleached rhodopsin in intact retinas and living frogs, Journal of Biological Chemistry, 271 (1996) 19826-19830.

[34] D. Fotiadis, Y. Liang, S. Filipek, D.A. Saperstein, A. Engel, K. Palczewski, Atomic-force microscopy: rhodopsin dimers in native disc membranes, Nature, 421 (2003) 127-128.

[35] D. Fotiadis, Y. Liang, S. Filipek, D.A. Saperstein, A. Engel, K. Palczewski, The G protein-coupled receptor rhodopsin in the native membrane, FEBS letters, 564 (2004) 281-288.

[36] A. Krebs, C. Villa, P.C. Edwards, G.F. Schertler, Characterisation of an improved two-dimensional p22 1 2 1 crystal from bovine rhodopsin, Journal of molecular biology, 282 (1998) 991-1003.

[37] P.S.-H. Park, S. Filipek, J.W. Wells, K. Palczewski, Oligomerization of G protein-coupled receptors: past, present, and future, Biochemistry, 43 (2004) 15643-15656.

[38] G.-J. Kremers, J. Goedhart, E.B. van Munster, T.W. Gadella, Cyan and yellow super fluorescent proteins with improved brightness, protein folding, and FRET Förster radius, Biochemistry, 45 (2006) 6570-6580.

[39] F.J. Kim, I. Kovalyshyn, M. Burgman, C. Neilan, C.C. Chien, G.W. Pasternak, Sigma 1 receptor modulation of G-protein-coupled receptor signaling: potentiation of opioid transduction independent from receptor binding, Molecular pharmacology, 77 (2010) 695-703.

[40] K.A. Gromek, F.P. Suchy, H.R. Meddaugh, R.L. Wrobel, L.M. LaPointe, U.B. Chu, J.G. Primm, A.E. Ruoho, A. Senes, B.G. Fox, The Oligomeric States of the Purified Sigma-1 Receptor Are Stabilized by Ligands, The Journal of biological chemistry, 289 (2014) 20333-20344.

[41] T.-P. Su, T. Hayashi, T. Maurice, S. Buch, A.E. Ruoho, The sigma-1 receptor chaperone as an inter-organelle signaling modulator, Trends in pharmacological sciences, 31 (2010) 557-566.

[42] F.J. Moss, P.I. Imoukhuede, K. Scott, J. Hu, J.L. Jankowsky, M.W. Quick, H.A. Lester, GABA transporter function, oligomerization state, and anchoring: correlates with subcellularly resolved FRET, The Journal of general physiology, 134 (2009) 489-521.

[43] A. Pal, A.R. Hajipour, D. Fontanilla, S. Ramachandran, U.B. Chu, T. Mavlyutov, A.E. Ruoho, Identification of regions of the sigma-1 receptor ligand binding site using a novel photoprobe, Molecular pharmacology, 72 (2007) 921-933.

[44] T. Zimmermann, J. Rietdorf, A. Girod, V. Georget, R. Pepperkok, Spectral imaging and linear un-mixing enables improved FRET efficiency with a novel GFP2-YFP FRET pair, FEBS letters, 531 (2002) 245-249.

[45] T. Karpova, C. Baumann, L. He, X. Wu, A. Grammer, P. Lipsky, G. Hager, J. McNally, Fluorescence resonance energy transfer from cyan to yellow fluorescent protein detected by acceptor photobleaching using confocal microscopy and a single laser, Journal of microscopy, 209 (2003) 56-70.

[46] W. Becker, Advanced time-correlated single photon counting techniques, Springer Science & Business Media, 2005.

[47] W. Becker, Fluorescence lifetime imaging--techniques and applications, Journal of microscopy, 247 (2012) 119-136.

[48] M.A. Rizzo, D.W. Piston, High-contrast imaging of fluorescent protein FRET by fluorescence polarization microscopy, Biophysical journal, 88 (2005) L14-L16.

[49] D.W. Piston, M.A. Rizzo, FRET by fluorescence polarization microscopy, Methods in cell biology, 85 (2008) 415-430.

[50] E.L. Snapp, Photobleaching Methods to Study Golgi Complex Dynamics in Living Cells, Methods in cell biology, 118 (2013) 195-216.

[51] E.A. Jares-Erijman, T.M. Jovin, FRET imaging, Nature biotechnology, 21 (2003) 1387-1395.

[52] G. Szentesi, G. Vereb, G. Horváth, A. Bodnár, Á. Fábián, J. Matkó, R. Gáspár, S. Damjanovich, L. Mátyus, A. Jenei, Computer program for analyzing donor photobleaching FRET image series, Cytometry Part A, 67 (2005) 119-128.

[53] A.L. Mattheyses, A.D. Hoppe, D. Axelrod, Polarized fluorescence resonance energy transfer microscopy, Biophys J, 87 (2004) 2787-2797.

81

[54] D.W. Piston, M.A. Rizzo, FRET by Fluorescence Polarization Microscopy, in: Methods in Cell Biology, vol. Volume 85, Academic Press, 2008, pp. 415-430.

[55] J. Perrin, Fluorescence et induction moleculaire par resonance, CR Hebd. Seances Acad. Sci, 184 (1927) 1097-1100.

[56] J.A. Levitt, D.R. Matthews, S.M. Ameer-Beg, K. Suhling, Fluorescence lifetime and polarization-resolved imaging in cell biology, Current opinion in biotechnology, 20 (2009) 28-36.

[57] D.W. Piston, G.-J. Kremers, Fluorescent protein FRET: the good, the bad and the ugly, Trends in biochemical sciences, 32 (2007) 407-414.

[58] J.J. Burbaum, N.H. Sigal, New technologies for high-throughput screening, Current Opinion in Chemical Biology, 1 (1997) 72-78.

[59] B. Valeur, M.N. Berberan-Santos, Molecular fluorescence: principles and applications, John Wiley & Sons, 2012.

[60] Y. Yan, G. Marriott, Analysis of protein interactions using fluorescence technologies, Current opinion in chemical biology, 7 (2003) 635-640.

[61] S. Weiss, Measuring conformational dynamics of biomolecules by single molecule fluorescence spectroscopy, Nature structural biology, 7 (2000) 724-729.

[62] S. Patowary, Luca F. Pisterzi, G. Biener, Jessica D. Holz, Julie A. Oliver, James W. Wells, V. Raicu, Experimental Verification of the Kinetic Theory of FRET Using Optical Microspectroscopy and Obligate Oligomers, Biophysical Journal, 108 (2015) 1613-1622.

[63] D.R. Singh, Q. Cao, C. King, M. Salotto, F. Ahmed, X.Y. Zhou, E.B. Pasquale, K. Hristova, Unliganded EphA3 dimerization promoted by the SAM domain, Biochem J, 471 (2015) 101-109.

[64] D.R. Singh, E.B. Pasquale, K. Hristova, A small peptide promotes EphA2 kinase-dependent signaling by stabilizing EphA2 dimers, Biochimica et biophysica acta, 1860 (2016) 1922-1928.

[65] D.R. Singh, F. Ahmed, C. King, N. Gupta, M. Salotto, E.B. Pasquale, K. Hristova, EphA2 Receptor Unliganded Dimers Suppress EphA2 Pro-tumorigenic Signaling, The Journal of biological chemistry, 290 (2015) 27271-27279.

[66] M.R. Stoneman, J.D. Paprocki, G. Biener, K. Yokoi, A. Shevade, S. Kuchin, V. Raicu, Quaternary structure of the yeast pheromone receptor Ste2 in living cells, Biochimica et biophysica acta, (2016).

[67] G. Biener, M.R. Stoneman, G. Acbas, J.D. Holz, M. Orlova, L. Komarova, S. Kuchin, V. Raicu, Development and experimental testing of an optical micro-spectroscopic technique incorporating true line-scan excitation, International journal of molecular sciences, 15 (2014) 261-276.

[68] OptiMis$^{TM}$ Trueline, in, vol. 2016, Aurora Spectral Technologies, LLC,.

[69] A.K. Mishra, M. Gragg, M. Stoneman, G. Biener, J.A. Oliver, P. Miszta, S. Filipek, V. Raicu, P. Park, Quaternary structures of opsin in live cells revealed by FRET spectrometry, Biochem J, (2016).

[70] C. King, M. Stoneman, V. Raicu, K. Hristova, Fully quantified spectral imaging reveals in vivo membrane protein interactions, Integr Biol (Camb), 8 (2016) 216-229.

# Chapter 4: Testing of the kinetic theory of FRET

The Kinetic theory of FRET, as defined in Chapter 2 [1], was tested using FRET-based techniques described in chapter 3. Here, I am reviewing two main studies done in order to validate the theory by experimental methods.

## 4.1. Overview

The kinetic theory of FRET is based on the average of FRET efficiency of all individual donors transferring energy to the acceptors within the complex of a multimeric complex [1-4]. An excited donor can lose energy via radiative deexcitation i.e. the emission of photons, or via nonradiative deexcitation i.e. the interaction with the surrounding environment, or by FRET with nearby acceptors. FRET opens additional pathways for losing the energy of the donors with nearby acceptors kinetically.

There are several methods which provide with FRET efficiencies but interpreting the experimentally obtained FRET efficiencies with various methods had been a challenge. To validate the kinetic theory of FRET, we need standards with known FRET efficiencies which can be compared with the FRET efficiencies extracted from experiments by performing FRET measurements over those constructs. In order to test the kinetic theory of FRET, one can use the obligate constructs of different kinds separately and then in some carefully chosen combinations, to observe how the experimentally extracted results of FRET efficiencies compare with those deduced using the kinetic theory of FRET.

## 4.2 Experimental testing of the kinetic theory

### 4.2.1 Using genetic constructs as standards for FRET efficiencies

The emergence of several spectral variants of green fluorescent protein and advancement in genetic engineering made it logical to prepare genetic constructs of various shapes and stoichiometry using suitable FRET pairs, to test the experimentally obtained FRET efficiencies. These constructs can be used as FRET reference or standards, and they can be easily distributed or replicated. These FRET standards, also called the artificial constructs or obligate FRET complexes, were first prepared by Vogel *et al*., in the year 2006, at Laboratory of Molecular Physiology, National Institute on Alcohol Abuse and Alcoholism, Bethesda, Maryland [5]. Several constructs were prepared with varying lengths of the linkers among the fluorescent molecules.

Cerulean (CFP variant) and Venus (YFP variant), were chosen ad FRET pair, where Cerulean and Venus are the donor and acceptor of energy respectively. Three Cerulean-Venus dimers of the linker lengths of 5,17 and 33 amino acids were constructed and called C5V, C17V, and C32V respectively. In all the constructs, the A206K mutation was introduced to create a monomeric form of the fluorescent protein. For the constructs of three different linker lengths, the donor fluorescence lifetime was measured by Vogel *et al*., and it was found to decrease as the linker size shortened, confirming an increase in FRET as the distance between the donor and acceptor pair decreased. This was consistent with the results found from the spectral FRET.

Donor's lifetime was compared in the situation of the absence and presence of an acceptor. The Cerulean chromophore is surrounded by a β barrel so that it would not be affected by other environmental factors. Thus, the change in the lifetime in the presence of Venus chromophores will confirm the occurrence of the FRET. With this assumption that the lifetime of Cerulean will

85

not change when attached to another protein because of the β barrel, when Venus is attached to it, the shortening of the lifetime was directly attributed to FRET.

Nevertheless, when Cerulean was attached to other non-fluorescent proteins, its lifetime is altered making it not very suitable reference as a Cerulean monomer. Therefore, using this for the lifetime of Cerulean alone, and to compare with the lifetime of Cerulean-Venus FRET pair, may raise some concerns. To fix this issue, a mutant of Venus was generated by mutating Tyrosine 67 in Venus, to Cysteine (Y67C mutation). This mutant was called Amber. Amber folds correctly but does not fluoresces [5]. Since Amber is non-fluorescent, it was used as a control molecule. Amber was used in combination with Cerulean to make Cerulean-Amber pair as a standard donor only construct.
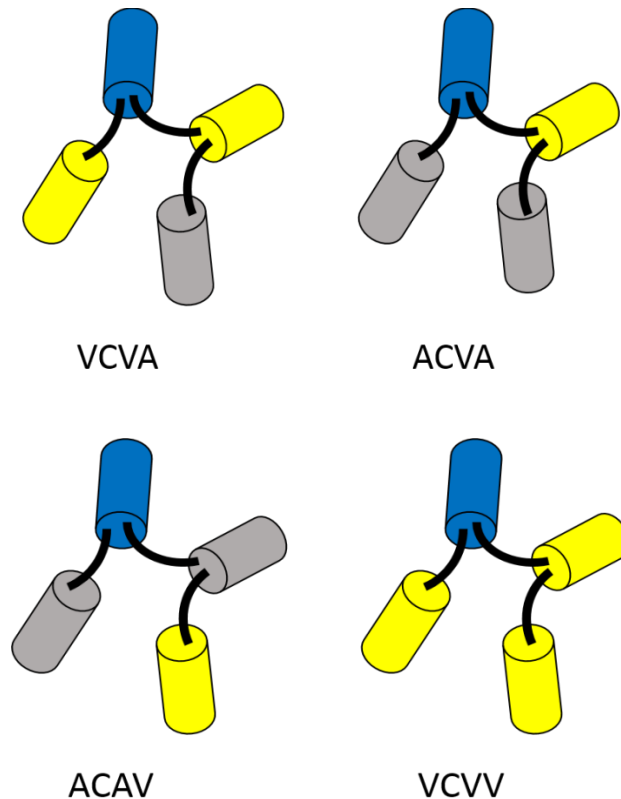


**Figure 4.1 Artificial genetic constructs as FRET standards.** Blue barrel represents donor (Cerulean), yellow represents acceptor (Venus), and gray represents Amber (non-fluorescent control).

Constructs of several sizes shapes are devised by using the above-mentioned three types of molecules including dimers, trimers, and tetramers [5]. Four different configurations of a tetramer as shown in figure 4.1. The distances among the fluorescent molecules are known. Using their relative distances, quantum yields ($Q^D$ or $Q^A$), average value of the orientation factor (equal to 2/3), as well as their overlap integral (as described in chapter 2), Förster radius could be predicted and hence, the apparent FRET efficiency ($E_{app}$) for each type of complex was estimated.

These constructs were then tested using different methods of FRET measurements, such as fluorescence lifetime spectroscopy [6, 7], sensitized acceptor emission [2, 8-13], and spectral imaging [14]. All valid FRET methods should provide the same FRET efficiency. The predicted values of FRET efficiencies were then compared with the experimentally extracted FRET efficiencies values, by applying standard methods of FRET measurements. It was to found that the measured FRET efficiencies were within the acceptable range of calculated FRET efficiencies of these FRET standards. Therefore, the results of these measurements were in good agreement with the theory of FRET. These tests proved these constructs to be good references for the FRET studies.

## 4.2.2 Reported discrepancies between the kinetic theory and experiment

In 2009, Koushik *et al* [3] reported the results of their testing of the kinetic theory of FRET by measuring ensemble FRET efficiencies of the two different shapes of the constructs which were trimers and tetramers, each of them containing single donor (Cerulean) and two or three acceptors (Venus), for the trimers and tetramers respectively [3]. Amber was used as a placeholder. Individual donor-acceptor pair FRET efficiencies were measured within these

complexes by mutating the acceptors one by one using the point mutation method, which made them non-fluorescent.

The study found that the amount of energy transferred to the acceptors was significantly greater than what was predicted by the kinetic theory of FRET, taking into account all the donor-acceptor pairs. Therefore, they stated, their results proved the kinetic theory to be incorrect or there existed some additional pathway of energy transfer between the donor and the acceptor besides FRET. The results of this study are shown in the table below.

**Table 4.1 Measured FRET efficiencies for the constructs with two acceptors.** The FRET efficiencies for three different trimeric constructs consisting Cerulean (as a donor or D) and Venus (as an acceptor or A), are shown with the standard errors, for three methods of FRET measurements. Amber, the non-fluorescent control is shown as N. Numbers of cells (n) used for each type of constructs and for each measurement type, are also shown. This table is reproduced with permission from [3].

| | FRET Constructs | | |
|---|---|---|---|
| **FRET Methods** | ADA | NDA | ADN |
| **FRET efficiency (sRET)** | 0.44± 0.08 <br><br> mean±SD, n=26 | 0.36± 0.09 <br><br> mean±SD, n=26 | 0.64± 0.05 <br><br> mean±SD, n=16 |
| **FRET efficiency (E-FRET)** | 0.45± 0.04 <br><br> mean±SD, n=82 | 0.38± 0.03 <br><br> mean±SD, n=52 | 0.69± 0.05 <br><br> mean±SD, n= 59 |
| **A/D (E-FRET)** | 0.96± 0.09 <br><br> mean±SD, n=82 | 0.95± 0.097 <br><br> mean±SD, n=52 | 1.96± 0.17 <br><br> mean±SD, n=59 |
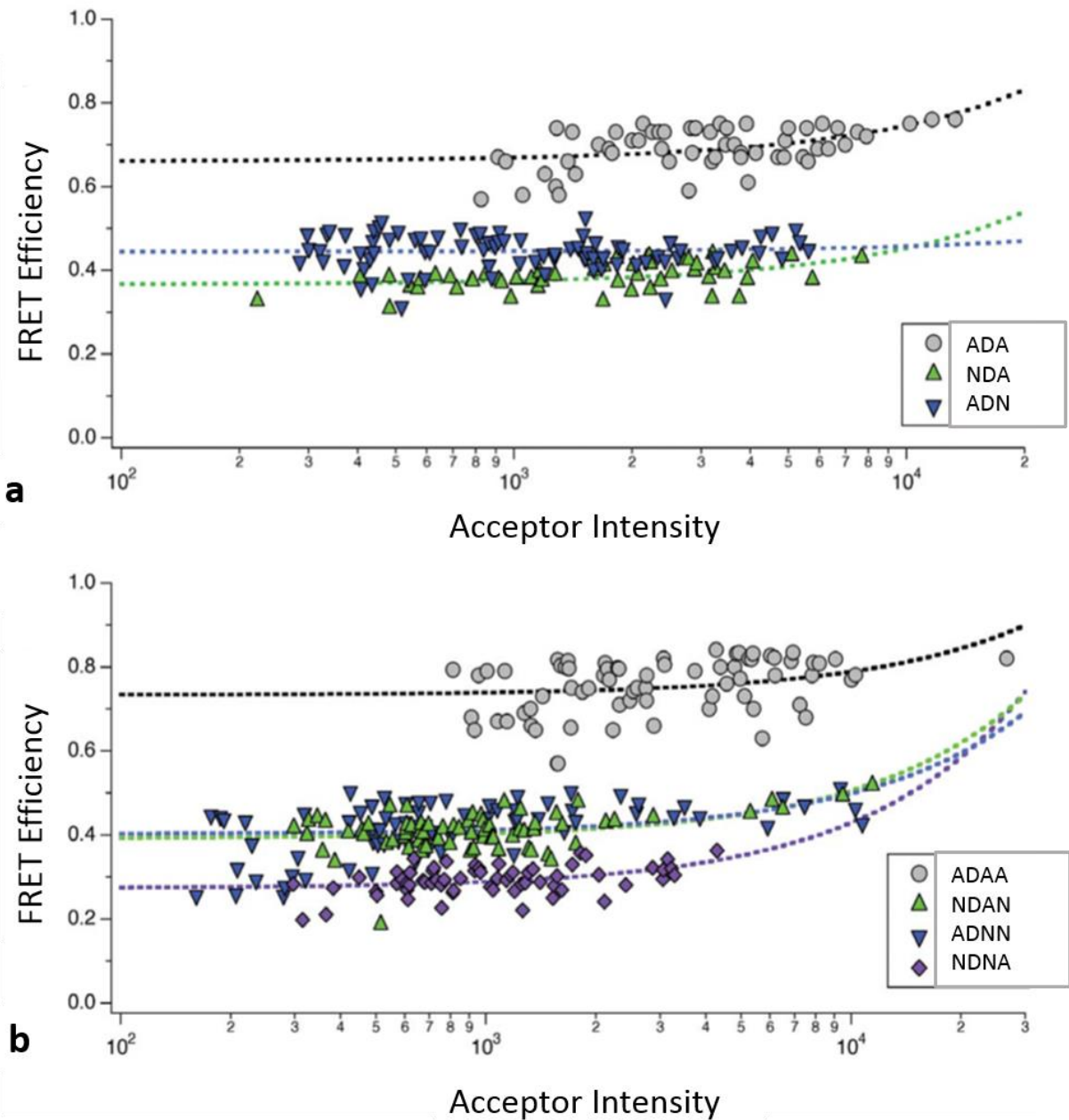
**Figure 4. 2 Results of the measurements of the intramolecular FRET efficiencies.** This shows the dependence of FRET efficiencies on the donor to acceptor ratio and the distance between the donors and the acceptors, (**a**) for the trimers, and (**b**) for the tetramers. The figure is reproduced with the permission from [3]. Where D, A, and N stand for Donor (Cerulean), Acceptor (Venus) and Neutral (Amber).

89

The table 4.1 and the figure 4.2 show the discrepancy in the kinetic theory of FRET. The FRET increased in the presence of more acceptors but it was less than what was predicted by the kinetic theory of FRET. The discrepancy was reported by both, one and two-photon excitations, and by using either laser or arc lamp as the excitation source, and, by using two FRET methods, spectral FRET [12-17] and acceptor desensitization FRET [8, 18].

Various possibilities were suggested for the anomaly shown between the above-described results and the theory, which include the Venus or the Amber behaving differently in different constructs. For example, the folding time of these proteins was observed to be different in the presence of different protein partners forming the constructs. Also, an occult energy transfer, which is not accounted in the kinetic theory of FRET, was considered.

### 4.2.3 Experimental confirmation of the kinetic theory of FRET

In 2015, the results of another experimental study were published for testing the kinetic theory of FRET by Patowary *et al*., using two-photon excitation and spectral FRET [2]. This study did not find any such discrepancy as previously reported. In this work, kinetic theory of FRET was tested using linked fluorescent proteins in cytoplasm and plasma membrane regions. This work was done using optical micro-spectroscope (OptiMiS) and two-photon excitation (TPE). The technology of OptiMiS is included in chapter 3. In this study, cytoplasmic and membrane-bound obligate fluorescent dimers and oligomers were used to the theory. Their method was based on the concept that the FRET efficiency of a multimeric complex can be computed by averaging the FRET efficiencies of the FRET dimers of donor-acceptor dimers of the different intermolecular distances, which are present in the multimeric complex.

Kinetic theory predicts average (apparent) FRET efficiency per donor ($E_{app}$), within a multimeric complex. Each donor in a multimeric complex may have multiple FRET pathways,

90

when there are more than one acceptors are present in the complex. An equivalent scenario could be created by constructing the dimers of one donor and one acceptor for each donor-acceptor disposition in the complex. When the experimentally obtained FRET efficiencies of all possible FRET dimers within the complex is averaged, it should be equal to the $E_{app}$ of the multimeric complex given by the kinetic theory of the FRET, within an acceptable range of standard errors.

Constructs were prepared with a blue fluorescent protein variant Cerulean [19] and a yellow variant Venus [20]. Cerulean served as a donor of the energy and Venus served as an energy acceptor. Three different lengths of dimeric constructs used for this study were 5, 17 and 32 amino acids long. The shorter the linker, higher the FRET efficiency should be. C5V is expected to have the highest FRET efficiency followed by C17V and the lowest is for C32V.

The two proteins were excited using the two-photon microscopy. Cerulean has an excitation peak at 820 nm and an emission maximum at 475 nm, while Venus has an excitation peak at 940 nm and an emission maximum at 528 nm. For the dimer pair of Cerulean and Venus, the mixture should have an equal ratio of donor and acceptor. The relative intensity of the two components in the composite spectra should be a function of the distance between them. This means that closer the donor (D) and acceptor (A) from each other, higher the FRET is, thereby; the ratio of donor to acceptor will be lower.

Human Embryo Kidney (HEK 293) cells were transfected with these constructs. Spectral imaging was performed and analyzed at pixel level [14, 21]. The samples were excited with 800, and 970 nm of two-photon excitations. There were two peaks in the emission spectrum, at 475 and 528 nm, which are the Cerulean and Venus emission peaks respectively. This confirmed the presence of Cerulean and Venus in the samples. Also, Venus peak was always higher for the samples of three different linker sizes than the Cerulean peaks, which has informed that there was

91

always some energy transferred in the form of FRET from donor to acceptor. The 528 peak was highest for the C5V, then for the C17V and shortest for the C32V, which confirmed that shorter the linker, higher the energy transferred via FRET is.

Besides, the 528 nm Venus emission peak also increased for each sample when the excitation wavelength was increased. This is happened due to the direct excitation of acceptors as the increase in the excitation wavelength brought it closer to the acceptor excitation peak and more acceptors were excited directly.
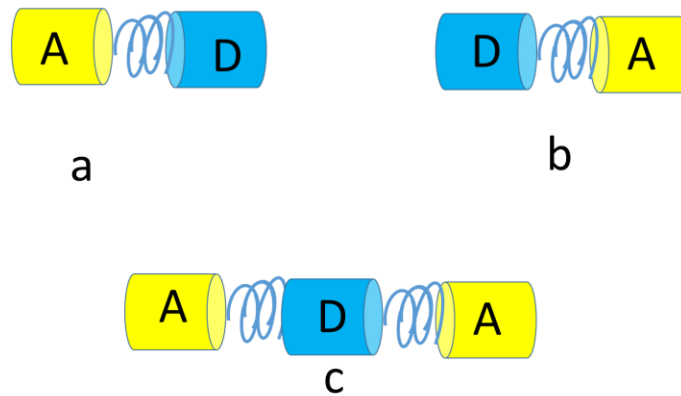


**Figure 4. 3 The schematic for obligate FRET constructs.** Dimers (a) & (b) and trimer (c) are connected by flexible linkers and their one end is attached to the membrane by a 32 amino acids linker.

The results of the above study are summarized in the table below.

**Table 4.2 Average of Measured Apparent FRET efficiencies (Eapp) of the cytoplasmic constructs.** The predicted mean ± SE value for the ADA construct is also listed. The numbers of the cells are shown in parentheses. The table is reproduced with permission from [2].

| Constructs | Eapp | |
|---|---|---|
| | Measured | Predicted |
| DA | 0.368± 5 0.015 (54) | — |
| AD | 0.254± 5 0.012 (48) | — |

92

| ADA | 0.515 ±5 0.009 (48) | 0.480 ±5 0.033 |

Here, a small but statistically significant difference was reported for the ADA trimer. The predicted value of the Eapp ($E_{predicted}$) was calculated using the equations (2.2) and error in the $E_{predicted}$ was calculated using equation (4.1), as shown below

$$E_{predicted} = \sum_{j=1}^{n-1} E_{j,} \tag{4.1}$$

where $E_j$ is the FRET efficiency contribution of the $j^{th}$ acceptor. For a complex, which has more than one donor, the following equation is used to calculate average FRET efficiency

$$E_{predicted} = \sum_j \frac{E_j/(1 - E_j)}{1 + \sum_j(E_j/(1 - E_j))} \tag{4.2}$$

Using the method of propagation of error, error in $E_{predicted}$ can be calculated, as given by the following equation

$$\delta E_{predicted} = E_{predicted} \frac{\sum_j \frac{\delta E_j}{(1 - E_j)^2}}{\left\{\sum_j \frac{\delta E_j}{(1 - E_j)}\right\}\left\{1 + \sum_j \frac{\delta E_j}{(1 - E_j)}\right\}} \tag{4.3}$$

The cytoplasmic construct used to test the kinetic theory of FRET were NDAN, ADNN, and NDNA. N stands for non-fluorescent entities, which are just placeholders. Average FRET efficiencies for these constructs were measured and plotted as logarithmic of the total donor concentration. It was found that the FRET efficiency for each construct increased only slightly as the expression level increased.

93
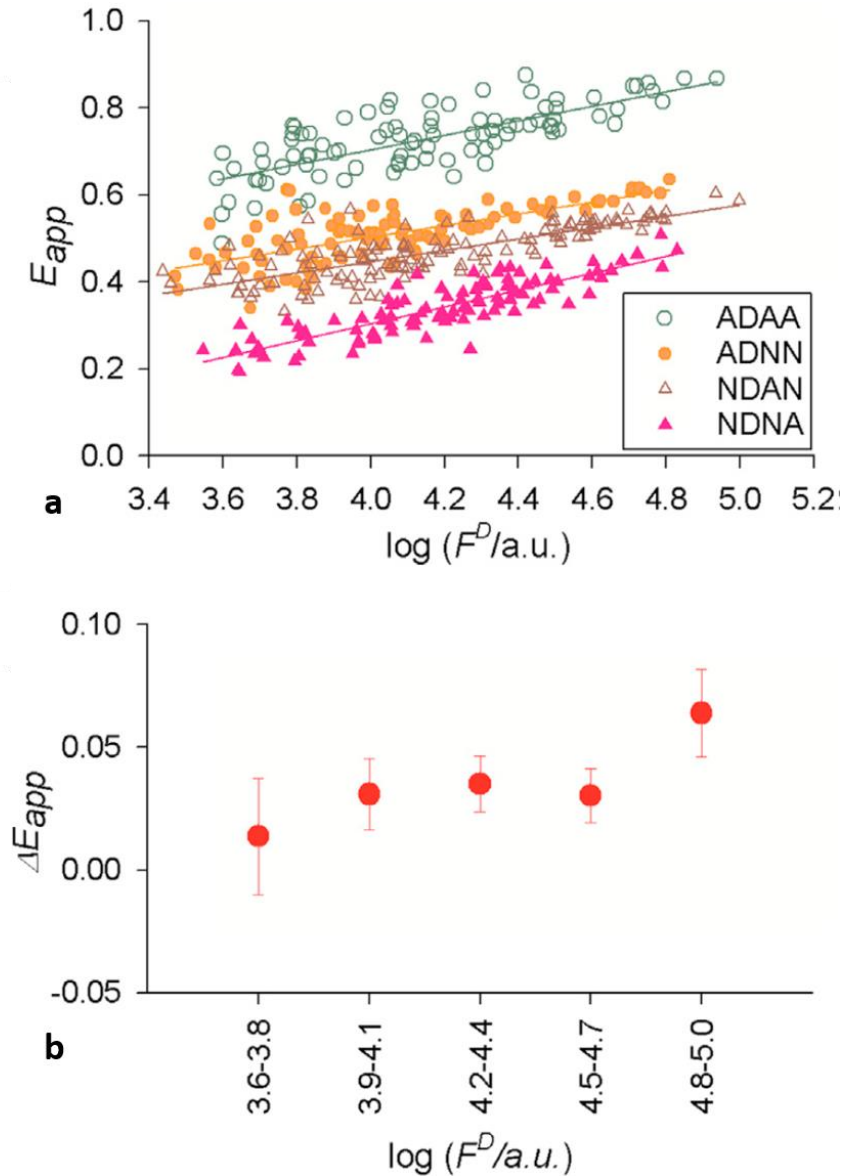
**Figure 4.4 Measured FRET efficiencies (Eapp) of the tetrameric constructs and their comparison with their predicted values.** (**a**) Apparent FRET efficiency for the four different cytoplasmic constructs ADAA, ADNN, NDAN, and NDNA. (**b**) The difference of measured and predicted FRET efficiencies plotted again log value of average donor expression level. The figure is adapted with permission from [2].

From the above-shown figure, the difference in the measured and the predicted FRET efficiencies is smaller than what was reported earlier as the discrepancy in the kinetic theory of FRET. This study shows that the kinetic theory of FRET is not violated by the experimental results

using acceptor sensitized emission FRET, when compared to the measured values of the FRET efficiencies for the FRET constructs expressed in the living cells.

## 4.3 Testing the kinetic theory of FRET using numerical simulations

To further put the kinetic theory to test, King et al [22] utilized numerical simulations on membrane protein receptors forming constitutive monomers, dimers or oligomers for different values of surface density. The surface density was calculated as the ratio of total receptor concentration and the membrane surface area. The simulations used 2700 data points with randomly chosen total values for the total concentration and with a variable acceptor molar fraction. Several distinct sizes of oligomers, besides monomers, ranging from dimers to hexamers were used for the simulations. For each order of the oligomerization, the simulation results were fitted with the theoretical curves obtained for each case using two different models which were:

1. Veatch and Stryer model proposed in 1977 [23]

2. Kinetic theory of FRET proposed by Raicu in 2007 [1] and as described in 4.2.3.

The study specially deals with proximity FRET or nonspecific FRET which occurs due to the crowding of macromolecules. Reduced Chi-square minimization was used to account for the concentration-dependent proximity FRET. Random noise of the Gaussian distribution was also incorporated into the simulations.

It was found that the Veatch and Stryer model did not predict the correct size of oligomers for the case of dimers at high protein concentrations. The Veatch and Stryer model prediction of oligomeric size depends on the concentration level giving a bigger oligomeric size for higher concentration.

95

Also, for the constitutive oligomer of the $E_p$ value equal to 0.30, simulation results were fitted with the models based on kinetic theory formalism. The results of the fits were consistently correct for the dimers or tetramers at all the concentration values.

According to the study by King et al, the kinetic theory of FRET proposed by Raicu is in full agreement with numerical simulations. As we have described above, it is also in agreement with experiment (see section 4.2.3).

# References

[1] V. Raicu, Efficiency of resonance energy transfer in homo-oligomeric complexes of proteins, J Biol Phys, 33 (2007) 109-127.

[2] S. Patowary, Luca F. Pisterzi, G. Biener, Jessica D. Holz, Julie A. Oliver, James W. Wells, V. Raicu, Experimental Verification of the Kinetic Theory of FRET Using Optical Microspectroscopy and Obligate Oligomers, Biophysical Journal, 108 (2015) 1613-1622.

[3] S.V. Koushik, P.S. Blank, S.S. Vogel, Anomalous surplus energy transfer observed with multiple FRET acceptors, PloS one, 4 (2009) e8031.

[4] S. Patowary, Protein Association in Living Cells Using Fret Spectrometry: Application to G-Protein Coupled Receptors, in: Physics, vol. Ph.D., University of Wisconsin Milwaukee (UWM) 2013.

[5] S.V. Koushik, H. Chen, C. Thaler, H.L. Puhl, S.S. Vogel, Cerulean, Venus, and Venus Y67C FRET reference standards, Biophysical journal, 91 (2006) L99-L101.

[6] X.F. Wang, A. Periasamy, B. Herman, D.M. Coleman, Fluorescence lifetime imaging microscopy (FLIM): instrumentation and applications, Critical Reviews in Analytical Chemistry, 23 (1992) 369-395.

[7] T.W. Gadella, T.M. Jovin, R.M. Clegg, Fluorescence lifetime imaging microscopy (FLIM): spatial resolution of microstructures on the nanosecond time scale, Biophysical chemistry, 48 (1993) 221-239.

[8] T. Zal, N.R. Gascoigne, Photobleaching-corrected FRET efficiency imaging of live cells, Biophysical journal, 86 (2004) 3923-3939.

[9] V. Raicu, M.R. Stoneman, R. Fung, M. Melnichuk, D.B. Jansma, L.F. Pisterzi, S. Rath, M. Fox, J.W. Wells, D.K. Saldin, Determination of supramolecular structure and spatial distribution of protein complexes in living cells, Nat Photon, 3 (2009) 107-113.

[10] D.R. Singh, V. Raicu, Comparison between Whole Distribution- and Average-Based Approaches to the Determination of Fluorescence Resonance Energy Transfer Efficiency in Ensembles of Proteins in Living Cells, Biophysical Journal, 98 (2010) 2127-2135.

[11] D.R. Singh, M.M. Mohammad, S. Patowary, M.R. Stoneman, J.A. Oliver, L. Movileanu, V. Raicu, Determination of the Quaternary Structure of a Bacterial ATP-Binding Cassette (ABC) Transporter in Living Cells, Integrative biology : quantitative biosciences from nano to macro, 5 (2013) 312-323.

[12] S. Patowary, E. Alvarez-Curto, T.R. Xu, J.D. Holz, J.A. Oliver, G. Milligan, V. Raicu, The muscarinic M3 acetylcholine receptor exists as two differently sized complexes at the plasma membrane, Biochem J, 452 (2013) 303-312.

[13] A.K. Mishra, T. Mavlyutov, D.R. Singh, G. Biener, J. Yang, J.A. Oliver, A. Ruoho, V. Raicu, The sigma-1 receptors are present in monomeric and oligomeric forms in living cells in the presence and absence of ligands, Biochem J, 466 (2015) 263-271.

[14] C. Thaler, S.V. Koushik, P.S. Blank, S.S. Vogel, Quantitative multiphoton spectral imaging and its use for measuring resonance energy transfer, Biophysical journal, 89 (2005) 2736-2749.

[15] V. Raicu, Efficiency of resonance energy transfer in homo-oligomeric complexes of proteins, Journal of biological physics, 33 (2007) 109-127.

[16] D.R. Singh, V. Raicu, Comparison between whole distribution- and average-based approaches to the determination of fluorescence resonance energy transfer efficiency in ensembles of proteins in living cells, Biophysics (2010).

[17] V. Raicu, D.R. Singh, FRET spectrometry: a new tool for the determination of protein quaternary structure in living cells, Biophysical journal, 105 (2013) 1937-1945.

[18] H. Chen, H.L. Puhl, S.V. Koushik, S.S. Vogel, S.R. Ikeda, Measurement of FRET efficiency and ratio of donor to acceptor concentration in living cells, Biophysical journal, 91 (2006) L39-L41.

[19] M.A. Rizzo, G.H. Springer, B. Granada, D.W. Piston, An improved cyan fluorescent protein variant useful for FRET, Nature biotechnology, 22 (2004) 445-449.

[20] T. Nagai, K. Ibata, E.S. Park, M. Kubota, K. Mikoshiba, A. Miyawaki, A variant of yellow fluorescent protein with fast and efficient maturation for cell-biological applications, Nature biotechnology, 20 (2002) 87-90.

[21] T. Zimmermann, J. Rietdorf, R. Pepperkok, Spectral imaging and its applications in live cell microscopy, FEBS letters, 546 (2003) 87-92.

[22] C.R. King, V. Raicu, K. Hristova, Understanding the FRET Signatures of Interacting Membrane Proteins, Biophysical Journal, 110 (2016) 428a.

[23] W. Veatch, L. Stryer, The dimeric nature of the gramicidin A transmembrane channel: conductance and fluorescence energy transfer studies of hybrid channels, Journal of molecular biology, 113 (1977) 89-102.

98

# Chapter 5: Oligomerization of sigma-1 receptor in living cells

As discussed in Chapter 1, the Sigma-1 receptor (S1R) is a molecular chaperone located in the plasma membrane of some mammalian cells, which regulates ion channels and interacts with several other proteins including GPCRs [1]. S1R seems to be implicated in substance abuse [2-5] and many other diseases [6-13]. S1R had been reported to interact with many exogenous ligands such as cocaine [4, 14, 15], haloperidol [2, 16-18] and pentazocine [10, 18]. It also interacts with endogenous molecules such as dimethyltryptamine [19, 20]. Understanding the quaternary structure of S1R (i.e., S1R oligomerization) may help using S1R as a drug target to cure certain diseases and addictions.

Effects of ligands on S1R dimerization and oligomerization have been investigated previously [21, 22], but never directly proven. We investigated the quaternary structure of S1R alone, as well as S1R in the presence of haloperidol or pentazocine plus, using spectral FRET and two-photon micro-spectroscopy in Cos-7 cells, using $GFP_2$ and YFP as a donor-tag and an acceptor-tag attached to S1R.

## 5.1 Materials and methods

### 5.1.1 Genetic constructs

The human S1R cDNA (NM_005866, Origene Technology) was PCR amplified using Pfx polymerase (Invitrogen, ThermoFisher Scientific, MA) replacing the stop codon with a MluI restriction enzyme recognition sequence (ACGCGT) and fused to the $GFP_2$ or YFP fluorophore's cDNA where the start ATG of the fluorophore was deleted to assure no expression of the fluorophore alone. The constructs were both C-terminal S1R fluorophore fusions. The reporter fluorophores were as described earlier [23, 24] and consisted of a modified GFP sequence

containing the point mutations F64L, A206K for GFP$_2$ and S65G, S72A, T203Y for the YFP. The C-fusion S1R donor and acceptor constructs were subcloned into a pCI (Promega, Inc., WI) eukaryotic expression vector and expressed by transient transfection using Lipofectamine 2000 (ThermoFisher Scientific, MA).

### 5.1.2 Source and use of drugs

(+)-Pentazocine was obtained from Sigma–Aldrich and haloperidol hydrochloride was obtained from Tocris Biosciences. (+)-Pentazocine was titrated with HCl in aqueous solution to a stock concentration of 10 mM. The aqueous stock of haloperidol HCl was also 10 mM. Cells were incubated with final concentrations of 100 μM for both the compounds in OptiMEM for approximately one hour prior to imaging.

### 5.1.3 Fluorescent tags

GFP$_2$ [25] and YFP [26, 27] were fused to two-sub-populations of the sigma 1 receptor. Between these two, GFP$_2$ acts as a donor and YFP as an acceptor of energy. GFP$_2$ has a large Stokes shift, and its emission spectrum overlaps well with the excitation spectrum of YFP. These two qualities make the GFP$_2$ and YFP an ideal FRET pair. Also, the two-photon excitation spectrum of GFP$_2$ and YFP fits well with the emission wavelengths of the Mai Tai™ (Spectra Physics, Santa Clara, CA) laser used. Both florescent proteins had the A206K mutation to prevent the specific tendency of GFP to form non-specific oligomers [28]

### 5.1.4 Culturing Cos-7 cells

Cos-7 cells were cultured in T25 flask Dulbecco's Modified Eagle Medium (DMEM, Life Technologies) with 10% FBS, 2 mM L-glutamine, 100 units/ml penicillin and 100 μg/ml streptomycin. The flasks were incubated at 37 °C and in the presence of 5% CO$_2$ for about 48 hours or until the flasks got about 80-90 % confluent. After a few passages, portions of these cells were

seeded in 0.17 mm thick (clear) Delta T® Culture Dishes (Bioptechs) in 2ml of above-mentioned cell-media. The dishes were incubated for ~24 hours at 37 °C and in an atmosphere containing 5% $CO_2$.

## 5.1.5 Plasmid transfection

After the dishes were taken out of the incubator, the Cos-7 cells were washed twice with Phosphate-buffered saline (PBS), and 2 ml of Opti-MEM® (Life Technologies, Carlsbad, CA)), Reduced Serum Medium (ThermoFisher Scientific, MA) was added to each dish.

Two μg each of sigma-1-mGFP$_2$ (i.e., sigma-1 fused with monomeric green fluorescent protein) and sigma-1-mYFP (sigma-1 fused with monomeric yellow fluorescent protein) were diluted into 5 μl of Opti-MEM. 5 μl of Lipofectamine 2000 was also diluted with 5 μl of Opti-MEM. After 5 minutes, the Lipofectamine dilutions were added to the plasmid dilutions. 20 minutes after that, the mixture of plasmids and Lipofectamine in Opti-MEM was added to the dishes. Cells were incubated again at the above-mentioned conditions, for about 24 hours, before they were taken out for imaging. The cells were washed again with PBS and 2 ml of Opti-MEM was added to each dish before imaging.

## 5.1.6 Imaging samples

The samples which had only Sigma-1 mGFP$_2$ or Sigma-1 mYFP were excited at 800 and 960 nm respectively, to generate the elementary spectra of the donors and acceptors respectively. These wavelengths are almost equal to the respective peak excitation wavelengths of GFP$_2$ and YFP.

Each sample was excited using a line-excitation mode [29]. The dwell time for each line (which also translates, for each pixel) was 35 ms. The excitation power used was 250 mW for the entire line or ~ 0.5 mW per pixel, while the spectral resolution was set to ~ 1nm.

101

### 5.1.7 Spectral analysis of protein standards

The GFP$_2$ protein solution was obtained from Lucigen Corporation, WI, which had a stock concentration of 167 µM. The stock solution was then subdivided into 50 µl aliquots, under orange light to prevent photobleaching, and stored at -70 °C. Before measurements, the protein solutions were diluted with PBS to get the following concentrations: 2.5, 5, 10 and 20 µM. These dilutions were imaged under same imaging conditions which were used to image the S1R samples with either GFP$_2$ or YFP fluorophores. The emission intensities were plotted against the molar concentrations of the protein solution dilutions. The slope of this graph gave the emission intensity per unit concentration of the fluorescent protein. This information was used to extract the donor concentration from the total donor emission intensity ($F^D$) for the FRET samples.

## 5.2 Analysis methods

### 5.2.1 Spectral unmixing and Eapp histograms

Cos-7 cells expressing Sigma-1-mGFP$_2$ or Sigma-1-mYFP samples were used to obtained pixel-level emission spectra averaged over a large number of pixels), to obtain good representative elementary spectra for the donor and acceptor, respectively. These spectra were used for unmixing the composite emission spectrum of the donor and acceptor obtained from the FRET samples (i.e., Cos-7 cells co-expressing both fusion proteins), using our in-house developed MATLAB routine for spectral unmixing which is based on the least square algorithm [30]. The composite spectrum (S) can be written in terms of the donor emission in the presence of acceptor ($k^{DA}$), acceptor emission in the presence of donor ($k^{AD}$), and the spectral integrals of the elementary spectra of donor ($w^D$) and acceptor ($w^A$), as following

$$S = k^{DA}w^D + k^{AD}w^A. \qquad (5.1)$$

www.manaraa.com

$k^{DA}$ and $k^{AD}$ obtained from equation (5.1), by pixel-level unmixing, were used to get the FRET efficiency ($E_{app}$) of each pixel of the spectral images using the equation (3.11).

A signal-to-noise ratio threshold of 1 was applied on each pixel of the $E_{app}$ images. By binning the $E_{app}$ pixels in intervals of 0.01 (or 1%) of FRET efficiency, $E_{app}$ histograms were created for each cell imaged.

## 5.2.2 Constructing Eapp meta-histograms

Different configurations of donors and acceptors within a given quaternary structure is characterized by different $E_{app}$ values, each of which can be expressed in terms of the FRET efficiency of a chosen single donor-acceptor pair in the oligomer chosen as a reference; this reference value is called *pairwise FRET efficiency* ($E_p$). When many different configurations are present in the pixels of a selected image region, and an $E_{app}$ histogram is built, those configurations that dominate in most of the pixels will constitute the dominant peak of the histogram [23]. With a few exceptions [24] it is rather uncommon to have all the peaks corresponding to all possible D-A configurations in a single histogram. To capture the $E_{app}$ values corresponding to all the possible configurations of donor and acceptor molecules in a multimeric complex, we collected the peak positions of all the $E_{app}$ histograms, and binned them again in a bin interval of 0.025 (or 2.5% )of FRET efficiency, to create a histogram of histograms, called meta-histogram, as described previously [23, 26, 31]. Therefore, the metahistogram should show $E_{app}$ peaks corresponding to all the FRET configurations of the quaternary structure.
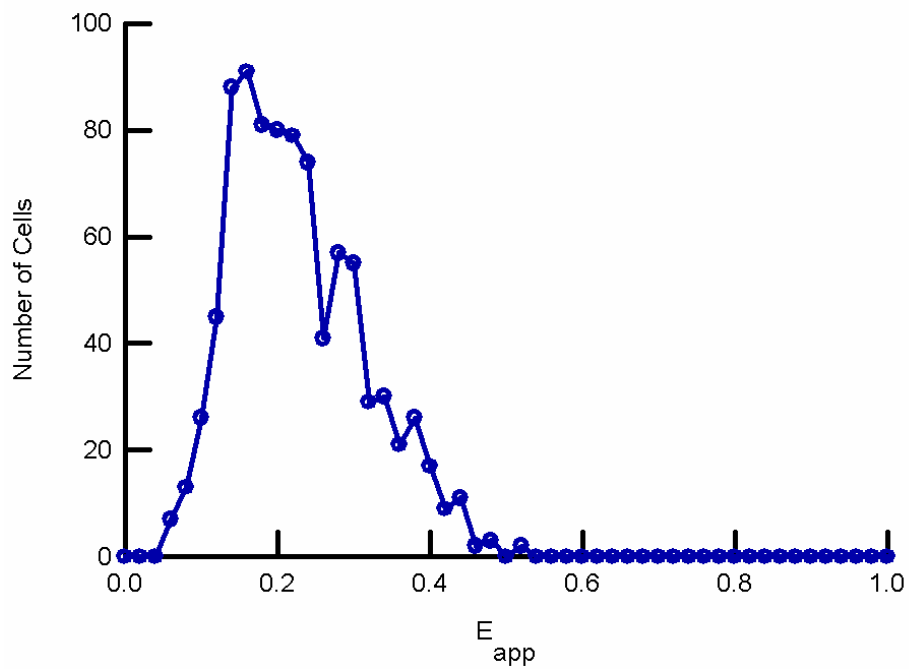
**Figure 5. 1 Metahistogram for 887 Coss7 cells expressing S1R alone.** $E_{app}$ histograms peaks were binned in the bin size of 2% of FRET efficiency to generate the meta-histogram.
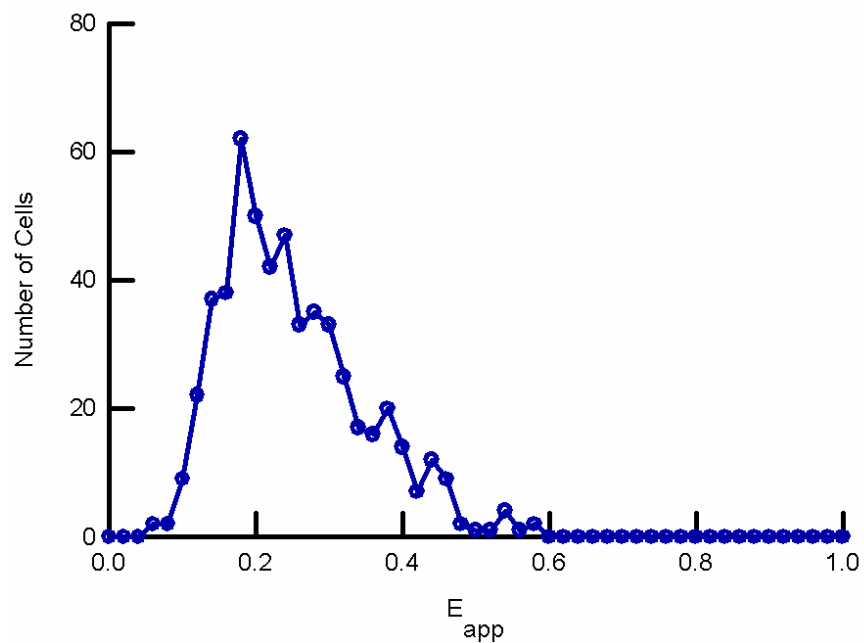


**Figure 5. 2 Metahistogram for 553 Coss7 cells expressing S1R in the presence of haloperidol.** $E_{app}$ histograms peaks were binned in the bin size of 2% of FRET efficiency to generate the meta-histogram.

104
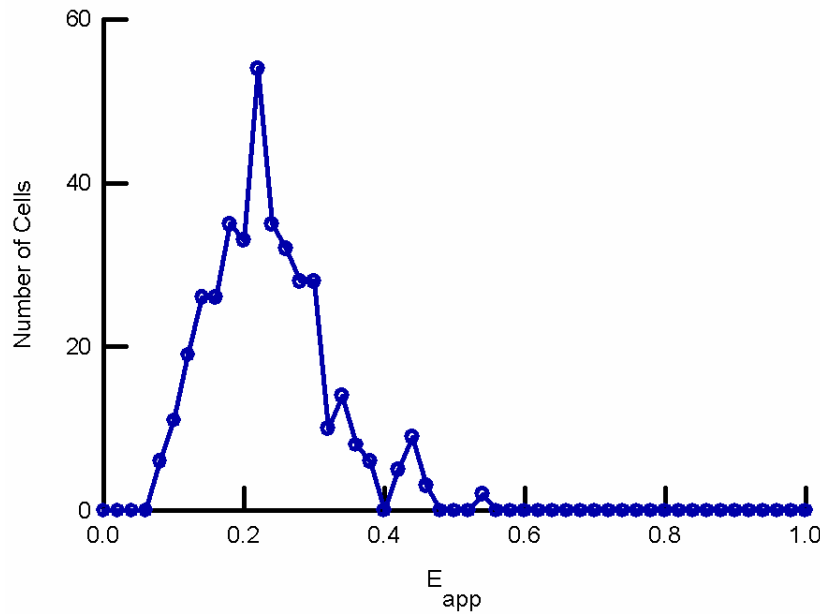
**Figure 5. 3 Metahistogram for 390 Coss7 cells expressing S1R in the presence of (+)-pentazocine.** $E_{app}$ histograms peaks were binned in the bin size of 2% of FRET efficiency to generate the meta-histogram.

All three metahistograms shown above were fitted with models of $E_{app}$, as discussed in the next section, to find the quaternary structure for each case which would correspond to the best fit model.

### 5.2.3 Fitting FRET models to the meta-histogram

FRET models corresponding to several possible quaternary structures, as described in the Kinetic Theory of FRET in Chapter 2, were fitted to the meta-histogram. Two of the models tested consisted of a parallelogram tetramer and a mixture of dimers and monomers. The parallelogram tetramer model is described in Chapter 2, and the dimers and monomers model is explained in the next section.

### 5.2.4 Dimers and monomers model

When there is a mixture of dimers and monomers present in the image pixels, the $E_{app}$ value of each pixel depends on the total number of donors in that pixel is given as below

105

$$E_{app} = \frac{l}{n} E \quad , \tag{5.1}$$

where $E_d$ is the pairwise FRET efficiency of the dimer, and $n$ is the number of donors in each pixel and $l$ can have any positive integer value, ranging between 0 and $n$. The $E_{app}$ value for each such configuration $E_{app}(l)$ corresponds to the ensemble of $n$ donors which form $l$ FRET dimers.

For a given number ($n$) of donors, there are $n$ possible combinations of dimers and monomers (see figure 5.1).

The $E_{app}$ model for the mixture of dimers and monomers is the sum of Gaussians with their peak positions defined by the above equation, and each Gaussian having its independent amplitude and standard deviation. $E_d$, $n$, amplitudes and standard deviations of the Gaussian are the fitting parameters, of this model, as given by the following equation:

$$f(E_{app}) = \sum_{l=1}^{n} G\left(\frac{l}{n} E_d\right). \tag{5.2}$$

The fitting residual which was minimized to find the best fit of a model to the data is given by the following equation:

$$\text{Fitting residual} = \frac{\sum_i |\text{Experimental}_i - \text{Simulated}_i|}{\text{Degree of freedom}}, \tag{5.3}$$

where $\text{Experimental}_i$ is the $i$th data point corresponding to experimental results and $\text{Simulated}_i$ is the simulated value given by the FRET model at the $i$th value of the independent variable in the data.

All possible FRET configurations for the dimers and monomers model in the case of nine donors in each pixel is given in figure 5.3. Number 9 was the value of the number of donors per

106

pixel as a best- fit parameter for the dimers and monomers model which best fitted the meta-histogram, as shown in the results section.
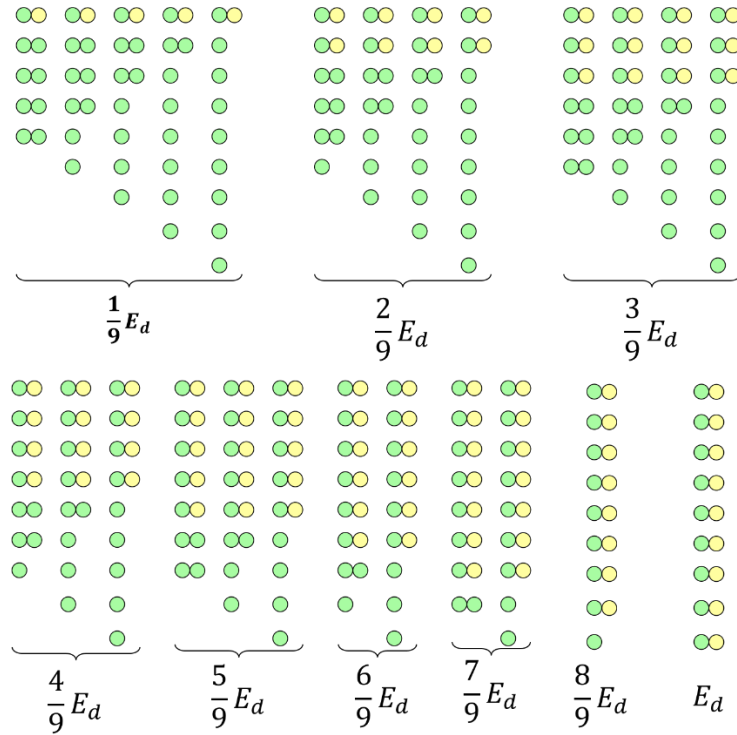


**Figure 5.4 Geometrical configurations and the corresponding mathematical expressions for apparent FRET efficiencies (Eapp) of mixtures of dimers and donors, for the case where each pixel contains on average 9 donors.** For larger numbers of donors, the number of predicted peaks increases proportionally. Free acceptors, as well as dimers containing only acceptors, were ignored as they are not excited directly by light and do not contribute to the measured signal. This figure is taken with permission from [17].

Even though this model accepts only a fixed number of donors as one of the fitting parameters, even though the expression level of the proteins per voxel of the sample (or per image pixel) cannot be a fixed number. Instead, there would be several such series of $E_{app}$, as given by the equation 5.2, each for a fixed number of donors. This situation will result into a superposition of such functions of $E_{app}$. The function which corresponds to the maximum number of the pixels in a region of interest would dominate the metahistogram features. The remaining function for all

other values of $n$, forms a uniform smooth curve, and the dominant population shapes the meta-histogram peaks.

### 5.2.5 Plotting Eapp vs. donor concentration (ND)

Average $E_{app}$ was computed for each cell, by simply averaging the $E_{app}$ value of each pixel. Also, the average donor concentration was computed for each cell, by comparing the average of the total donor emission intensity and comparing it to the emission intensity of the donor in a solution of known donor-concentration.

The averaged total donor intensity was computed by averaging the donor intensity over all the pixels of a cell or region of interest. The total donor emission intensity ($F^D$) for each pixel was computed using the equation 4.1 (Chapter 4).

The graph of $E_{app}$ vs. $N_D$ was plotted for $N_D$ (horizontal) axis shown in $\log^-_{10}$, to expand the scatter along the horizontal direction for visualization purpose.

### 5.3 Results

The results of spectral unmixing, the process which is described in the theoretical section of this chapter, for three representative cells are shown in figure 5.2. $E_{app}$ histograms were created for the entire cell selections. The varying position of the peaks in the $E_{app}$ histograms for the three cells shows that the dominant configuration of donor and acceptor for the quaternary structure varies cell to cell.
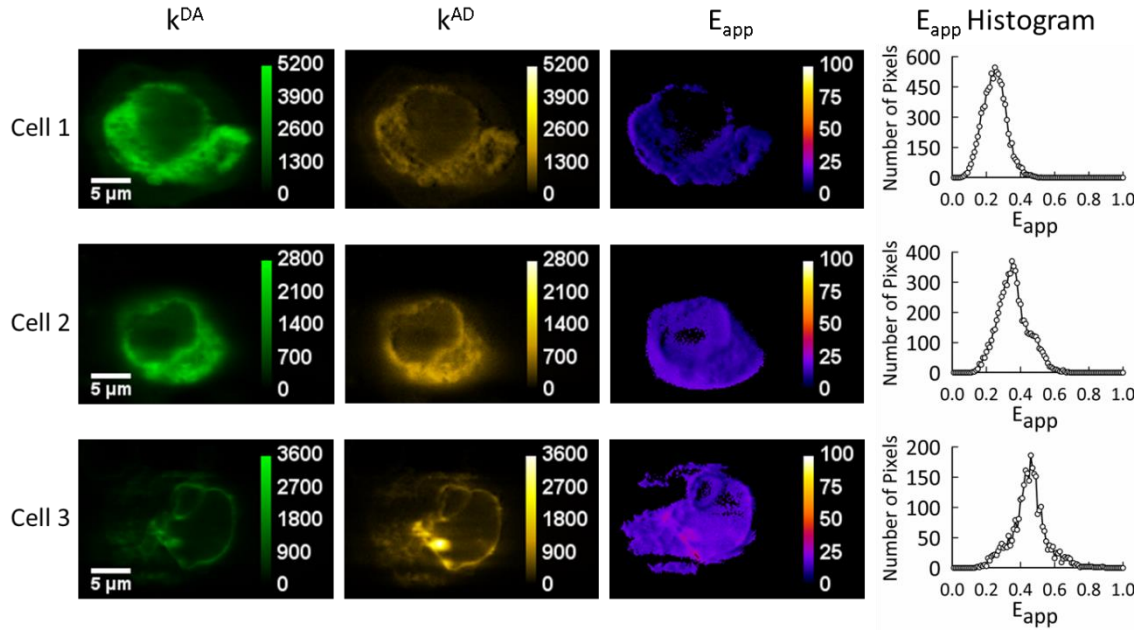
**Figure 5. 5 The spectral unmixing of GFP2 and YFP, attached to the sigma-1 receptor, expressed in Cos-7 cells.** The spectral maps, for donor in the presence of acceptor ($k^{DA}$), acceptor in the presence of donor ($k^{AD}$), and the pixel level FRET efficiency ($E_{app}$) map. Histograms were plotted using the $E_{app}$ pixels falling into the complete cell selections and binning them into the bin of 0.01 or 1% FRET efficiency. This figure is reproduced, with permission, from [17]

$E_{app}$ was calculated at pixel level by using the values of $K^{DA}$ and $K^{AD}$ for each pixel, applying equation 4.14. A threshold of the signal to noise ratio equal to one was applied to the $K^{DA}$ and $K^{AD}$, while calculating $E_{app}$ values, to eliminate false $E_{app}$ values which may occur due to noise only, in the low signal area. $E_{app}$ map gives the distribution of FRET efficiencies over the entire image. $E_{app}$ histograms were created by circling each cell and binning the pixels into the bin interval of 0.01 or 1% of FRET efficiency. $E_{app}$ histogram peaks should give the $E_{app}$ values corresponding to the dominant permutation of donors and acceptors in a multimeric complex, in each cell.

## 5.3.1 Results of the meta-histograms

Meta-histograms for the three cases, sigma-1 alone, in the presence of haloperidol and in the presence of pentazocine plus are shown, in figures 5.5 (a), 5.6 (a) and 5.7 (a) respectively.
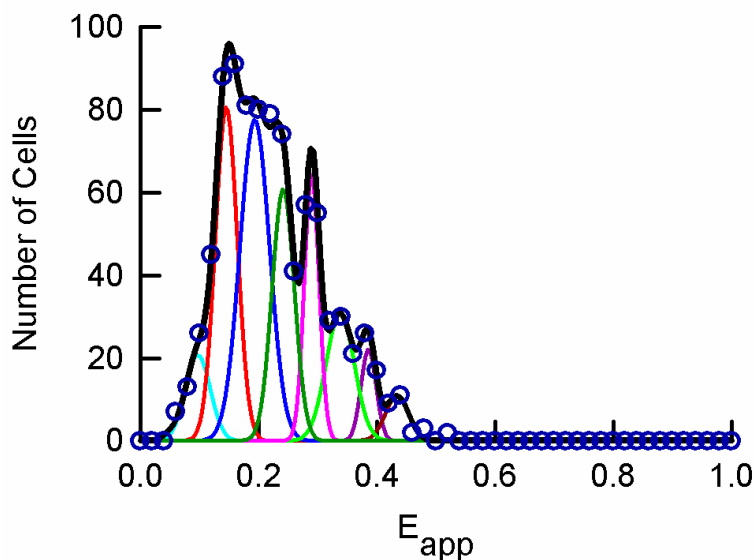


**Figure 5. 6 Metahistogram for 887 Coss7 cells expressing S1R alone, fitted with a mixture of dimers and monomers model.** $E_{app}$ histograms peaks were binned in the bin size of 2% of FRET efficiency to generate the meta-histogram. The best-fit value for $E_d$ is 0.433 and the most probable value of the number of donors per pixel (***n***) is 9. Reduced fitting residual for the fitting is 4.42. Fittings for n equal to 8 and 10 are shown in Appendix B.
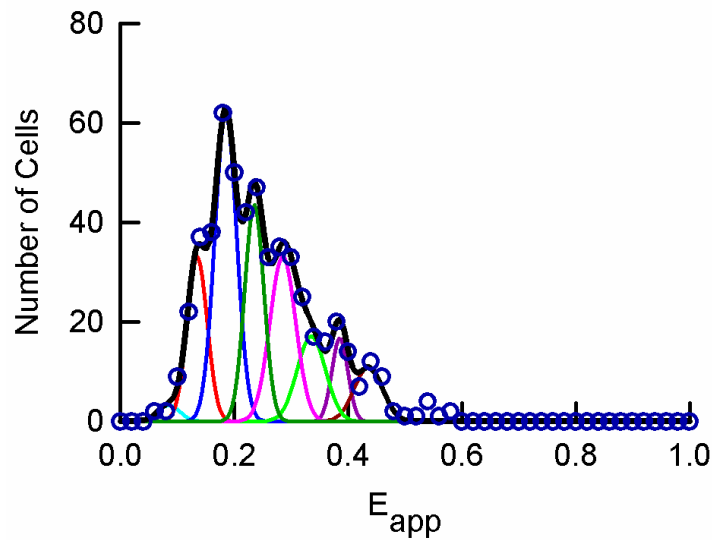
**Figure 5. 7 Metahistogram for 553 Coss7 cells expressing S1R in the presence of haloperidol, fitted with a mixture of dimers and monomers model.** $E_{app}$ histograms peaks were binned in the bin size of 2% of FRET efficiency to generate the meta-histogram. The best-fit value for $E_d$ is 0.435 and the most probable value of the number of donors per pixel ($n$) is 9. Reduced fitting residual for the fitting is 6.70. Fittings for n equal to 8 and 10 are shown in Appendix B.
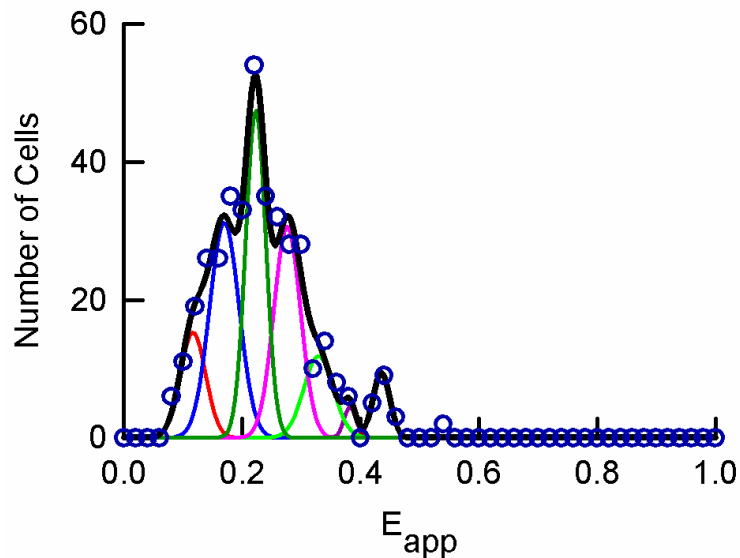


**Figure 5. 8 Metahistogram for 390 Coss7 cells expressing S1R in the presence of (+)-pentazocine, fitted with a mixture of dimers and monomers model.** *$E_{app}$* histograms peaks were binned in the bin size of 2% of FRET efficiency to generate the meta-histogram. The best-fit value for $E_d$ *is 0.435* and the most probable value of the number of donors per pixel ($n$) is 10. Reduced fitting residual for the fitting is 1.83. Fittings for n equal to 9 and 11 are shown in Appendix B.

111

S1R histograms in the absence or presence of the haloperidol or (+)-pentazocine were fitted best by a model consisting of a mixture of dimers and monomers. Also, the two main fitting parameters came out very similarly for the three cases, i.e., in the absence or presence of the above mentioned ligands.

## 5.3.2 Results of the cellular average of Eapp vs. number of donors (ND)

$E_{app}$ vs. $N_D$ for the three cases, sigma-1 alone, in the presence of haloperidol and in the presence of pentazocine plus are shown, in figures 5.8, 5.9 and 5.10 respectively.
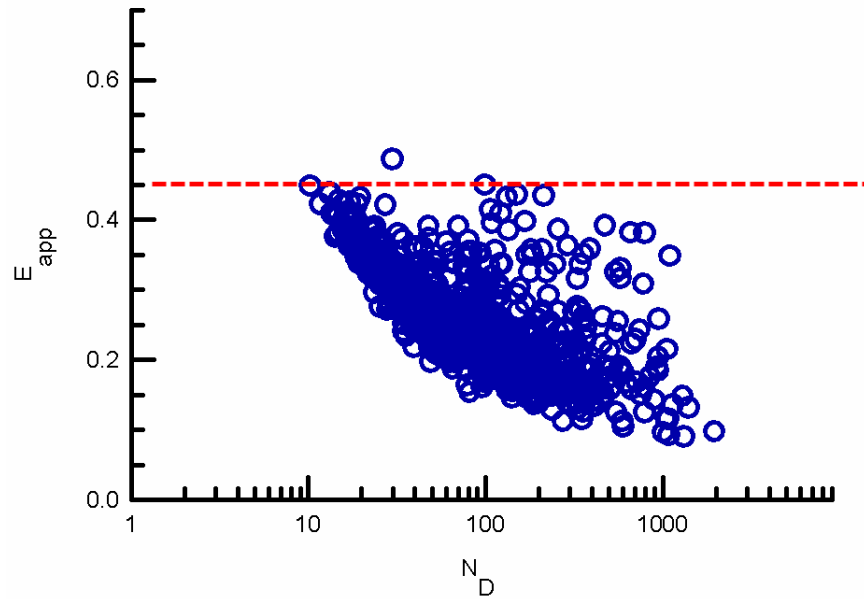


**Figure 5. 9 Average FRET efficiency (Eapp) vs. average donor expression (ND) graph for sigma-1 receptor alone. The donor expressed is given in the logarithmic scale of base 10.** The dashed red line shows the E$_{app}$ value for the dimers and monomers model, obtained by fitting the model to the E$_{app}$ meta-histogram.
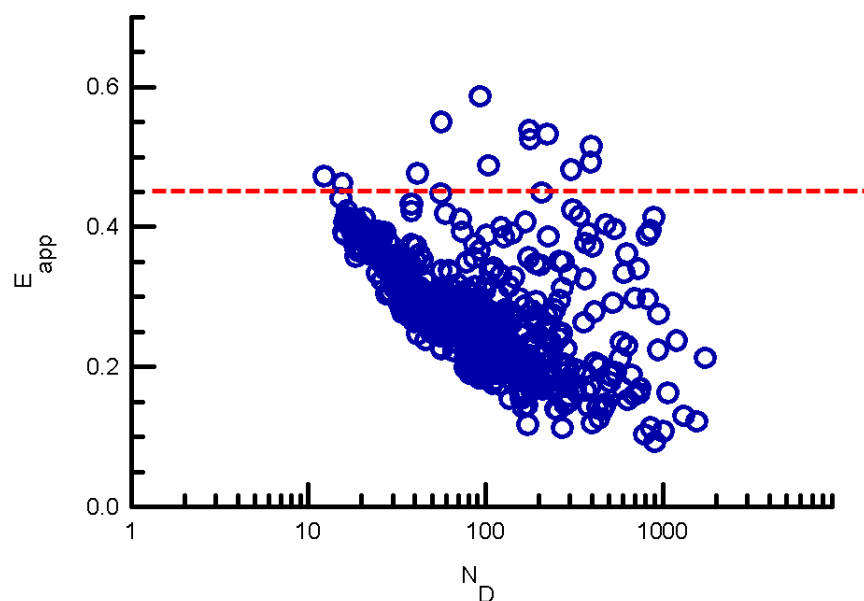
**Figure 5. 10 Average FRET efficiency (Eapp) vs. average donor expression (ND) graph for the sigma-1 receptor in the presence of haloperidol.** The donor expressed is given in the logarithmic scale of base 10. The dashed red line shows the $E_{app}$ value for the dimers and model, obtained by fitting the model to the $E_{app}$ meta-histogram.
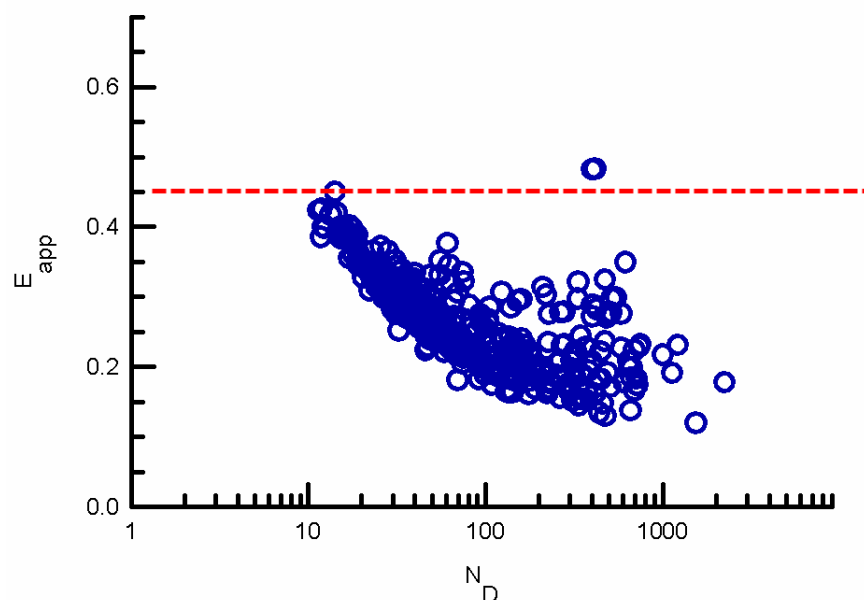


**Figure 5. 11 Average FRET efficiency (Eapp) vs. average donor expression (ND) graph for the sigma-1 receptor in the presence of (+)-pentazocine.** The donor expressed is given in the logarithmic scale of base 10. The dashed red line shows the $E_{app}$ value for the dimers and monomers model, obtained by fitting the model to the $E_{app}$ meta-histogram.

113

## 5.4 Discussion

The mixture of dimers and monomers was the best-fitting model into the $E_{app}$ metahistograms for all three cases: S1R alone, in the presence of haloperidol or (+)-pentazocine. Also, the two main fitting parameters, the pairwise FRET efficiency of the dimer ($E_d$) and the number of donors per pixel ($n$), for each of the three cases were similar. This confirms they had same dominant population present which metahistograms preferentially show.

Results of the other analysis method that fits models into $E_{app}$ vs. $N_D$ graphs show that for the extremely low concentration, i.e., the far-left side of the $E_{app}$ vs. $N_D$ graphs, all three graphs approach about the same value of the same FRET efficiency which is about 0.45.

$E_{app}$ vs. $N_D$ graphs can show the results of low expression and high expression. The right side of the graphs shows that at higher donor concentration, they receptor tend to form a broader distributing of FRET efficiencies, which indicate the presence of higher order oligomers at high expression levels.

S1R in the presence of haloperidol helps the spread more than the no ligand case. Pentazocine, however, seems to stabilize the spread of oligomeric forms, to dimers.

Although care was taken to not have any endogenous receptors, the presence of the sigma-1 receptor produced constitutively by the Cos-7 cells cannot be completely ruled out; its presence could cause the quaternary structure to be perceived smaller than the structure the receptors actually presented, when the detection methods are based on fluorescent protein tagging.

Also, photobleaching can cause the similar effect as the endogenous S1R receptors. However, since we used line scanning method, it is much less likely to photobleach the fluorescent proteins, in a single scan. Especially if compared to point scanning, the line scanning will have very small chance and rate of photobleaching [29].

www.manaraa.com

## 5.5 Comparison to the literature

Using the spectral FRET approach [24, 32], we found that S1R receptor resides in the forms of monomers and dimers at lower expression levels, and may form higher-order oligomers at higher expression levels when transiently expressed in Cos-7 cells.

S1R agonist haloperidol caused further spreading of FRET efficiencies when compared to the case of S1R alone. While the S1R agonist pentazocine plus diminished the FRET efficiency spread for the higher $E_{app}$ values, which indicate that at higher concentration the functional form of the receptor is likely not as higher order oligomer, as in the cases of S1R alone and in the presence of the receptor antagonist. In other words, pentazocine favored the dimeric form of the receptor.

S1R oligomerization in relation to ligand-binding is reported in the literature For example, in vitro analyses of highly purified MBP S1R fusion protein (MBP–4Ala–S1R) in dodecylmaltoside (DDM) showed oligomeric forms, including tetramers and hexamers/octamers that specifically bound -(+)-pentazocine [22].

The oligomeric forms were stabilized by both S1R agonists and antagonists. The monomeric form of the S1R did not bind -(+)-pentazocine [22]. High affinity radioiodinated S1R photoaffinity probes identified oligomeric forms of S1R in rat liver membranes [33]. The GXXXG sequence that occurs in putative TM2 of S1R is an important motif that, in part, determines the ability of the MBP–4Ala–S1R to oligomerize [22]. Additional residues of the S1R have also been implicated in S1R dimerization/oligomerization [34].

# References

[1] T.-P. Su, T. Hayashi, T. Maurice, S. Buch, A.E. Ruoho, The sigma-1 receptor chaperone as an inter-organelle signaling modulator, Trends in pharmacological sciences, 31 (2010) 557-566.

[2] D.W. Piston, G.-J. Kremers, Fluorescent protein FRET: the good, the bad and the ugly, Trends in biochemical sciences, 32 (2007) 407-414.

[3] J.J. Burbaum, N.H. Sigal, New technologies for high-throughput screening, Current Opinion in Chemical Biology, 1 (1997) 72-78.

[4] B. Valeur, M.N. Berberan-Santos, Molecular fluorescence: principles and applications, John Wiley & Sons, 2012.

[5] S. Weiss, Measuring conformational dynamics of biomolecules by single molecule fluorescence spectroscopy, Nature structural biology, 7 (2000) 724-729.

[6] J. Perrin, Observations sur la fluorescence, 1925.

[7] F. Perrin, Polarisation de la lumière de fluorescence. Vie moyenne des molécules dans l'etat excité, J. phys. radium, 7 (1926) 390-401.

[8] J.R. Gispert, Coordination chemistry, Wiley-VCH Weinheim, 2008.

[9] K.A. Franz, W.G. Kehr, A. Siggel, J. Wieczoreck, W. Adam, Luminescent materials, Ullmann's Encyclopedia of Industrial Chemistry, (2000).

[10] S.P. McGlynn, T. Azumi, M. Kinoshita, Molecular spectroscopy of the triplet state, (1969).

[11] D.J. Griffiths, E.G. Harris, Introduction to quantum mechanics, American Journal of Physics, 63 (1995) 767-768.

[12] A.A. Lamola, G.S. Hammond, Mechanisms of photochemical reactions in solution. XXXIII. Intersystem crossing efficiencies, The Journal of Chemical Physics, 43 (1965) 2129-2135.

[13] A. Renaudo, S. L'Hoste, H. Guizouarn, F. Borgese, O. Soriani, Cancer cell cycle modulated by a functional coupling between sigma-1 receptors and Cl- channels, The Journal of biological chemistry, 282 (2007) 2259-2267.

[14] J. Sharkey, K.A. Glen, S. Wolfe, M.J. Kuhar, Cocaine binding at sigma receptors, European journal of pharmacology, 149 (1988) 171-174.

[15] S.Y. Tsai, J.Y. Chuang, M.S. Tsai, X.F. Wang, Z.X. Xi, J.J. Hung, W.C. Chang, A. Bonci, T.P. Su, Sigma-1 receptor mediates cocaine-induced transcriptional regulation by recruiting chromatin-

remodeling factors at the nuclear envelope, Proceedings of the National Academy of Sciences of the United States of America, 112 (2015) E6562-6570.

[16] P.J. Brent, G. Pang, G. Little, P.J. Dosen, D.F. Van Helden, The sigma receptor ligand, reduced haloperidol, induces apoptosis and increases intracellular-free calcium levels [Ca2+]i in colon and mammary adenocarcinoma cells, Biochemical and biophysical research communications, 219 (1996) 219-226.

[17] A.K. Mishra, T. Mavlyutov, D.R. Singh, G. Biener, J. Yang, J.A. Oliver, A. Ruoho, V. Raicu, The sigma-1 receptors are present in monomeric and oligomeric forms in living cells in the presence and absence of ligands, Biochem J, 466 (2015) 263-271.

[18] R.E. Dale, J. Eisinger, W. Blumberg, The orientational freedom of molecular probes. The orientation factor in intramolecular energy transfer, Biophysical journal, 26 (1979) 161.

[19] T.P. Su, T. Hayashi, D.B. Vaupel, When the endogenous hallucinogenic trace amine N,N-dimethyltryptamine meets the sigma-1 receptor, Science signaling, 2 (2009) pe12.

[20] E. Buxbaum, Fundamentals of protein structure and function, Springer, 2007.

[21] F.J. Kim, I. Kovalyshyn, M. Burgman, C. Neilan, C.C. Chien, G.W. Pasternak, Sigma 1 receptor modulation of G-protein-coupled receptor signaling: potentiation of opioid transduction independent from receptor binding, Molecular pharmacology, 77 (2010) 695-703.

[22] K.A. Gromek, F.P. Suchy, H.R. Meddaugh, R.L. Wrobel, L.M. LaPointe, U.B. Chu, J.G. Primm, A.E. Ruoho, A. Senes, B.G. Fox, The Oligomeric States of the Purified Sigma-1 Receptor Are Stabilized by Ligands, The Journal of biological chemistry, 289 (2014) 20333-20344.

[23] D.R. Singh, M.M. Mohammad, S. Patowary, M.R. Stoneman, J.A. Oliver, L. Movileanu, V. Raicu, Determination of the Quaternary Structure of a Bacterial ATP-Binding Cassette (ABC) Transporter in Living Cells, Integrative biology : quantitative biosciences from nano to macro, 5 (2013) 312-323.

[24] V. Raicu, M.R. Stoneman, R. Fung, M. Melnichuk, D.B. Jansma, L.F. Pisterzi, S. Rath, M. Fox, J.W. Wells, D.K. Saldin, Determination of supramolecular structure and spatial distribution of protein complexes in living cells, Nat Photon, 3 (2009) 107-113.

[25] T. Zimmermann, J. Rietdorf, A. Girod, V. Georget, R. Pepperkok, Spectral imaging and linear un-mixing enables improved FRET efficiency with a novel GFP2-YFP FRET pair, FEBS letters, 531 (2002) 245-249.

[26] S. Patowary, E. Alvarez-Curto, T.R. Xu, J.D. Holz, J.A. Oliver, G. Milligan, V. Raicu, The muscarinic M3 acetylcholine receptor exists as two differently sized complexes at the plasma membrane, Biochem J, 452 (2013) 303-312.

[27] J. Lippincott-Schwartz, E. Snapp, A. Kenworthy, Studying protein dynamics in living cells, Nature Reviews Molecular Cell Biology, 2 (2001) 444-456.

[28] D.A. Zacharias, J.D. Violin, A.C. Newton, R.Y. Tsien, Partitioning of lipid-modified monomeric GFPs into membrane microdomains of live cells, Science (New York, N.Y.), 296 (2002) 913-916.

[29] G. Biener, M.R. Stoneman, G. Acbas, J.D. Holz, M. Orlova, L. Komarova, S. Kuchin, V. Raicu, Development and experimental testing of an optical micro-spectroscopic technique incorporating true line-scan excitation, International journal of molecular sciences, 15 (2014) 261-276.

[30] D.W. Marquardt, An algorithm for least-squares estimation of nonlinear parameters, Journal of the society for Industrial and Applied Mathematics, 11 (1963) 431-441.

[31] V. Raicu, D.R. Singh, FRET spectrometry: a new tool for the determination of protein quaternary structure in living cells, Biophys J, 105 (2013) 1937-1945.

[32] F.J. Moss, P.I. Imoukhuede, K. Scott, J. Hu, J.L. Jankowsky, M.W. Quick, H.A. Lester, GABA transporter function, oligomerization state, and anchoring: correlates with subcellularly resolved FRET, The Journal of general physiology, 134 (2009) 489-521.

[33] A. Pal, A.R. Hajipour, D. Fontanilla, S. Ramachandran, U.B. Chu, T. Mavlyutov, A.E. Ruoho, Identification of regions of the sigma-1 receptor ligand binding site using a novel photoprobe, Molecular pharmacology, 72 (2007) 921-933.

[34] M. Kinoshita, Y. Matsuoka, T. Suzuki, J. Mirrielees, J. Yang, Sigma-1 receptor alters the kinetics of Kv1.3 voltage gated potassium channels but not the sensitivity to receptor ligands, Brain research, 1452 (2012) 1-9.

# Chapter 6: Oligomerization of rhodopsin in living cells

Rhodopsin, a prototypical GPCR located in the cone and rod cells of the retina of the eye, is a light receptor involved in the sense of vision. As mentioned in chapter 1, AFM images suggested that rhodopsin molecules form arrays of dimers. However, other studies have shown that the functional form of rhodopsin is monomeric [1] or that it forms dimers [2]. Therefore, there have been suggestions in the literature that the rhodopsin oligomerization seen in room temperature AFM studies may be artifacts of phase separation between the cell membrane lipids and rhodopsin due to low temperatures [3]. To help solve this dilemma, we used spectral FRET and two-photon micro-spectroscopy, as described in chapter 4, to investigate rhodopsin oligomerization at body temperature. We show that rhodopsin forms a mixture of dimers and tetramers at body temperature at relatively lower concentrations and may form higher order oligomers at higher concentration levels [4].

## 6.1 Experimental methods

### 6.1.1 Preparation of plasmids and fluorescent protein solutions

Genetic constructs and purified fluorescent proteins were prepared by our collaborators, Megan Gregg and Prof. Paul Park, in the Department of Ophthalmology and Visual Sciences, at the Case Western Reserve University, Cleveland, OH.

The fluorescent proteins of our choice were mTurquoise (mTq) and SYFP2, which are brighter and more photostable variants of the widely used yellow fluorescent protein (YFP) and cyan fluorescent protein respectively [5, 6].

To prepare the DNA constructs used to express the fusion proteins formed by rhodopsin and the fluorescent proteins, the vectors pmRho-SYFP2-1D4 and pmRho-mTq-1D4 were generated as described previously [7, 8]. The full CMV Q1 promoter in these vectors was replaced

by a truncated CMV promoter to decrease the expression level of rhodopsin. The truncated CMV promoter, CMVd3, was generated by PCR using the primers 5′-ACGATGATTATATGGGCGGTAGGCGTGTACG and 5′-GGTAGCGCTAGCGGATCTGA and included an AseI restriction site at the 5′-end and a NheI restriction site at the 3′-end. The amplified CMVd3 replaced the endogenous full CMV promoter in pmRho-SYFP2-1D4 and pmRho-mTQ-1D4 at the AseI and NheI restriction sites to generate the vectors pCMVd3-mRho-SYFP2-1D4 and pCMVd3-mRho-mTQ-1D4.

To prepare the purified fluorescent proteins, two vectors, pRSET-SYFP2, and pRSET-mTq, were generated [9, 10]. BL21 (DE3) competent cells (purchased from NEB, Ipswich, MA) were transformed with pRSET-SYFP2 or pRSET-mTq and plated on Luria broth (LB) agar with 50 mg/ml ampicillin and incubated overnight at 37°C. Five tubes of 6 ml of LB broth with 50 mg/ml ampicillin were inoculated with bacteria picked from individual colonies and incubated overnight at 37°C with orbital shaking. Fluorescent protein expression was induced by adding 40 µl of IPTG (100 mM stock) and incubating further for 4 hours at 37°C with orbital shaking. The cultures were spun down at 4500×g for 10 min and placed at −80°C for 1 hour. Cells were lysed using the CelLytic B-Plus kit (Sigma-Aldrich, St. Louis, MO). Cell pellets were pooled from the five tubes, resuspended in 2 ml of CelLytic B-Plus working solution, and incubated at room temperature for 10 min with shaking. The cell lysate was centrifuged at 1900×g for 10 min. The supernatant containing the fluorescent protein was collected and loaded by gravity flow on a 1 ml HisPur Ni-NTA spin column (Thermo Fisher Scientific, Waltham, MA), which was equilibrated with 2 ml of 10 mM imidazole in phosphate-buffered saline (PBS), and incubated for 30 min at room temperature. The column was centrifuged at 700×g for 2 min. The column was washed three times by the addition of 2 ml of 25 mM imidizole in PBS and centrifuged at 700×g for 2 min. The

120

bound fluorescent protein was eluted with 1 ml of 250 mM imidazole in PBS and centrifuged at 700×g for 2 min. Imidazole was removed using a 2 ml ZebaSpin desalting spin column (Thermo Fisher Scientific, Waltham, MA). Eluant (700 µl) was loaded on the desalting column equilibrated with PBS. Purified fluorescent protein was collected by centrifugation at 1000×g for 2 min. The concentration of purified fluorescent protein was determined by UV/Vis absorbance spectroscopy on a Nanodrop2000c (Thermo Fisher Scientific, Waltham, MA). The $\lambda_{max}$ and extinction coefficient for SYFP2 were 515 nm and $101 \times 103$ M$-1$ cm$-1$, respectively, and those for mTq were 434 nm and $30 \times 103$ M$-1$ cm$-1$, respectively.

### 6.1.2 Cell culture

Chinese Hamster Ovary (CHO) cells were maintained in T-25 flasks in 5 ml of Dulbecco's Modified Eagle Medium (DMEM), Thermo Fisher Scientific, Waltham, MA) containing 10% fetal bovine serum and 1% non-essential amino acids. The flasks were incubated at 37 °C and 5% $CO_2$ and subcultured when they were about 80-90% confluent. Cells were seeded at about 40% confluency in Delta-T temperature controlled dishes (Bioptechs, Inc., Butler, PA), in the above-mentioned cells media. The dishes were incubated for about 24 hours at 37 °C and 5% $CO_2$ before they were taken out for transfection.

### 6.1.3 Plasmids transfection

Two plasmid vectors used for the transfection were: pCMVd3-mRho-SYFP2-1D4 and pCMVd3-mRho-mTQ-1D4.

Six types of samples were used for each experiment, out of which five samples were transfected, each with 4 µg of plasmids; one sample, which did not contain any plasmids, was used as a negative control. Out of five transfected samples, two were used with either donor-tagged or acceptor-tagged plasmid. These two samples were used to acquire the elementary spectrum of the

121

donor and acceptor proteins. The other three transfected samples, which were transfected with donor and acceptor-tagged plasmids in the donor-to-acceptor ratio of 3:1, 1:1, and 1:3, were used to determine FRET. Different ratios were intentionally selected so that as broad a range of donor-to-acceptor protein ratio as possible is achieved. As discussed below, this leads to broad meta-histograms of $E_{app}$, which are very helpful in analyzing the data.

For each sample type, total 4 µg of plasmids and 5 µl of Lipofectamine® (Invitrogen, Carlsbad, CA) were separately diluted with 250 µl of Opti-MEM® (2 ml; Life Technologies, Carlsbad, CA), and after five minutes the two types of dilution were combined separately for each sample type. After twenty minutes, the combined solutions were added to each sample dish, and the dishes were incubated for ~24 hours in the above-mentioned conditions before they were taken out for imaging.

### 6.1.4 Fluorescence microscopy

A portable incubator (Darwin Chambers Company, St. Louis, MO) was used to transport the samples, at 37°C, from the tissue culture facility to the imaging facility. The microscope was equipped with a temperature-controlled microscope stage, Delta-T temperature-control system (Bioptechs, Inc., Butler, PA), to maintain the temperature of cells at ~37°C throughout the image acquisition process.

Samples were excited by a tunable femtosecond laser (Mai Tai™, Spectra Physics, Santa Clara, CA) and imaged using a two-photon optical microspectroscope, OptiMiS™ TruLine (Aurora Spectral Technologies, Milwaukee, WI), coupled to an inverted microscope (Nikon Eclipse Ti™, Nikon Instruments, Inc., Melville, NY) equipped with a 100× oil-immersion objective (NA=1.45 ). Each sample was line-scanned [11], applying an average power of 350 mW of laser light per line (0.23 mW per excitation voxel), successively at two wavelengths 815 and

960 nm. The image integration time was set to 30 ms per line and a spectral resolution of ~1 nm was used to collect the fluorescence emission.

### 6.1.5 Measurement of fluorescent protein solutions

For fluorescent protein solution measurements, the same type of dishes as described above were coated with 1% bovine serum albumin in PBS (1-hour incubation at 37°C) to prevent binding of the protein molecules to the dish bottom. Fluorescent protein standard solutions of mTq and SYFP2 (stored at −70°C), prepared as mentioned above, were diluted with deionized water, to bring the final concentrations to 5, 10, 20, or 40 mM. These samples were then imaged under the same imaging conditions, as the rhodopsin samples were imaged.

## 6.2 Analysis methods

### 6.2.1 Spectral tags and unmixing

Images from singly expressing samples were used to obtain the elementary spectra of mTQ and sYFP2 as donor and acceptor of energy, respectively, which were used in spectral unmixing as described below.

Pixel-level spectral unmixing of the composite signal was performed using the elementary spectra, quantum yields, and spectral integrals of the donor and acceptor [12] This was performed with the help of a MATLAB routine for unmixing, produced in-house, which is based on the least-squares minimization method, to generate the images of donor emission in presence of the acceptor ($k^{DA}$) and acceptor emission in the presence of donor ($k^{AD}$) ([11, 13] FRET efficiency ($E_{app}$) images were generated by computing the pixel-level FRET from the $k^{DA}$ and $k^{AD}$ images using equation (4.14). Three representative cells are shown in figure 6.1, one cell per row, to illustrate the unmixing process.

123
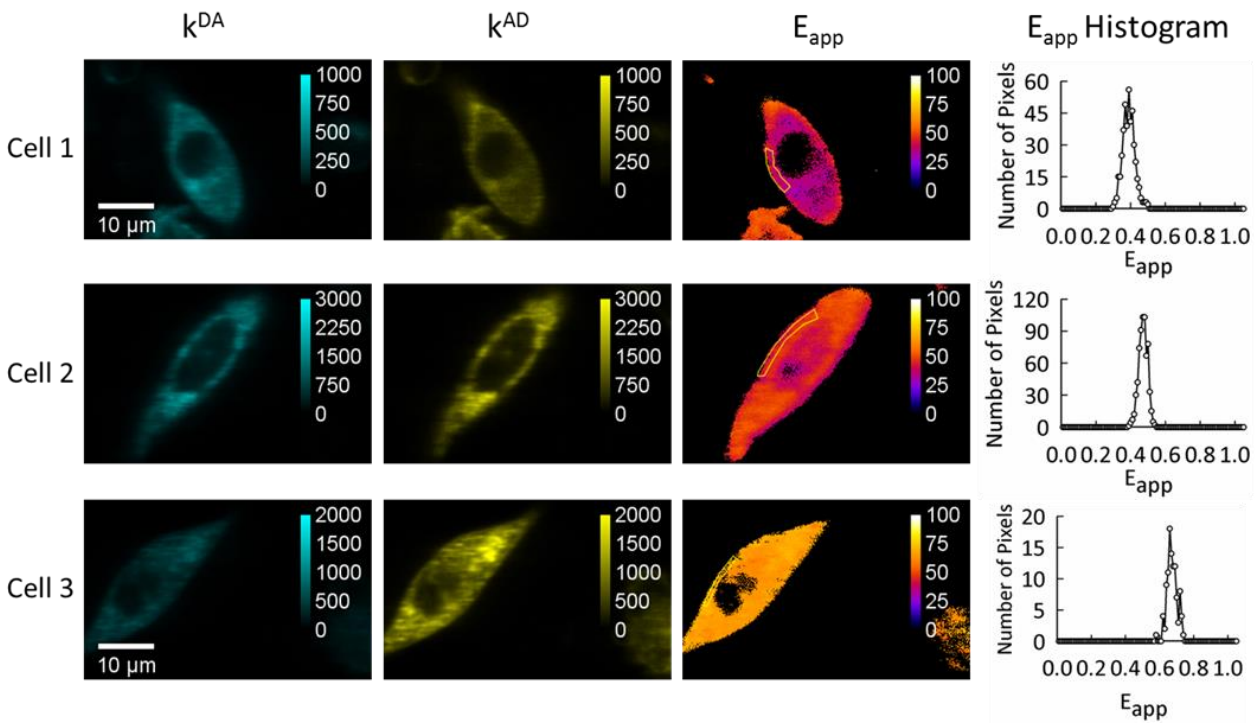
**Figure 6. 1 Spectral Images, FRET efficiency (Eapp) map and Eapp-histograms for three Representative Cell. CHO cells coexpressing m-Turquoise-WT-opsin and m-SYFP2-WT-opsin.** The three columns are the result of the spectral unmixing of the combined signal from donor and acceptor, giving donor in presence of acceptor ($k^{DA}$), acceptor in presence of donor ($k^{AD}$), and the $E_{app}$ distribution computed from the corresponding pixels in $k^{DA}$ and $k^{AD}$ micro-spectrographs, while applying a threshold on the signal-to-noise ratio of 3. The $E_{app}$ pixels for the selected membrane regions as shown in the $E_{app}$ images were binned in the bin interval of 1% of the FRET efficiency, to create $E_{app}$ histograms. This figure is reproduced with permission from [4].

Regions of interests (ROIs) are shown in the $E_{app}$ maps. The $E_{app}$ histograms in the right-most column were computed from ROI's for each cell.

## 6.2.2 $E_{app}$ meta-histogram

For each membrane region selected, a histogram of bin size of 0.01, or 1% of $E_{app}$, was created by binning the pixels of $E_{app}$ image, which fell into the selected region of interest. The tallest peak positions of these histograms were binned in bin size of 0.02, to get the meta-histogram [4, 12-18], as shown in figure 6.2.
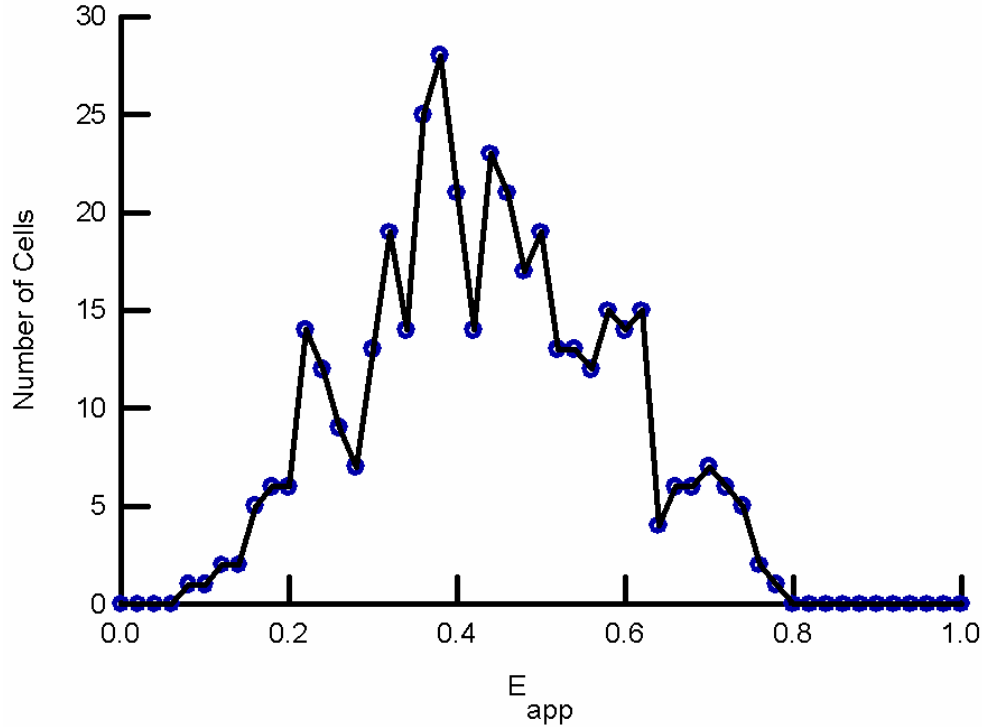
**Figure 6. 2 Meta-histogram of peak positions corresponding to regions of interests obtained from 398 cells.** Peak positions of $E_{app}$ histograms were binned in intervals of 2% of $E_{app}$ to generate the meta-histogram, shown by the open circles. The line The line through the circles is for visualization purpose only.

In order to represent all possible configurations of the donors and acceptors within a multimeric complex, a range of donor to acceptor ratio is required to be present in the samples. To achieve that, we used several samples with different transfection ratios as discussed earlier in this chapter. Effect of the donor to acceptor transfection ratio on meta-histogram is shown in appendix C.

## 6.2.3 Meta-histogram fitted with the theoretical models of Eapp

Several theoretical $E_{app}$ models for different stoichiometry and geometry were fitted into the meta-histogram. Among other models, the model consisting of a mixture of dimers and monomers, which was described and used in the analysis presented in chapter 5, and was the best fitting model for sigma-1 receptors, was also tested. The data fitting to that model is shown in Appendix C.

125

Dimers-only is a special case of the dimers and monomers model, when the alternating peaks of the model have zero amplitudes. Based on the fitting of the dimers and monomers model, the possibility of dimers-only was ruled out.

The best fitting model consisted of a parallelogram tetramer, as shown in figure 6.3. This model is discussed in Appendix A. In short, the meta-histogram was fitted with a set of seven correlated Gaussians prescribed by the parallelogram model. The peak positions of the Gaussian were determined by three independent fitting parameters, namely, pair-wise FRET efficiency ($E_p$), the ratio of the sides of the parallelogram ($r_1/r_2$) and the angle between the two sides ($\alpha$). The amplitudes and standard deviations of the Gaussians were also independent fitting parameters

Also, fittings using a different model, that of a mixture of dimers and monomers, are presented in appendix A.



126
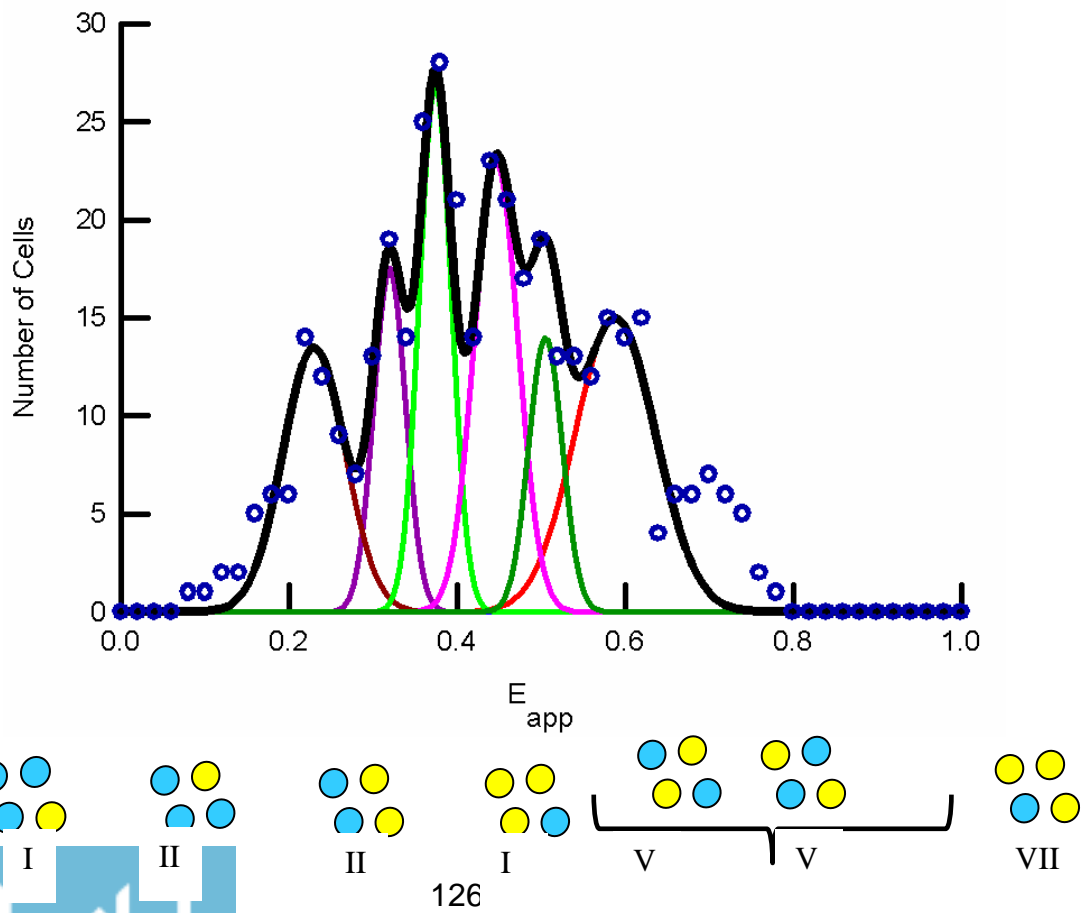
**Figure 6. 3 Metahistogram for regions of interest of the membrane areas of CHO cells expressing rhodopsin, fitted with a parallelogram model.** The values of the FRET efficiency ($E_p$), along with the horizontal side of the tetramer, ratio of the sides ($r_1/r_2$), and the angle between the two sides ($\alpha$) as the geometrical fitting parameters are 0.380, 0.934, and 62.170 respectively. The other fitting parameters are the amplitudes and standard deviations for the Gaussians. The reduced fitting residual for this model is 6.40. The bottom panel of the figure shows the parallelogram configurations, each of which represents a Gaussian in the figure, expect for the peaks five and six, which coincide numerically for the best-fit parameters, thus fitted with a single Gaussian (dark green).

For the best-fit parameters, 6th and 7th peaks numerically coincided, so only one of them is shown in figure 6.3. The reduced fitting residual for the parallelogram model was the lowest among all the models tested, making the parallelogram tetramer the best choice. However, the right-hand-side feature of the meta-histogram could not be fitted with this model. We suggested that the far-right feature of the meta-histogram comes from the presence of higher order oligomer, which is discussed later in this chapter.

### 6.2.4. Reduced fitting residual as a measure of the goodness of fits

Throughout the analysis, we used reduced fitting residuals, e.g., when calculating the fitting residuals for the meta-histogram fittings. The reduced fitting residual is given by:

$$Reduced\ fitting\ residul = \frac{fitting\ residual}{degrees\ of\ freedom}, \tag{6.9}$$

where the degree of freedom was calculated as

$$degrees\ of\ freedom$$
$$= number\ of\ variables - number\ of\ fitting\ parameters. \tag{6.10}$$

The number of fitting parameters is given by the total number of amplitudes and standard deviations for all the Gaussians and other fitting parameters, such as pairwise FRET efficiency ($E_p$ or $E_d$) and the number of donors per pixel $n$.

## 6.2.5 Estimating rhodopsin concentrations

The average fluorescence intensity of several dilutions of the protein solutions was plotted against the protein solution concentration for each of the two, donor and acceptor, fluorescent proteins. Each such graph was best fitted with a straight line. The slope of these lines gave the fluorescence counts per µM of the protein concentration. The slopes for the donor and acceptor protein solutions were used to estimate the concentration of the rhodopsin molecules attached with either type of fluorescent markers in the CHO cell membranes.

## 6.2.6 Average Eapp vs. XA

Although the parallelogram tetramers model best fitted the meta-histogram, the simultaneous presence of dimers and tetramers could not be ruled out. To test whether both dimers and tetramers were present, we used another method of analysis, a statistical ensemble approach based on the average FRET efficiency ($E_{app}$) vs. acceptor molar concentration ($X_A$). The procedure of this analysis is described below.

For each membrane ROI selected, average $E_{app}$ was computed from the average $K^{DA}$ and $K^{AD}$ values. The average values for $K^{DA}$ and $K^{AD}$ were obtained by averaging them over the pixels which fell into each ROI. Average $E_{app}$ values were corrected for direction excitation of acceptors using the images acquired at two wavelengths. Also, average acceptor molar fraction for each ROI was estimated using the following equation

$$X_A = \frac{[A]}{[D] + [A]},$$  (6.11)

where [D] and [A] are the donor and acceptor molar concentrations.

## 6.2.7 E_app vs. X_A fitted with the theoretical models of E_app

Each point of the $E_{app}$ vs. $X_A$ graph was compared with the theoretical value of average $E_{app}$. These theatrical values of $E_{app}$ were calculated by using the experimental $X_A$ and taking the weighted

average of the $E_{app}$ values of the dimers and tetramers of different donor-acceptor configurations, where the weights are the probabilities of each donor-acceptor configuration, which can be determined from the average $X_A$ value of each ROI.

The $E_{app}$ vs. $X_A$ graph is fitted with a theoretical model of the mixture of dimers and parallelogram shape tetramer. The geometry of the tetramer, which was extracted from the metahistogram fits, was fixed for the $E_{app}$ vs. $X_A$ fittings. And the intermolecular distance of the dimers was also fixed and set equal to the length of a side of the tetramer.

The fitting of the $E_{app}$ vs. $X_A$ graph by the dimers-only model are shown in figure 6.4.
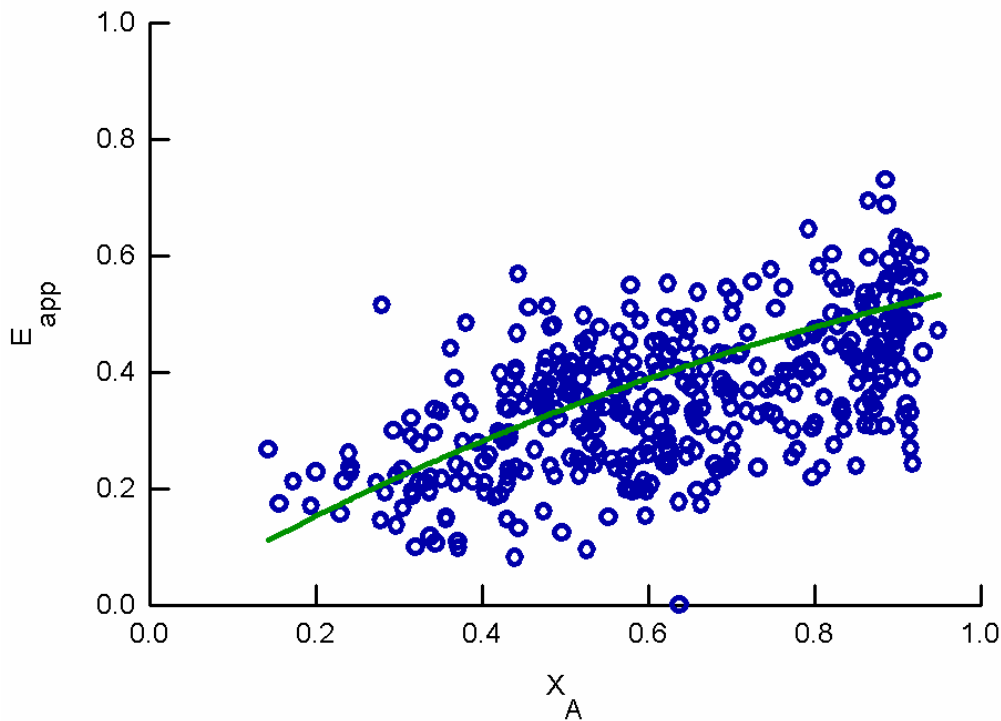


**Figure 6. 4 Average apparent FRET efficiency (Eapp) versus acceptor mole fraction (XA) fitted by Dimer model.** The average $E_{app}$ and $X_A$ were computed from pixel-level FRET efficiencies for plasma membranes of individual CHO cells. Data were fitted with models assuming the presence of only dimers (blue dashed line). The best-fit value of the FRET efficiency for a model consisting of only dimers was 0.550 and the corresponding fitting residual was 2.212.

Also, the $E_{app}$ vs. $X_A$ graph was fitted with a mixture of the dimers and tetramers, for which the fittings are shown in figure 6.5.
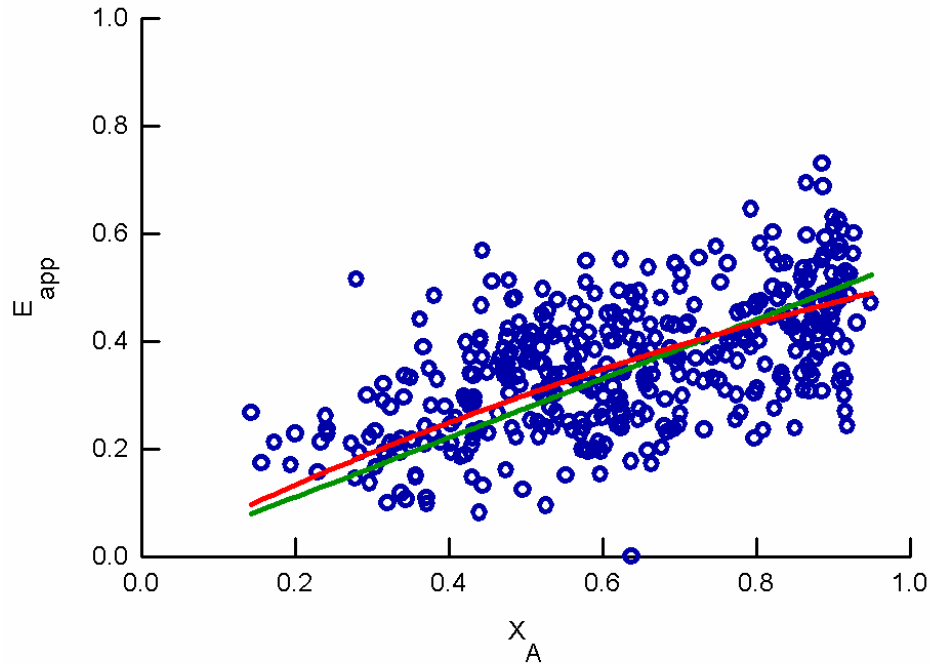


**Figure 6. 5 Average apparent FRET efficiency (Eapp) versus acceptor mole fraction (XA) fitted by a mixture of tetramer and dimer model.** The average $E_{app}$ and $X_A$ were computed from pixel-level FRET efficiencies for plasma membranes of individual CHO cells. Data were fitted with models assuming the presence of only dimers (solid black line) or a mixture of dimers and parallelogram tetramers (solid red line). The best-fit value of the FRET efficiency for a model consisting of only dimers was 0.550 and the corresponding fitting residual was 2.212. When incorporating tetramers to the fitting model, the values of $E_p$, the main parallelogram angle ($\alpha$), and the ratio between the lengths of the sides were fixed to the values obtained from the meta-histogram analysis displayed in figure 6.3. The best-fit value for the tetramer-to-dimer ratio ($\rho$) was 1.47 and the corresponding fitting residual was 2.127.

## 6.2.8 Eapp vs. XA for receptor concentration ranges, fitted with the theoretical models of the mixture of dimers and tetramers

Since $E_{app}$ vs. $X_A$ for all the cells (ROIs) fittings showed the presence of both dimers and tetramers, there would be a dynamic equilibrium of the two species and the ratio of the two population is

130

governed by the Law of Mass Action. Thus, the tetramer to dimer dissociation constant ($K_{t \rightleftharpoons d}$) depends on the total receptor concentration, [A] + [D].

The sum of the differences of the calculated and experimental $E_{app}$ value for each experimental $X_A$ value is the fitting residual, which was minimized for the single fitting parameter- tetramer to dimer ratio ($\rho$), where $\rho$ is given by the following equation

$$\rho = [t]/[d], \tag{6.12}$$

where [t] and [d] are the tetramer and dimer concentrations respectively.

Molecular concentration is a driving force for change in the relative presence of different species in a biochemical reaction. Therefore, in order to perform a study of concentration dependence, we divided the cells into three, four or five concentration ranges, each having about the same number of cells. For each such concentration sub-range, we plotted the $E_{app}$ vs. $X_A$ graph again and fitted them by a mixture of the dimers and parallelogram tetramers. The fittings for the case of four ranges are shown in figure 6.6.
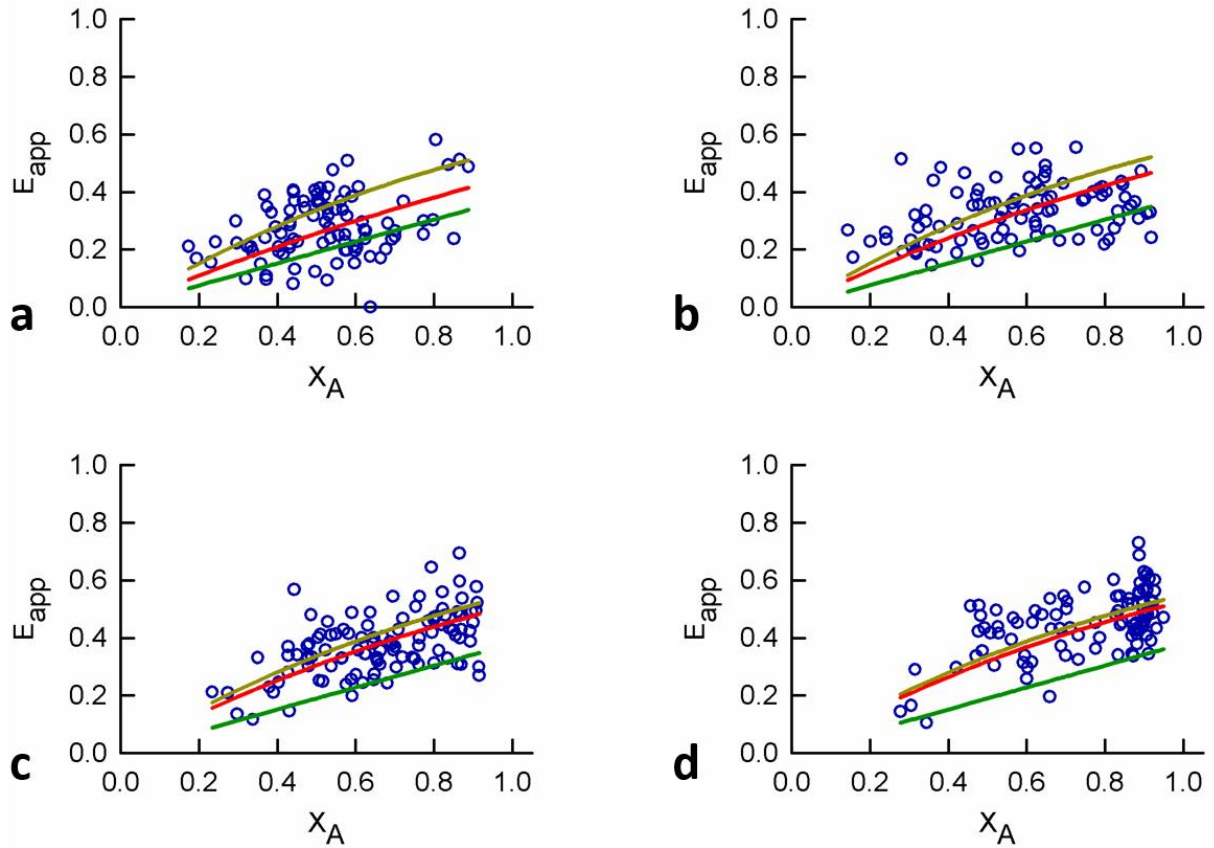
**Figure 6. 6 Average apparent FRET efficiency (Eapp) versus acceptor molar fraction (XA) determined from cells expressing different concentrations of opsin.** Data in Figure 6.5 were split into four subsets according to the concentration of opsin in the plasma membrane of the cell. The ranges of concentrations of opsin represented in each subset are as follows: **(a)** <402 molecules/$\mu m^2$ (average, 227 molecules/$\mu m^2$), **(b)** 402–804 molecules/$\mu m^2$ (average, 591 molecules/$\mu m^2$), **(c)** 804–1607 molecules/$\mu m^2$ (average, 1147 molecules/$\mu m^2$), and **(d)** >1607 molecules/$\mu m^2$ (average, 3400 molecules/$\mu m^2$). The data were fit with a model assuming a mixture of parallelogram-shaped tetramers and dimers (red solid line). The values of $E_p$, the main parallelogram angle ($\alpha$), and the ratio between the lengths of the sides were fixed to the values obtained from the meta-histogram analysis displayed in Figure 6.3. The best-fit values for the tetramer-to-dimer ratios ($\rho$) were: **(a)** 0.401, **(b)** 1.08, **(c)** 1.79, and **(d)** 484. The corresponding fitting residuals were: **(a)** 1.165, **(b)** 1.049, **(c)** 0.937, and **(d)** 0.903. The individual lines corresponding to the dimer component (dotted blue line) and the tetramer component (dashed green line) are also indicated for each concentration range. The first three values of the $\rho$ and their respective error estimates (standard deviations), using bootstrapping method, are $0.40 \pm 0.14$, $1.20 \pm 0.52$ and $1.74 \pm 0.17$.

The only fitting parameters were tetramer to dimer ratio ($\rho$). Using the first two, three or

four concentration ranges for the cases of the three, four and five ranges and their respective values

of $\rho$, we estimated the value of the dissociation constant, which is discussed in the next section.

132

## 6.2.9 Estimating the value of the tetramer to dimer dissociation constant

To recap the $E_{app}$ vs. $X_A$ analysis done so far, we used $\alpha$, $r_1/r_2$ and $E_p$ from the meta-histogram fits to constrain the fit of the $E_{app}$ vs. $X_A$. In order to estimate the change in $\rho$ as a function of concentration, we also separated the average $E_{app}$ vs. $X_A$ plots, as shown in Figure 6.6, and repeated the analysis described above.

We plotted the $\rho$ ratios as a function of the total expression level and we simulated that using the equation below

$$4\rho^2 + 2\rho - \frac{[A] + [D]}{K_{t \to d}} = 0, \qquad (6.3)$$

where, the dissociation constant, $K_{t \to d}$ is defined as

$$K_{t \to d} = \frac{d^2}{t} \qquad (6.4)$$

Tetramer to dimer ratio was plotted against the average concentration of each range for the three, four or five ranges, and a theoretical model built on equation 6.3, was fitted into the first two, three, or four data points, leaving the highest data point out. The highest data point ($\rho$ value) value for each case was way too high which could not be fitted by the same curve which fitted decently the lower concentration $\rho$ values. The fitting for the case of the four ranges, are shown in Figure 6.7.
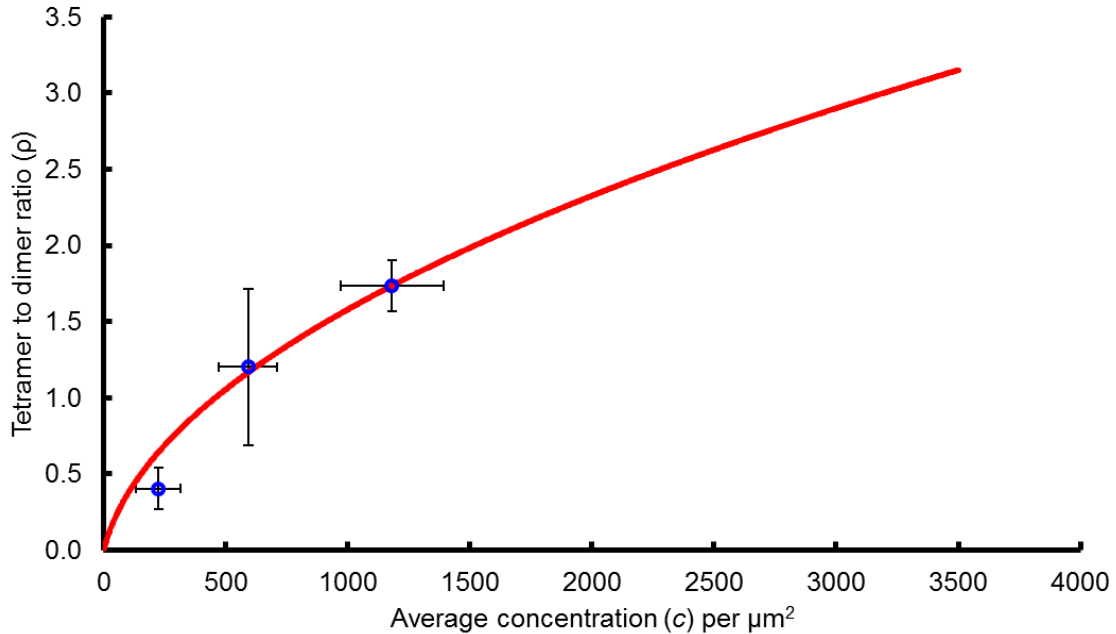
**Figure 6. 7 Tetramer to dimer ratio ($\rho$) vs. average rhodopsin concentration.** The value of $\boldsymbol{\rho}$, extracted from the experiments (open circles), is fitted with a theoretical model for $\boldsymbol{\rho}$. The theoretical model is based on the Law of Mass Action.

To determine which concentration ranges are the best choice, we calculated the error (standard deviation) in estimating the $\rho$ value for each range, by applying bootstrapping method that is randomly resampling the data points with replacement. The bootstrapping method used in this analysis is given, in more details, in Appendix C.

By using errors calculated by the bootstrapping method, we calculated the total reduced Chi-square value for the three, four or five ranges. The lowest value of the reduced Chi-square was 0.45 which came out from the five-ranges of concentration. The value of the dissociation constant for the five ranges was46.50 ± 27.24, which is the most acceptable value of the dissociation constant as extracted from our data by the analysis methods mentioned above.

Values of the reduced Chi-square and the dissociation constant for the other two ranges are given in Appendix C.

134

### 6.2.10 Meta-histogram for the concentration ranges fitted by the parallelogram tetramer

Now, I return to the possible presence of higher order rhodopsin oligomers, which are bigger than tetramer. Since we performed the $E_{app}$ vs. $X_A$ analysis, we decided to do the same for the meta-histogram as well. Therefore, we created meta-histograms for each concentration range, same ranges as used for the $E_{app}$ vs. $X_A$ analysis in the previous section, and fitted them with the parallelogram tetramer model with the same geometrical parameters which were extracted from the fittings of the meta-histogram of all the cells. These fitting are shown in Figure 6.8. To further explain these fittings; we only fitted the amplitudes and standard deviations of the Gaussians, into the meta-histograms for the cells divided by the four concentration ranges, while their peak positions were fixed by the above-mentioned predetermined geometry of the tetramer structure.

As shown in the figure, the right-side features which we hypothesized earlier, evolves as the concentration rises. The features only start showing up from the second highest concentration range, and then it grows bigger for third and the biggest for the fourth and highest concentration level. This trend strongly suggests the presence of bigger than tetrameric quaternary structure at increased concertation levels.
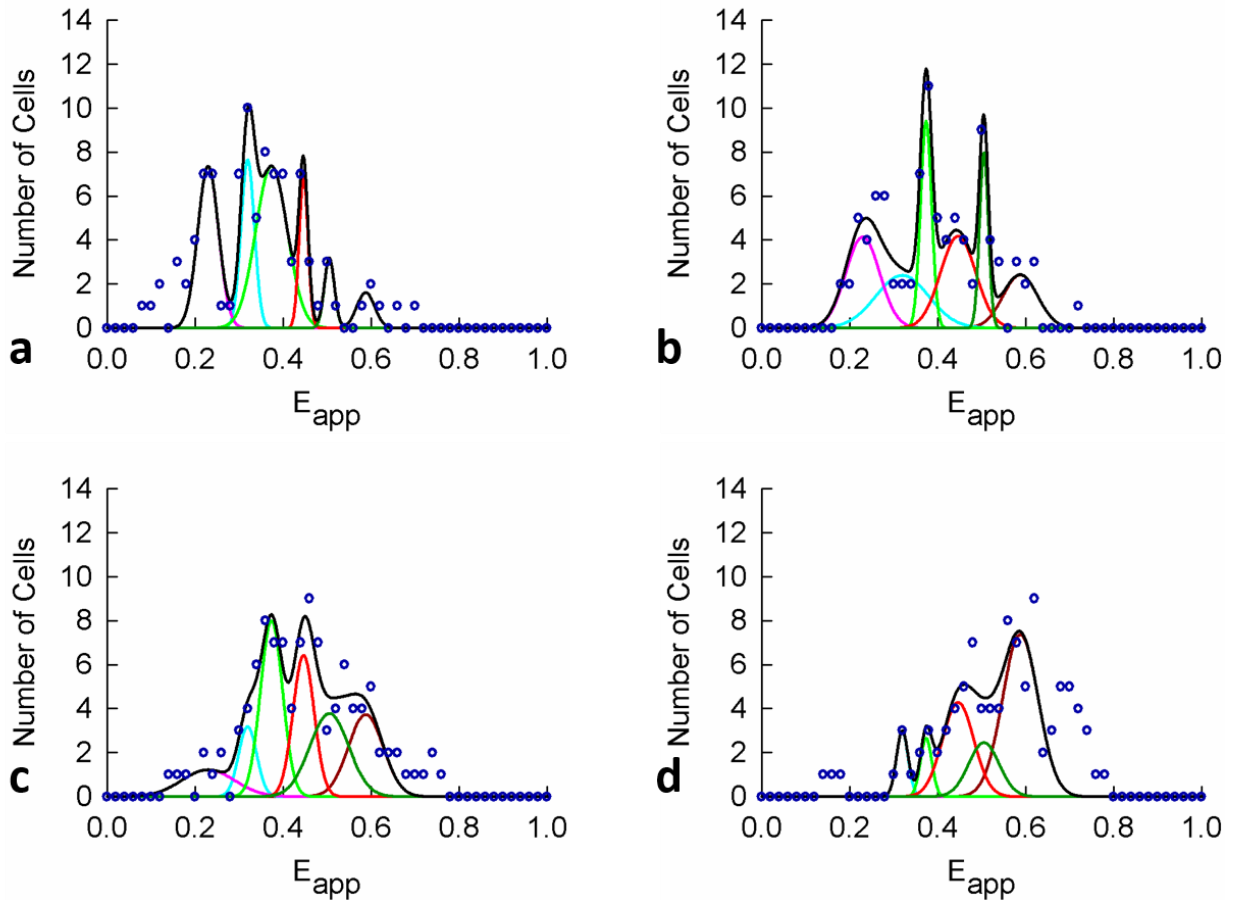
**Figure 6. 8 Meta-histograms for different concentrations of opsin. Data in Figure 6.3 were split into four subsets according to the concentration of opsin in the plasma membrane of the cell.** The range of concentrations of opsin represented in each subset are as follows: (a) less than 400 molecules/$\mu m^2$ (average, ~225 molecules/$\mu m^2$), (b) 400 - 800 molecules/$\mu m^2$ (average, ~600 molecules/$\mu m^2$), (c) 800 – 1600 molecules/$\mu m^2$ (average, ~1150 molecules/$\mu m^2$), and (d) greater than 1650 molecules/$\mu m^2$ (average, ~3400 molecules/$\mu m^2$). The fitting parameters, $E_p$ = 0.380, $\alpha = 62.2^\circ$, and $r_1/r_2 = 0.93$, are the same as those derived from the meta-histogram fit to data from all cells.

And the disproportionally high tetramer to dimer ratio (484 compared to the theoretical prediction of 3.4) for the most concentrated range is likely due to the higher average $E_{app}$ contribution from these larger quaternary structures. Bigger quaternary structures provide on average, more possibilities (resonance energy transfer pathways) for donors to lose energy via FRET, compared to the smaller quaternary structures, giving a higher value for $E_{app}$ for those quaternary structures. In other words, for bigger quaternary structures, a fraction of molecules

136

being inside, to being on the outer sides of the geometry of the quaternary structure is higher, hence donors are likely to see more acceptors nearby.

We explored such bigger structures, and the first such natural choice was hexamer, which can be formed due to the association of a dimer and a tetramer, or three dimers. We systematically drew all the possible configuration of such hexamers, with their mathematical FRET efficiency ($E_{app}$) expressions. These hexamers were created using the same parallelogram geometry as reported earlier in this chapter, and growing it to hexamer, along with the longer side of the tetramer. These expressions are shown in Appendix A

We also calculated the numerical values for the structures bigger than hexamer such as two hexamers vertically stacked to each other, or 12-mer. Some of these numerical values for $E_{app}$, which are higher than 0.70 or 70%, are shown in Figure 6.9.
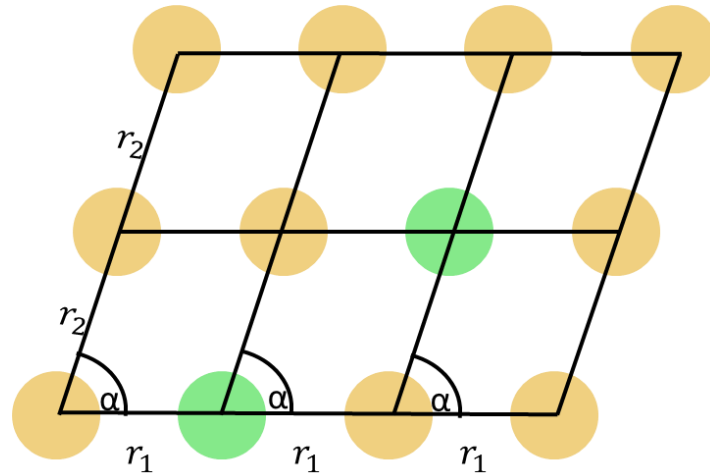


**Figure 6. 9 Schematic of a parallelogram-shaped 12-mer. Green and yellow filled circles represent donors and acceptors respectively.**

Therefore, those higher $E_{app}$ peaks (right-hand-side features) in the meta-histograms can be explained with higher order structures which are founded on the parallelogram structure obtained from the meta-histogram fit.

137

## 6.3 Conclusion and comparing our results with the literature

We conclude based on our spectral FRET study of the rhodopsin oligomerization, that rhodopsin exists as a combination of dimer and tetramer at an average total concentration of 227 molecules/$\mu$m$^2$ and at average concentration of 591 molecules/$\mu$m$^2$, there is a little fraction of molecules start forming higher structures. For concentrations, higher than 804 molecules/$\mu$m$^2$ it may predominately from higher order oligomers, like hexamers, and if two hexamer stack vertically, it may from a 12-mer. We showed the configurations of 12-mer, which can generate higher order FRET efficiencies to support our hypothesis. We show that rhodopsin forms dimers and tetramer at lower concentrations, which is in contrast to some previous studies showing that dimers are stable oligomers or rhodopsin resides only in dimeric form or reporting only monomer-dimer equilibrium.

We also extracted the value of dissociation constant from our concentration dependent study, which was equal to 87 molecules/$\mu$m$^2$. Other studies have also estimated the value of dissociation constant. One study conducted using fluorescent cross-correlation spectroscopy (FCS), in Cos-7 cells, reported the equilibrium dissociation constant of 1010 molecules/$\mu$m$^2$, any other study was done on the GPCR N-formyl peptide estimated the value of equilibrium for 3.6 molecules/$\mu$m$^2$. Both of these studies reported monomer-dimer equilibrium of rhodopsin molecules. In the FCS study, the estimate was indirectly inferred, leaving room for errors. The difference of CHO vs Cos-7 as host cells also may contribute partly to the difference in their estimation from our value of the dissociation constant. In the case of N-formyl peptide, their estimate is consistent with our value when the monomer-dimer equilibrium dissociation constant is projected for that of the dimer-tetramer system.

Rhodopsin forms dimers and tetramers at lower concentrations and may form bigger structures, such as hexamer, 12-mer at higher concentrations. The array of dimers shown by a previous study had used AFM for the disc patches of rod cells, which have much higher receptor (rhodopsin) concentration than what we have reported. Therefore, the AFM study showing larger structure is not inconsistent with our findings, and the concerns regarding experimental artefacts to which the AFM study could have been subjected are unfounded.

# References

[1] M. Chabre, M. le Maire, Monomeric G-protein-coupled receptor as a functional unit, Biochemistry, 44 (2005) 9395-9403.

[2] M. Chabre, R. Cone, H. Saibil, Biophysics: is rhodopsin dimeric in native retinal rods?, Nature, 426 (2003) 30-31.

[3] A.V. Botelho, T. Huber, T.P. Sakmar, M.F. Brown, Curvature and hydrophobic forces drive oligomerization and modulate activity of rhodopsin in membranes, Biophys J, 91 (2006) 4464-4477.

[4] A.K. Mishra, M. Gragg, M. Stoneman, G. Biener, J.A. Oliver, P. Miszta, S. Filipek, V. Raicu, P. Park, Quaternary structures of opsin in live cells revealed by FRET spectrometry, Biochemical Journal, (2016) BCJ20160422.

[5] G.J. Kremers, J. Goedhart, E.B. van Munster, T.W. Gadella, Jr., Cyan and yellow super fluorescent proteins with improved brightness, protein folding, and FRET Forster radius, Biochemistry, 45 (2006) 6570-6580.

[6] J. Goedhart, L. van Weeren, M.A. Hink, N.O.E. Vischer, K. Jalink, T.W.J. Gadella, Bright cyan fluorescent protein variants identified by fluorescence lifetime screening, Nat Meth, 7 (2010) 137-139.

[7] L.M. Miller, M. Gragg, T.G. Kim, P.S.-H. Park, Misfolded opsin mutants display elevated β-sheet structure, FEBS letters, 589 (2015) 3119-3125.

[8] M. Gragg, T.G. Kim, S. Howell, P.-H. Park, Wild-type opsin does not aggregate with a misfolded opsin mutant, Biochimica et Biophysica Acta (BBA)-Biomembranes, 1858 (2016) 1850-1859.

[9] S. Ferré, The GPCR heterotetramer: challenging classical pharmacology, Trends in pharmacological sciences, 36 (2015) 145-152.

[10] G. Milligan, The Prevalence, Maintenance, and Relevance of G Protein-Coupled Receptor Oligomerization, Molecular pharmacology, 84 (2013) 158-169.

[11] G. Biener, M.R. Stoneman, G. Acbas, J.D. Holz, M. Orlova, L. Komarova, S. Kuchin, V. Raicu, Development and experimental testing of an optical micro-spectroscopic technique

incorporating true line-scan excitation, International journal of molecular sciences, 15 (2014) 261-276.

[12] A.K. Mishra, T. Mavlyutov, D.R. Singh, G. Biener, J. Yang, J.A. Oliver, A. Ruoho, V. Raicu, The sigma-1 receptors are present in monomeric and oligomeric forms in living cells in the presence and absence of ligands, Biochem J, 466 (2015) 263-271.

[13] S. Patowary, Luca F. Pisterzi, G. Biener, Jessica D. Holz, Julie A. Oliver, James W. Wells, V. Raicu, Experimental Verification of the Kinetic Theory of FRET Using Optical Microspectroscopy and Obligate Oligomers, Biophysical Journal, 108 (2015) 1613-1622.

[14] D.R. Singh, M.M. Mohammad, S. Patowary, M.R. Stoneman, J.A. Oliver, L. Movileanu, V. Raicu, Determination of the Quaternary Structure of a Bacterial ATP-Binding Cassette (ABC) Transporter in Living Cells, Integrative biology : quantitative biosciences from nano to macro, 5 (2013) 312-323.

[15] V. Raicu, D.R. Singh, FRET spectrometry: a new tool for the determination of protein quaternary structure in living cells, Biophys J, 105 (2013) 1937-1945.

[16] S. Patowary, Protein Association in Living Cells Using Fret Spectrometry: Application to G-Protein Coupled Receptors, in: Physics, vol. Ph.D., University of Wisconsin Milwaukee (UWM) 2013.

[17] S. Patowary, E. Alvarez-Curto, T.R. Xu, J.D. Holz, J.A. Oliver, G. Milligan, V. Raicu, The muscarinic M3 acetylcholine receptor exists as two differently sized complexes at the plasma membrane, Biochem J, 452 (2013) 303-312.

[18] A.K. Mishra, M. Gragg, M.R. Stoneman, G. Biener, J.A. Oliver, P. Miszta, S. Filipek, V. Raicu, P.S.-H. Park, Quaternary structures of opsin in live cells revealed by FRET spectrometry, Biochemical Journal, 473 (2016) 3819-3836.

# Chapter 7: Conclusion and Directions for Future Research

The purpose of this thesis work was to investigate the quaternary structure of membrane receptors in living cells. *Membrane receptors* transfer information from the environment to the cell's interior [1-3]. Quaternary structure of the membrane receptors is highly researched yet rather controversial [4-8]. I addressed this issue using fluorescent tags and FRET spectrometry for two such receptors: (i) Sigma-1 receptors and (ii) Rhodopsin.

In the Sigma-1 receptor (S1R) project, we used S1R-GFP$_2$ and S1R-YFP plasmids, and expressed them in Cos-7 cells. We conducted FRET spectroscopy measurements on these cells, in the presence and absence of haloperidol and pentazocine plus.

We used two different approaches to analyze the FRET data, one involving meta-histograms of apparent FRET efficiencies ($E_{app}$) and the other used plots of average $E_{app}$ vs. donor concentration ($N_D$). For the metahistogram approach, we found two different models giving good visual fittings, which were a parallelogram tetramer and a mixture of dimers and monomers. However, the dimers and monomers model gave about 50% lower fitting residual, making it a better choice. We extracted a value for the most-probable number of donors per pixel ($n$) from the metahistogram fittings, which was equal to 8 donors/pixel. Using the $E_{app}$ vs. $N_D$ analysis method, we confirmed that S1R forms a mixture of dimers and monomers at low donor expressions for each case, i.e., in the absence and presence of the drugs. However, at higher donor expression levels, S1R alone and those in the presence of haloperidol, showed at wide spread of $E_{app}$ values, indicating the presence of higher order oligomers, which actually increased in proportion in the presence of haloperidol. In contrast, S1R in the presence of pentazocine-plus mostly appeared to stabilize the quaternary structure in the dimers-monomers form.

All experiments involving S1Rs relied on a single excitation wavelength, which excited the donors only. In the future, experiments could be conducted where S1R can be imaged following two different excitation wavelengths. That will enable one to calculate both donor and acceptor concentrations, from which the total receptor concentrations could be obtained. With that information, analysis of $E_{app}$ vs. the molar acceptor fraction ($X_A$) can be performed, similar to what we did as part of the rhodopsin project, summarized below. By dividing the total concatenation range into sub-ranges, we may be able to determine at what receptor concentration higher oligomers start to form, both in the absence or presence of ligands.

For the rhodopsin project, we expressed the wild-type rhodopsin at body temperature, in Chinese Hamster Ovary (CHO) cells which are a very competent medium for expression of wild type rhodopsin, and used the method of FRET spectrometry[9-19], to determine the quaternary structure of wild type rhodopsin at room temperature. In contrast to the model proposed by Fotiadis et al.[20], we observed that the wild type rhodopsin forms a mixture or dimers and tetramers in CHO cells at body temperature and that the oligomeric state of wild type rhodopsin is dynamic. We performed the concentration dependent study and extracted tetramer to dimer dissociation constant. We compared our value of the constant to those available in the literature.

Besides, we detected the presence of the higher order oligomers at higher rhodopsin concentrations. We used two methods for detecting the higher order oligomers; one method is based on the $E_{app}$ histogram peaks, and other involves average cellular $E_{app}$ dependence on acceptor molar concentration $X_A$. Our findings were consistent for both analysis methods.

More work needs to be done in the future. For instance, one could assess whether rhodopsin with G188R mutation forms oligomers in living cells. If the quaternary structure of the mutants is

143

found different than the wild-type, then this will allow one to find correlations between the protein misfolding and its quaternary structure [21, 22].

Our purpose of maintaining the body temperature for wild-type rhodopsin experiments was to avoid the possibility that phase separation can drive oligomerization [4, 23, 24]. However, it would be also interesting to investigate the effect of temperature on oligomerization. By performing a temperature-dependence study using the same experiential design and analysis methods, it can be further demonstrated that the temperature does not have any effect on the wildtype rhodopsin oligomerization.

In summary, the primary contributions of my doctoral research to this field are in the area of theoretical modeling and experimental method development. Specifically,

1.  I extended the FRET tetramer model to include arbitrary side lengths and angles between sides, and

2.  Developed a methodology for concentration-dependent study of macromolecules oligomerization states, relying on two wavelength excitations.

Using these advances, I was able to discover that:

3.  The quaternary structure of the sigma-1 receptors is affected by binding of agonist and antagonist ligands;

4.  The prototypical GPCR rhodopsin forms dimers, which upon increasing the concentration may associate to form tetramers as well as higher order oligomers.

5.  This allowed me to estimate the numerical value for tetramer-to-dimer dissociation constant of rhodopsin in living cells.

# References

[1] J.M. Berg, J.L. Tymoczko, L. Stryer, Biochemistry, The Citric Acid Cycle, 5 (2006).

[2] H. Lodish, Molecular cell biology, Macmillan, 2008.

[3] J.E. Hall, Guyton and Hall textbook of medical physiology, Elsevier Health Sciences, 2015.

[4] M. Chabre, R. Cone, H. Saibil, Biophysics: is rhodopsin dimeric in native retinal rods?, Nature, 426 (2003) 30-31.

[5] M. Chabre, M. le Maire, Monomeric G-protein-coupled receptor as a functional unit, Biochemistry, 44 (2005) 9395-9403.

[6] K. Palczewski, T. Kumasaka, T. Hori, C.A. Behnke, H. Motoshima, B.A. Fox, I. Le Trong, D.C. Teller, T. Okada, R.E. Stenkamp, M. Yamamoto, M. Miyano, Crystal structure of rhodopsin: A G protein-coupled receptor, Science (New York, N.Y.), 289 (2000) 739-745.

[7] D. Fotiadis, Y. Liang, S. Filipek, D.A. Saperstein, A. Engel, K. Palczewski, The G protein-coupled receptor rhodopsin in the native membrane, FEBS letters, 564 (2004) 281-288.

[8] D. Fotiadis, Y. Liang, S. Filipek, D.A. Saperstein, A. Engel, K. Palczewski, The G protein-coupled receptor rhodopsin in the native membrane, FEBS letters, 564 (2004) 281-288.

[9] D.R. Singh, Mohammad, M.M., Patowary, S., Stoneman, M.R., Oliver, J.A., Movileanu, L., and Raicu, V., Determination of the Quaternary Structure of a Bacterial ATP-Binding Cassette (ABC) Transporter in Living Cells, J Biol Chem, Submitted (2012).

[10] D.R. Singh, V. Raicu, Comparison between whole distribution- and average-based approaches to the determination of fluorescence resonance energy transfer efficiency in ensembles of proteins in living cells, Biophysics (2010).

[11] D.R. Singh, V. Raicu, Comparison between Whole Distribution- and Average-Based Approaches to the Determination of Fluorescence Resonance Energy Transfer Efficiency in Ensembles of Proteins in Living Cells, Biophysical Journal, 98 (2010) 2127-2135.

[12] V. Raicu, M.R. Stoneman, R. Fung, M. Melnichuk, D.B. Jansma, L.F. Pisterzi, S. Rath, M. Fox, J.W. Wells, D.K. Saldin, Determination of supramolecular structure and spatial distribution of protein complexes in living cells, Nat Photon, 3 (2009) 107-113.

[13] D.R. Singh, M.M. Mohammad, S. Patowary, M.R. Stoneman, J.A. Oliver, L. Movileanu, V. Raicu, Determination of the Quaternary Structure of a Bacterial ATP-Binding Cassette (ABC) Transporter in Living Cells, Integrative biology : quantitative biosciences from nano to macro, 5 (2013) 312-323.

[14] G. Biener, M.R. Stoneman, G. Acbas, J.D. Holz, M. Orlova, L. Komarova, S. Kuchin, V. Raicu, Development and experimental testing of an optical micro-spectroscopic technique incorporating true line-scan excitation, International journal of molecular sciences, 15 (2014) 261-276.

[15] V. Raicu, D.R. Singh, FRET spectrometry: a new tool for the determination of protein quaternary structure in living cells, Biophys J, 105 (2013) 1937-1945.

[16] S. Patowary, E. Alvarez-Curto, T.R. Xu, J.D. Holz, J.A. Oliver, G. Milligan, V. Raicu, The muscarinic M3 acetylcholine receptor exists as two differently sized complexes at the plasma membrane, Biochem J, 452 (2013) 303-312.

[17] M.G. Gustafsson, L. Shao, P.M. Carlton, C.R. Wang, I.N. Golubovskaya, W.Z. Cande, D.A. Agard, J.W. Sedat, Three-dimensional resolution doubling in wide-field fluorescence microscopy by structured illumination, Biophysical journal, 94 (2008) 4957-4970.

[18] A.K. Mishra, M. Gragg, M. Stoneman, G. Biener, J.A. Oliver, P. Miszta, S. Filipek, V. Raicu, P. Park, Quaternary structures of opsin in live cells revealed by FRET spectrometry, Biochemical Journal, (2016) BCJ20160422.

[19] A.K. Mishra, T. Mavlyutov, D.R. Singh, G. Biener, J. Yang, J.A. Oliver, A. Ruoho, V. Raicu, The sigma-1 receptors are present in monomeric and oligomeric forms in living cells in the presence and absence of ligands, Biochem J, 466 (2015) 263-271.

[20] D. Fotiadis, B. Jastrzebska, A. Philippsen, D.J. Muller, K. Palczewski, A. Engel, Structure of the rhodopsin dimer: a working model for G-protein-coupled receptors, Current opinion in structural biology, 16 (2006) 252-259.

[21] P. Garriga, X. Liu, H.G. Khorana, Structure and function in rhodopsin: correct folding and misfolding in point mutants at and in proximity to the site of the retinitis pigmentosa mutation Leu-125--> Arg in the transmembrane helix C, Proceedings of the National Academy of Sciences, 93 (1996) 4560-4564.

[22] X. Liu, P. Garriga, H.G. Khorana, Structure and function in rhodopsin: correct folding and misfolding in two point mutants in the intradiscal domain of rhodopsin identified in retinitis pigmentosa, Proceedings of the National Academy of Sciences, 93 (1996) 4554-4559.

[23] A. Kusumi, J.S. Hyde, Spin-label saturation-transfer electron spin resonance detection of transient association of rhodopsin in reconstituted membranes, Biochemistry, 21 (1982) 5978-5983.

[24] P. Li, S. Banjade, H.-C. Cheng, S. Kim, B. Chen, L. Guo, M. Llaguno, J.V. Hollingsworth, D.S. King, S.F. Banani, Phase transitions in the assembly of multivalent signalling proteins, Nature, 483 (2012) 336-340.

# Appendix A

## A-1 Theoretical FRET efficiency models for a parallelogram hexamer

Extending the parallelogram tetramer structure to a parallelogram hexamer, we get 64 different

configurations. However, almost half of them have mirror images of the others. Thus leaving 32

Eapp expresssions, which are tabulated in table 2.2. Also, two simplyfy these eqautions, we left

out the insignificant  terms out the insignificant terms of the Eapp expressions in table 2.2, which

gives as another Table 2.3, shown right ater Table 2.2.

**Table A-1.  Parallelogram hexamer configurations, and their FRET efficiencies.**

| figuration # | Geometric Configurations | FRET Efficiency Per Donor |
|:---:|:---:|:---:|
| 1. |  | $0$ |
| 2. |  | |
| 3. |  | $\dfrac{E_1\left(\dfrac{r_1}{r_{d3}}\right)^6}{1-E_1+E_1\left(\dfrac{r_1}{r_{d3}}\right)^6},\dfrac{E_1\left(\dfrac{r_1}{r_{d1}}\right)^6}{1-E_1+E_1\left[\left(\dfrac{r_1}{r_{d1}}\right)^6\right]},E_1,\dfrac{E_1\left(\dfrac{r_1}{r_2}\right)^6}{1-E_1+E_1\left[\left(\dfrac{r_1}{r_2}\right)^6\right]},\dfrac{E_1\left(\dfrac{1}{2}\right)^6}{1-E_1+E_1\left[\left(\dfrac{1}{2}\right)^6\right]}$ |
| 4. |  | |
| 5. |  | $\dfrac{E_1\left(\dfrac{r_1}{r_{d1}}\right)^6}{1-E_1+E_1\left[\left(\dfrac{r_1}{r_{d1}}\right)^6\right]},E_1,\dfrac{E_1\left(\dfrac{r_1}{r_{d2}}\right)^6}{1-E_1+E_1\left[\left(\dfrac{r_1}{r_{d2}}\right)^6\right]},\dfrac{E_1\left(\dfrac{r_1}{r_2}\right)^6}{1-E_1+E_1\left[\left(\dfrac{r_1}{r_2}\right)^6\right]},$ $\dfrac{E_1\left(\dfrac{r_1}{r_2}\right)^6}{1-E_1+E_1\left[\left(\dfrac{r_1}{r_2}\right)^6\right]}$ |
| 6. |  | |
| 7. |  | $E_1,\dfrac{E_1\left(\dfrac{r_1}{r_{d1}}\right)^6}{1-E_1+E_1\left[\left(\dfrac{r_1}{r_{d1}}\right)^6\right]},\dfrac{E_1\left(\dfrac{r_1}{r_{d3}}\right)^6}{1-E_1+E_1\left[\left(\dfrac{r_1}{r_{d3}}\right)^6\right]},\dfrac{E_1\left(\dfrac{1}{2}\right)^6}{1-E_1+E_1\left[\left(\dfrac{1}{2}\right)^6\right]},$ $\dfrac{E_1\left(\dfrac{r_1}{r_2}\right)^6}{1-E_1+E_1\left[\left(\dfrac{r_1}{r_2}\right)^6\right]}$ |

150

| 8. |  | $$\frac{E_1\left[\left(\frac{r_1}{r_{d1}}\right)^6 + \left(\frac{r_1}{r_2}\right)^6\right]}{1 - E_1 + E_1\left[\left(\frac{r_1}{r_{d1}}\right)^6 + \left(\frac{r_1}{r_2}\right)^6\right]}, \frac{E_1\left[1 + \left(\frac{1}{2}\right)^6\right]}{1 + E_1\left(\frac{1}{2}\right)^6},$$ $$\frac{E_1\left[\left(\frac{r_1}{r_{d1}}\right)^6 + \left(\frac{r_1}{r_2}\right)^6\right]}{1 - E_1 + E_1\left[\left(\frac{r_1}{r_{d1}}\right)^6 + \left(\frac{r_1}{r_2}\right)^6\right]}, \frac{E_1\left[1 + \left(\frac{1}{2}\right)^6\right]}{1 + E_1\left(\frac{1}{2}\right)^6}$$ |
| 9. |  | $$\frac{E_1\left[\left(\frac{1}{2}\right)^6 + 1\right]}{1 + E_1\left(\frac{1}{2}\right)^6}, \frac{E_1\left[\left(\frac{r_1}{r_2}\right)^6 + \left(\frac{r_1}{r_{d2}}\right)^6\right]}{1 - E_1 + E_1\left[\left(\frac{r_1}{r_2}\right)^6 + \left(\frac{r_1}{r_{d2}}\right)^6\right]},$$ $$\frac{E_1\left[\left(\frac{1}{2}\right)^6 + 1\right]}{1 + E_1\left(\frac{1}{2}\right)^6}, \frac{E_1\left[\left(\frac{r_1}{r_2}\right)^6 + \left(\frac{r_1}{r_{d2}}\right)^6\right]}{1 - E_1 + E_1\left[\left(\frac{r_1}{r_2}\right)^6 + \left(\frac{r_1}{r_{d2}}\right)^6\right]}$$ |
| 10. |  | $$\frac{E_1\left[\left(\frac{r_1}{r_{d3}}\right)^6 + \left(\frac{r_1}{r_{d1}}\right)^6\right]}{1 - E_1 + E_1\left[\left(\frac{r_1}{r_{d3}}\right)^6 + \left(\frac{r_1}{r_{d1}}\right)^6\right]}, \frac{E_1\left[\left(\frac{r_1}{r_{d1}}\right)^6 + 1\right]}{1 + E_1\left(\frac{r_1}{r_{d1}}\right)^6}, \frac{E_1\left[1 + \left(\frac{r_1}{r_{d2}}\right)^6\right]}{1 + E_1\left(\frac{r_1}{r_{d2}}\right)^6},$$ |
| 11. |  | $$\frac{E_1\left[\left(\frac{1}{2}\right)^6 + \left(\frac{r_1}{r_2}\right)^6\right]}{1 - E_1 + E_1\left[\left(\frac{1}{2}\right)^6 + \left(\frac{r_1}{r_2}\right)^6\right]}$$ |
| 12. |  | $$\frac{E_1\left[\left(\frac{r_1}{r_2}\right)^6 + \left(\frac{r_1}{r_{d3}}\right)^6\right]}{1 - E_1 + E_1\left[\left(\frac{r_1}{r_2}\right)^6 + \left(\frac{r_1}{r_{d3}}\right)^6\right]}, \frac{E_1\left[1 + \left(\frac{r_1}{r_2}\right)^6\right]}{1 - E_1 + E_1\left(\frac{r_1}{r_2}\right)^6},$$ |
| 13. |  | $$\frac{E_1\left[1 + \left(\frac{r_1}{r_2}\right)^6\right]}{1 + E_1\left(\frac{r_1}{r_2}\right)^6}, \frac{E_1\left[\left(\frac{r_1}{r_{d2}}\right)^6 + \left(\frac{1}{2}\right)^6\right]}{1 - E_1 + E_1\left[\left(\frac{r_1}{r_{d2}}\right)^6 + \left(\frac{1}{2}\right)^6\right]}$$ |

| # | | |
|---|---|---|
| 14. | | $$\frac{E_1\left[\left(\frac{1}{2}\right)^6 + \left(\frac{r_1}{r_{d2}}\right)^6\right]}{1 - E_1 + E_1\left[\left(\frac{1}{2}\right)^6 + \left(\frac{r_1}{r_{d2}}\right)^6\right]}, \frac{E_1\left[\left(\frac{r_1}{r_2}\right)^6 + 1\right]}{1 + E_1\left(\frac{r_1}{r_2}\right)^6},$$ |
| 15. | | $$\frac{E_1\left[\left(\frac{r_1}{r_2}\right)^6 + 1\right]}{1 + E_1\left(\frac{r_1}{r_2}\right)^6}, \frac{E_1\left[\left(\frac{r_1}{r_{d4}}\right)^6 + \left(\frac{r_1}{r_2}\right)^6\right]}{1 - E_1 + E_1\left[\left(\frac{r_1}{r_{d4}}\right)^6 + \left(\frac{r_1}{r_2}\right)^6\right]}$$ |
| 16. | | $$\frac{E_1\left[\left(\frac{r_1}{r_{d1}}\right)^6 + 1\right]}{1 + E_1\left(\frac{r_1}{r_{d2}}\right)^6}, \frac{E_1\left[1 + \left(\frac{r_1}{r_{d2}}\right)^6\right]}{1 + E_1\left(\frac{r_1}{r_{d2}}\right)^6}, \frac{E_1\left[\left(\frac{r_1}{r_{d2}}\right)^6 + \left(\frac{r_1}{r_{d4}}\right)^6\right]}{1 - E_1 + E_1\left[\left(\frac{r_1}{r_{d2}}\right)^6 + \left(\frac{r_1}{r_{d4}}\right)^6\right]},$$ |
| 17. | | $$\frac{E_1\left[\left(\frac{r_1}{r_2}\right)^6 + \left(\frac{1}{2}\right)^6\right]}{1 - E_1 + E_1\left[\left(\frac{r_1}{r_2}\right)^6 + \left(\frac{1}{2}\right)^6\right]},$$ |
| 18. | | $$\frac{E_1\left[\left(\frac{r_1}{r_{d4}}\right)^6 + 1\right]}{1 + E_1\left(\frac{r_1}{r_{d4}}\right)^6}, \frac{E_1\left[\left(\frac{r_1}{r_{d1}}\right)^6 + \left(\frac{r_1}{r_{d2}}\right)^6\right]}{1 - E_1 + E_1\left[\left(\frac{r_1}{r_{d1}}\right)^6 + \left(\frac{r_1}{r_{d2}}\right)^6\right]},$$ |
| 19. | | $$\frac{E_1\left[1 + \left(\frac{r_1}{r_{d3}}\right)^6\right]}{1 + E_1\left(\frac{r_1}{r_{d3}}\right)^6}, \frac{E_1\left[\left(\frac{r_1}{r_2}\right)^6 + \left(\frac{r_1}{r_2}\right)^6\right]}{1 - E_1 + E_1\left[\left(\frac{r_1}{r_2}\right)^6 + \left(\frac{r_1}{r_2}\right)^6\right]}$$ |
| 20. | | $$\frac{E_1\left[\left(\frac{1}{2}\right)^6 + \left(\frac{r_1}{r_{d3}}\right)^6\right]}{1 - E_1 + E_1\left[\left(\frac{1}{2}\right)^6 + \left(\frac{r_1}{r_{d3}}\right)^6\right]}, \frac{E_1\left[\left(\frac{r_1}{r_2}\right)^6 + \left(\frac{r_1}{r_{d1}}\right)^6\right]}{1 - E_1 + E_1\left[\left(\frac{r_1}{r_2}\right)^6 + \left(\frac{r_1}{r_{d1}}\right)^6\right]},$$ |
| 21. | | $$\frac{E_1\left[\left(\frac{r_1}{r_{d2}}\right)^6 + \left(\frac{r_1}{r_2}\right)^6\right]}{1 - E_1 + E_1\left[\left(\frac{r_1}{r_{d2}}\right)^6 + \left(\frac{r_1}{r_2}\right)^6\right]}, \frac{E_1\left[\left(\frac{r_1}{r_{d4}}\right)^6 + \left(\frac{1}{2}\right)^6\right]}{1 - E_1 + E_1\left[\left(\frac{r_1}{r_{d4}}\right)^6 + \left(\frac{1}{2}\right)^6\right]}$$ |

| | | |
|---|---|---|
| 22. |  | $$\frac{E_1\left[\left(\frac{r_1}{r_2}\right)^6+\left(\frac{r_1}{r_{d1}}\right)^6\right]}{1-E_1+E_1\left[\left(\frac{r_1}{r_2}\right)^6+\left(\frac{r_1}{r_{d1}}\right)^6\right]},\frac{E_1\left[\left(\frac{r_1}{r_{d2}}\right)^6+\left(\frac{r_1}{r_2}\right)^6\right]}{1-E_1+E_1\left[\left(\frac{r_1}{r_{d2}}\right)^6+\left(\frac{r_1}{r_2}\right)^6\right]},$$ $$\frac{E_1\left[\left(\frac{r_1}{r_{d1}}\right)^6+\left(\frac{r_1}{r_2}\right)^6\right]}{1-E_1+E_1\left[\left(\frac{r_1}{r_{d1}}\right)^6+\left(\frac{r_1}{r_2}\right)^6\right]},\frac{E_1\left[\left(\frac{r_1}{r_{d2}}\right)^6+\left(\frac{r_1}{r_2}\right)^6\right]}{1-E_1+E_1\left[\left(\frac{r_1}{r_{d2}}\right)^6+\left(\frac{r_1}{r_2}\right)^6\right]}$$ |
| 23. |  | $$\frac{E_1\left[\left(\frac{r_1}{r_{d1}}\right)^6+1+\left(\frac{r_1}{r_2}\right)^6\right]}{1+E_1\left[\left(\frac{r_1}{r_{d1}}\right)^6+\left(\frac{r_1}{r_2}\right)^6\right]},\frac{E_1\left[1+\left(\frac{r_1}{r_{d2}}\right)^6+\left(\frac{1}{2}\right)^6\right]}{1+E_1\left[\left(\frac{r_1}{r_{d2}}\right)^6+\left(\frac{1}{2}\right)^6\right]},\frac{E_1\left[1+\left(\frac{1}{2}\right)^6+\left(\frac{r_1}{r_2}\right)^6\right]}{1+E_1\left[\left(\frac{1}{2}\right)^6+\left(\frac{r_1}{r_2}\right)^6\right]}$$ |
| 24. |  | |
| 25. |  | $$\frac{E_1\left[\left(\frac{r_1}{r_{d3}}\right)^6+\left(\frac{r_1}{r_{d1}}\right)^6+1\right]}{1+E_1\left[\left(\frac{r_1}{r_{d3}}\right)^6+\left(\frac{r_1}{r_{d1}}\right)^6\right]},\frac{E_1\left[\left(\frac{r_1}{r_{d1}}\right)^6+1+\left(\frac{r_1}{r_{d2}}\right)^6\right]}{1+E_1\left[\left(\frac{r_1}{r_{d1}}\right)^6+\left(\frac{r_1}{r_{d2}}\right)^6\right]},\frac{E_1\left[1+\left(\frac{r_1}{r_{d2}}\right)^6+\left(\frac{r_1}{r_{d4}}\right)^6\right]}{1+E_1\left[\left(\frac{r_1}{r_{d2}}\right)^6+\left(\frac{r_1}{r_{d4}}\right)^6\right]}$$ |
| 26. |  | |
| 27. |  | $$\frac{E_1\left[\left(\frac{r_1}{r_{d1}}\right)^6+1+\left(\frac{r_1}{r_2}\right)^6\right]}{1+E_1\left[\left(\frac{r_1}{r_{d1}}\right)^6+\left(\frac{r_1}{r_2}\right)^6\right]},\frac{E_1\left[1+\left(\frac{r_1}{r_{d2}}\right)^6+\left(\frac{1}{2}\right)^6\right]}{1+E_1\left[\left(\frac{r_1}{r_{d2}}\right)^6+\left(\frac{1}{2}\right)^6\right]},\frac{E_1\left[1+\left(\frac{1}{2}\right)^6+\left(\frac{r_1}{r_2}\right)^6\right]}{1+E_1\left[\left(\frac{1}{2}\right)^6+\left(\frac{r_1}{r_2}\right)^6\right]}$$ |
| 28. |  | |
| 29. |  | |

| 30. |  | $$\frac{E_1\left[\left(\frac{1}{2}\right)^6+\left(\frac{r_1}{r_{d3}}\right)^6+\left(\frac{r_1}{r_{d1}}\right)^6\right]}{1-E_1+E_1\left[\left(\frac{1}{2}\right)^6+\left(\frac{r_1}{r_{d3}}\right)^6+\left(\frac{r_1}{r_{d1}}\right)^6\right]},\frac{E_1\left[\left(\frac{r_1}{r_2}\right)^6+\left(\frac{r_1}{r_{d1}}\right)^6+1\right]}{1+E_1\left[\left(\frac{r_1}{r_2}\right)^6+\left(\frac{r_1}{r_{d1}}\right)^6\right]},$$ $$\frac{E_1\left[\left(\frac{r_1}{r_{d4}}\right)^6+\left(\frac{1}{2}\right)^6+\left(\frac{r_1}{r_2}\right)^6\right]}{1-E_1+E_1\left[\left(\frac{r_1}{r_{d4}}\right)^6+\left(\frac{1}{2}\right)^6+\left(\frac{r_1}{r_2}\right)^6\right]}$$ |
|---|---|---|
| 31. |  | $$\frac{E_1\left[\left(\frac{r_1}{r_{d1}}\right)^6+\left(\frac{r_1}{r_{d2}}\right)^6+\left(\frac{r_1}{r_2}\right)^6\right]}{1-E_1+E_1\left[\left(\frac{r_1}{r_{d1}}\right)^6+\left(\frac{r_1}{r_{d2}}\right)^6+\left(\frac{r_1}{r_2}\right)^6\right]},\frac{E_1\left[1+\left(\frac{r_1}{r_{d3}}\right)^6+\left(\frac{1}{2}\right)^6\right]}{1+E_1\left[\left(\frac{r_1}{r_{d3}}\right)^6+\left(\frac{1}{2}\right)^6\right]},$$ |
| 32. |  | $$\frac{E_1\left[\left(\frac{r_1}{r_2}\right)^6+\left(\frac{r_1}{r_{d1}}\right)^6+\left(\frac{r_1}{r_2}\right)^6\right]}{1-E_1+E_1\left[\left(\frac{r_1}{r_2}\right)^6+\left(\frac{r_1}{r_{d1}}\right)^6+\left(\frac{r_1}{r_2}\right)^6\right]}$$ |
| 33. |  | $$\frac{E_1\left[\left(\frac{r_1}{r_2}\right)^6+\left(\frac{r_1}{r_{d3}}\right)^6 1\right]}{1+E_1\left[\left(\frac{r_1}{r_2}\right)^6+\left(\frac{r_1}{r_{d3}}\right)^6\right]},\frac{E_1\left[1+\left(\frac{r_1}{r_{d3}}\right)^6+\left(\frac{r_1}{r_2}\right)^6\right]}{1+E_1\left[\left(\frac{r_1}{r_{d3}}\right)^6+\left(\frac{r_1}{r_2}\right)^6\right]},\frac{E_1\left[\left(\frac{r_1}{r_2}\right)^6+1+\left(\frac{r_1}{r_2}\right)^6\right]}{1+E_1\left[\left(\frac{r_1}{r_2}\right)^6+1+\left(\frac{r_1}{r_2}\right)^6\right]}$$ |
| 34. |  | |
| 35. |  | $$\frac{E_1\left[\left(\frac{1}{2}\right)^6+\left(\frac{r_1}{r_{d3}}\right)^6+1\right]}{1+E_1\left[\left(\frac{1}{2}\right)^6+\left(\frac{r_1}{r_{d3}}\right)^6\right]},\frac{E_1\left[\left(\frac{r_1}{r_2}\right)^6+\left(\frac{r_1}{r_{d1}}\right)^6+\left(\frac{r_1}{r_{d2}}\right)^6\right]}{1-E_1+E_1\left[\left(\frac{r_1}{r_2}\right)^6+\left(\frac{r_1}{r_{d1}}\right)^6+\left(\frac{r_1}{r_{d2}}\right)^6\right]},$$ |
| 36. |  | $$\frac{E_1\left[\left(\frac{r_1}{r_2}\right)^6+\left(\frac{r_1}{r_{d2}}\right)^6+\left(\frac{r_1}{r_2}\right)^6\right]}{1-E_1+E_1\left[\left(\frac{r_1}{r_2}\right)^6+\left(\frac{r_1}{r_{d2}}\right)^6+\left(\frac{r_1}{r_2}\right)^6\right]}$$ |
| 37. |  | $$\frac{E_1\left[\left(\frac{r_1}{r_2}\right)^6+\left(\frac{1}{2}\right)^6+\left(\frac{r_1}{r_{d3}}\right)^6\right]}{1-E_1+E_1\left[\left(\frac{r_1}{r_2}\right)^6+\left(\frac{1}{2}\right)^6+\left(\frac{r_1}{r_{d3}}\right)^6\right]},\frac{E_1\left[1+\left(\frac{r_1}{r_{d2}}\right)^6+\left(\frac{r_1}{r_2}\right)^6\right]}{1+E_1\left[\left(\frac{r_1}{r_{d2}}\right)^6+\left(\frac{r_1}{r_2}\right)^6\right]},$$ |
| 38. |  | $$\frac{E_1\left[\left(\frac{r_1}{r_{d1}}\right)^6+\left(\frac{r_1}{r_{d3}}\right)^6+\left(\frac{1}{2}\right)^6\right]}{1-E_1+E_1\left[\left(\frac{r_1}{r_{d1}}\right)^6+\left(\frac{r_1}{r_{d3}}\right)^6+\left(\frac{1}{2}\right)^6\right]}$$ |

| | | |
|---|---|---|
| 39. |  | $\dfrac{E_1\left[\left(\frac{1}{2}\right)^6+\left(\frac{r_1}{r_{d3}}\right)^6+1\right]}{1+E_1\left[\left(\frac{1}{2}\right)^6+\left(\frac{r_1}{r_{d3}}\right)^6\right]},\dfrac{E_1\left[\left(\frac{r_1}{r_2}\right)^6+\left(\frac{r_1}{r_{d1}}\right)^6+\left(\frac{r_1}{r_{d2}}\right)^6\right]}{1-E_1+E_1\left[\left(\frac{r_1}{r_2}\right)^6+\left(\frac{r_1}{r_{d1}}\right)^6+\left(\frac{r_1}{r_{d2}}\right)^6\right]},$ |
| 40. |  | $\dfrac{E_1\left[\left(\frac{r_1}{r_2}\right)^6+\left(\frac{r_1}{r_{d2}}\right)^6+\left(\frac{r_1}{r_2}\right)^6\right]}{1-E_1+E_1\left[\left(\frac{r_1}{r_2}\right)^6+\left(\frac{r_1}{r_{d2}}\right)^6+\left(\frac{r_1}{r_2}\right)^6\right]}$ |
| 41. |  | $\dfrac{E_1\left[\left(\frac{r_1}{r_2}\right)^6+\left(\frac{r_1}{r_{d1}}\right)^6+1\right]}{1+E_1\left[\left(\frac{r_1}{r_2}\right)^6+\left(\frac{r_1}{r_{d1}}\right)^6\right]},\dfrac{E_1\left[\left(\frac{r_1}{r_2}\right)^6+\left(\frac{r_1}{r_{d4}}\right)^6+\left(\frac{r_1}{r_2}\right)^6\right]}{1-E_1+E_1\left[\left(\frac{r_1}{r_2}\right)^6+\left(\frac{r_1}{r_{d4}}\right)^6+\left(\frac{r_1}{r_2}\right)^6\right]},$ |
| 42. |  | $\dfrac{E_1\left[\left(\frac{r_1}{r_2}\right)^6+\left(\frac{1}{2}\right)^6+\left(\frac{r_1}{r_{d1}}\right)^6\right]}{1-E_1+E_1\left[\left(\frac{r_1}{r_2}\right)^6+\left(\frac{1}{2}\right)^6+\left(\frac{r_1}{r_{d1}}\right)^6\right]}$ |
| 43. |  | $\dfrac{E_1\left[\left(\frac{r_1}{r_{d1}}\right)^6+1+\left(\frac{r_1}{r_{d2}}\right)^6+\left(\frac{r_1}{r_2}\right)^6\right]}{1+E_1\left[\left(\frac{r_1}{r_{d1}}\right)^6+\left(\frac{r_1}{r_{d2}}\right)^6+\left(\frac{r_1}{r_2}\right)^6\right]},\dfrac{E_1\left[1+\left(\frac{r_1}{r_{d2}}\right)^6+\left(\frac{r_1}{r_{d4}}\right)^6+\left(\frac{1}{2}\right)^6\right]}{1+E_1\left[\left(\frac{r_1}{r_{d2}}\right)^6+\left(\frac{r_1}{r_{d4}}\right)^6+\left(\frac{1}{2}\right)^6\right]}$ |
| 44. |  | |
| 45. |  | $\dfrac{E_1\left[\left(\frac{r_1}{r_{d2}}\right)^6+\left(\frac{r_1}{r_{d4}}\right)^6+\left(\frac{1}{2}\right)^6+\left(\frac{r_1}{r_2}\right)^6\right]}{1-E_1+E_1\left[\left(\frac{r_1}{r_{d2}}\right)^6+\left(\frac{r_1}{r_{d4}}\right)^6+\left(\frac{1}{2}\right)^6+\left(\frac{r_1}{r_2}\right)^6\right]},$ |
| 46. |  | $\dfrac{E_1\left[\left(\frac{r_1}{r_2}\right)^6+\left(\frac{1}{2}\right)^6+\left(\frac{r_1}{r_{d3}}\right)^6+\left(\frac{r_1}{r_{d1}}\right)^6\right]}{1-E_1+E_1\left[\left(\frac{r_1}{r_2}\right)^6+\left(\frac{1}{2}\right)^6+\left(\frac{r_1}{r_{d3}}\right)^6+\left(\frac{r_1}{r_{d1}}\right)^6\right]}$ |

| | | |
|---|---|---|
| 47. |  | $$\frac{E_1\left[\left(\frac{1}{2}\right)^6 + \left(\frac{r_1}{r_{d3}}\right)^6 + \left(\frac{r_1}{r_{d1}}\right)^6 + 1\right]}{1 + E_1\left[\left(\frac{1}{2}\right)^6 + \left(\frac{r_1}{r_{d3}}\right)^6 + \left(\frac{r_1}{r_{d1}}\right)^6\right]}, \frac{E_1\left[\left(\frac{r_1}{r_2}\right)^6 + \left(\frac{r_1}{r_{d1}}\right)^6 + 1 + \left(\frac{r_1}{r_{d2}}\right)^6\right]}{1 + E_1\left[\left(\frac{r_1}{r_2}\right)^6 + \left(\frac{r_1}{r_{d1}}\right)^6 + \left(\frac{r_1}{r_{d2}}\right)^6\right]}$$ |
| 48. |  | |
| 49. |  | $$\frac{E_1\left[\left(\frac{r_1}{r_2}\right)^6 + \left(\frac{r_1}{r_{d3}}\right)^6 + \left(\frac{r_1}{r_{d1}}\right)^6 + 1\right]}{1 + E_1\left[\left(\frac{r_1}{r_2}\right)^6 + \left(\frac{r_1}{r_{d3}}\right)^6 + \left(\frac{r_1}{r_{d1}}\right)^6\right]}, \frac{E_1\left[1 + \left(\frac{r_1}{r_{d2}}\right)^6 + \left(\frac{r_1}{r_{d4}}\right)^6 + \left(\frac{r_1}{r_2}\right)^6\right]}{1 + E_1\left[\left(\frac{r_1}{r_{d2}}\right)^6 + \left(\frac{r_1}{r_{d4}}\right)^6 + \left(\frac{r_1}{r_2}\right)^6\right]}$$ |
| 50. |  | |
| 51. |  | $$\frac{E_1\left[\left(\frac{r_1}{r_2}\right)^6 + 1 + \left(\frac{r_1}{r_{d2}}\right)^6 + \left(\frac{r_1}{r_2}\right)^6\right]}{1 + E_1\left[\left(\frac{r_1}{r_2}\right)^6 + \left(\frac{r_1}{r_{d2}}\right)^6 + \left(\frac{r_1}{r_2}\right)^6\right]}, \frac{E_1\left[\left(\frac{r_1}{r_2}\right)^6 + \left(\frac{1}{2}\right)^6 + \left(\frac{r_1}{r_{d3}}\right)^6 + 1\right]}{1 + E_1\left[\left(\frac{r_1}{r_2}\right)^6 + \left(\frac{1}{2}\right)^6 + \left(\frac{r_1}{r_{d3}}\right)^6\right]}$$ |
| 52. |  | |
| 53. |  | $$\frac{E_1\left[1 + \left(\frac{r_1}{r_{d3}}\right)^6 + \left(\frac{1}{2}\right)^6 + \left(\frac{r_1}{r_2}\right)^6\right]}{1 + E_1\left[\left(\frac{r_1}{r_{d3}}\right)^6 + \left(\frac{1}{2}\right)^6 + \left(\frac{r_1}{r_2}\right)^6\right]}, \frac{E_1\left[\left(\frac{r_1}{r_2}\right)^6 + \left(\frac{r_1}{r_{d1}}\right)^6 + 1 + \left(\frac{r_1}{r_2}\right)^6\right]}{1 + E_1\left[\left(\frac{r_1}{r_2}\right)^6 + \left(\frac{r_1}{r_{d1}}\right)^6 + \left(\frac{r_1}{r_2}\right)^6\right]}$$ |
| 54. |  | |
| 55. |  | $$\frac{E_1\left[1 + \left(\frac{r_1}{r_{d2}}\right)^6 + \left(\frac{1}{2}\right)^6 + \left(\frac{r_1}{r_2}\right)^6\right]}{1 + E_1\left[\left(\frac{r_1}{r_{d2}}\right)^6 + \left(\frac{1}{2}\right)^6 + \left(\frac{r_1}{r_2}\right)^6\right]}, \frac{E_1\left[1 + \left(\frac{r_1}{r_{d2}}\right)^6 + \left(\frac{1}{2}\right)^6 + \left(\frac{r_1}{r_2}\right)^6\right]}{1 + E_1\left[\left(\frac{r_1}{r_{d2}}\right)^6 + \left(\frac{1}{2}\right)^6 + \left(\frac{r_1}{r_2}\right)^6\right]}$$ |
| 56. |  | $$\frac{E_1\left[\left(\frac{r_1}{r_2}\right)^6 + \left(\frac{1}{2}\right)^6 + \left(\frac{r_1}{r_{d1}}\right)^6 + 1\right]}{1 + E_1\left[\left(\frac{r_1}{r_2}\right)^6 + \left(\frac{1}{2}\right)^6 + \left(\frac{r_1}{r_{d1}}\right)^6\right]}, \frac{E_1\left[\left(\frac{r_1}{r_2}\right)^6 + \left(\frac{1}{2}\right)^6 + \left(\frac{r_1}{r_{d1}}\right)^6 + 1\right]}{1 + E_1\left[\left(\frac{r_1}{r_2}\right)^6 + \left(\frac{1}{2}\right)^6 + \left(\frac{r_1}{r_1}\right)^6\right]}$$ |

| 57. |  | $$\frac{E_1\left[\left(\frac{r_1}{r_2}\right)^6 + \left(\frac{r_1}{r_{d1}}\right)^6 + \left(\frac{r_1}{r_{d2}}\right)^6 + \left(\frac{r_1}{r_2}\right)^6\right]}{1 - E_1 + E_1\left[\left(\frac{r_1}{r_2}\right)^6 + \left(\frac{r_1}{r_{d1}}\right)^6 + \left(\frac{r_1}{r_{d2}}\right)^6 + \left(\frac{r_1}{r_2}\right)^6\right]},$$ $$\frac{E_1\left[\left(\frac{r_1}{r_2}\right)^6 + \left(\frac{r_1}{r_{d1}}\right)^6 + \left(\frac{r_1}{r_{d2}}\right)^6 + \left(\frac{r_1}{r_2}\right)^6\right]}{1 - E_1 + E_1\left[\left(\frac{r_1}{r_2}\right)^6 + \left(\frac{r_1}{r_{d1}}\right)^6 + \left(\frac{r_1}{r_{d2}}\right)^6 + \left(\frac{r_1}{r_2}\right)^6\right]}$$ |
|-----|-----|-----|
| 58. |  | |
| 59. |  | $$\frac{E_1\left[\left(\frac{r_1}{r_2}\right)^6 + \left(\frac{1}{2}\right)^6 + \left(\frac{r_1}{r_{d3}}\right)^6 + \left(\frac{r_1}{r_{d1}}\right)^6 + 1\right]}{1 + E_1\left[\left(\frac{r_1}{r_2}\right)^6 + \left(\frac{1}{2}\right)^6 + \left(\frac{r_1}{r_{d3}}\right)^6 + \left(\frac{r_1}{r_{d1}}\right)^6\right]}$$ |
| 60. |  | |
| 61. |  | $$\frac{E_1\left[\left(\frac{r_1}{r_2}\right)^6 + \left(\frac{r_1}{r_{d1}}\right)^6 + 1 + \left(\frac{r_1}{r_{d2}}\right)^6 + \left(\frac{r_1}{r_2}\right)^6\right]}{1 + E_1\left[\left(\frac{r_1}{r_2}\right)^6 + \left(\frac{r_1}{r_{d1}}\right)^6 + \left(\frac{r_1}{r_{d2}}\right)^6 + \left(\frac{r_1}{r_2}\right)^6\right]}$$ |
| 62. |  | |
| 63. |  | $$\frac{E_1\left[1 + \left(\frac{r_1}{r_{d2}}\right)^6 + \left(\frac{r_1}{r_{d4}}\right)^6 + \left(\frac{1}{2}\right)^6 + \left(\frac{r_1}{r_2}\right)^6\right]}{1 + E_1\left[\left(\frac{r_1}{r_{d2}}\right)^6 + \left(\frac{r_1}{r_{d4}}\right)^6 + \left(\frac{1}{2}\right)^6 + \left(\frac{r_1}{r_2}\right)^6\right]}$$ |
| 64. |  | N/A |

**Table A-2. Parallelogram-shaped hexamer configurations and FRET efficiency for each donor.** Same configurations as in table 2, but with non-significant FRET terms removed.

| Configuration # | Geometric Configurations | FRET Efficiency Per Donor |
|---|---|---|
| 1. |  | 0 |
| 2. |  | $$\frac{E_1\left(\frac{r_1}{r_{d1}}\right)^6}{1-E_1+E_1\left[\left(\frac{r_1}{r_{d1}}\right)^6\right]}, E_1, \frac{E_1\left(\frac{r_1}{r_2}\right)^6}{1-E_1+E_1\left[\left(\frac{r_1}{r_2}\right)^6\right]}$$ |
| 3. |  | |
| 4. |  | $$\frac{E_1\left(\frac{r_1}{r_{d1}}\right)^6}{1-E_1+E_1\left[\left(\frac{r_1}{r_{d1}}\right)^6\right]}, E_1, \frac{E_1\left(\frac{r_1}{r_{d2}}\right)^6}{1-E_1+E_1\left[\left(\frac{r_1}{r_{d2}}\right)^6\right]}, \frac{E_1\left(\frac{r_1}{r_2}\right)^6}{1-E_1+E_1\left[\left(\frac{r_1}{r_2}\right)^6\right]},$$ |
| 5. |  | $$\frac{E_1\left(\frac{r_1}{r_2}\right)^6}{1-E_1+E_1\left[\left(\frac{r_1}{r_2}\right)^6\right]}$$ |
| 6. |  | $$E_1, \frac{E_1\left(\frac{r_1}{r_{d1}}\right)^6}{1-E_1+E_1\left[\left(\frac{r_1}{r_{d1}}\right)^6\right]}, \frac{E_1\left(\frac{r_1}{r_2}\right)^6}{1-E_1+E_1\left[\left(\frac{r_1}{r_2}\right)^6\right]}$$ |
| 7. |  | |

| | | |
|---|---|---|
| 8. |  | $$\frac{E_1\left[\left(\frac{r_1}{r_2}\right)^6+\left(\frac{r_1}{r_{d1}}\right)^6\right]}{1-E_1+E_1\left[\left(\frac{r_1}{r_2}\right)^6+\left(\frac{r_1}{r_{d1}}\right)^6\right]},E_1,$$ $$\frac{E_1\left[\left(\frac{r_1}{r_{d1}}\right)^6+\left(\frac{r_1}{r_2}\right)^6\right]}{1-E_1+E_1\left[\left(\frac{r_1}{r_{d1}}\right)^6+\left(\frac{r_1}{r_2}\right)^6\right]},E_1$$ |
| 9. |  | $$E_1,\frac{E_1\left[\left(\frac{r_1}{r_2}\right)^6+\left(\frac{r_1}{r_{d2}}\right)^6\right]}{1-E_1+E_1\left[\left(\frac{r_1}{r_2}\right)^6+\left(\frac{r_1}{r_{d2}}\right)^6\right]},$$ $$E_1,\frac{E_1\left[\left(\frac{r_1}{r_2}\right)^6+\left(\frac{r_1}{r_{d2}}\right)^6\right]}{1-E_1+E_1\left[\left(\frac{r_1}{r_2}\right)^6+\left(\frac{r_1}{r_{d2}}\right)^6\right]}$$ |
| 10. |  | $$\frac{E_1\left(\frac{r_1}{r_{d1}}\right)^6}{1-E_1+E_1\left(\frac{r_1}{r_{d1}}\right)^6},\frac{E_1\left[\left(\frac{r_1}{r_{d1}}\right)^6+1\right]}{1+E_1\left(\frac{r_1}{r_{d1}}\right)^6},\frac{E_1\left[1+\left(\frac{r_1}{r_{d2}}\right)^6\right]}{1+E_1\left(\frac{r_1}{r_{d2}}\right)^6},$$ |
| 11. |  | $$\frac{E_1\left(\frac{r_1}{r_2}\right)^6}{1-E_1+E_1\left(\frac{r_1}{r_2}\right)^6}$$ |
| 12. |  | $$\frac{E_1\left(\frac{r_1}{r_2}\right)^6}{1-E_1+E_1\left(\frac{r_1}{r_2}\right)^6},\frac{E_1\left[1+\left(\frac{r_1}{r_2}\right)^6\right]}{1-E_1+E_1\left(\frac{r_1}{r_2}\right)^6},$$ |
| 13. |  | $$\frac{E_1\left[1+\left(\frac{r_1}{r_2}\right)^6\right]}{1+E_1\left(\frac{r_1}{r_2}\right)^6},\frac{E_1\left(\frac{r_1}{r_{d2}}\right)^6}{1-E_1+E_1\left(\frac{r_1}{r_{d2}}\right)^6}$$ |

160

| | | |
|---|---|---|
| 14. |  | $$\frac{E_1\left(\frac{r_1}{r_{d1}}\right)^6}{1 - E_1 + E_1\left(\frac{r_1}{r_{d1}}\right)^6}, \frac{E_1\left[\left(\frac{r_1}{r_2}\right)^6 + 1\right]}{1 + E_1\left(\frac{r_1}{r_2}\right)^6},$$ |
| 15. |  | $$\frac{E_1\left[\left(\frac{r_1}{r_2}\right)^6 + 1\right]}{1 + E_1\left(\frac{r_1}{r_2}\right)^6}, \frac{E_1\left(\frac{r_1}{r_2}\right)^6}{1 - E_1 + E_1\left(\frac{r_1}{r_2}\right)^6}$$ |
| 16. |  | $$\frac{E_1\left[\left(\frac{r_1}{r_{d1}}\right)^6 + 1\right]}{1 + E_1\left(\frac{r_1}{r_{d1}}\right)^6}, \frac{E_1\left[1 + \left(\frac{r_1}{r_{d2}}\right)^6\right]}{1 + E_1\left(\frac{r_1}{r_{d2}}\right)^6}, \frac{E_1\left(\frac{r_1}{r_{d1}}\right)^6}{1 - E_1 + E_1\left(\frac{r_1}{r_{d1}}\right)^6},$$ |
| 17. |  | $$\frac{E_1\left(\frac{r_1}{r_2}\right)^6}{1 - E_1 + E_1\left(\frac{r_1}{r_2}\right)^6},$$ |
| 18. |  | $$E_1, \frac{E_1\left[\left(\frac{r_1}{r_{d1}}\right)^6 + \left(\frac{r_1}{r_{d2}}\right)^6\right]}{1 - E_1 + E_1\left[\left(\frac{r_1}{r_{d1}}\right)^6 + \left(\frac{r_1}{r_{d2}}\right)^6\right]},$$ |
| 19. |  | $$E_1, \frac{E_1\left[\left(\frac{r_1}{r_2}\right)^6 + \left(\frac{r_1}{r_2}\right)^6\right]}{1 - E_1 + E_1\left[\left(\frac{r_1}{r_2}\right)^6 + \left(\frac{r_1}{r_2}\right)^6\right]}$$ |
| 20. |  | $$\frac{E_1\left[\left(\frac{r_1}{r_2}\right)^6 + \left(\frac{r_1}{r_{d1}}\right)^6\right]}{1 - E_1 + E_1\left[\left(\frac{r_1}{r_2}\right)^6 + \left(\frac{r_1}{r_{d1}}\right)^6\right]},$$ |
| 21. |  | $$\frac{E_1\left[\left(\frac{r_1}{r_{d2}}\right)^6 + \left(\frac{r_1}{r_2}\right)^6\right]}{1 - E_1 + E_1\left[\left(\frac{r_1}{r_{d2}}\right)^6 + \left(\frac{r_1}{r_2}\right)^6\right]}$$ |

| 22. |  | $$\frac{E_1\left[\left(\frac{r_1}{r_2}\right)^6+\left(\frac{r_1}{r_{d1}}\right)^6\right]}{1-E_1+E_1\left[\left(\frac{r_1}{r_2}\right)^6+\left(\frac{r_1}{r_{d1}}\right)^6\right]},\frac{E_1\left[\left(\frac{r_1}{r_{d2}}\right)^6+\left(\frac{r_1}{r_2}\right)^6\right]}{1-E_1+E_1\left[\left(\frac{r_1}{r_{d2}}\right)^6+\left(\frac{r_1}{r_2}\right)^6\right]},$$ $$\frac{E_1\left[\left(\frac{r_1}{r_{d1}}\right)^6+\left(\frac{r_1}{r_2}\right)^6\right]}{1-E_1+E_1\left[\left(\frac{r_1}{r_{d1}}\right)^6+\left(\frac{r_1}{r_2}\right)^6\right]},\frac{E_1\left[\left(\frac{r_1}{r_{d2}}\right)^6+\left(\frac{r_1}{r_2}\right)^6\right]}{1-E_1+E_1\left[\left(\frac{r_1}{r_{d2}}\right)^6+\left(\frac{r_1}{r_2}\right)^6\right]}$$ |
|---|---|---|
| 23. |  | $$\frac{E_1\left[\left(\frac{r_1}{r_{d1}}\right)^6+1+\left(\frac{r_1}{r_2}\right)^6\right]}{1+E_1\left[\left(\frac{r_1}{r_{d1}}\right)^6+\left(\frac{r_1}{r_2}\right)^6\right]},\frac{E_1\left[1+\left(\frac{r_1}{r_{d2}}\right)^6\right]}{1+E_1\left[\left(\frac{r_1}{r_{d2}}\right)^6\right]},\frac{E_1\left[1+\left(\frac{r_1}{r_2}\right)^6\right]}{1+E_1\left(\frac{r_1}{r_2}\right)^6}$$ |
| 24. |  | |
| 25. |  | $$\frac{E_1\left[\left(\frac{r_1}{r_{d1}}\right)^6+1\right]}{1+E_1\left(\frac{r_1}{r_{d1}}\right)^6},\frac{E_1\left[\left(\frac{r_1}{r_{d1}}\right)^6+1+\left(\frac{r_1}{r_{d2}}\right)^6\right]}{1+E_1\left[\left(\frac{r_1}{r_{d1}}\right)^6+\left(\frac{r_1}{r_{d2}}\right)^6\right]},\frac{E_1\left[1+\left(\frac{r_1}{r_{d2}}\right)^6\right]}{1+E_1\left(\frac{r_1}{r_{d2}}\right)^6}$$ |
| 26. |  | |
| 27. |  | $$\frac{E_1\left[\left(\frac{r_1}{r_{d1}}\right)^6+1+\left(\frac{r_1}{r_2}\right)^6\right]}{1+E_1\left[\left(\frac{r_1}{r_{d1}}\right)^6+\left(\frac{r_1}{r_2}\right)^6\right]},\frac{E_1\left[1+\left(\frac{r_1}{r_{d2}}\right)^6\right]}{1+E_1\left(\frac{r_1}{r_{d2}}\right)^6},\frac{E_1\left[1+\left(\frac{r_1}{r_2}\right)^6\right]}{1+E_1\left(\frac{r_1}{r_2}\right)^6}$$ |
| 28. |  | |
| 29. |  | $$\frac{E_1\left(\frac{r_1}{r_{d1}}\right)^6}{1-E_1+E_1\left(\frac{r_1}{r_{d1}}\right)^6},\frac{E_1\left[\left(\frac{r_1}{r_2}\right)^6+\left(\frac{r_1}{r_{d1}}\right)^6+1\right]}{1+E_1\left[\left(\frac{r_1}{r_2}\right)^6+\left(\frac{r_1}{r_{d1}}\right)^6\right]},\frac{E_1\left(\frac{r_1}{r_2}\right)^6}{1-E_1+E_1\left(\frac{r_1}{r_2}\right)^6}$$ |
| 30. |  | |

| | | |
|---|---|---|
| 31. |  | |
| 32. |  | $$\frac{E_1\left[\left(\frac{r_1}{r_{d1}}\right)^6+\left(\frac{r_1}{r_{d2}}\right)^6+\left(\frac{r_1}{r_2}\right)^6\right]}{1-E_1+E_1\left[\left(\frac{r_1}{r_{d1}}\right)^6+\left(\frac{r_1}{r_{d2}}\right)^6+\left(\frac{r_1}{r_2}\right)^6\right]}, E_1, \frac{E_1\left[\left(\frac{r_1}{r_2}\right)^6+\left(\frac{r_1}{r_{d1}}\right)^6+\left(\frac{r_1}{r_2}\right)^6\right]}{1-E_1+E_1\left[\left(\frac{r_1}{r_2}\right)^6+\left(\frac{r_1}{r_{d1}}\right)^6+\left(\frac{r_1}{r_2}\right)^6\right]}$$ |
| 33. |  | |
| 34. |  | $$\frac{E_1\left[\left(\frac{r_1}{r_2}\right)^6+1\right]}{1+E_1\left(\frac{r_1}{r_2}\right)^6}, \frac{E_1\left[1+\left(\frac{r_1}{r_2}\right)^6\right]}{1+E_1\left(\frac{r_1}{r_2}\right)^6}, \frac{E_1\left[\left(\frac{r_1}{r_2}\right)^6+1+\left(\frac{r_1}{r_2}\right)^6\right]}{1+E_1\left[\left(\frac{r_1}{r_2}\right)^6+\left(\frac{r_1}{r_2}\right)^6\right]}$$ |
| 35. |  | |
| 36. |  | $$E_1, \frac{E_1\left[\left(\frac{r_1}{r_2}\right)^6+\left(\frac{r_1}{r_{d1}}\right)^6+\left(\frac{r_1}{r_{d2}}\right)^6\right]}{1-E_1+E_1\left[\left(\frac{r_1}{r_2}\right)^6+\left(\frac{r_1}{r_{d1}}\right)^6+\left(\frac{r_1}{r_{d2}}\right)^6\right]}, \frac{E_1\left[\left(\frac{r_1}{r_2}\right)^6+\left(\frac{r_1}{r_{d2}}\right)^6+\left(\frac{r_1}{r_2}\right)^6\right]}{1-E_1+E_1\left[\left(\frac{r_1}{r_2}\right)^6+\left(\frac{r_1}{r_{d2}}\right)^6+\left(\frac{r_1}{r_2}\right)^6\right]}$$ |
| 37. |  | |
| 38. |  | $$\frac{E_1\left(\frac{r_1}{r_2}\right)^6}{1-E_1+E_1\left(\frac{r_1}{r_2}\right)^6}, \frac{E_1\left[1+\left(\frac{r_1}{r_{d2}}\right)^6+\left(\frac{r_1}{r_2}\right)^6\right]}{1+E_1\left[\left(\frac{r_1}{r_{d2}}\right)^6+\left(\frac{r_1}{r_2}\right)^6\right]},$$ $$\frac{E_1\left(\frac{r_1}{r_{d1}}\right)^6}{1-E_1+E_1\left(\frac{r_1}{r_{d1}}\right)^6}$$ |
| 39. |  | |
| 40. |  | $$E_1, \frac{E_1\left[\left(\frac{r_1}{r_2}\right)^6+\left(\frac{r_1}{r_{d1}}\right)^6+\left(\frac{r_1}{r_{d2}}\right)^6\right]}{1-E_1+E_1\left[\left(\frac{r_1}{r_2}\right)^6+\left(\frac{r_1}{r_{d1}}\right)^6+\left(\frac{r_1}{r_{d2}}\right)^6\right]}, \frac{E_1\left[\left(\frac{r_1}{r_2}\right)^6+\left(\frac{r_1}{r_{d2}}\right)^6+\left(\frac{r_1}{r_2}\right)^6\right]}{1-E_1+E_1\left[\left(\frac{r_1}{r_2}\right)^6+\left(\frac{r_1}{r_{d2}}\right)^6+\left(\frac{r_1}{r_2}\right)^6\right]}$$ |

163

| | | |
|---|---|---|
| 41. |  | $\dfrac{E_1\left[\left(\frac{r_1}{r_2}\right)^6 + \left(\frac{r_1}{r_{d1}}\right)^6 + 1\right]}{1 + E_1\left[\left(\frac{r_1}{r_2}\right)^6 + \left(\frac{r_1}{r_{d1}}\right)^6\right]}, \dfrac{E_1\left[\left(\frac{r_1}{r_{d2}}\right)^6 + \left(\frac{r_1}{r_2}\right)^6\right]}{1 - E_1 + E_1\left[\left(\frac{r_1}{r_{d2}}\right)^6 + \left(\frac{r_1}{r_2}\right)^6\right]},$ |
| 42. |  | $\dfrac{E_1\left[\left(\frac{r_1}{r_2}\right)^6 + \left(\frac{r_1}{r_{d1}}\right)^6\right]}{1 - E_1 + E_1\left[\left(\frac{r_1}{r_2}\right)^6 + \left(\frac{r_1}{r_{d1}}\right)^6\right]}$ |
| 43. |  | $\dfrac{E_1\left[\left(\frac{r_1}{r_{d1}}\right)^6 + 1 + \left(\frac{r_1}{r_{d2}}\right)^6 + \left(\frac{r_1}{r_2}\right)^6\right]}{1 + E_1\left[\left(\frac{r_1}{r_{d1}}\right)^6 + \left(\frac{r_1}{r_{d2}}\right)^6 + \left(\frac{r_1}{r_2}\right)^6\right]}, \dfrac{E_1\left[1 + \left(\frac{r_1}{r_{d2}}\right)^6\right]}{1 + E_1\left(\frac{r_1}{r_{d2}}\right)^6}$ |
| 44. |  | |
| 45. |  | $\dfrac{E_1\left[\left(\frac{r_1}{r_{d2}}\right)^6 + \left(\frac{r_1}{r_2}\right)^6\right]}{1 - E_1 + E_1\left[\left(\frac{r_1}{r_{d2}}\right)^6 + \left(\frac{r_1}{r_2}\right)^6\right]}, \dfrac{E_1\left[\left(\frac{r_1}{r_2}\right)^6 + \left(\frac{r_1}{r_{d1}}\right)^6\right]}{1 - E_1 + E_1\left[\left(\frac{r_1}{r_2}\right)^6 + \left(\frac{r_1}{r_{d1}}\right)^6\right]}$ |
| 46. |  | |
| 47. |  | $\dfrac{E_1\left[\left(\frac{r_1}{r_{d1}}\right)^6 + 1\right]}{1 + E_1\left(\frac{r_1}{r_{d1}}\right)^6}, \dfrac{E_1\left[\left(\frac{r_1}{r_2}\right)^6 + \left(\frac{r_1}{r_{d1}}\right)^6 + 1 + \left(\frac{r_1}{r_{d2}}\right)^6\right]}{1 + E_1\left[\left(\frac{r_1}{r_2}\right)^6 + \left(\frac{r_1}{r_{d1}}\right)^6 + \left(\frac{r_1}{r_{d2}}\right)^6\right]}$ |
| 48. |  | |
| 49. |  | $\dfrac{E_1\left[\left(\frac{r_1}{r_2}\right)^6 + \left(\frac{r_1}{r_{d1}}\right)^6 + 1\right]}{1 + E_1\left[\left(\frac{r_1}{r_2}\right)^6 + \left(\frac{r_1}{r_{d1}}\right)^6\right]}, \dfrac{E_1\left[1 + \left(\frac{r_1}{r_{d2}}\right)^6 + \left(\frac{r_1}{r_2}\right)^6\right]}{1 + E_1\left[\left(\frac{r_1}{r_{d2}}\right)^6 + \left(\frac{r_1}{r_2}\right)^6\right]}$ |

164

| | | |
|---|---|---|
| 50. |  | |
| 51. |  | $$\dfrac{E_1\left[\left(\frac{r_1}{r_2}\right)^6 + 1 + \left(\frac{r_1}{r_{d2}}\right)^6 + \left(\frac{r_1}{r_2}\right)^6\right]}{1 + E_1\left[\left(\frac{r_1}{r_2}\right)^6 + \left(\frac{r_1}{r_2}\right)^6 + \left(\frac{r_1}{r_2}\right)^6\right]} , \dfrac{E_1\left[\left(\frac{r_1}{r_2}\right)^6 + 1\right]}{1 + E_1\left(\frac{r_1}{r_2}\right)^6}$$ |
| 52. |  | |
| 53. |  | $$\dfrac{E_1\left[1 + \left(\frac{r_1}{r_2}\right)^6\right]}{1 + E_1\left(\frac{r_1}{r_2}\right)^6} , \dfrac{E_1\left[\left(\frac{r_1}{r_2}\right)^6 + \left(\frac{r_1}{r_{d1}}\right)^6 + 1 + \left(\frac{r_1}{r_2}\right)^6\right]}{1 + E_1\left[\left(\frac{r_1}{r_2}\right)^6 + \left(\frac{r_1}{r_{d1}}\right)^6 + \left(\frac{r_1}{r_2}\right)^6\right]}$$ |
| 54. |  | |
| 55. |  | $$\dfrac{E_1\left[1 + \left(\frac{r_1}{r_{d2}}\right)^6 + \left(\frac{r_1}{r_2}\right)^6\right]}{1 + E_1\left[\left(\frac{r_1}{r_{d2}}\right)^6 + \left(\frac{r_1}{r_2}\right)^6\right]} , \dfrac{E_1\left[1 + \left(\frac{r_1}{r_{d2}}\right)^6 + \left(\frac{r_1}{r_2}\right)^6\right]}{1 + E_1\left[\left(\frac{r_1}{r_{d2}}\right)^6 + \left(\frac{r_1}{r_2}\right)^6\right]}$$ |
| 56. |  | $$\dfrac{E_1\left[\left(\frac{r_1}{r_2}\right)^6 + \left(\frac{r_1}{r_{d1}}\right)^6 + 1\right]}{1 + E_1\left[\left(\frac{r_1}{r_2}\right)^6 + \left(\frac{r_1}{r_{d1}}\right)^6\right]} , \dfrac{E_1\left[\left(\frac{r_1}{r_2}\right)^6 + \left(\frac{r_1}{r_{d1}}\right)^6 + 1\right]}{1 + E_1\left[\left(\frac{r_1}{r_2}\right)^6 + \left(\frac{r_1}{r_{d1}}\right)^6\right]}$$ |
| 57. |  | $$\dfrac{E_1\left[\left(\frac{r_1}{r_2}\right)^6 + \left(\frac{r_1}{r_{d1}}\right)^6 + \left(\frac{r_1}{r_{d2}}\right)^6 + \left(\frac{r_1}{r_2}\right)^6\right]}{1 - E_1 + E_1\left[\left(\frac{r_1}{r_2}\right)^6 + \left(\frac{r_1}{r_{d1}}\right)^6 + \left(\frac{r_1}{r_{d2}}\right)^6 + \left(\frac{r_1}{r_2}\right)^6\right]},$$ $$\dfrac{E_1\left[\left(\frac{r_1}{r_2}\right)^6 + \left(\frac{r_1}{r_{d1}}\right)^6 + \left(\frac{r_1}{r_{d2}}\right)^6 + \left(\frac{r_1}{r_2}\right)^6\right]}{1 - E_1 + E_1\left[\left(\frac{r_1}{r_2}\right)^6 + \left(\frac{r_1}{r_{d1}}\right)^6 + \left(\frac{r_1}{r_{d2}}\right)^6 + \left(\frac{r_1}{r_2}\right)^6\right]}$$ |
| 58. |  | $$\dfrac{E_1\left[\left(\frac{r_1}{r_2}\right)^6 + \left(\frac{r_1}{r_{d1}}\right)^6 + 1\right]}{1 + E_1\left[\left(\frac{r_1}{r_2}\right)^6 + \left(\frac{r_1}{r_{d1}}\right)^6\right]}$$ |

| | | |
|---|---|---|
| 59. | | |
| 60. | | $\dfrac{E_1\left[\left(\frac{r_1}{r_2}\right)^6 + \left(\frac{r_1}{r_{d1}}\right)^6 + 1 + \left(\frac{r_1}{r_{d2}}\right)^6 + \left(\frac{r_1}{r_2}\right)^6\right]}{1 + E_1\left[\left(\frac{r_1}{2}\right)^6 + \left(\frac{r_1}{r_{d1}}\right)^6 + \left(\frac{r_1}{r_{d2}}\right)^6 + \left(\frac{r_1}{r_2}\right)^6\right]}$ |
| 61. | | |
| 62. | | $\dfrac{E_1\left[1 + \left(\frac{r_1}{r_{d2}}\right)^6 + \left(\frac{r_1}{r_2}\right)^6\right]}{1 + E_1\left[\left(\frac{r_1}{r_{d2}}\right)^6 + \left(\frac{r_1}{r_2}\right)^6\right]}$ |
| 63. | | |
| 64. | | N/A |

## A-2 Expression for the FRET efficiency for circular octamer shaped complexes

So far, I discussed the $E_{app}$ expression for the quaternary structures of linear, square or parallelogram geometries. Just to add a different flavor, a circular octamer oligomer is considered, in this section.
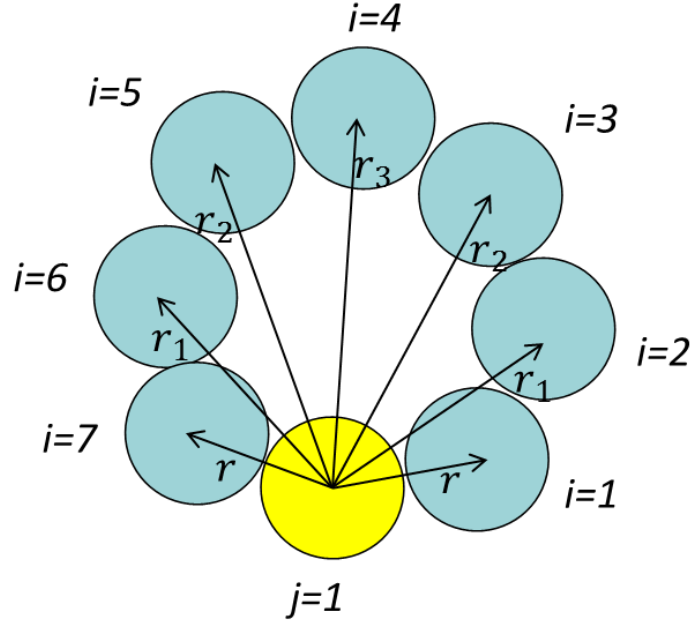
**Figure A- 1 Cconfiguration of a circular octamer model.** The figure shows one fo the confiugration, which has seven donors (turquoise color) and one acceptor (yellow). $r$, $r_1$, $r_2$, $r_3$ and $r_4$ represent the distances between the donors from the acceptor. $i$ and $j$ represent the donors and acceptor respectively.

The FRET efficiency for this confugration is given by

$$E_{app} = \frac{1}{7}\sum_{i=1}^{7} E_{ij}, \tag{2.31}$$

which exapands to the following

$$E_{app} = \frac{1}{7}\left(2\frac{\Gamma^{FRET}/(\Gamma^r + \Gamma^{nr})}{1 + \Gamma^{FRET}/(\Gamma^r + \Gamma^{nr})} + 2\frac{\Gamma_1^{FRET}/(\Gamma^r + \Gamma^{nr})}{1 + \Gamma_1^{FRET}/(\Gamma^r + \Gamma^{nr})} \right.$$

$$\left. + 2\frac{\Gamma_2^{FRET}/(\Gamma^r + \Gamma^{nr})}{1 + \Gamma_2^{FRET}/(\Gamma^r + \Gamma^{nr})} + \frac{\Gamma_3^{FRET}/(\Gamma^r + \Gamma^{nr})}{1 + \Gamma_3^{FRET}/(\Gamma^r + \Gamma^{nr})}\right). \tag{2.32}$$

The factor two in front of the first, second and third fractions account for the fact that FRET efficiencies for donors one and seven, two and six, three and five with one acceptor are identical, assuming circular symmetry of the problem, i.e., that either static or dyanamic averaging of the orientation factor applies[1]. Since the second , third and the fourth term are manifold less than the first term, therefore, in the first order approximation the above equation can be writte as

167

$$E_{app} \simeq \frac{2}{7} \frac{\Gamma^{FRET}/(\Gamma^r + \Gamma^{nr})}{1 + \Gamma^{FRET}/(\Gamma^r + \Gamma^{nr})} \qquad (2.33)$$

But the pairwise FRET efficency is given by

$$E_p = \frac{\Gamma^{FRET}/(\Gamma^r + \Gamma^{nr})}{1 + \Gamma^{FRET}/(\Gamma^r + \Gamma^{nr})} \qquad (2.34)$$

Hence

$$E_{app} \simeq \frac{2}{7} E_p \qquad (2.35)$$

Similarly the expressions for other configurations of ciruclar octamer can be obtained. The configurations which will give distinct FRET efficiency are summarized in Table 2.4.

**Table C-2: Eapp peaks predicted by circular octamer model**

| Peak Number | $E_{app} = f(E_p)$ | Configurations |
|---|---|---|
| 1 | $\frac{2}{7} E_p$ |  |
| 2 | $\frac{1}{3} E_p$ |  |
| 3 | $\frac{2}{3} E_p$ |  |

| | | |
|---|---|---|
| 4 | $\frac{1}{2}E_p$ |  |
| 5 | $\frac{E_p}{3}\frac{2+E_p}{1+E_p}$ |  |
| 6 | $\frac{2E_p}{5}\frac{2+E_p}{1+E_p}$ |  |
| 7 | $\frac{2}{3}E_p$ |  |
| 8 | $\frac{4}{5}E_p$ |  |
| 9 | $\frac{E_p}{2}\frac{2+E_p}{1+E_p}$ |  |

| | | |
|---|---|---|
| 11 | $E_p$ |  |
| 12 | $\dfrac{2E_p}{5}\dfrac{3+2E_p}{1+E_p}$ |  |
| 13 | $\dfrac{2E_p}{3}\dfrac{2+E_p}{1+E_p}$ |  |
| 14 | $\dfrac{2+E_p}{1+E_p}$ |  |

# Appendix B

## B-1 S1R metahistograms fitted by the mixture of dimers and monomers for 8, 10 or 11 donors/pixel

### B-1-1 S1R-no-lignand-treated metahistogram fitted by the mixture of dimers and monomers for 8 or 10 donors/pixel
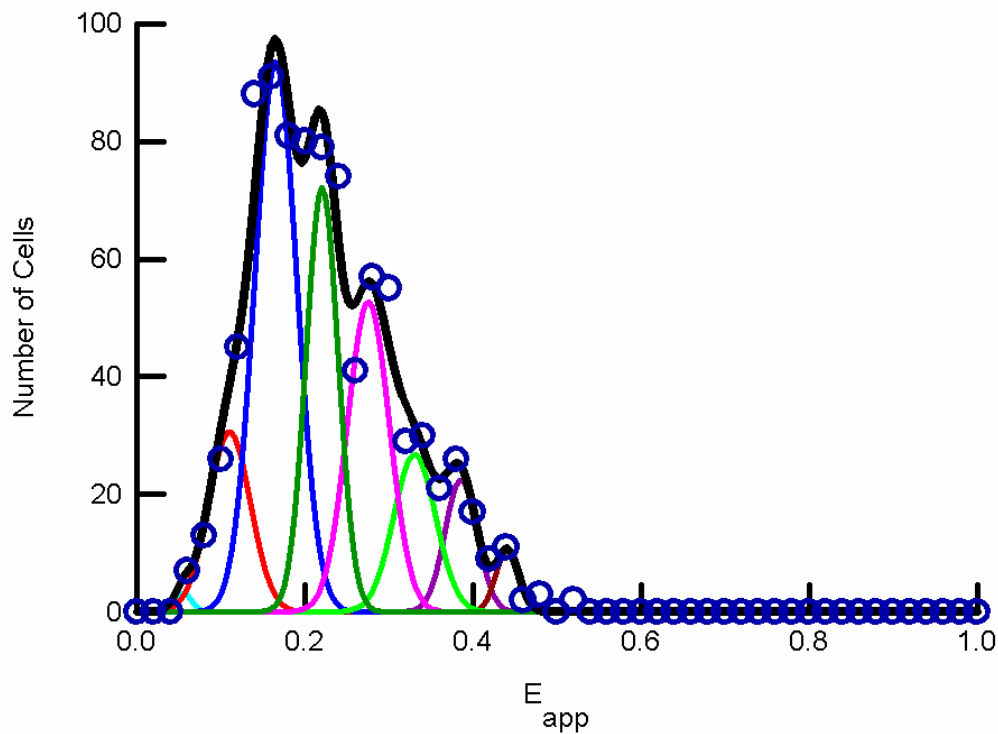


**Figure B-1 Metahistogram for S1R, without ligand treatment, fitted with a theoretical model representing the mixture of dimers and monomers model for 8 donors per pixel.** Reduced fitting residual for the fitting is 24.8.
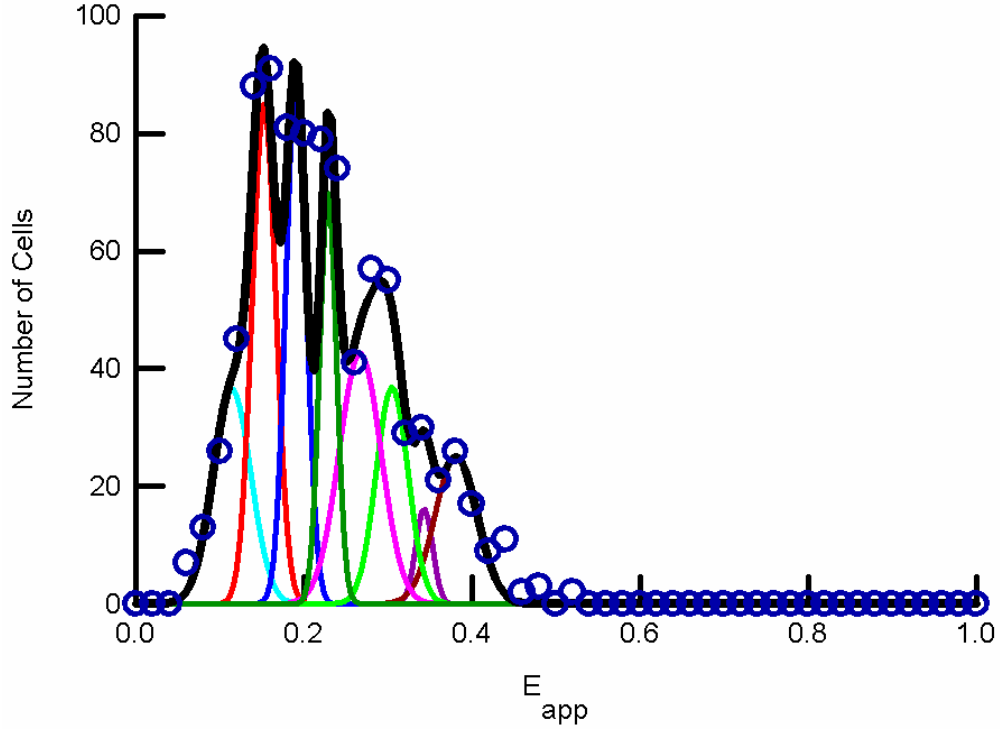
**Figure B-2 Metahistogram for S1R, without ligand treatment, fitted with a theoretical model representing the mixture of dimers and monomers model for 10 donors per pixel.** Reduced fitting residual for the fitting is 37.38.

172
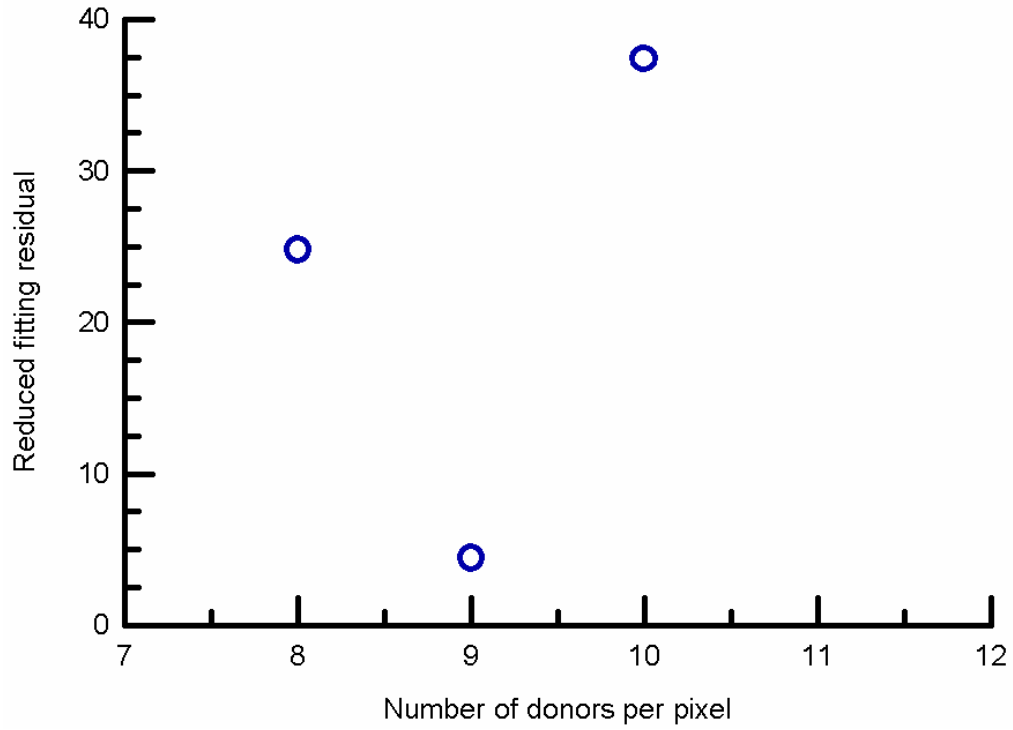
**Figure B-3 Dependence of reduced fitting residual on number of donors per pixel, for S1R, without ligand treatment, metahistogram fitting.**

**Figure B-4 Metahistogram for S1R, treated with haloperidol, fitted with a theoretical model representing the mixture of dimers and monomers model for 8 donors per pixel.** Reduced fitting residual for the fitting is 25.78.

174
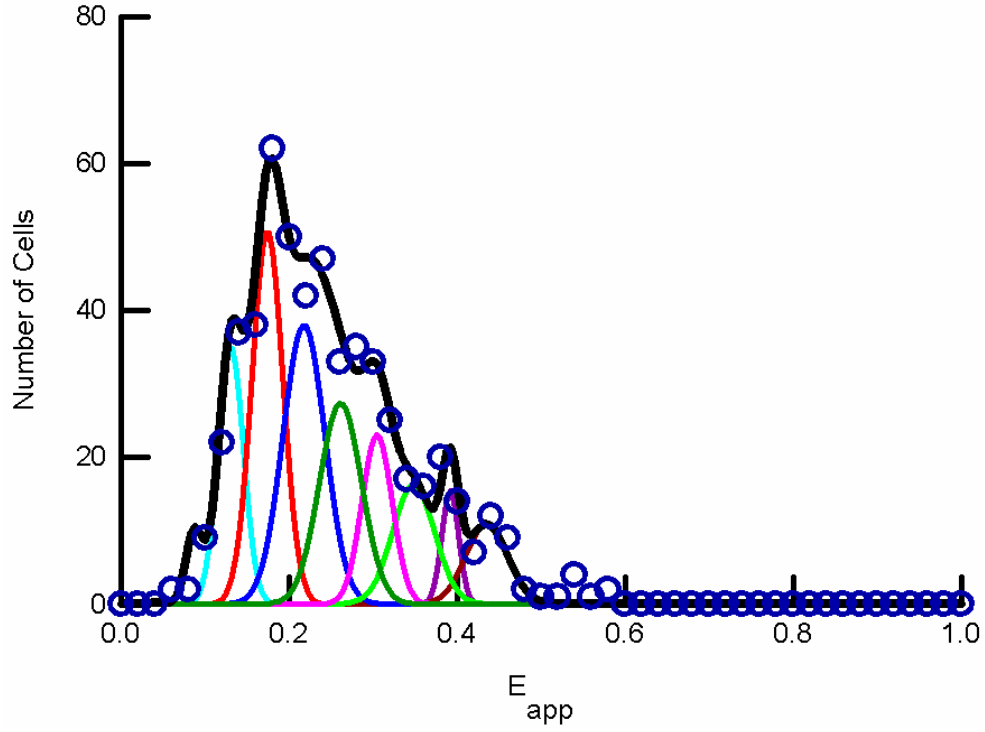
**Figure B-5 Metahistogram for S1R, treated with haloperidol, fitted with a theoretical model representing the mixture of dimers and monomers model for 10 donors per pixel.** Reduced fitting residual for the fitting is 8.95.
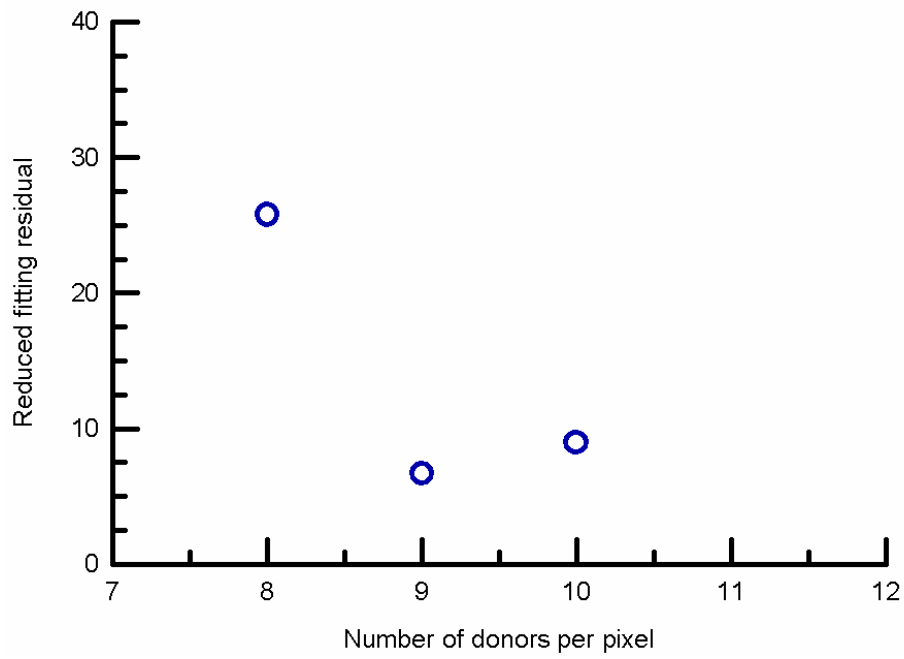
**Figure B-6 Dependence of reduced fitting residual on number of donors per pixel, for S1R, treated with haloperidol, metahistogram fitting.**
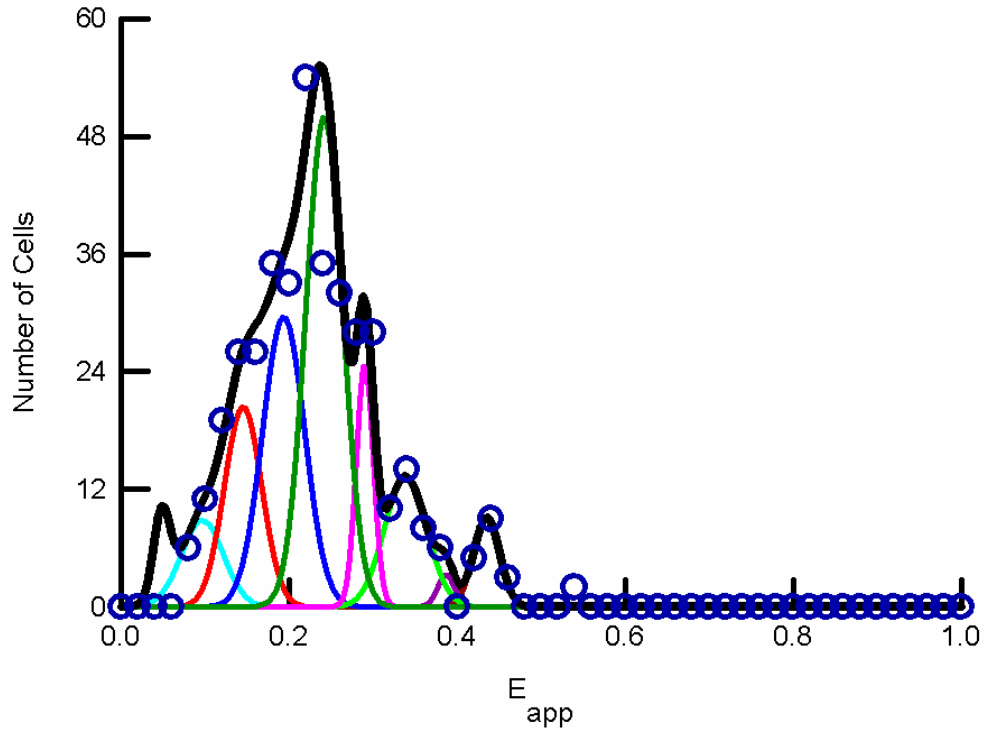
**Figure B-7 Metahistogram for S1R, treated with (+)-pentazocine, fitted with a theoretical model representing the mixture of dimers and monomers model for 9 donors per pixel.** Reduced fitting residual for the fitting is 17.75.
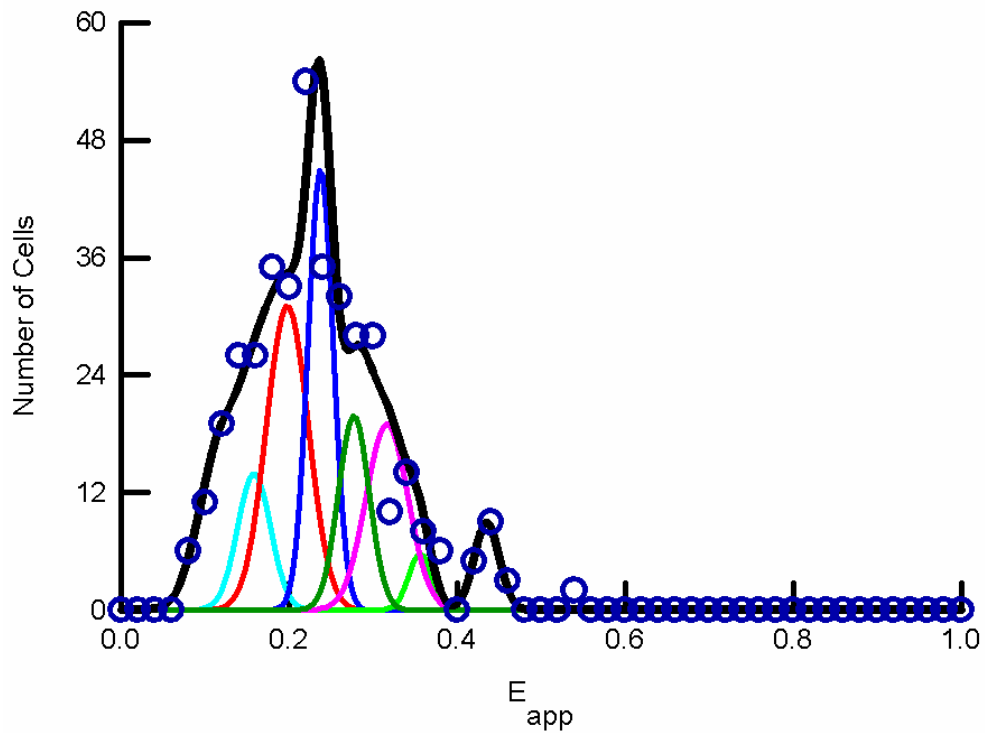
**Figure B-8 Metahistogram for S1R, treated with (+)-pentazocine, fitted with a theoretical model representing the mixture of dimers and monomers model for 11 donors per pixel.** Reduced fitting residual for the fitting is 21.64.
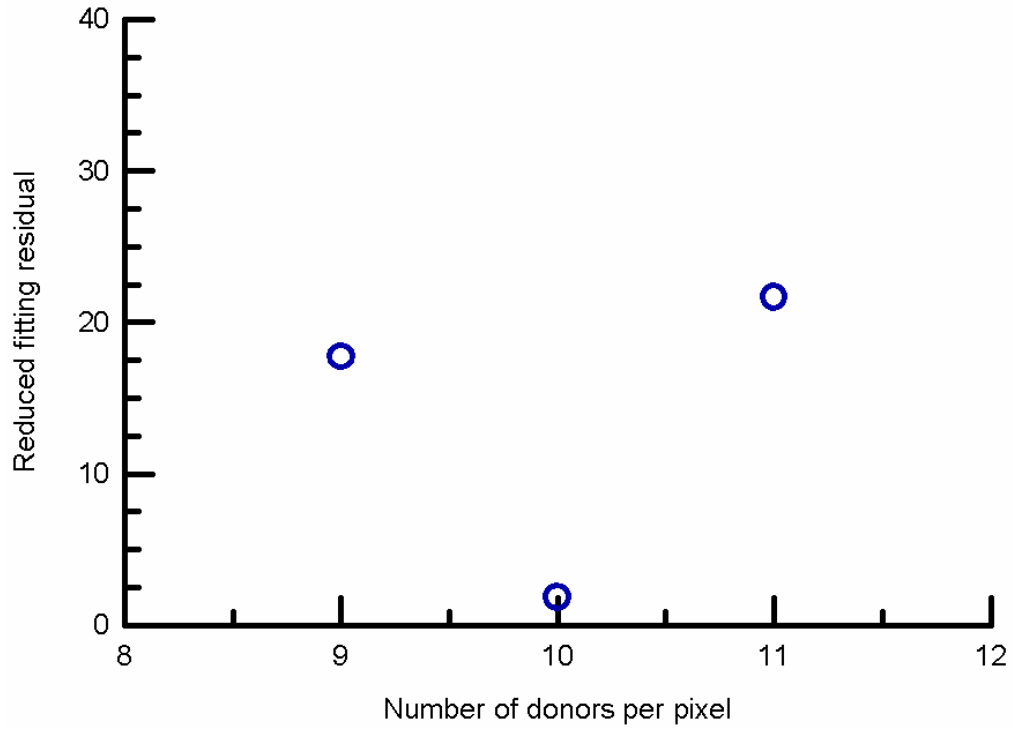
**Figure B-9 Dependence of reduced fitting residual on number of donors per pixel, for S1R, treated with (+)-pentazocine, metahistogram fitting.**

# Appendix C

## C-1 Metahistograms for transfection ratios

Metahistogram for different acceptor transfection ratio ([D]/[A]) show peaks in different regions of the $E_{app}$ range, as shown in Figure C-1. The reason behind is, that different [D]/[A] ratios favor different configurations of the donors and acceptors. For example, a ratio of 3-to-1 will more likely generate the tetrameric complexes with three donors and one acceptors than any other combinations, such as combining in equal number of donors and acceptors within a complex.
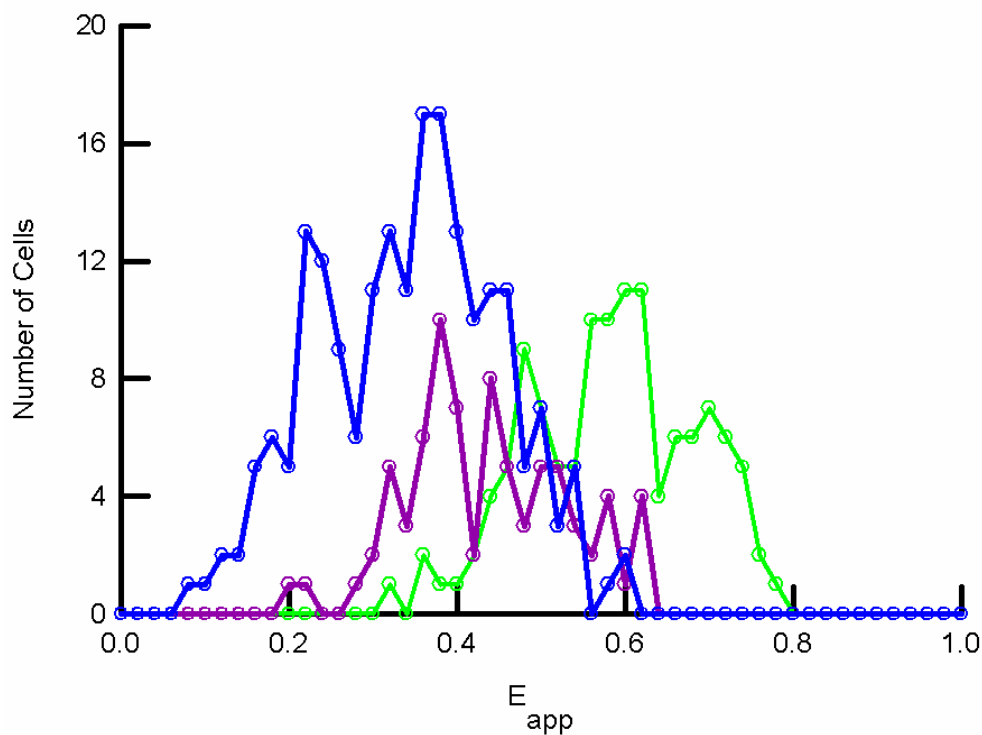


**Figure C- 1  Metahistograms for donor to acceptor transfection ratios. Three transfection ratios are 3-to-1, 1-to-1, and 1-to-3, and the corresponding metahistograms are shown by blue, purple and green curves, respectively.**

For this reason, samples of different transfection ratios were used, to give all the combination of donors and acceptors a fair chance to show up in the histogram peaks, which translate to the metahistogram peaks.

## C-2 Fitting for metahistogram for rhodopsin with dimers and monomers model

Dimers and monomers model was the best fitting model in sogma-1 receptor (S1R) as shown in chapter 5. We tested the same model for rhodopsin as well. The fittings with this model are shown in Figure C-2.
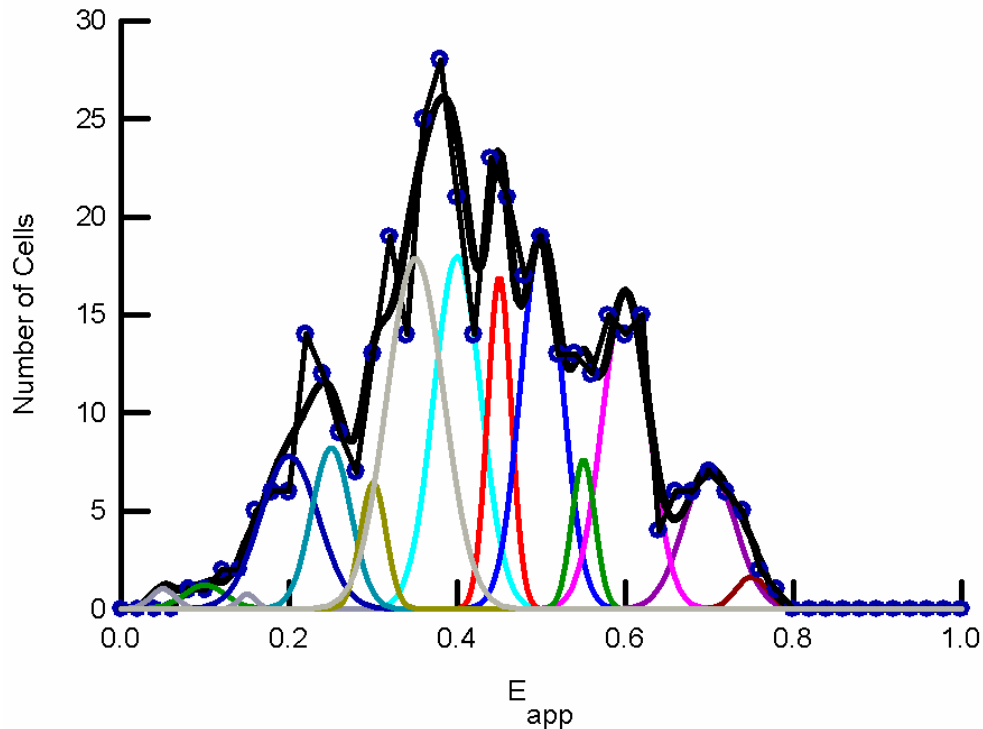


**Figure C- 2 Eapp metahistogram expressing, same as in Figure 6.3, fitted with a mixture of dimer and monomer model.** The values for the number of donors per pixel (*n*) and the FRET efficiency of the dimer ($E_d$) as two of the fitting parameters are 15 and 0.750 respectively. The reduced fitting residual is 6.56.

Based on the reduced fitting residual, this model did not fit as well as the parallelogram model, as shown in Figure 6.3.

## C-3 Error calculation for tetramer to dimer ratio by bootstrapping

$E_{app}$ vs. total concentration ($c$) model was fitted into the data for three, four and five ranges of the total concentration. Tetramer to dimer ratio ($\rho$) was calculated, for the fitting of the model into the three four and five ranges. For each category of ranges, dissociation constant ($K_{t\rightarrow d}$) was calculated. Error in the best fit value for $\rho$ was calculated using bootstrapping method, which is described as follows. For each concentration subrange, 150 subsamples were generated by randomly choosing pairs of data points ($E_{app}$ and $X_A$) with replacement, from the original data of said concentration range. A value of $\rho$ was then obtained for each of the 150 subsamples by fitting each subsample with the model for $E_{app}$ vs. $X_A$, as described in chapter 6. The standard deviation of $\rho$ was then calculated from the distribution of 150 $\rho$ values obtained for a given range. The average and standard deviation of $\rho$ was determined for multiple concentration ranges by the bootstrapping method and these values were fitted with equation C-1 for each category of concentration ranges; the goodness of fit was judged using a reduced Chi-square statistic. This procedure was repeated for the cases when the experimental data was broken into 3, 4, and 5 concentration subranges. The $K_{t\rightarrow d}$ value for the category of concentration subranges with the lowest reduced Chi-square value was accepted as best fit value of $K_{t\rightarrow d}$. Error in $K_{t\rightarrow d}$ was calculated for each data point in $\rho$ vs. $c$ plot, by applying the method of error propagation to the expression of $K_{t\rightarrow d}$ which depends on $\rho$ and $c$ as given below

$$K_{t\rightarrow d} = \frac{c}{4\rho^2 + 2\rho} \tag{C-1}$$

The net error in $K_{t\rightarrow d}$ was calculated by averaging the error in $K_{t\rightarrow d}$ for each data point of $\rho$ vs. $c$ plot.

182
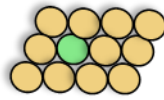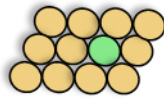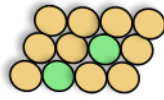
## C-3-1 Values of the reduced Chi-square and the dissociation constant for three and four ranges

The reduced Chi-square value for three and four ranges were 0.74 and 1.67. The values of the dissociation constant for the three and four ranges were $82.20 \pm 36.64$ and $76.01 \pm 30.24$.

## C-4 Parallelogram 12-mer configurations and FRET efficiency for each donor

Only the configurations of the 12-mer of the geometry as shown in Figure 6.9, for which $E_{app}$ value is higher than 0.70 are shown in this table. Donor and acceptor molecules are shown by green and yellow filled circles respectively. These configurations have their $E_{app}$ values falling in the range which contains the metahistogram peaks which could not be fitted by the tetramer model alone.

**Table C- 1 Configurations for 12- mer, with E$_{app}$ > 0.70.** Donor and acceptor molecules are shown with green and yellow filled circles respectively.

| Configuration # | Geometric Configurations | FRET Efficiency Per Donor |
|---|---|---|
| 1. |  | $$\frac{E_1\left[\left(\frac{r_1}{r_{d1}}\right)^6 + \left(\frac{r_1}{r_2}\right)^6 + \left(\frac{r_1}{r_{d2}}\right)^6 + \left(\frac{r_1}{r_{d1}}\right)^6 + \left(\frac{r_1}{r_2}\right)^6 + \left(\frac{r_1}{r_{d2}}\right)^6 + 1 + 1\right]}{1 + E_1 + E_1\left[\left(\frac{r_1}{r_{d1}}\right)^6 + \left(\frac{r_1}{r_2}\right)^6 + \left(\frac{r_1}{r_{d2}}\right)^6 + \left(\frac{r_1}{r_{d1}}\right)^6 + \left(\frac{r_1}{r_2}\right)^6 + \left(\frac{r_1}{r_{d2}}\right)^6 + 1\right]}$$ |
| 2. |  | |
| 3. |  | $$\frac{E_1\left[1 + 1 + \left(\frac{r_1}{r_{d2}}\right)^6 + \left(\frac{r_1}{r_2}\right)^6\right]}{1 + E_1\left[1 + \left(\frac{r_1}{r_{d2}}\right)^6 + \left(\frac{r_1}{r_2}\right)^6\right]},$$ |

183

| | | |
|---|---|---|
| | | $$\frac{E_1\left[\left(\frac{r_1}{r_{d1}}\right)^6 + \left(\frac{r_1}{r_2}\right)^6 + \left(\frac{r_1}{r_{d2}}\right)^6 + 1 + \left(\frac{r_1}{r_{d1}}\right)^6 + \left(\frac{r_1}{r_2}\right)^6 + \left(\frac{r_1}{r_{d2}}\right)^6 + 1\right]}{1 + E_1 + E_1\left[\left(\frac{r_1}{r_{d1}}\right)^6 + \left(\frac{r_1}{r_2}\right)^6 + \left(\frac{r_1}{r_{d2}}\right)^6 + 1 + \left(\frac{r_1}{r_{d1}}\right)^6 + \left(\frac{r_1}{r_2}\right)^6 + \left(\frac{r_1}{r_{d2}}\right)^6\right]}$$ |
| 4. | | $$\frac{E_1\left[\left(\frac{r_1}{r_{d1}}\right)^6 + \left(\frac{r_1}{r_2}\right)^6 + \left(\frac{r_1}{r_{d1}}\right)^6 + \left(\frac{r_1}{r_2}\right)^6 + \left(\frac{r_1}{r_{d2}}\right)^6 + 1 + 1\right]}{1 + E_1 + E_1\left[\left(\frac{r_1}{r_{d1}}\right)^6 + \left(\frac{r_1}{r_2}\right)^6 + \left(\frac{r_1}{r_{d1}}\right)^6 + \left(\frac{r_1}{r_2}\right)^6 + \left(\frac{r_1}{r_{d2}}\right)^6 + 1\right]}\, ,$$ $$\frac{E_1\left[1 + 1 + \left(\frac{r_1}{r_{d1}}\right)^6 + \left(\frac{r_1}{r_{d2}}\right)^6\right]}{1 + E_1\left[1 + \left(\frac{r_1}{r_{d1}}\right)^6 + \left(\frac{r_1}{r_{d2}}\right)^6\right]},$$ |
| 5. | | $$\frac{E_1\left[\left(\frac{r_1}{r_2}\right)^6 + \left(\frac{r_1}{r_{d2}}\right)^6 + \left(\frac{r_1}{r_{d1}}\right)^6 + \left(\frac{r_1}{r_2}\right)^6 + 1\right]}{1 + E_1 + E_1\left[\left(\frac{r_1}{r_2}\right)^6 + \left(\frac{r_1}{r_{d2}}\right)^6 + \left(\frac{r_1}{r_{d1}}\right)^6 + \left(\frac{r_1}{r_2}\right)^6\right]}\, ,$$ $$\frac{E_1\left[\left(\frac{r_1}{r_{d1}}\right)^6 + \left(\frac{r_1}{r_2}\right)^6 + \left(\frac{r_1}{r_{d2}}\right)^6 + 1 + \left(\frac{r_1}{r_{d1}}\right)^6 + \left(\frac{r_1}{r_2}\right)^6 + \left(\frac{r_1}{r_{d2}}\right)^6 + 1\right]}{1 + E_1 + E_1\left[\left(\frac{r_1}{r_{d1}}\right)^6 + \left(\frac{r_1}{r_2}\right)^6 + \left(\frac{r_1}{r_{d2}}\right)^6 + 1 + \left(\frac{r_1}{r_{d1}}\right)^6 + \left(\frac{r_1}{r_2}\right)^6 + \left(\frac{r_1}{r_{d2}}\right)^6\right]}$$ |
| 6. | | $$\frac{E_1\left[\left(\frac{r_1}{r_{d1}}\right)^6 + \left(\frac{r_1}{r_2}\right)^6 + \left(\frac{r_1}{r_{d2}}\right)^6 + \left(\frac{r_1}{r_{d1}}\right)^6 + \left(\frac{r_1}{r_2}\right)^6 + \left(\frac{r_1}{r_{d2}}\right)^6 + 1 + 1\right]}{1 + E_1 + E_1\left[\left(\frac{r_1}{r_{d1}}\right)^6 + \left(\frac{r_1}{r_2}\right)^6 + \left(\frac{r_1}{r_{d2}}\right)^6 + \left(\frac{r_1}{r_{d1}}\right)^6 + \left(\frac{r_1}{r_2}\right)^6 + \left(\frac{r_1}{r_{d2}}\right)^6 + 1\right]}\, ,$$ $$\frac{E_1\left[\left(\frac{r_1}{r_{d1}}\right)^6 + \left(\frac{r_1}{r_2}\right)^6 + \left(\frac{r_1}{r_{d2}}\right)^6 + 1 + \left(\frac{r_1}{r_{d1}}\right)^6 + \left(\frac{r_1}{r_2}\right)^6 + \left(\frac{r_1}{r_{d2}}\right)^6 + 1\right]}{1 + E_1 + E_1\left[\left(\frac{r_1}{r_{d1}}\right)^6 + \left(\frac{r_1}{r_2}\right)^6 + \left(\frac{r_1}{r_{d2}}\right)^6 + 1 + \left(\frac{r_1}{r_{d1}}\right)^6 + \left(\frac{r_1}{r_2}\right)^6 + \left(\frac{r_1}{r_2}\right)^6\right]}$$ |

184

# Curriculum vitae: Ashish Kumar Mishra

**EDUCATION**

- **Doctor of Philosophy (Ph.D.): Physics**                                                    2010- 2017
  University of Wisconsin, Milwaukee, WI, USA
- **Masters of Science (M.S.): Physics**                                                        2006-2009
  Washington State University, Pullman, WA, USA
- **Masters of Science (M.Sc.):  Physics**
  Jawaharlal Nehru University, New Delhi, India                                    2002-2005
- **Bachelor of Science (B.Sc.):  Physics, Mathematics, and Chemistry**
  Lucknow University, Lucknow, U.P., India                                           1997-2001

**CURRENT POSITION**

Visiting Assistant Professor (Physics and Math)                         Jan 2017-present
Viterbo University, La Crosse, WI

**TRAINING**

**Technological:** Laser alignment

**Molecular biology:**  Protein purification, Molecular cloning, DNA amplification.

**Teaching:** Online teaching training, Socrates Facilitator Orientation, by Education Management

Corporation for The Art Institute of Pittsburgh Online Division

**TEACHING EXPERIENCE:**

*University of Wisconsin, Milwaukee*
- Instructor, Math undergraduate level                                        Fall 2016
- Instructor, Physics undergraduate level labs                          Fall 2013-Spring 2016
- Teaching Assistant, Physics undergraduate level discussion classes, algebra and calculus
  based                                                                                      Fall 2010-Spring 2016

*Washington State University, Pullman*
- Teaching Assistant, Physics undergraduate  level lab            Fall 2007-Spring 2009
- Teaching Assistant,   Astronomy undergraduate level lab                     Spring 2007

**RESEARCH EXPERIENCE:**

- **Ph.D. Thesis Research,** University of Wisconsin
  Faculty Advisor: Prof. Valerică Raicu
  Investigating protein complexes structure, with the help of fluorescently labelled proteins,
  And two-photon microscopy, in living cells

- **M.S. Research,** Washington State University
  Faculty Advisor: Prof. Yi Gu
  Characterized ZnO nanowires using transmission Electron Microscopy (TEM)

**SKILLS & EXPERIENCE**

**Engineering Skills:** Tensile strength and compressive strength of materials, fracture analysis,

mechanical grinding, and polishing.

**Microscopy:** Two-photon microscopy, Transmission Electron Microscopy

**Programming Languages:** FORTRAN, MATLAB, Python

**Computer Software Programs**: MS Office, ImageJ

**Forster Resonance Energy Transfer (FRET):** Determination of Oligomer size  and quaternary
Structure of proteins using FRET

**Cellular Biology:** Tissue Culture, Transfection, Transformation

**Protein Interactions:** Investigating protein-protein (homo and hetero) and protein-ligand

interactions using FRET

**WORK EXPERIENCE:**

- *Research scholar*, Mechanical and Material Engineering (MME) Program     2009-2010
  Washington State University, Pullman WA, USA
  Faculty Advisor: Prof. Indranath Dutta

  Developed a proof of concept- of magnetic saw, using combination of magnetic force and
  mechanical loading

## TEACHING INTERESTS

- Physics Undergraduate Lectures and Labs, calculus or algebra based
- Student involvement by assigning them group projects, and using modern teaching methods

## RESEARCH INTERESTS

- Experimental and computational physics
- Biophysics, FRET analysis, data modeling, and optimization techniques

## AWARDS:

- *Chancellor's Graduate Student Award*     Fall 2010, Spring 2011, Spring 2014, Fall 2015
- *Research Excellence Award*                                Spring & Fall 2015
- *Physics Graduate Student/Foundation (DIN) Award*                Spring 2011
- Passed *National Eligibility Test* and was awarded *Junior Research Fellowship* by the Council of Scientific and Industrial Research or CSIR, India                December 2004

## PUBLICATIONS:

1. Mishra, A.K., Megan Gregg, Michael Stoneman, Gabriel Biener, Julie A. Oliver, Joachim Goedhart, Slawomir Filipek,  Paul S. Park, Valerică Raicu, "Quaternary structure of opsin in live cells at body temperature using FRET spectrometry", manuscript submitted.
2. Mishra, A. K., Mavlyutov, T., Singh, D. R., Biener, G., Yang, J., Oliver, J. A., Ruoho, A., and Raicu, V. (2015) "The sigma-1 receptors are present in monomeric and oligomeric forms in living cells in the presence and absence of ligands", *The Biochemical journal 466*, 263-271.
3. P. Kumar, A. Mishra, T. Watt, I. Dutta, D.L.Bourell, U. Sahaym, "*Electromagnetic jigsaw: metal-cutting by combining electromagnetic and mechanical Forces"* Procedia CIRP, 2013. **6**: p. 600-604.
4. Feng Xu, Qingqun Qin, Ashish Mishra, Yi Gu, and Yong Zhu. (2010) "Mechanical properties of ZnO nanowires under different loading modes", *Nano Research 3, 271-280*

## CONFERENCES:

1. <u>Ashish K. Mishra</u> (presenter), Megan Gregg, Michael Stoneman, Gabriel Biener, Julie A. Oliver, Paul S. Park, Valerică Raicu, Graduate Student Research Symposium, "Investigation of Membrane Receptors' Oligomers Using Fluorescence Resonance Energy Transfer and Multiphoton Microscopy in Living Cells", UW-Milwaukee, Dec 2016

2. <u>Ashish K. Mishra</u> (presenter), Megan Gregg, Michael Stoneman, Gabriel Biener, Sugato Ray, Julie A. Oliver, Paul S. Park, Valerică Raicu, "Quaternary structure of rhodopsin *in vivo* at body temperature using multi-wavelength excitations and FRET spectrometry", 3rd Biennial Symposium: Optical Micro-spectroscopy & Molecular Imaging, Milwaukee, WI, August 2015

3. <u>Ashish K. Mishra</u> (presenter), Deo R. Singh, Tae Gyun Kim, Julie A. Oliver, Paul S. Park, and Valerică Raicu, "Determination of Quaternary Structure of Rhodopsin at Room and Body Temperature using Spectral FRET" Poster, *Biophysical Society Annual Meeting*, Philadelphia, PA, February 2013.

4. <u>Ashish K. Mishra</u> (presenter), Deo R. Singh, Tae Gyun Kim, Julie A. Oliver, Paul S. Park, and Valerică Raicu, "Investigation of rhodopsin oligomerization at room and body temperature using spectral FRET" Poster, FASEB, Colorado, CO, June 2012.

5. Deo R. Singh, <u>Ashish K. Mishra</u>, Tae Gyun Kim, Julie A. Oliver, Paul S. Park, and Valerică Raicu, "Quaternary structure of wild type and mutated rhodopsin at room and body temperature using spectral FRET" Oral Presentation, OWLS, Genoa, Italy, July 2012.